MODELLING TRIBOLOGY OF SLIDER AND DISK IN A COMPUTER HARD DRIVE SYSTEM

JILL COLLINS

Doctor of Philosophy

THE UNIVERSITY OF ASTON IN BIRMINGHAM

September 2001

MODELLING TRIBOLOGY OF SLIDER AND DISK IN A COMPUTER HARD DRIVE SYSTEM

JILL COLLINS

Doctor of Philosophy

September 2001

SUMMARY

Issues of wear and tribology are increasingly important in computer hard drives as slider flying heights are becoming lower and disk protective coatings thinner to minimise spacing loss and allow higher areal density. Friction, stiction and wear between the slider and disk in a hard drive were studied using Accelerated Friction Test (AFT) apparatus.

Contact Start Stop (CSS) and constant speed drag tests were performed using commercial rigid disks and two different air bearing slider types.

Friction and stiction were captured during testing by a set of strain gauges. System parameters were varied to investigate their effect on tribology at the head/disk interface. Chosen parameters were disk spinning velocity, slider fly height, temperature, humidity and inter-cycle pause. The effect of different disk texturing methods was also studied. Models were proposed to explain the influence of these parameters on tribology.

Atomic Force Microscopy (AFM) and Scanning Electron Microscopy (SEM) were used to study head and disk topography at various test stages and to provide physical parameters to verify the models. X-ray Photoelectron Spectroscopy (XPS) was employed to identify surface composition and determine if any chemical changes had occurred as a result of testing.

The parameters most likely to influence the interface were identified for both CSS and drag testing. Neural Network modelling was used to substantiate results.

Topographical AFM scans of disk and slider were exported numerically to file and explored extensively. Techniques were developed which improved line and area analysis. A method for detecting surface contacts was also deduced, results supported and explained observed AFT behaviour.

Finally surfaces were computer generated to simulate real disk scans, this allowed contact analysis of many types of surface to be performed. Conclusions were drawn about what disk characteristics most affected contacts and hence friction, stiction and wear.

ACKNOWLEDGEMENTS

I would like to thank my supervisor, Professor John L. Sullivan for his support throughout this project. His encouragement and guidance have proved invaluable in this work.

I also thank my sponsoring company Xyratex (Havant, UK) for the supply of experimental apparatus and samples.

I am also grateful all members of the Surface Science Research Group for helping to create an excellent and warm working environment.

CONTENTS

List of Figures

List of Tables

1 Introduction and Literature Survey

1.1 Introduction

Improvements in disk drive performance have been occurring steadily since the1950's due to a variety of measures [1,2], these have included

- reducing recording head - disk spacing
- improved magnetic materials
- improved signal readback methods
- shrinking drive component dimensions
- positioning of recording head more quickly/with better accuracy

The first of these measures in particular has introduced significant problems of tribology that could previously have been neglected. Low flying heads give improved magnetic performance but can lead to head crash and/or mechanical wear of the interface, however this has been the major factor in increasing recording density. Figure 1.1 shows the relationship between slider fly height and disk/slider protective overcoat thickness with areal density [3], with areal density defined as the product of disk tracks per inch and bits per inch.

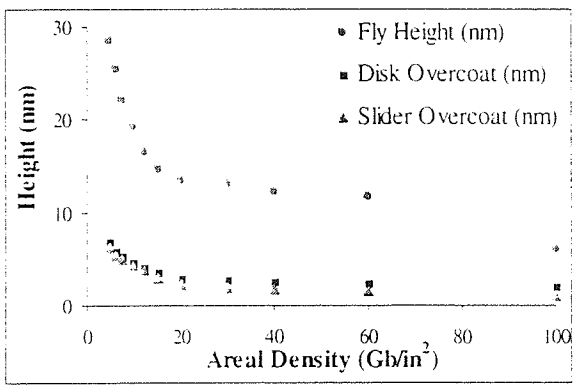

Figure 1.1 Increase in areal density attained by decreasing head - disk spacing

Issues of wear and tribology are increasingly important in computer hard drives as flying heights are becoming lower and protective coatings thinner to minimise spacing loss and allow higher areal density. A detailed literature survey was carried out to investigate the problems of tribology in computer hard drives; this is presented in Chapter 1.

Clearly, if future improvements in hard drive recording density are to be made extensive investigative studies into the factors affecting tribology must be carried out. In this project, Accelerated Friction Test (AFT) apparatus was used to simulate a computer disk drive and perform such investigations.

In Chapter 2, description of tribological testing using standard rigid disks and two different air bearing recording head types is given. Static and dynamic friction were measured during testing using the AFT apparatus. The experimental set-up is also fully described.

Tests were performed in various conditions of temperature and humidity to determine how these affected friction, stiction and wear. In addition, the effects of parameters such as disk velocity, texture and slider type and fly height were studied.

Surface analysis techniques, such as Atomic Force Microscopy (AFM) and Scanning Electron Microscopy (SEM) were used to study head and disk topography. X-ray Photoelectron Spectroscopy (XPS) was employed to identify surface composition and determine if any chemical changes had occurred as a result of testing. These techniques are also described in Chapter 2.

The findings from AFT testing are presented and discussed in Chapter 3, as are surface analysis results.

In Chapter 4 models are proposed for friction and stiction in terms of time, disk velocity, slider fly height, temperature and humidity. Investigation into slider-disk contact was also carried out, with a numerical method to calculate real contact area proposed.

Knowledge from the literature survey is used in conjunction with experimental results to produce an in-depth discussion of the work in Chapter 5. Possible explanations for disk and slider wear are given, with the most significant parameters identified.

Finally, in Chapter 6 conclusions are drawn from the investigation and proposals are made for future research.

1.2 Literature Survey

1.2.1 Magnetic Recording

Techniques for recording data onto magnetic media have improved greatly since their invention for all applications. The concept of rotating memories (by IBM in 1957) was of great importance.

In terms of hard drives, recording patterns today consist of the same alternating magnetic transitions as were seen on early machines, except now each bit of information occupies a tiny fraction of the area. Storing more data on smaller media area is the ultimate goal in magnetic recording.

1.2.1.1 Applications of Magnetic Recording

Computer disks (hard drive and floppy), audio, video and back-up tapes, as well as items such as credit cards all use magnetic recording. The original information can be sound (audiotapes), pictures plus sound (videotapes), or data in the form of coded numbers and letters (computer disks and cards with magnetic strips).

Magnetic storage is the most economical means of data storage since it allows re-usability of media. Today hard disk drives provide nearly half of all computer storage [4]. Although, it is the case that large data sets, such as image data and program files, can benefit from optical and magneto-optical disk storage, the low cost and short access times of the hard disk drives has resulted in a demand for provision of devices. Magnetic storage densities have increased with compound growth rate approaching 60% per annum over the last 10 years [5].

1.2.1.2 Magnetic Recording Process

Magnetic recording is achieved by the interaction between magnetic storage media and a magnetic head in relative motion to each another. Passing a current through a coil wound round a electromagnet induces a flux in the magnet and across the gap in the magnet, this flux aligns the magnetic domains of the magnetic material in the media [6, 7].

Thus, by changing the polarity of the write signal, the magnetic domains in the disk are aligned accordingly. Thus as the signal alternates, data is written in bits of information, eight of these bits constitute one byte. It should be mentioned that 1 bit is not strictly equal to one flux reversal. The process is illustrated schematically in Figure 1.2.

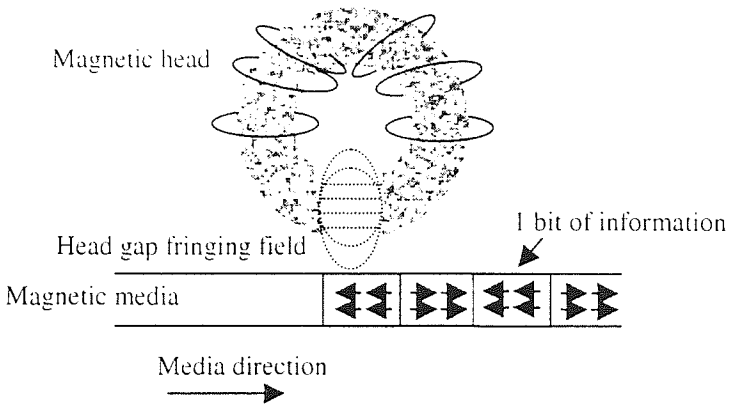

Figure 1.2 Illustrating magnetic recording with magnetic ring head structure

The deep gap field output from the head, H is inversely proportional to the length of gap between the pole tips, g, such that

$$H = \frac{NI\varepsilon}{g} \qquad \textbf{Equation 1.1}$$

where N is the number of turns in the coil, I the current in the coil and ε a scaling factor [8, 9]. The head provides an induced voltage on readback, reflecting the rate of change of magnetisation recorded on the magnetic track. This type of head would be known as inductive. (Note, in Section 1.3.5.3 another method of readback will be discussed).

$$V = -Nv\frac{d\Phi}{dx} \qquad \textbf{Equation 1.2}$$

where N is the number of turns in the coil, v is relative velocity of the head-disk, Φ is the sensed flux and x is a measure of disk position [10].

Hence, the head translates the information from electrical signals into magnetic fields and writes the information on the moving magnetic media. The magnetic information is later read by moving the magnetised regions past the same or another head, which converts the information back into varying electrical signals. Reading does not destroy the information - it can be read again and again. Information can also be erased or overwritten by fresh data.

The type of recording illustrated above is known as longitudinal, where the magnetisation lies in the plane of the media with the direction of magnetisation parallel to the direction of motion. All present commercial disk drive systems operate using longitudinal recording. Although, this configuration is probably the least favourable for achieving the maximum bit density because succeeding bits are magnetised head to head and tail to tail, producing the maximum demagnetising effect on one another [5].

There exists other methods of recording known as transverse and perpendicular. In the former magnetisation lies in the plane of the media but the direction is perpendicular to the direction of motion, this method is very rarely used. In perpendicular recording magnetisation lies perpendicular to the plane of the media, thus demagnetising fields are stabilising rather than de-stabilising and the grains can be larger since they can be situated columnarly, this is illustrated in Figure 1.3. There have been many studies on perpendicular recording but no commercially available systems presently use this method.

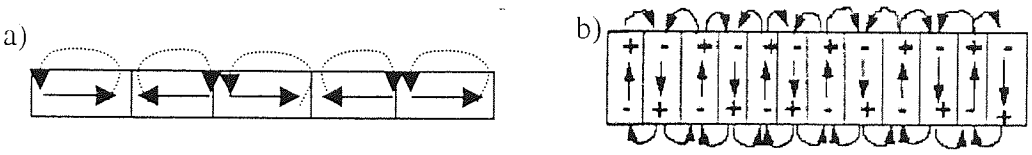

Figure 1.3 Illustrating a) de-stabilizing and b) stabilizing demagnetisation fields as would be experienced in longitudinal and perpendicular recording respectively

Notice, the type of recording described in this section is digital, that is it only involves two distinct states of magnetisation. There exists another type of recording known as analogue which is more complex as it involves many states of magnetisation, this type of recording does not apply to disk drives.

1.2.2 Hard Drive Overview

A hard (or rigid) disk drive is a non-removable, sealed unit which offers permanent storage for a computer's operating system, programmes and data [11].

The first hard disk drive was developed by IBM in 1957; it stored approximately 5 Mb of data on fifty 24" diameter disks. The drive in today's PC typically contains two 2:5" or 3:5" diameter disks and can store at between 10-20 Gb of data.

To illustrate the developments in storage capacity and performance since early days of hard drives, the key features of several different hard drives are shown in Table 1.1. Note, all figures are taken from [4].

Product	Year	Capacity (MB)	Data Rate (MB/s)	Seek Time (ms)	Number of disks	Bits per inch (BPI)	Tracks per inch (TPI)
IBM 2314	1966	29.2	2.5	60	11	221	10
Seagate ST506	1979	5	5	85	2	516	25
Seagate Barracuda	1993	1689	80	8	8	5220	305
Maxtor MXL	1993	105	32	25	2	5801	269
IBM Travelstar	1996	2106	75	12	3	15301	861

Table 1.1 Key features of different hard drive products, BPI and TPI are explained fully in Section 1.2.4.1.

The Seagate ST506 was the first drive based on 5:25" diameter disks, the Seagate Barracuda drive was one of the first drives to operate at >7000 rpm. The Maxtor drive was based on the 1.8" disk format and the IBM Travelstar uses the 2:5" disk format.

Typical hard drive components are shown in Figure 1.4 with descriptions given in the following sections [12]. Note components are usually sealed in casing to keep out dust and other unwanted contaminants.

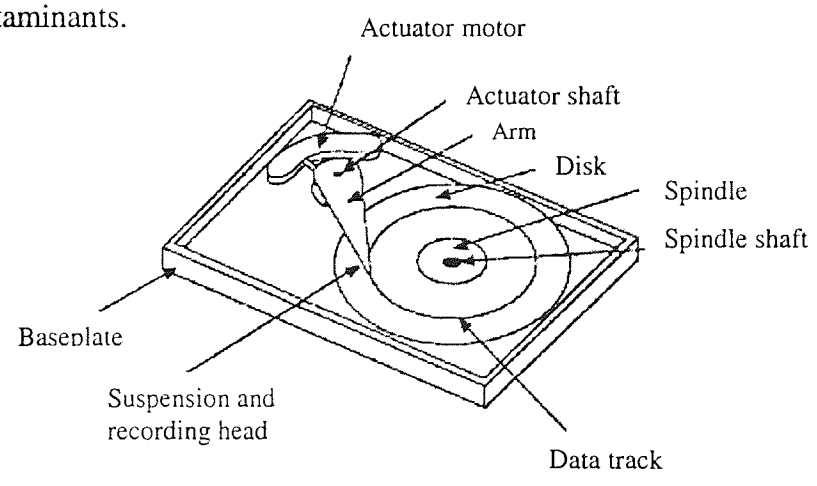

Figure 1.4 Typical hard drive components

1.2.2.1 Disk Stack

The concept of multiple disks in an array was motivated primarily by the desire for greater fault tolerance and higher data transfer rates than those achievable with a single disk, this idea was developed during the 1960's [13,14].

The disk stack comprises of a multiple set of hard disks; these may also be double sided thus doubling capacity. Disk surfaces are numbered in ascending order from the top of the stack, hence surface #0 is always the top surface.

All disks are permanently stored inside the drive and are attached to the spindle at their inner diameter by a clamping mechanism that prevents unwanted movement of disks during drive non-operation [15]. However, it has been reported by Tian and Lee in [16], that this clamping can occasionally lead to disk distortion in the form of local curvature.

During drive production a servo signal will be written onto one of the disk surfaces (usually #0), this provides information (track number, sector number and tracking information) for precise positioning of the head. The servo signal ensures that the head finds the required position and stays there even in the event of external vibration, aerodynamic influences or changes due to temperature. There are various servo methods available, some of these are now discussed.

Dedicated Servo

Here an entire disk surface and head are used to store and read servo information exclusively. The servo head constantly reads the signal and positions itself (and other heads) accordingly. This closed loop method provides fast positioning information but does reduce available storage space significantly.

Embedded Servo

This type is commonly used today, it allows higher storage capacity as the servo signal is written in small wedges between data blocks on the disk surface. It is an open-loop system and is therefore slower than the above method.

Hybrid Servo

As the name suggests, this is a combination of the above methods having a separate servo head and disk surface and embedded servo. This gives the best performance, but worst storage density.

A technique whereby the servo signal was recorded radially on a magnetic layer underneath the circumfrentially recorded data layer on the same track was reported by Tan et al in [17]. Both layers were fabricated from Co-Cr-Ta. Separate heads were used to record the two layers (at different frequencies - the servo signal was at 50 times lower frequency) and an isolation layer of Cr was applied between them. This in effect meant there would be no need for a separate servo surface or track offering an improvement on current servo methods with respect to storage capacity.

1.2.2.2 Recording Heads

Typically a read/write head flies over each rotating disk surface during drive operation. All heads are attached to rigid, lightweight arm by means of a suspension mechanism. All arms are attached to a common carriage, thus heads move in unison across the disk surfaces.

1.2.2.3 Actuator

This moves the read/write heads with precision to the required position on disk. There are two main types in use.

Rotary Actuators

These give a pivotal or arc type movement of the heads giving great precision and also allow more compact design. These are most commonly found in drives today since they also require lower motor power consumption.

Linear Actuators

These move heads radially across the disks, heads are positioned at 90° to track direction. These require higher motor power than rotary actuators so are rarely used today.

Both actuator types are usually driven by Voice-Coil motors under bang-bang control, that is full forward power is applied for half the time required to reach the destination and then full

reverse power, zero velocity is then reached at the required position. Current seek times are between 10-20 milliseconds [18].

The recording head can be place over an incorrect track for a number of reasons, especially at high recording densities, where tracks are narrow. The most common causes of track misregistration (TMR) are spindle runout, disk vibration, thermal track-shift or improperly recorded servo.

1.2.2.4 Spindle Motor

Most of the power required by the disk drive is for the spindle motor which gives rotation of the disk stack to high rotational velocity (currently around 10000 rpm). Due to their smaller, more efficient designs, current drives require relatively little power to keep their platters spinning. However, when the hard disk is first started up, the motor can draw a peak level of power that is more than double this steady state operating value.

High speeds are employed to reduce latency time (usually quoted as the average access time taken for one half revolution of disk) giving faster data transfer rates. Note, high rotational speeds demand rigidity of disks. However, the useful operational speed range and disk thickness are limited by a critical speed phenomenon. Hard disk drives cannot tolerate the large transverse deflections that occur near/at their critical speed [19].

Spindle motors are usually ball or fluid/air bearing type, the latter type has the advantage of an order of magnitude less run out. Also, with fluid/air bearings the bearing stiffness increases at high velocity and the absence of surface contact minimises wear of the motor parts.

1.2.3 Regimes of Hard Drive Recording

Generally, there are three regimes of hard drive recording conventional, true contact and proximity recording. In conventional recording an air bearing forms during flying which completely separates the head and disk. In true contact recording the head and disk are in continuous contact with each other during operation, there is no air bearing support whatsoever. A recently developed technique, proximity recording (also known as near or partial contact recording) is a combination of conventional and total contact recording in that

the trailing edge of the slider flies below the glide avalanche level of the disk. Glide avalanche is the limiting distance below which the head is not able to fly without some contact due to disk texture. Thus, in proximity recording the slider and disk are in close approximation and intermittent contacts between the highest asperities on the disk and the slider are allowed to occur at normal operating velocities.

Typical head/disk spacing values for the three types of recording are given in Table 1.2.

Mode of Recording	Nominal Fly Height (nm)
Conventional	20-40
Proximity	5 - 20
Total contact	<5

Table 1.2 Nominal Flying Heights for 3 Recording Modes

The majority of this work focuses on conventional recording, where other modes are discussed this will be clarified in the text.

1.2.4 Disk Overview

1.2.4.1 Disk Areal Density

Data is held in concentric circles on the disk known as tracks, a section of one track is called a sector. Each sector holds an equal number of bits (usually 512). All tracks have the same amount of sectors even though tracks at the outer diameter of the disk have a much larger area than those at the inside. The current number of sectors per track is typically between 100-300.

The storage capacity or areal density of the disk is usually defined as circumfrential bits per inch (BPI) multiplied by the radial tracks per inch (TPI), overall storage per square inch is measured in Gigabytes (10^9 bits) per square inch. Note this should be multiplied by the area of the disk, then number of disks in the platter and again by two if these disks are double sided to give the overall areal density for the drive.

To gain higher areal density TPI has been increasing steadily, with current values being around 8000. The allowable track density, D_t, was found to be an inverse function of track misregistration (TMR), as follows

$$D_t = \frac{1}{8TMR_{3\sigma}} \qquad \textbf{Equation 1.3}$$

where $TMR_{3\sigma}$ is the value from the probability function of TMR at 3 standard deviation's from the mean.

1.2.4.2 Disk Dimensions

Common sizes of hard disks in use today are 3.5" and increasingly 2.5" and 1.8" diameter. Disks having smaller surface area offer lower head seek time, decrease latency and increase drive performance.

It has also been reported that disk vibration decreases by an amount proportional to the 4^{th} power of disk diameter during rotation, thus smaller disks are also more stable during normal operation [13]. However in the event of the recording head crashing onto the disk lower disk rigidity gives better shock performance because the collision energy is lost by means of vibration of the disk [20]. Since disk rigidity is given as

$$K = \frac{Ct^3}{r^2} \qquad \textbf{Equation 1.4}$$

where t is disk thickness, r is disk radius and C is a constant. Small radius disks would perform worse in this scenario.

1.2.4.3 Recording Disks - Composition and Fabrication

Rigid disks can be divided into two types - thin film and particulate, these are now discussed.

Thin film disks

Thin film disks are exclusively used in high density recording today, they consist of a rigid non-magnetic substrate with a textured base layer and a variety of thin layers deposited upon it. Figure 1.5 illustrates a cross-section of a typical thin film rigid disk [21,18], each layer is discussed below.

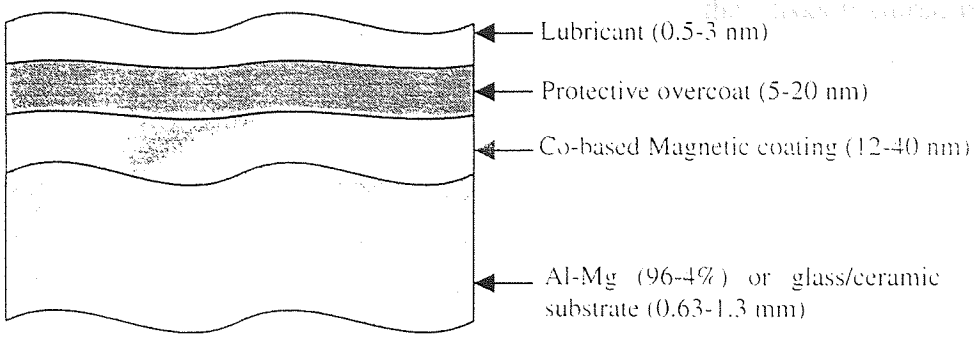

Figure 1.5 Composition of a typical thin-film disk

Substrate

Rigid substrates are required for the high speed operations that occur during hard drive recording. Normally high purity alloys of aluminium, magnesium are used although exploration of glass and ceramics is now taking place. Glass disks are smoother allowing lower head flying height; they also have improved elastic and mechanical properties.

A stable base layer may be applied to the substrate, for example nickel phosphate, this is then polished to required smoothness. If a glass or ceramic substrate is used this base layer is not required as material is already smooth, instead an aluminium nitride layer may be applied to give hardness. Higher hardness of disk gives better shock performance with hardness found to be a more important parameter than rigidity [15].

Substrate Texturing

The need for smooth disks for low flying height is in direct contradiction with the need for roughness to aid friction performance.

Texturing of disks is routinely performed to reduce the amount of surface area that is contact with the recording head. Until around 3 years ago texturing methods have mainly been mechanical with the most common styles being circumfrential and crosshatched.

Disks were mechanically textured using fixed or free abrasive tape method, in the former abrasives are fixed to a tape which is run over disk and in the latter abrasives are continually fed into the interface between a cloth tape and disk surface. Initially disks are textured using 1-3 μm sized abrasive particles to obtain micro-grooves, then smaller (<1 μm) particles to burnish off high asperities. Hard particles of Al_2O_3 or diamond were commonly used in

mechanical texturing. It was reported by Tian and Chao in [22], that disks textured by the free abrasive tape method gave disks with superior performance in low flying and friction tests.

Mirzamaani and Doerner [23] reported that the disk texturing methods previously mentioned are limited to NiP or Al-Mg substrates. A new texturing method was proposed which could be used on any substrate. Here Al nitride was deposited on the substrate layer to form an 'island' type structure. The size and distribution density of these could be controlled by sputtering parameters and the films had amorphous structure.

Sputtering was performed in Ar and then in Ar/N_2. Notice the presence of N_2 gave discreteness to bumps, due to implantation, which was shown advantageous to the interface, Figure 1.6.

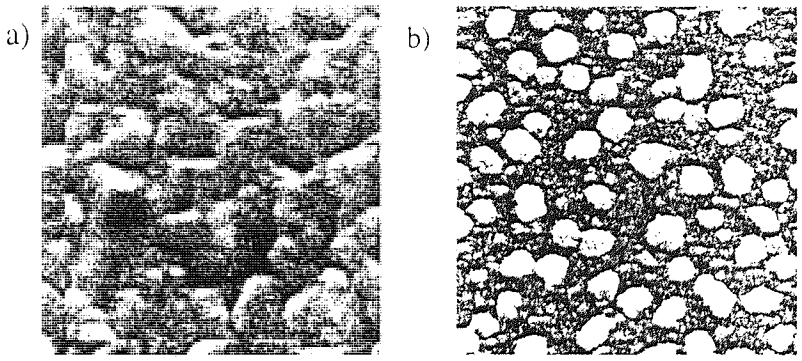

Figure 1.6 SEM images of Al nitride sputtered onto glass disks in a) Ar and b) Ar/N_2 mixture

Full surface abrasion, which textures the whole area of the disk, is now becoming obsolete and instead texturing of the disk landing zone only is becoming widely used [24,25]. Laser texturing can be used to produce disks with a dedicated textured take-off/landing zone at the disk inner diameter, with the remainder of the disk untextured to allow lower flying. Thus, the texture of the landing and data zones can be optimised independently.

The process of laser texturing relies on the fact that if a pulsed laser-beam is incident on a metal surface part of the energy is adsorbed. If the energy is sufficiently intense, it will locally melt the metal and surfaces tension will cause the molten pool to deform. This molten pool instantly solidifies due to the high rate of heat dissipation into the surrounding material when the incident beam is terminated [26].

Laser bumps on a disk are placed in a spiral formation, generated by a train of high repetition rate laser pulses focused to spots on the rotating disk surface. Various bump shapes are given by varying laser parameters, such as energy, pulse width and beam profile, see Figure 1.7.

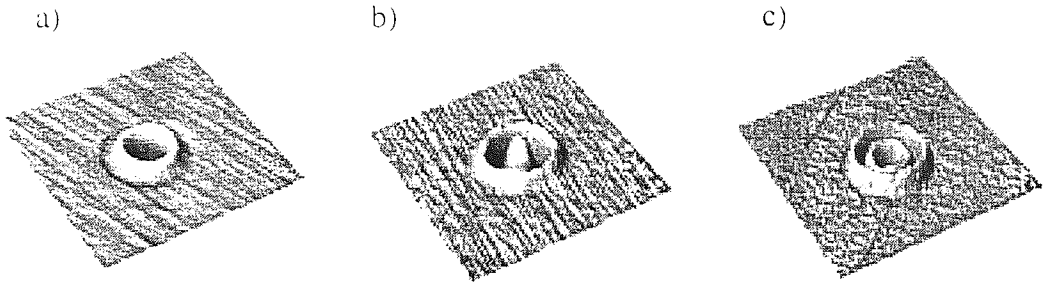

Figure 1.7 Illustrating three different designs of laser bump, a) volcano, b) sombrero and c) w-type

It was also shown that resulting disk roughness was proportional to laser beam current. Bump spacing used in circumfrential and radial directions was typically 100 μm and 50 μm respectively, note this would give bump density of 200/mm^2. Zhao and Talke [27] reported on laser textured disks having bump density 250/mm^2 and stated that uniform of bump height was of critical importance when fabricating media.

Magnetic Layer

The magnetic layer contains cobalt giving magnetic properties and hardness, platinum and/or titanium to expand lattice spacing and increase coercivity (the field required to reduce the magnetisation to zero). This also helped to prevent corrosion. The layer can also contain chromium, which separates magnetic grains and forms a protective oxide layer. The magnetic layer may be deposited on a seed layer - usually chromium - which determines the eventual crystallographic orientation of the magnetic layer. This layer is usually around 50 nm thick [4].

Kitamoto [28] reported that recording media for ultra high densities required Co-Cr thin films with fine microstructure and excellent c-axis orientation. During sputtering low Ar pressure (0.15 mTorr) was used to deposit films composed of closely packed grains without distinct columnar structure. Sometimes atoms did not have sufficient energy to migrate onto the substrate and highly charged Ar atoms would recoil and cause defects in the films giving poor c-axis orientation. A new method known as Facing Target Sputtering (FTS) was reported to give good structural and magnetic properties. Since the plasma was confined between the two targets it was found not to bombard the substrates.

Films with low deviation in orientation angle were deposited by FTS at very low pressure (0.15 mTorr) by optimising the facing distance. Whereas conventional sputtering requires around 1.3 mTorr, meaning the growing films must suffer the heavy bombardment of energetic particles. FTS apparatus also has the advantage of being more compact than conventional, being only $25cm^3$; it still allows uniformity of deposition thickness of under +/- 5%. This means it is large enough to fabricate a 3.5" rigid disk. C-axis orientation was also good with standard deviation being in the order of 3.5-4.5%.

Investigation into using barium ferrite thin-film as magnetic layer has also taken place, Sui et al [29]. This material has the advantage of not requiring a protective overcoat due to its high hardness and excellent chemical properties. Barium ferrite films would support both longitudinal and perpendicular recording due to its columnar structure, however film roughness must be reduced before becoming commercially available.

Disk Overcoat

Protection of the magnetic layer from corrosion and destructive slider contacts are the two major functions of any disk overcoat [30].

Huu et al [31] reported that diamond-like-carbon (DLC) and other hard carbon films gave unique combination of excellent technological properties, such as high hardness, good wear resistance and low coefficient of friction.

Amorphous Carbon Nitride (CN) films deposited on thin-film disks were found to have advantages over the DLC carbon overcoats currently used with respect to durability, nano-indentation hardness and surface morphology [32]. The improved performance was attributed their good surface finish, better mechanical properties and good adhesion to the substrate.

However the nitrogen component was shown to introduce voids in the CN film. Chemical analysis of CN overcoated disk revealed 1% Co signal (from 'naked' magnetic layer). Thus, continuity of coverage had not been achieved.

With respect to scratch resistance, hydrogenated carbon overcoats were found to perform better than carbon or CN films [30]. This was attributed to films being deposited using an ion-

beam deposition (IBD) technique which gave high sp_3 bonding content which was known to enhance wear performance. In addition, finished disks had low defect density.

Koinkar and Bhushan [33] further studied carbon overcoat deposition methods, namely sputtering, ion beam and cathodic arc, both AFM and Lateral Force Microscopy (LFM) were used to determine surface roughness, microfriction, microscratch and microwear. Nano-indentation was performed to investigate hardness of films. The findings will now be discussed.

Sputtered surfaces were found to be rougher than ion beam or cathodic arc, but associated friction forces were lower. Particulates were observed on sputtered surface, with peaks corresponding to areas of lower friction, this suggested that the high nodules might have incurred some change in structure.

Up to normal force of 60 μN sputtered carbon exhibited the best scratch resistance, above this however the carbon coating breaks catastrophically without warning and the scanning tip penetrated the silicone substrate. Particles were present around the scratch after normal load of 80 μN for sputtered carbon. For the ion beam film scratch depth increased linearly with normal force, with maximum depth of 5 nm at 80 μN. Cathodic arc surfaces showed excellent scratch resistance compared to other two and the surface never broke during testing [33]. This method utilised highly ionised plasma during deposition.

Microwear studies again showed cathodic arc surface to be most resistant, with only a small amount of material removed after 75 test cycles involving scanning with a hard diamond tip. Other surfaces failed long before this (after <10 cycles). For sputtered surface a single test cycle yielded loose travelling debris and eventual penetration of overcoat by tip by the third cycle. The inferior performance of sputtered surface was explained by poor adhesion of carbon to substrate.

Cathodic arc exhibited the highest hardness (24.9 GPa in this experiment) in nano-indentation testing with a normal force of 700 μN, sputtered coating was next hardest at 17.2 GPa but this exhibited poor scratch and wear performance. Ion beam surface was the least hard at 15.2 GPa.

Clearly, the kinetic energy of deposition method had a distinct effect on film behaviour, with coatings deposited under high kinetic energy (i.e. cathodic arc) being more durable and scratch resistant, than those deposited under low kinetic energy (i.e. sputtering). Current hardness of 80 GPa was reported to be achievable using cathodic arc.

A major factor in choosing deposition method was the attraction of the lubricant layer to the applied overcoat. Sputtered DLC overcoats had relatively high graphitic content rich in sp_2 bonds which meant that lubricant bonded well to their surface.

Several other materials have been investigated for use as disk overcoats, Jorgensen [14] reports the use of Zirconia films (ZrO_2) and Suganuma [34] stated that a spin coated SiO_2 overcoat had excellent wear performance.

The tribological behaviour of various disk overcoats is discussed in Section 1.2.6.

Lubricant

Lubricant was applied to finished disks to reduce friction and wear at the interface caused by head-disk contact. Lubricant was usually applied by dip coating disks in a bath of lubricant and solvent solution. Gao et al [35] gave lubricant concentration to be around 0.1%.

Following immersion disks were raised vertically at constant speed from the bath [36]. The relationship between resulting lubricant film thickness, l, and withdrawal speed from the bath was given as

$$l = 4.33\left(\frac{q}{0.2}\right)u^{0.42} \qquad \textbf{Equation 1.5}$$

where u is withdrawal speed (mm/s) and q is the volume concentration of lubricant in the solution. Note, l was measured in nm. Notice, the angle of disk on withdrawal may affect the eventual layer thickness due to surface tension.

Gao et al [37] also gives resulting lubricant thickness to be dependent of the density of the solution which causes drainage of liquid back to the bulk solution and surface tension which modifies the competition between viscous and gravitational forces.

Usually an unbonded layer of lubricant (around 0.5-3 nm) is applied topically over a bonded layer (around 0-2 nm). The eventual lubricant layer usually comprised of between 40-65% mobile phase for conventional recording.

This concept had the advantage of being able protect the disk while self-healing any areas of disk which may become depleted of lubricant during operation [38,39,60]. Lubricant bonding was done thermally, with resulting layer thickness increasing with baking temperature, baking time and initial applied lubricant thickness. The bonded fraction of the lubricant is defined as the part that cannot be removed by solvent washing. However, in very modern systems this dual layer lubricant was of concern since it put an additional limit on head flying height.

Bhushan [40] states that Perfluoropolyether lubricants (PFPE's), such as Z-Dol and AM2001, were chemically stable lubricants and are most commonly used on rigid disks today. Bonding of these is done thermally, for example, by baking dipped disks at 150°C for 30 minutes (baking for longer or at higher temperature will increase the degree of bonding). A totally bonded lubricant film would be obtained by washing the thermally treated film in solvent, which removes the unbonded fraction. Further is given in Section 1.2.6.4.

Particulate disks

Instead of the thin-film layer these disks have a layer of magnetic particles dispersed in a polymeric binder, the particles may be either metal (Co-Cr, Co-Pt-Ni, Co-Pt-Cr) or oxide (γ-Fe_2O_3) and are usually acicular with aspect ratio 9:1. Particles are usually packed in a binder to a ratio of 1:3, with non-magnetic particles such as Al_2O_3 often added to the binder to improve disk abrasion resistance[41,42]. This layer is coated onto a rigid substrate as before, but does not have a protective overcoat. Figure 3.7 shows a sketch of disk composition.

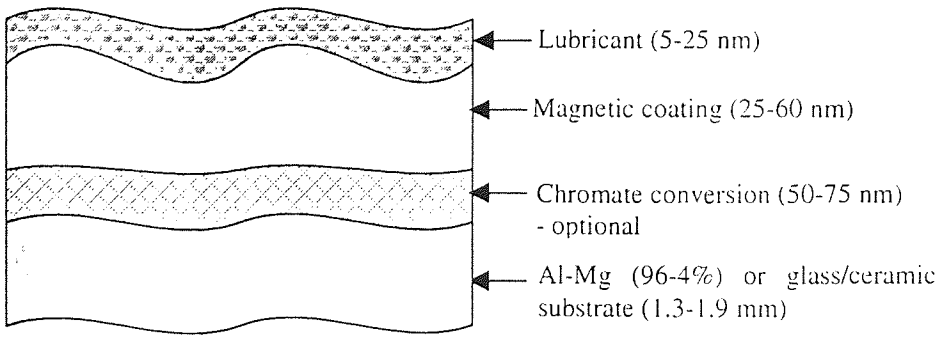

Figure 1.8 Composition of a typical particulate disk

From Figure 1.8 it can be seen that the lubricant layer appears very thick, however Mate et al [43] reported that in particulate media most of the applied lubricant resided below the disk surface in the media porosity with the surface lubricant being molecularly thin.

It was found that coercivity was an inverse function of magnetic particle size due to the length loss effect, Jakusch and Veitch [44]. Since high coercivity is required in recording medium (to retain the recorded signal) the ideal particle size would be very small. Such particles limit coercivity by not being able to be fabricated small enough, hence these disks can not support such high density recording as thin film disks. Another limitation on particle size is the notion of thermal demagnetisation, which can occur at room temperature when particle size falls below 60nm. Additionally, Sato et al [45] reported that reduction in ferromagnetic grain diameter reduced media noise, but unfortunately increased intergranular coupling. Due to these reasons, this type of disk is rarely used nowadays, in fact it reached its recording density limit around 1982.

Patterned Media

Patterned media offers the possibility of substantial extension of achievable bit density. Patterned media comes in several varieties such as perpendicularly magnetised rods or thin film islands magnetised either longitudinally or perpendicularly. There is also a variety that resembles present particulate media (above). Thin film islands in particular offer real promise for future magnetic disk recording offering thermal stability, good signal/noise at high and advantages for tracking [5].

A novel method for pinning magnetic domains on pre-formatted pinning sites has been developed for perpendicular recording thin film media by Wuu et al [46]. The pinning sites were artificial lattices, fabricated by patterning a gold grid on the substrate. An example of patterned domains is shown in Figure 1.9.

Figure 1.9 Example of thin-film patterned media

1.2.4.4 Disk Design for Proximity Recording

Talke [47] stated that disks designed for traditional recording do not have sufficient tribological properties for proximity recording. Required are disks with superior wear characteristics at the data zone along with excellent stiction performance in the landing zone.

Investigated disk materials, such as Ni-P, Co, C were softer than slider materials, thus the disk is most likely to suffer wear during sliding, wear can be either smooth burnishing wear or catastrophic wear. The former type of wear has been proven to be unavoidable in proximity recording.

Agarwal et al [48] stated that disk texture, overcoat and lubrication method were critical parameters in interface performance during proximity recording.

Texture

The shape of disk texture must be optimised for stability and wear, Doan [49] stated that flatter profile texture disks were more suited to proximity recording even where disks have similar average surface heights.

Meyer et al [50] stated that care must be taken with zone textured media (e.g. laser textured disks) as in- situ fly height adjustment may not give the correct flying height for every radius of the disk. However, development of advanced air bearing sliders was shown to reduce this variability to some extent.

Disk Overcoat

Disk overcoats should be very hard with complete carbon coverage critical to avoid corrosion during proximity recording.

Talke [47] compared nitrogenated and hydrogenated carbon overcoats and found that although hydrogenated carbon was harder than nitrogenated carbon, it showed more susceptibility to degradation during proximity sliding. In addition, the nitrogenated overcoat bonded better with the AMXXXX family of lubricants used in proximity recording. Thus, it gave better contact performance at the interface.

Lubricant

Hsiao et al [51] stated that lubricants for proximity recording must have high viscosity, being stiffer these allow the slider to approach the disk surface more closely without fully contacting it.

The traditional method of dip-coating disks in lubricant has given cause for concern since surface conformation of lubricant can add to tribological performance variations. Chao and Russak [52] report on post-lubrication methods such as energy buffing or heating which can alter the confirmation of polymer chains and increase the final coverage of the lubricant which is vital in proximity recording.

Optimum lubricant bonding ratio for proximity recording disks differs from that used for conventional disks [48]. Measured as the ratio of the lubricant remaining on the disk after vapour washing with PF5052 to the original lubricant thickness, this was found to be around 15%. This meant that the largest proportion of lubricant was mobile which is able to replenish any areas of disk depleted of lubricant during operation.

1.2.5 Head Overview

For hard drives the recording head comprises of an air bearing surface (ABS) with magnetic read/write elements situated upon it. this configuration is commonly referred to as the slider. The slider is attached to the actuator cantilever by means of a thin, suspension mechanism usually fabricated from aluminium. This lightweight suspension is laser welded to the slider via a non-magnetic steel flexure.

1.2.5.1 Air Bearing Surface

The ABS is typically made of non-magnetic Al_2O_3-TiC with investigation into alternative materials such as SiC becoming common [53]. Al_2O_3-TiC is a two phase material comprising of around 70% alumina and 30% titanium carbide [54].

The ABS is designed to fly over the disk at a constant height during read/write operations. The leading edge is cut away to develop compression of air and give lift, this tapered area is known as the chamfer, Figure 1.10.

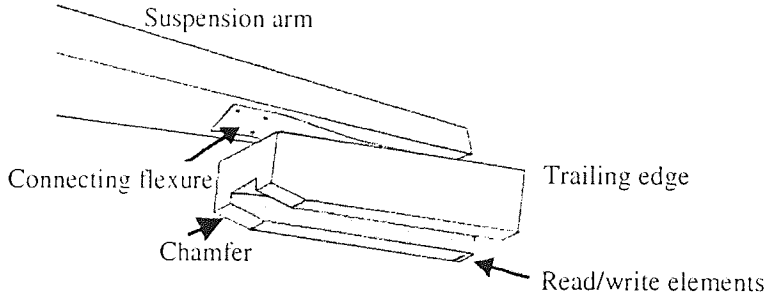

Figure 1.10 Showing read/write element position on trailing edge of slider and chamfer

As the disk rotates air is sucked into the space underneath the slider, due to viscosity of air. The air is compressed to around 1.5 atmospheres as it passes under the chamfer. The pressurised air pushes the slider up. The head is pressed down by a spring suspension.

Thus, the spacing between head and disk is determined by the difference between air pressure and spring tension.

The flexure holds the head at the correct angles, both pitch (defined as the flying angle about the slider's width) and roll (defined as the flying angle about the slider's length), see Figure 1.11. The flexure also accommodates slider movement.

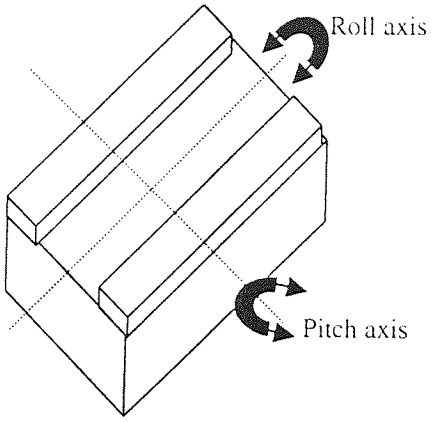

Figure 1.11 Illustrating pitch and roll axes of slider

Early sliders were called taper flat sliders, they were two rail sliders with a chamfer at one end. The chamfer angle used was originally 15 milliradians. It was then found that a shallower angle provided better contact stability, dynamic response and take-off performance. Seagate introduced an 8 milliradian taper in 1988 and set the standard for the rest of the industry at that time. Today even shallower tapers are in use.

Current ABS's have a subamient, recessed region to provide negative pressure or suction force during flying, a recess depth of around 5μm is usually sufficient for this purpose. The advantages of these negative pressure air bearings include lower flying height, less flying height sensitivity to disk velocity and faster take-off [55]. Figure 1.12 shows three common slider designs. Note, slider surfaces are fabricated almost cylindrically to reduce contact with disk when in parked contact.

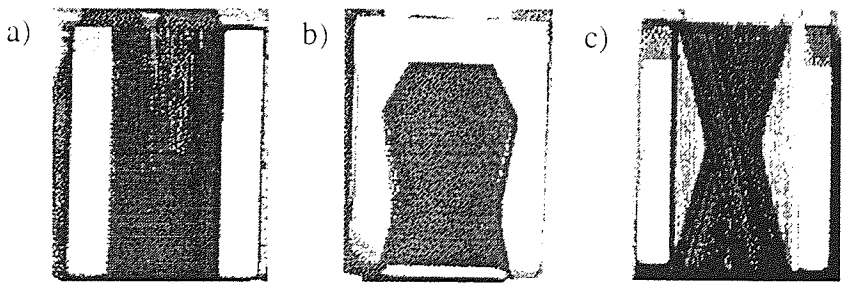

Figure 1.12 Common slider designs a) standard two-rail taper flat slider, b) negative pressure air bearing slider and c) two-rail shaped cavity slider

O'Hara and Bogy [56] used current optimisation techniques including Genetic Algorithms and Simulated Annealing to optimise the design of air bearing sliders. Firstly the two dimensional problem of positioning high-pressure rails on existing slider rails was solved. The algorithms were used to find the independent optimal position for each rail with respect to lowering slider fly height variation from centre to outer radius of disk. A five dimensional problem was also solved using the algorithms, here solutions were found to optimise the shape of the cavity, vertices position and its depth.

Investigation into slider geometry has led to miniaturisation. In recent years slider size has been reduced in all directions and 70%, 50% and 30% scaled versions of the standard full size slider are now common. (full size dimensions are 4.1 by 3.1 by 1.3 mm). Reducing the size of the slider narrower disk track width to be used (i.e. higher TPI) and lower flying heights to be achieved.

Smaller head size also means lower preload which gives less damage if head-crash occurs. Kaneko et al [57] reported on very small sliders (mass <10 mg) which gave almost zero disk wear as compared to 100% sliders, which have mass 3-7g. In addition, since many more sliders can be make from each wafer sheet, smaller sliders are less expensive to produce.

Currently most sliders are made from Al_2O_3-TiC. Due to differences in hardness between alumina and titanium carbide, a differential wear rate exists during lapping. This results in a rougher surface than would be experienced by a single-phase material. A monophase material - SiC - was investigated for use as slider material by Sharma and Talke in [58]. The benefits of this material were physical, thermomechanical and tribological, in particular SiC had high hardness, elastic modulus and low coefficient of thermal expansion which gives lower flash temperatures in the event of disk contacts. The higher elastic modulus gave smaller area of contact and lower friction than Al_2O_3-TiC slider.

Slider material must be compatible with media [59] (such as similar hardness to counteract abrasion) and compliant with read/write element fabrication methods (such as thermal annealing, baking, etc.). In addition, the material must be congruent with entire slider fabrication, such as formation of the ABS, taper lapping and welding of suspension mechanism. Commonly used slider material Al_2O_3-TiC was compared to several other possibilities including Si and sapphire. It was found that sapphire is of similar hardness to

Al_2O_3-TiC but more durable due to its single crystal make-up. Si sliders caused earlier interface failure. Overall, results gave

$$D_{Al2O3\text{-}TiC} \equiv D_{Mn\text{-}Zn} \leq D_{Si} \leq D_{Sapphire} \leq D_{Carbon}$$

Where D was the sliding distance before failure for each material as indicated by its subscript.

Occasionally, the ABS was fabricated from magnetic material, such as Mn-Zn ferrite, then the slider itself actually became part of the read/write element, thus simplifying head design [60].

A recent improvement in slider design has been the application of a hard, chemically inert, DLC overcoat [61]. This gives protection to the read/write elements from hostile environments while improving tribological performance. Since the slider would have similar hardness to the disk there would be less wear at the interface. The slider overcoat could also be textured to further reduce contact with disk [62]. In contrast to disk overcoats, slider overcoat should have low affinity to disk lubricant, thus, overcoats rich in sp_3 bonds were desirable.

1.2.5.2 Slider Design for Proximity and Contact Recording

Contacts at the interface during proximity recording would rapidly wear conventional sliders leading to early catastrophic failure of the drive. Uy [63] reported on the addition of DLC overcoats for ceramic Al_2O_3-TiC sliders to give comparable hardness to disks. Air bearing stiffness was also studied, concluding that low stiffness gave less stress at the interface and gentler wear process with smaller sizes of debris generated. Texturing of the overcoated slider was also found beneficial.

Note, sliders for proximity recording had a contact pad on their trailing edge that housed their read/write elements. They are designed such that the trailing edge flies at a height below the media glide avalanche on a smooth glass disk [50]. Hence, the contact pad would then be in contact on an ordinary textured disk at that flying height due to disk texture, Figure 1.13.

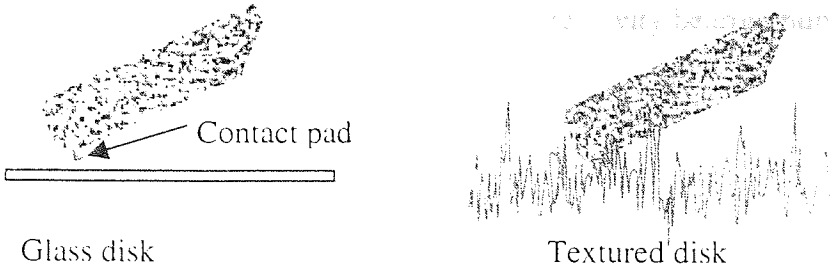

Figure 1.13 Illustrating glide avalanche

There are several slider designs available for proximity recording, the two most common will now be discussed.

Negative Pressure Air Bearings

Most slider designs for proximity recording have air bearing surfaces to provide lifting force and a subambient recessed region to provide suction force, Figure 1.14.

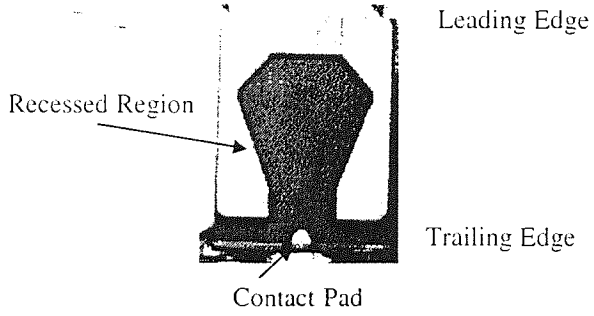

Figure 1.14 Example of a proximity negative pressure air bearing slider

Peng and Hardie [55] reported that it would be useful to find the optimum recess depth for maximum suction force and hence lowest flying height. However, due to different designs and sizes of sliders straight comparison of cavity depths was not appropriate, instead the cavity bearing numbers, Λ, must be compared and not depths. The cavity bearing number was defined as

$$\Lambda = \frac{6\mu UL}{p_a h^2} \qquad \textbf{Equation 1.6}$$

where μ was the viscosity of air, U was bearing velocity which was radius dependant, L was bearing breadth, p_a ambient pressure and h the mean recess depth.

It was found that for maximum suction force during flying cavity bearing number should have value $\Lambda \approx 2$.

Tri-pad Air Bearings

Another type of proximity slider is the tri-pad [49], shown in Figure 1.15.

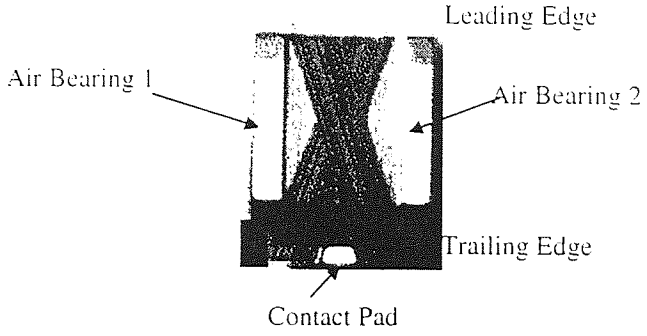

Figure 1.15 An example of a proximity tri-pad air bearing

Here there are three air bearings including the contact pad, which support the majority of the load during flying.

Microfabricated Heads for Contact Recording

For completeness a brief description of slider types for true contact recording will now be given.

Li and Bhushan [64] report on microfabricated sliders, which as the name suggests, are much smaller than conventional sliders (dimensions 17x36x7μm). They consist of and integrated head, flexure and conductor structure and are a step away from air bearing technology. There is a single pole embedded in amorphous hydrogenated carbon that forms the contact pad. Normal load is reduced by 2-3 orders of magnitude, which benefits friction, stiction and wear.

Another type of microfabricated head is the Censtor Flexhead, as reported by Suk [65], this assembly has integrated head and slider but no conventional flexure, instead this was an integrated part of the ABS itself. The dimensions are 15x30x5μm and the mass is <50 mg. Again the small mass is favourable in case of the head being loaded erratically onto disk, it also allows greater disk packing. However, there are handling difficulties due to its size and the absence of a welded flexure makes the interface very stiff.

1.2.5.3 Flying Characteristics

Fly Height

Dynamics during flight of the slider (including suspension and flexure) over disk can be given by the solution to the 2nd order differential equation below [66].

$$Mx''+Cx'+Kx = F \qquad \textbf{Equation 1.7}$$

where M is slider mass, C is suspension damping, K is spring stiffness and F is forcing term (containing air bearing inertia and contact forces where appropriate). Fung et al [67] quoted fly height in current drives as around 25 nm and Komvopoulos [18] reported that very soon sliders will fly only 5-10 nm above disk surface.

There was evidence to suggest that surface fluctuations on the disk surface were followed closely by the head giving variations in flying height [16]. Thus, Equation 1.7 gave an idealised estimate of slider fly height that was independent of disk topography. Also, in light of recent slider miniaturisation, M would become negligible and change the solution to the equation.

Donovan and Bogy [68] reported that when disk linear velocity dropped below 1 m/s, slider fly height decreased sharply. This was due to reduction in slider pitch caused by less airflow at low velocity. Lubrication regime became boundary (see Section 1.2.6.1) and the contacts that occurred caused further slider oscillation, eventually causing collapse of the air bearing.

Schardt et al [69] site other causes of fly height variation as ABS manufacture differences, disk texture, suspension load and disk stack offset. Together these may lead to variations of between 3-7 nm. This does not take dynamic effects such as fly height variation during a high speed seek operation into account. Such variations would cause by changes in the direction and speed of airflow under the air bearing and can be responsible for reduction in fly height of between 2.5 and 12.75 nm.

Air Flow under Bearing

The disk drive industry has long used the simplified version of the Navier-Stokes equation - the Reynolds equation - to predict the pressure under taper flat sliders. It was shown that the assumptions that allow simplifications to be made do not hold for the case of negative pressure air bearing sliders [70]. The simplification procedure was as follows.

The Navier Stokes equation in the x-direction for two dimensional, steady, non-buoyant, incompressible flow is

$$\rho u\frac{\partial u}{\partial x}+\rho v\frac{\partial u}{\partial y}+\frac{\partial p}{\partial x}=\mu\left(\frac{\partial^2 u}{\partial x^2}+\frac{\partial^2 u}{\partial y^2}\right) \qquad \textbf{Equation 1.8}$$

where u and v are velocity parallel and normal to disk motion respectively. x and y are the associated directions. Also, ρ and μ are the density and viscosity of the fluid (here air).

For flow under a slider, viscous flow in the x direction is negligible compared to that in the y direction, thus this term can be dropped as shown.

$$\rho u\frac{\partial u}{\partial x}+\rho v\frac{\partial u}{\partial y}+\frac{\partial p}{\partial x}=\mu\left(\cancel{\frac{\partial^2 u}{\partial x^2}}+\frac{\partial^2 u}{\partial y^2}\right) \qquad \textbf{Equation 1.9}$$

When values are substituted into this for a two rail, taper flat slider it is given that

$$10^5+10^5+\frac{\partial p}{\partial x}=10^{10} \qquad \textbf{Equation 1.10}$$

The first two terms for momentum are small compared to the viscous stress term, thus these can also be dropped [70]. Hence, the Navier-Stokes equation becomes simplified to

$$\frac{\partial p}{\partial x}=\mu\frac{\partial^2 u}{\partial y^2} \qquad \textbf{Equation 1.11}$$

Assuming the viscosity of air is constant this can be solved to give

$$u=\frac{1}{2\mu}\frac{\partial p}{\partial x}y(y-h)+U\left(1-\frac{y}{h}\right) \qquad \textbf{Equation 1.12}$$

where h is the height of slider above disk and U is the velocity in x direction when y=0.

The flow rate in the x direction per unit of depth is therefore given by

$$q_x = \int_0^h u dy \qquad \textbf{Equation 1.13}$$

By continuity of mass, $\frac{\partial q_x}{\partial x} = 0$, applying this the Reynold's equation is formed as shown

$$\frac{\partial}{\partial x}\left(h^3 \frac{\partial \rho}{\partial x} \right) = 6U\mu \frac{\partial h}{\partial x} \qquad \textbf{Equation 1.14}$$

In the case of a negative pressure air bearing with cavity depth 5.1μm, the values in the Navier-Stokes equation become

$$10^5 + 10^3 + \frac{\partial \rho}{\partial x} = 10^7 \qquad \textbf{Equation 1.15}$$

Now the momentum terms are important in relation to the viscosity term and cannot be dropped [70]. Thus, the Reynolds's equation cannot be used to determine the behaviour in the negative pressure cavity.

Numerical results on airflow for negative pressure sliders were presented for the Navier-Stokes and Reynold's model as shown in Figure 1.16.

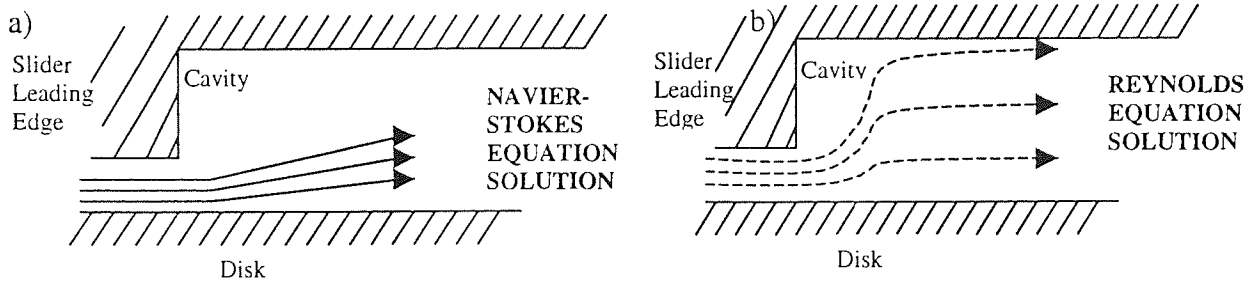

Figure 1.16 Results on air flow under slider cavity as given by a) Navier-Stokes and b) Reynold's equations

In the Reynolds model viscous effects only affected the flow, with air making a 90° degree turn on entering the cavity and travelling to the top of the cavity where it changed direction again. This behaviour decreased pressure significantly.

For the Navier-Stokes solution, a balance of force is observed as air enters the cavity, the momentum force keeps flow following disk direction, whilst viscous force diffuses flow slightly into the cavity. Slight pressure change was given in the cavity.

The conclusion of the work was that Reynold's equation should not be used to predict the flow under air bearing sliders in the presence of large depth variations, such as negative pressure cavities.

Donovan and Bogy [68] also reported that Reynold's equation only held when the slider and disk were almost parallel. However, in reality changes in the air film thickness and slider pitch affected this and the equation frequently became invalid.

1.2.5.4 Recording Head Technology

Inductive Head

In disk drives the magnetic core (fabricated from wear resistant Mn-Zn ferrite) is glass bonded to ceramic (usually alumina) on the extreme trailing edge of the slider between two pole tips. Usually made of Ni-Fe or Permalloy, the pole tips have low coercivity and high permeability (to allow ease of demagnetisation and remagnetisation respectively). Classically, a copper coil would have been wound round the core to generate the write current but more recently this would be applied by sputtering.

The top view of an inductive structure is shown in Figure 1.17

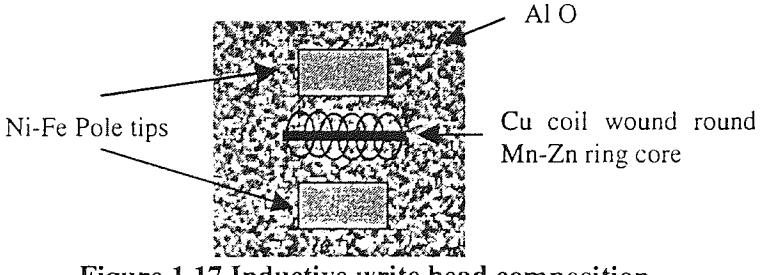

Figure 1.17 Inductive write head composition

Heads are miniaturised using thin-film technology, where layers are deposited using vacuum deposition and photolithographic techniques similar to those used in semiconductor wafer processing. Highly controllable dimensions and characteristics are achieved in this way. The coil windings are deposited on a ceramic base, creating extremely small heads with equally small and precisely measured gaps between the poles.

Han et al [71] reported that ferrite was commonly chosen as pole material since it is good high frequency transducer, however there exists a problem of low saturation magnetisation. Exploration was carried out into using Fe based films with amorphous/nanocrystalline structure and good soft magnetic properties which allow high read/write frequencies. One such film, Fe-Si_3N_4, was found to have low coercivity and high permeability making it a possible choice for pole material.

Induced voltage on signal readback, V, was given by Equation 1.2, where Φ is flux and x is position.

Clearly, voltage was dependent on velocity, the implication of this is that the reading process must take place at the same relative velocity as the writing process. This is the major limitation in the use of inductive heads.

Also, inductive heads use a dual function head, that is, the same element controls both read and write performance, therefore some compromise between the two functions has to be made.

Inductive Write/Magnetoresistive Read Head

One of the most significant innovations in head technology was the development of the Magnetoresistive (MR) read head. This type of head comprises of a MR read element to which an inductive write element is added.

The MR element can not be used for writing, but reads the signal written by a separate inductive head. By incorporating dedicated elements in this way, each part of the head can be independently optimised for best performance. Insulating shield layers of alumina are used each side of the MR element for thermal protection and structural support. The read and write elements can be separate or are more usually combined into one. A schematic of a MR read element is shown in Figure 1.18.

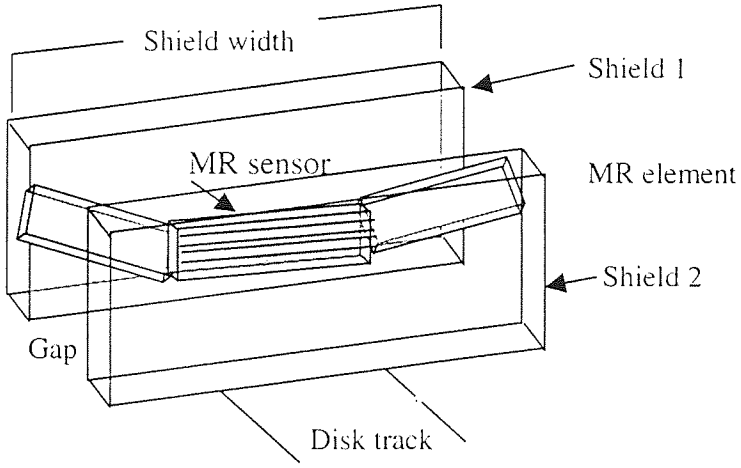

Figure 1.18 Typical MR Head Structure

The MR element does not sense the rate of change of flux, but the presence of flux itself. A change in flux in the medium causes a change in the magnetic direction in the MR sensor. This results in a change in resistance and therefore measured current. Thus, with MR heads, readback voltage is independent of the rotational speed of the disk [8].

For a single layer MR element, the angle of magnetisation ,θ, is related to resistance, R, by the equation

$$R = R_0 + \Delta R \cos^2 \theta \qquad \textbf{Equation 1.16}$$

where R_0 is the initial resistance of the strip and ΔR the change in resistance.

In order to increase areal density, disk track widths have been getting progressively narrower, this has put limitations on the width of the MR intershield spacing - with current values given as around 0.1 μm [72]. Narrowing track widths has also meant that there is less flux available for the read head to sense. However, this has been overcome to some extent by the development of very powerful MR heads, such as the Giant MR (GMR).

The GMR head contains a complex multi-layer sensor for high flux sensitivity. A particular type of GMR is the spin-valve, containing two magnetic layers separated by a thin non-magnetic layer, its composition is shown in Figure 1.19. The layers are biased transversely to produce the optimum magnetic rotation in the MR strip with respect to the sensed flux.

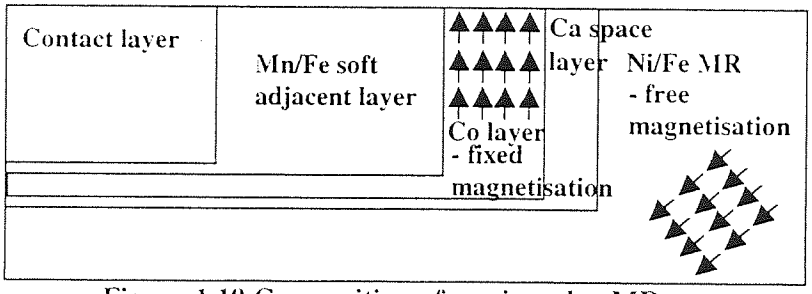

Figure 1.19 Composition of a spin-valve MR sensor

Tian and Lee [73] give the relationship between temperature, T and MR resistance, R, as

$$\frac{R - R_o}{R_o} = \lambda(T - T_o) \qquad \textbf{Equation 1.17}$$

where R_o, and T_o are initial resistance and temperature respectively and λ is an experimental constant (value found to be 0.0024 in this work).

Lambeth [74] reported that spin valve transducer technology may be extendible to yield beyond 100 Gbit/inch^2.

Fabrication of good MR materials is not difficult, the problem arises adding the inductive element to the head. This requires very high temperatures that can cause the magnetoresistive effect of the MR sensor to be lost.

Ishiwata et al [75] reported that since resistance in the MR strip is proportional to temperature, the effect of changes in relative resistance, $\Delta R/R$, become less noticeable at high temperature. This problem was overcome by depositing an underlayer below the MR sensor, which gives constant change in R with increasing temperature.

It was found that electrostatic discharge (ESD) can cause electrothermal failure in the MR strip due to localised Joule heating which could melt the MR strip with the rest of the head remaining intact. A model for temperature rise was proposed as follows

$$\frac{\Delta T(t)}{1+\lambda\Delta T(t)} = \frac{i_p^2 R_o \sqrt{\tau}}{2A_p^1 C_p^1 \sqrt{\pi k / \rho C_p}} \int_0^{t/\tau} \frac{\exp(-2x)}{t/(\tau - x)} dx \qquad \textbf{Equation 1.18}$$

Where A_p^1 is the area wall of the plane, ρ and C_p^1 are the density and specific heat of MR strip, t is time, τ is time constant and x is a dummy variable of integration. This model predicted temperature rises in the order of several thousand degrees.

The effect of shield width in MR elements was studied. A tri-layered MR element consisting of an amorphous CoZrMo as soft adjacent layer, Ti magnetic separation layer and a Ni-Fe film as magnetoresitive layer was fabricated [76].

The distance at which the signal dropped by 6dB was found to be exactly equal to the shield width. Thus, wide shields give a wide signal output plateau, which prevented high track density being achieved.

1.2.5.5 Noise and Signal Loss

Noise

The formula for noise from neighbouring tracks, known as crosstalk was given as

$$C = 10\log\left(\frac{V_o^2}{\sum V_i^2}\right) \qquad \textbf{Equation 1.19}$$

where V_o is ontrack signal and V_i signal from neighbouring tracks. It was found crosstalk can be reduced by decreasing MR shield width and/or increasing MR shield thickness.

Ishiwata et al [75] compared two types of MR heads - exchange coupling and permanent magnet head - with respect to narrowing track widths on disks.

The exchange coupling type was susceptible to crosstalk since the soft adjacent layer film ran along the entire shield width, allowing interference from neighbouring tracks to be sensed. The permanent magnet type, which had adjacent layer along track width only, offered improvement in crosstalk since the off-track region was less susceptible to noise.

Noise was categorised as either medium noise or other system noise by Obernosterer and Oehme [77], with the former category being further sub-divided into fixed and semi-variable. It was found that fixed noise, the source of which being disk texture induced changes in fly height for example, was deterministic. Whereas, semi-variable noise, such as the occurrence of variations in magnetic microstructure, was purely stochastic. Crosstalk was categorised as other system noise, along with amplifier and head noise.

Signal Loss

During write mode bits of data are written to the disk with digital representation of wavelength, λ, such that

$$\lambda = \frac{U}{f} \qquad \textbf{Equation 1.20}$$

where U is relative velocity and f the frequency of the input signal [6].

Signal to noise ratio, SNR, was defined by Grundy [4] as

$$SNR = \frac{2w\lambda}{\pi d^2} \qquad \text{Equation 1.21}$$

where w is track width and d is a measure of magnetic grain size. This equation confirms the need for small grain size, also note that narrowing of track width results in signal loss as expected.

Spacing Loss

Loss in the recorded signal occurs with increased flying height, h. This spacing loss, SL, was given in [78] as

$$SL \propto \exp\left(\frac{-2\pi h}{\lambda}\right) \qquad \textbf{Equation 1.22}$$

This can be expressed in decibels and is then known as the Wallace loss as reported in [13],

$$SL_{dB} \propto 54.6\frac{h}{\lambda} \qquad \textbf{Equation 1.23}$$

Hence, a large value of h results in a high amount of spacing loss, thus it is necessary to have low flying over the disk surface. From [3] it was given that to achieve areal density of 20 Gb/inch^2 it would be necessary to fly the slider at a height 13.4 nm above disk, to achieve 100 Gb/inch^2 this fly height would have to be reduced to 5 nm.

Patton and Bhushan [79] report that pole tip recession (PTR) can lead to increased spacing loss during operation. PTR occurs when the slider suffers differential wear, that is the softer Ni-Fe pole material is worn preferentially before the surrounding harder alumina. This can separate the slider and disk by an additional 10 nm which is undesirable in terms of signal performance.

Coating Thickness Loss

Loss of signal is also known to be proportional to media overcoat thickness. coating thickness loss, CL is defined as

$$CL = 1 - \frac{\exp(\frac{-2\pi\delta}{\lambda})}{\frac{2\pi\delta}{\lambda}} \qquad \textbf{Equation 1.24}$$

where δ is the media coating thickness, hence thinner films gave less signal loss.

Menon [3] reported that to attain 20Gb/inch^2 areal density, disk and slider overcoats would have thickness of 3 nm and 2.2 nm thick respectively. To increase the data density to 100 Gb/inch^2 these thickness would have to be reduced to 2 nm and 1 nm.

Yang et al [80] reported on 'zone' carbon coated disks, that is to use a thicker carbon overcoat at the landing zone (at disk inner diameter) and thinner carbon overcoat at the data zone (at disk outer diameter). This gave disk durability at the landing zone while decreasing coating thickness loss for optimum read/write performance at the data zone. The change in disk slope, ΔDS , was defined as

$$\Delta DS = \tan^{-1}\left(\frac{T_{ID} - T_{OD}}{D_{ID} - D_{OD}}\right) \qquad \textbf{Equation 1.25}$$

where T_{ID}, T_{OD}, D_{ID}, D_{OD} represent disk thickness and diameter at inner and outer diameter respectively. However, it was found that large ΔDS gave a proportional change in recording head roll during flying which was undesirable.

Gap Loss

For reading signals, a large gap between poles is required for efficiency in an inductive head, but when the gap becomes equal to one wavelength, the output signal tends to zero. The gap loss, GL, is given by

$$GL = \text{sinc}\left(\frac{\pi g}{\lambda}\right) \qquad \textbf{Equation 1.26}$$

where $\text{sinc}(x) = \frac{\sin(x)}{x}$ and g is gap length.

For high density recording a small head write gap is required, the general rule is the gap length should be less than or equal to the bit length. Current write gaps are quoted as being in the order of 0.2 μm [72].

1.2.6 Tribology

Tribology is the study of the contacts that occur between the moving parts of any two materials. Previously, the tribology of the hard disk system was not a limiting factor and as a consequence the subject has been largely neglected.

In magnetic recording, the term is chiefly used in connection with the contacts that occur at the head-media interface. In hard drive recording where components (head and disk) are becoming smaller and head-disk spacing is decreasing many tribological problems are created.

Talke [47] reported that in current hard drives the flying height is less than 30 nm, which is of the same magnitude as the roughness of the disk. Hence, there will be occasional contact between the head and the disk during operation. The majority of the load involved in this contact, however, is supported by the ABS, which reduces friction and wear but does not eliminate it entirely.

1.2.6.1 Interface Friction

Friction can be described as resistance to motion that is experienced when one solid body slides over another.

The coefficient of dynamic friction, μ, is defined as the ratio of tangential force to normal force, that is

$$\mu = \frac{F}{N} \qquad \textbf{Equation 1.27}$$

with μ usually in the range [0-1]. It should be mentioned that μ was usually constant only for a particular pair of surfaces sliding under a given set of operating conditions, e.g. temperature, humidity and velocity.

There are several ways of measuring friction in a hard drive, these include strain gauges, spindle torque monitoring, and drive level torque monitoring. Often correlation between methods is poor. In addition, correlation between experimental test stands and actual drive measurements was found to be poor [81]. In the hard drive industry, friction force is usually given in grams.

Friction at the interface can be illustrated by the Stribeck Curve [82, 83]. The curve shows μ plotted against the dimensionless parameter known as the Bearing Number, BN, where

$$BN = \frac{nv}{P} \qquad \textbf{Equation 1.28}$$

with n being viscosity of lubricant, v is relative sliding speed and P is the pressure due to the loading of one body against the other. Notice, the value of n will vary depending on whether the lubricating fluid is lubricant or air. The typical curve for a hydrodynamic bearing is shown in Figure 1.20.

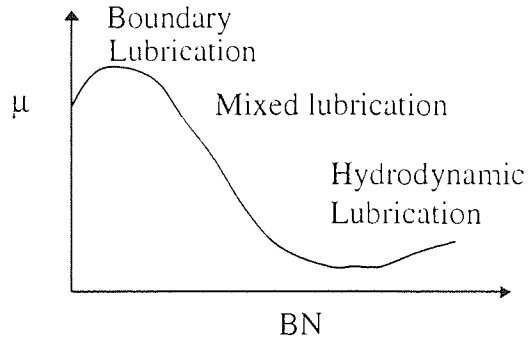

Figure 1.20 Typical Stribeck curve

In conventional recording, friction followed the Stribeck curve from high initial value at low operating speeds and/or high loading. During this time friction is in the boundary lubrication regime where surfaces are separated only by a layer of lubricant. Large asperities can break through this layer and contacts may occur.

At higher BN, hydrodynamic lubrication takes place because of low loading or high rotational speed. It entails complete separation of the two surfaces by a wedge of air. The amount of separation is dependent on the viscosity of air and the rotational speed of the disk. During normal drive operation lubrication is in this regime, that is, friction force will be almost entirely due to the shearing of the air bearing film between head and disk.

In true contact recording lubrication at the interface remains in the boundary region. Lubricant is adsorbed into the two interacting bodies. The adsorbed lubricant (chemisorbed or physisorbed) forms a molecular layer which ideally should separate the two surfaces. Large asperities break through the boundary layer, hence asperity contact will occur. This lubrication regime is influenced by the material properties of the sliding surfaces.

In proximity recording the friction experienced is close to the minimum value in the Stribeck curve. Since, a thin air bearing separates head and disk surfaces, the intermittent contacts that occur during this type of recording mean friction will have a value slightly to the left of the minimum on the curve. The lubrication could be described as a combination of boundary and hydrodynamic.

Bhushan [60] stated that the load present when two surfaces come into contact is supported by contacting asperity tips. Friction force is due to the adhesion of these contacting asperities. For unlubricated and lubricated contact the friction force due to adhesion, F_A , was given as

$$F_A = A_r r_a \qquad \textbf{Equation 1.29}$$

$$F_A = A_r [\alpha r_a + (1 - \alpha) r_l] \qquad \textbf{Equation 1.30}$$

respectively, where A_r is the real area of contact of the asperities, α the fraction of area unlubricated (this is dependant on temperature and pressure), and r_a and r_l are the shear strengths of the dry and lubricated contacts with

$$r_l = \eta_l U / h \qquad \textbf{Equation 1.31}$$

where η_l is absolute lubricant viscosity, U is sliding velocity and h is lubricant film thickness.

It was observed that friction initially increased with drive running time, this was due to surfaces becoming smoother and the real area of contact A_r increasing which in turn increased friction. Note that, in contact between very smooth surfaces the real area of contact, A_r will be high and hence so will the friction force.

It was reported that protective carbon overcoat thickness does not affect friction. Films of thickness 5.10 and 25 nm films were tested by Jiang et al [84]. However, in the presence of excessive lubricant on the disk this gave high friction [43].

Coefficient of friction measurements were notorious for their large spread - surface topography, contact conditions (sliding velocity, load, temperature, sliding distance and contact geometry and humidity) have been recognised as sources of this scatter [85].

Yang et al [86] report on constant drag testing of slider over disk, which was used to study the friction coefficient under a variety of conditions. Slow sliding velocities of 0.1 and 0.2 m/s showed initial increasing friction coefficient that became constant after 30,000 disk revolutions. Higher velocity of 0.4m/s gave increasing friction coefficient over a higher number of revolutions. This was due to the temperatures created during increased sliding speed being in excess of those required for tribochemical reactions to occur.

The interface design for proximity recording, along with that of the slider and disk must be very robust to withstand repeated high-speed contacts. These contacts and stresses mean that friction and wear become of vital importance at the interface and that lubrication is critical to prevent drive failure.

Agarwal et al [48] performed friction tests using a tri-pad proximity slider and found that the coefficient of friction decreased with increasing dwell time velocity. This was attributed to increased slider fly height at higher velocity. Friction was measured by a strain gauge on the cantilever arm that held the slider.

1.2.6.2 Interface Stiction

Static friction force at drive start-up was of great importance at the interface. Known as stiction, F_S, this defined as the force required to initiate motion between head and disk, it consisted of a surface tension or meniscus component, F_M, and a rate dependant viscous component, F_V. Stiction force, F_s, was defined by Mate and Homola [87] as

$$F_s = \mu(N + F_A + F_M) + F_V \qquad \textbf{Equation 1.32}$$

where μ is coefficient of friction, N is normal load, F_A force due to adhesion and F_V rate dependant viscous force.

Li and Menon [88] gave the time at which this breakaway stiction peak occurred, the time τ_b, could be estimated by

$$\tau_b = \sqrt{\frac{2(\mu_s L - m\alpha))}{k\alpha}} \qquad \textbf{Equation 1.33}$$

where μ_s was stiction coefficient, L was slider preload, m was slider mass, α was acceleration and k was the spring stiffness constant. As expected stiction peak time was inversely related to disk acceleration.

Stiction was usually higher than friction force. Before sliding begins, the bonds between the two surfaces must be broken, asperities may plough across the surface of the other body in the contact, which will lead to deformation. Stick-slip may sometimes occur, this is where the surfaces stick together until the elastic energy of the system has built up and a sudden forward slip takes place resulting in vibration and noise. It has been reported by Mate and Homola [87] that stiction force could sometimes be large enough to pull the slider completely off its suspension. Bhushan [42] proposed a short oscillatory micro-motion immediately before drive start up to break strongest bonds.

Investigation into stiction behaviour usually involved carrying out contact start stop (CSS) tests, whereby the maximum lateral force required to separate the head and disk on drive start-up was measured. Usually, mechanical strain gauges attached to the slider were used for this purpose as described by Wang et al [89]. Although, Milby et al [90] describe a method whereby the total current applied to the motor was controlled and measured, while rotation of the spindle was recognised by Hall sensor magnets.

During non-operation most hard drive designs allowed the slider to park on the disk surface. The slider can adhere to the disk while in contact with it. Bhushan et al [91] report this parking or rest time can be minutes or even days or weeks. In general it was found that stiction increased with rest time due to the formation of menisci bonds, creep (or plastic flow) of

contacting asperities and chemical contamination. Koka [92] reported that stiction force of up to 25 grams was recorded following rest time.

Increase in stiction with rest time generally followed a power law relationship, with the rate of increase being inversely related to liquid viscosity and surface smoothness. After some time stiction reached an equilibrium whereby liquid had migrated to form stable menisci around the contacting and non-contacting asperities.

In present day drives where surfaces are very smooth, a thin film of liquid on either disk or slider may result in very high stiction. The source of liquid being either topically applied lubricant film or condensed water from a humid environment. Any wetting liquid between two contacting bodies resulted in the formation of curved menisci bridges which gave an attractive force due to surface tension.

The surface topography of the disk influenced this migration of lubricant, with certain patterns can accelerate the flow while others impede it. This can mean certain areas of disk become unlubricated whilst other areas had puddles of excess lubricant. It was found that disks with large asperity radius took longer to reach their equilibrium stiction.

With laser textured disks smoothing of the landing zone did not increase the real area of contact as much as with mechanically textured disks, so the number of meniscus bridges remains almost constant. Even at high humidity, the uniformly spaced bumps restrain the formation of additional meniscus bridges ensuring stiction did not increase.

Since high stiction can lead to loss of data and physical damage to the interface investigation into dynamic head loading (DHL) has taken place [93]. In DHL the slider parks off the disk surface on a designated ramp area, once the spindle has reached the required speed the head is then loaded over the disk surface. Thus in theory, the head should never contact the disk. This method avoids large power usage on drive start-up so has possibilities for use in portable drives. A spring-loaded inertial lock keeps the heads off-disk even in the event of some external vibration or shock. Additionally the use of thick protective coatings is not required which would minimise coating thickness loss. However, Fu and Bogy [94] report that high speed contacts may still occur during DHL due to shock impact or contamination particles. This can cause severe damage to the interface, it was shown that in the event of contact during

DHL data loss would be very probable [95]. Peng [96] reported that having slider flexure stiffness much higher than for conventional drives would decrease the chance of such contacts significantly.

Since surface texture was known to affect stiction, an experimental disk was fabricated consisting of smooth and rough textures at inner and outer diameter respectively by Best [97]. Both regions were fabricated identically with respect to layer composition and thickness. Stiction was measured by sampling at random positions on the disk, allowing a 5-second slider park time before ramping velocity to 3600 rpm. A map of the stiction force was produced. Distinction between the two textured areas could be seen, Figure 1.21.

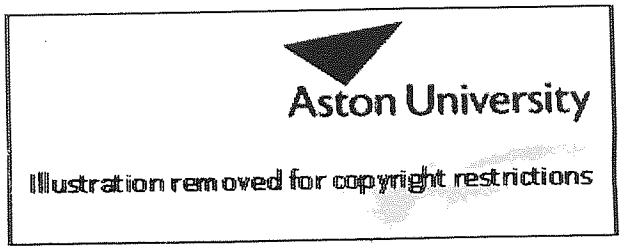

Figure 1.21 Stiction map showing 2 distinct regions

The lighter area observed at the disk inner diameter indicated higher stiction was experienced at this smoother region. This was due to the real area of contact being larger. Conversely, the rougher outer diameter is darker indicating lower stiction. Two light rings were observed at the texture borders, these were created by the slider rails landing on the transition area and experiencing very high stiction.

Stiction was found to increase monotonically with cycle number for both textures, this was due to smoothing of the initially rough surfaces leading to higher real area of contact. Suganuma et al [34] also observed that stiction was found to increase during cycling due to surface smoothing and lubricant transfer.

Kasamatsu et al [98] reported on the development of Stiction Free Sliders (SFS) for use with super smooth disks. The SFS had small cylindrical pads fabricated on their air bearing surfaces, the height of these was uniform at around 40 nm. Different pad area was studied

with 0.1-0.002 mm^2 pads investigated. Stiction was measured by a strain gauge as the maximum friction force at drive start-up after a 60 minute sliding test, test velocity used was 1rpm. Stiction growth was largest with small area pads, excessive reduction of pad area also led to head and disk wear.

Fly/stiction was the term used for excessively high stiction following a long period of flight over a disk, due to liquid accumulated on the head during flying (e.g. lubricant and organic contaminants) being spread on to the disk surface during parking. The effect of laser bump texturing on fly stiction with two types of media was studied. Disks were identical in terms of composition and bump height, but one with twice as many bumps. The higher bump density media gave lower fly/stiction, this was due less real area of contact dwell time parking. However, Harris et al [99] showed that laser bump density was negligible with respect to head-disk contact during flight.

Gui and Marchon [100] designed a fly/stiction test as follows: a slider was flown over a disk continuously for 18 hours and then parked on the disk for 2 hours. Due to the long dwell time, stiction readings were excessively high. Water droplets were seen on slider using XPS imaging, these droplets were also observed in areas of the head not in contact with disk (e.g. the cavity bearing).

Laser bump height was found to be critical in friction/stiction performance, Knigge et al [101] reported poor performance when the height of laser bump and slider fly height were close. Since slider fly height could vary by a few nanometers, for example during a high speed seek operation, and contact disk. Careful optimisation of laser bump height must be performed, since high bumps interfere with slider flight and cause failure as observed, whilst bumps which were too low give no stiction advantage over a smooth untextured disk. The radius of curvature of laser bumps was also significant, with the volcano type giving highest stiction due to its large radius.

In a real drive, where there are multiple interfaces in a disk stack, total stiction force was equal to the summation of individual forces for each head-disk pairing [102]. Results showed that a high standard deviation of stiction for each interface was desirable in order to reduce the probability of overall drive failure.

Talke [47] studied the Gammak number, Gk. this was defined as the ratio of dynamic to true static friction. It was found from this work that mechanically textured disks usually had Gk=0.4-0.6, whereas laser textured disks had Gk ≈ 1.

1.2.6.3 Interface Wear

Wear was categorised as adhesive, fatigue, abrasive, erosive or corrosive. The first four types are classed as physical wear and the fifth chemical wear [78].

Physical wear usually leads to a catastrophic break down of the media, whereas chemical wear is a much more gradual process [103]. In reality, wear was not dominated by a single wear mechanism but by a combination of wear regimes, interactions can lead to unpredictable behaviour. Definitions of individual wear mechanisms and examples of their damaging effects follow.

Adhesive Wear

This arises when junctions weld together and then become broken by relative motion. Material transfer can be an indication of adhesive wear [104]. Particles may be removed from one surface via fatigue (see below) and then become adhered to another.

The majority of forces at the head-media interface are adhesive and lead to debris particles being formed [105]. In a clean environment, fine wear debris is generated which results in light, uniform disk wear. Over time this wear increases friction and eventually can lead to drive failure [41].

Bhushan and Forehand [21] described an experimental procedure that could make in-situ localised measurements of the wear processes on magnetic thin-film disks. The optical reflectance of a disk track was constantly monitored during cycling by the apparatus shown in Figure 1.22.

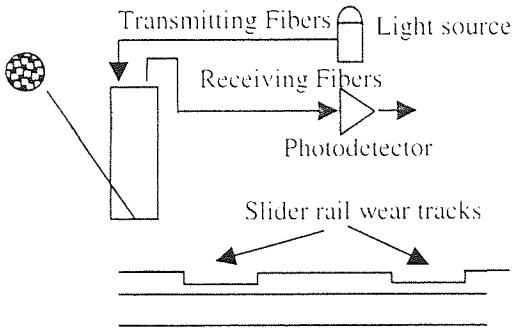

Figure 1.22 Optical device for measuring disk wear track reflectivity

A probe transmits and receives light through a fibre-optic bundle. The transmitting and receiving fibres are 50 μm in diameter and are arranged randomly within the probe. Light from an incandescent halogen lamp inside the mainframe is sent through the transmitting fibres, while reflected light from the test surface is captured by the receiving fibres. The reflected light is then sent to a photodetector in the mainframe, which converts the light intensity into an electrical signal (voltage). The signal is amplified and digitised and sent to a PC. The probe is scanned radially across the disk surface by means of a stepper motor. Test results are shown in Figure 1.23.

Disk wear was observed to follow a pattern of lubricant depletion followed by increased head-disk asperity contacts, following this wear tracks were formed.

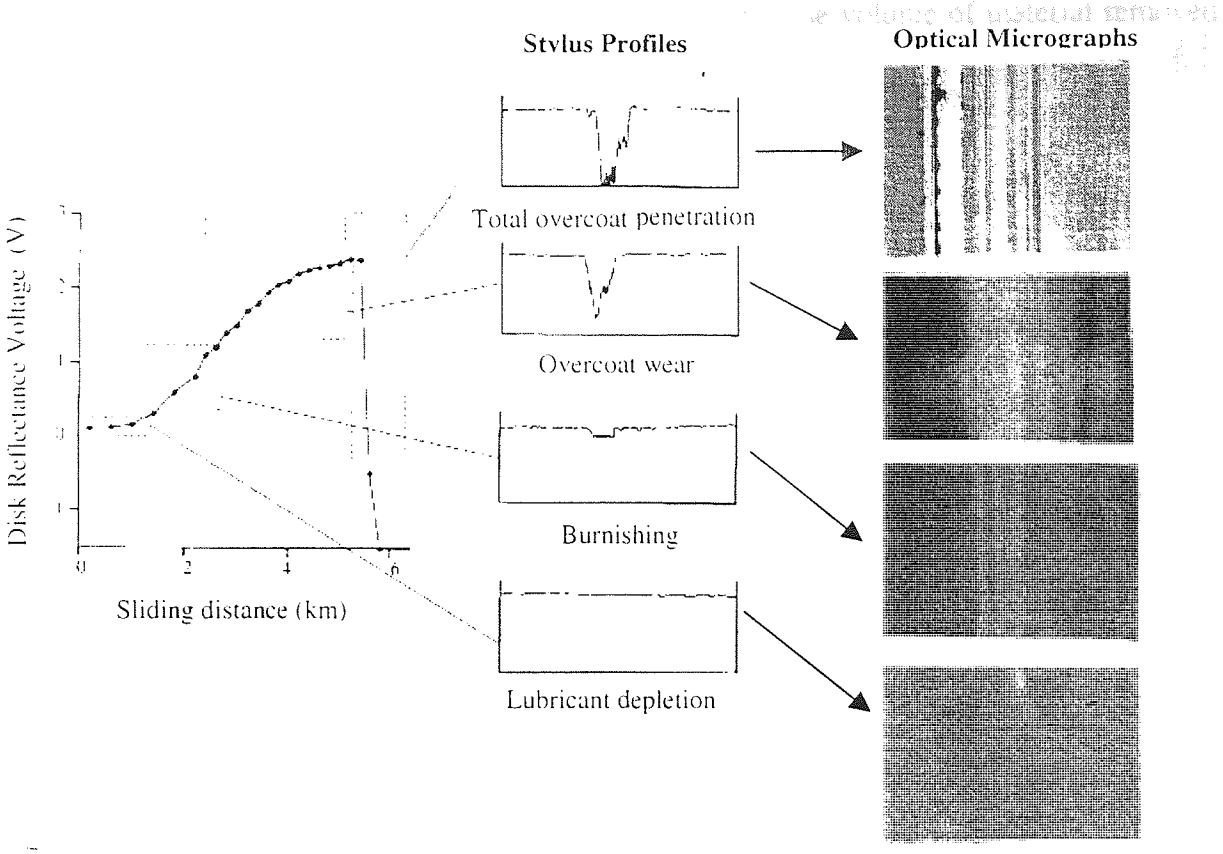

Figure 1.23 Results of wear testing with optical reflectivity apparatus

Lubricant was found to extend disk wear life, as did a polished surface texture. Ideally lubricant should be thick initially to provide burnish protection and worn off an initial sliding period, leaving cover only at the inner diameter for start/stop contacts.

Chun et al [106] stated that sliding contact was the active element in lubricant depletion. Hsiao et al [107] reported on two types of lubricant thinning that could occur under sliding - thermal and shear. Even at slow sliding speeds shear thinning occurred, thermal thinning occurred due to viscous heating at higher speeds.

Surfaces may be hardened or coated to reduce wear, wear can also be minimised by good component design. Air bearing surfaces have been designed to support over 99 % of slider load whilst flying.

A simplified model of wear is the Archard law [108], it states the volume of material removed, Q, per unit sliding distance can be given by

$$Q = \frac{kN}{H} \qquad \textbf{Equation 1.34}$$

where k is the wear coefficient (which diminishes at the low loads experienced during slider flying), N is the normal load and H hardness of the softer material.

Although the primary objective of wear studies has been to reduce wear, in some instances wear was beneficial. For example 'running-in wear', the initial smoothing/burnishing process that removes highest asperities during the initial stages of operation lessened long term slider-disk contacts.

In proximity recording, wear does not continue at a uniform rate but instead reaches some steady state level. In an alternative form of Archard's Law, wear volume is given as a function of interface contact force, such that

$$Q = c\left(\frac{F}{H}\right)s \qquad \textbf{Equation 1.35}$$

where c is the wear coefficient, F is the contact force, H the material hardness and s the sliding distance.

With burnishable proximity heads, the contact force was not constant since the air bearing continually defines the contact pad position with respect to the disk. So as wear occurs at the trailing edge the flying height self-adjusts by an amount sufficient to remove almost all contact force. This is known as in-situ fly height adjustment.

In order to reach the steady state level of wear it was vital that only very light load contacts occurred initially since most in-situ fly height adjustment took place in the first hours of flying. Failure to do this resulted in early nanoscopic degradation of head and disk surface and led to drive failure. To avoid excessive initial contacts a trade off between low stiffness air

bearings for contact, and high stiffness air bearings for flying must be made. It is also important that head materials are such that minimal debris is produced [50].

Softer air bearings produced less disk wear at the expense of the slider. However, slider materials being harder tolerated more wear. By having a stiff pitch angle slider wear is limited to the extreme trailing edge, this also prevents slider rails contacting the disk.

Meyer et al [50] reported that a negative pressure proximity slider (as shown in Figure 1.14) flying over the same track on a hard disk experienced many contacts in the initial stages of operation. Contacts were measured by an AE sensor. Since first documented around 1980, Acoustic Emission (AE) has become a popular method to monitor slider-disk interaction, the high frequency AE waves originate from the deformation of solids. AE signals contain higher frequency components due to slider body vibration and lower frequency components due to air bearing vibration. O'Brien and Harris [109] report that the method requires frequency selective electronics to discriminate between the signal resulting from slider-disk contact and that from other sources (for example resonant frequencies in the transducer, slider body vibration, fixtures and suspension). Filtering of AE signal was usually required, in this study a Butterworth high pass type was used to target the natural frequencies present in the slider. It was found that natural frequencies were measured above 500 KHz, running the AE test without filtering allows frequencies much lower, hence those not associated with head/disk contact. Khurshudov and Talke [110] state that AE signal gives a more reliable indication of surface contacts than friction measurement.

Meyer et al [50] report that after between 10-40 hours of flying there was a noticeable decrease in the number of contacts occurring, this suggested that material was being removed from the interface. When the head was moved to a virgin track on the disk the AE signal continued to decay, this implies that the material has been worn away from the slider and head not the disk.

A Tencor trace taken across the head confirmed the result and AFM images showed the trailing edge was more polished than before. In addition, 5 nm of pole material was removed but little signal degradation experienced. The head had experienced natural burnishing during the early stages of operation. It was found that the material removed from the head can be rolled and appear as small spherical particles that are stored on the slider rails.

Fatigue Wear

Continuous stressing at the disk surface may initiate the formation of cracks, which can lead to delamination at the surface/sub-surface. Thin flakes or laminae of carbon overcoat or magnetic layer can be removed from the disk surface [41]. Similarly, Xu and Bhushan [53] reported fatigue wear of a recording head, Figure 1.24 shows SEM image of cracked poles of an Al_2O_3-TiC slider indicating fatigue wear had occurred.

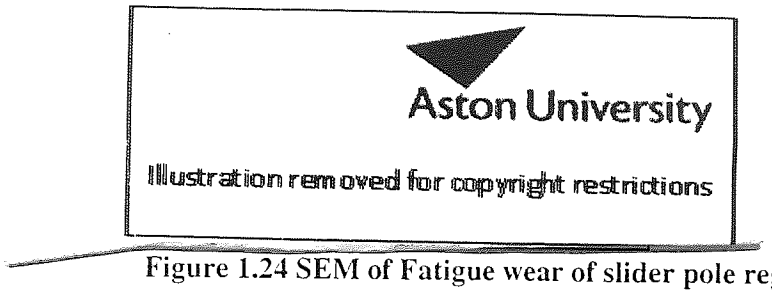

Figure 1.24 SEM of Fatigue wear of slider pole region

Pugh [104] reported that with fatigue wear, initially no indication of wear will be present, then a small amount of delamination may be observed. Following this deterioration of the surface will be very rapid.

Cha et al and Sharma et al ([111] and [112] respectively) described wear tests for hard drives, these consisted of a constant dragging of slider over disk for long periods of time. To accelerate wear and failure this was usually done at low velocity (i.e. when airflow was such that slider flying had not initiated). Wear tests were performed on disks with different thickness of hydrogenated carbon overcoats by Jiang and Stott in [113]. Scanning Probe Microscopy (SPM) was used to examine disks for wear. Results showed wear marks were initially smooth and became rough as parts of the film were actually removed, the surface then becomes smooth again as the film was totally removed. The wear cycle at which the film started to be removed was known as the critical cycle, it was used as a parameter to distinguish between the wear resistance of different films of the same thickness. It was found that thicker films wore better than thin, although coating thickness loss then became an issue.

The effect of hydrogen in the disk's carbon overcoat was studied by Wang et al [89], using disks where the hydrogen content of the carbon overcoat was increased from 12% to 36%. The same disk track was scanned periodically during testing and changes in lubricant and overcoat thicknesses of 0.1 nm were detectable.

CSS durability of disks in ambient was found to increase with increasing hydrogen content, with cycles until wear increasing from 500 for 12% H content to 20-25K for ≥18% H content. Lowest friction and stiction measurements given were also from the disk with the highest hydrogen content. Delamination of disk surface occurred more readily with lower H content overcoats. It was also found that more disk lubricant material was transferred to the slider with high H disk overcoats, although lubricant preservation on disk and slider surfaces was better for high H content films, this latter finding could explain the improved wear behaviour observed.

Wear

Abrasive wear is basically 'cutting' of a softer surface by a harder one as they move relative to each other. There are two main methods of abrasive wear as follows. When a hard surface slides over a softer one two-body abrasion occurs. When hard particles become entrapped between two sliding surfaces three-body abrasion occurs. Both types of abrasion lead to localised damage of the disk surface. Chung et al [105] report that disk or slider grooving can be an indication that abrasive wear has occurred.

Most disk carbon overcoats were chosen to be of comparable hardness to the slider in an attempt to overcome two-body abrasion [78].

Xie and Bhushan [114] reported that debris particles formed by three-body abrasion were an order of magnitude smaller than those formed by two-body abrasion. Severity of wear was thought to increase with debris particle size. Debris particle size was also reported to be proportional to load and sliding velocity.

However, debris formation could be advantageous on occasion. Jiang and Stott [113] also report that during sliding wear can go from severe to mild due to the development of protective layers from accumulated debris particles. These protective layers could be in the form of compact debris particle layers (if low temperatures were experienced at the interface) or smooth glaze layers (if high temperatures were experienced).

Erosive Wear

This is similar to three-body abrasion except material is removed by particles impacted in one or both of the mating surfaces. These particles become impacted during collision of asperities.

Bhushan [40] reported that in a clean environment only fine debris was generated, resulting in burnishing and uniform wear. However, in the presence of contamination, such as eroded particles of slider alumina, the disk overcoat was readily worn, giving severe surface damage.

Cha et al [111] stated that the most common site for impacted particles was on the edges of the sliders' air bearing surfaces.

Corrosive Wear

Corrosion is a form of chemical wear. As already mentioned seldom is any one type of wear found in isolation, this is especially true of chemical or corrosive wear.

Fung et al [67] conducted accelerated corrosion tests on magnetic disks with/without carbon overcoats, tests consisted of disks being exposed to a corrosive environment for long periods of time. The specimens were placed in an enclosed environment saturated with 0.5 M of hydrochloric acid (HCl) vapours at room temperature for 24 hours. An image analyser - Zeiss image analysis system - was then used to examine the size and density of corrosive spots.

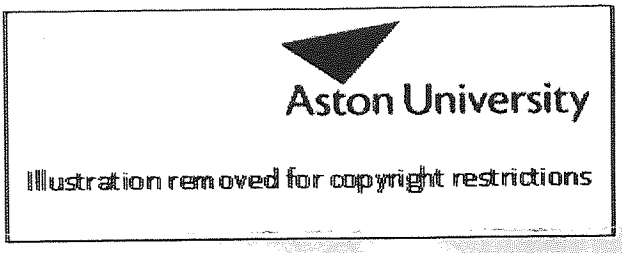

Figure 1.25 Corrosion test results, disk images a) without, b) with DLC and c) with nitrogenated carbon overcoat

The image in Figure 1.25a) shows a disk with no overcoat after being exposed to the corrosive environment. Evidently, the density and size of the corroded spots were extensive. The spots were mostly distributed near the sample edge and the size of these corroded scars was approximately 40 nm. These corroded scars arose from the chemical reaction between the chloride ions and the metal surface. Where chemical protection was provided by a DLC overcoat with density of corrosion sites and their sizes are lessened, see Figure 1.25b).

However, where a nitrogenated carbon overcoat was used corrosion resistance deteriorated as seen in Figure 1.25c). Nitrogenated carbon developed a higher density of corroded pores due

to the formation of intergranular voids. Pore size was also large because nitrogen incorporation obstructed the formation of sp_3 carbon bonds and cross-linkage. Hence, the presence of nitrogen in amorphous carbon structure resulted in films with a lower atomic density due to a higher content of graphitic phase. Since corrosion was known to start at the least dense regions this was problematic.

Sliding surfaces can also cause chemical reactions to occur under certain environments. Initially this reaction will be rapid and usually a film will be formed on one or both surfaces. The reaction will then slow down or cease. The film may be removed by continued sliding and the reaction will continue. Alternatively, the film may remain on the surface and add to wear protection depending on it's own wear properties [104].

Surface oxidisation of carbon overcoat when oxygen is entered into operating environment and hydroxide formation on ceramics, glasses and ferrites are both examples of chemical wear [103].

Pugh [104] stated that wear rate was dependent on loading, lubrication and environment. Under steady operating conditions, where hydrodynamic lubrication prevailed, wear should be minimal. However, where start/stopping takes place rapid changes in load will occur and lubrication regime will become boundary and more wear will be experienced.

Sullivan [115] reported that under boundary lubrication, contacting surfaces were separated only by an adsorbed polar molecular film when load/velocity is such that little or no fluid/air film support existed. Ideally shearing should occur in the adsorbed film only providing low friction and negligible wear. However, in practice polar molecules continuously desorb and re-adsorb from and to the surface even at low temperatures. At highly loaded contacts the energy dissipated may generate temperatures high enough to yield total desorption of molecules allowing asperity contact and increase in friction. Immediately following the contact event temperatures remain too high for re-adsorption to take place, instead oxidation of the dissolved oxygen in the fluid occurs. After the contact the asperity cools drastically and allows polar molecules to adsorb on to the oxide surface.

1.2.6.4 Lubrication

Lubricant was applied topically to disks in an attempt to reduce friction and wear in the event of head contact.

Perfluropolyethers (PFPE's) were found to be chemically stable lubricants and were commonly used for coating rigid disks. However, a new class of lubricant - phosphazene - was shown to reduce stiction at the head/disk interface and the lubricating property seemed to improve in extreme environments [111]. Phosphazenes are nearly spherical molecules of about 1.2 nm diameter which protect the disk overcoat by forming a single monolayer. Since conventional lubricants (such as PFPE's) are long chain polymers with open spaces between the chains, it seemed advantageous to mix phosphazene with conventional lubricants for complete coverage of lubricant on thin film disks.

Talke [47] reported that single component lubricants have been shown to be inadequate for proximity recording especially in hot/humid conditions. Combining a standard lubricant (such as AMXXXX or Zdol) with additives has been shown to provide better wear resistance, minimise friction and debris. Chao and Russak [52] stated that Cyclic Phosphazene (known as X-1P) has excellent tribological properties when used as an additive to standard lubricants under elevated and high temperature/humidity.

Zhao and Bhushan [39] compared disks coated with fully bonded, mobile and partly bonded lubricant with respect to friction, stiction and durability. Bonded lubricants gave lowest friction/stiction but lower durability over time since bonded molecules cannot replenish areas of disk depleted of lubricant. Tian and Chao [22] quantified limits on the proportions of mobile/bonded lubricant used. It was found that < 40% mobile phase gave problems of wear, while >65% mobile gave high stiction due to increased meniscus component at asperity contacts.

Lubricant degradation was reported to occur in the presence of aluminium oxide from slider material, Sharma and Talke [58]. It was observed that at elevated temperatures alumina reacted with the acetyl units of PFPE's degrading the lubricant. Thermal degradation of lubricant due to flash temperatures at slider/disk contacts cause this. Flash temperatures for an alternative slider material, SiC, were reported to be substantially lower due to the higher thermal conductivity of the material thus the lubricant degradation should be less severe.

In addition, Xu and Bhushan [53] reported that local lubricant transfer was observed on Al_2O_3-TiC slider by SEM, the resulting film was patchy and was assumed to comprise of the mobile lubricant layer from disk. The film transferred to the SiC slider was mainly continuous and formed a protective layer. The surface of the SiC slider changed from being hydrophilic to hydrophobic reducing stiction force especially at high humidity. However, debris collection was more likely to occur on the SiC surface.

Pan and Novotny [59] found that detectable wear of the carbon overcoat began at the time when most of the lubricant had been removed from the disk track, with sliding being the most significant element in depletion.

Karis et al [116] proposed a method of reducing stiction by replacing the liquid lubricant film with a solid low surface energy overcoat. However, it was known that solid fluorocarbon films sputtered or deposited by plasma have been found to be inadequate during long-term testing due to thickness and non-mobility of the films. A new method of ion beam deposition of fluorocarbon films known as Ion Beam Lubricant (IBL) was described. Resulting film was thin, solid and polymeric.

Start-Stop-Drag tests were repeatedly performed, where the slider was flown over disk for 1 minute, then had 5 start-ups performed followed by being dragged over disk at 0.5 m/s for 190 seconds. Stiction on disks with IBL was constant throughout tests, due to absence of meniscus force. No damage to test track was seen by either AFM or SEM, but Kelvin probe scan did identify a higher surface potential over used track.

In [117] Bhushan and Zhao showed that if $l/\sigma > 0.75$, where l was total lubricant layer thickness and σ standard deviation of surface heights, stiction could increase dramatically to very high values.

Since too thin lubricant coverage could lead to premature wear and too thick leads to high stiction, it was important to quantify the critical thickness required. Moulder et al [118] used XPS to measure lubricant thickness on disks with fluorocarbon lubricant. Different take-off angles of photoelectrons were known to alter the sampling depth, with angles normal to the surface causing ejection of electrons from the deepest layers (up to around 10 nm) and

shallower angles giving more surface specific information. In this work angles of 0°, 20°, 30° and 90° were chosen. Since, vacuum compatibility of fluorocarbon lubricant and thinning agent can be of concern, thus minimum time in the vacuum was used.

Spectrums for the pure lubricant and that of the lubricant on the disk surface were not identical. Indicating that a chemical change occurred during the bonding process.

The Fadley model for lubricant thickness, l, was used it is given as

$$\log\left(\frac{R}{R_{\infty}+1}\right)=\frac{l}{\lambda\sin\theta} \qquad \textbf{Equation 1.36}$$

where R is the ratio of area of fluorine containing C1s peaks to non-fluorine containing peaks at angle θ, R_{∞} is the ratio of areas of C1s peaks for pure lubricant and disk and λ is the mean-free path of the C1s photoelectrons in the overlayer.

The model assumed uniform overlayer thickness, which did not reflect reality, fluctuations in both substrate and lubricant thickness mean this was never the case. However, the model did provide a good average estimate of 7.5 nm lubricant thickness for the disk studied (Note, more recent disks would have a thinner layer than this).

Linder and Mee [119] also used XPS to study disk lubricant thickness. It was found that when all surface lubricant was etched away using argon ion etching, it occasionally was found to return to the surface after a time (up to 50 minutes). This migration of lubricant signified porosity of some types of disk and could be an important factor when comparing the lubricant thickness of different disk types. An alternative lubricant thickness model was proposed, as

$$L = e\ln(aR+1) \qquad \textbf{Equation 1.37}$$

where e was electron escape depth, a is carbon atom density relative to that in the lubricant and R was measured fluorocarbon density .

AFM can also be used to measure lubricant thickness [43]. Multiple measurements allowed distribution of the lubricant to be calculated. Comparison of a virgin disk and a disk used over

three years was made. In both disks, lubricant was evenly distributed but the virgin disk had a higher standard deviation, that is the used disk had more even coverage although slightly thinner. This indicated that lubricant spin-off may have occurred over time.

Yokozawa [120] described techniques for characterising the lubricant used on hard disks. Many techniques cannot cope with the very small amounts of lubricant present on hard disks, XPS can quantify the small amounts but can only identify the structure of the main frames present. Identification of the end-groups is only possible using Static Ion Mass Spectroscopy (SIMS) even then this can be difficult.

1.2.6.5 Surface Contacts

Flying Contacts

A Laser Asperity Detector (LAD) was used to study slider flying dynamics over disk asperities of various heights [63]. The LAD focuses a laser beam on a small mirror attached to the slider and monitoring the reflected beam, pitch and roll were recorded. Tests were conducted at 40% of normal flying height with unlubricated disks to accelerate collisions. Since pitch changes had a more significant effect than role with respect to signal loss, these changes were concentrated on in the literature. Head-disk collisions were categorised into three types as follows.

Type 1: When asperity height was less than the slider mid-length flying height. Trailing edge hits sending trailing edge up and leading edge down, Figure 1.26. This led to signal spacing loss.

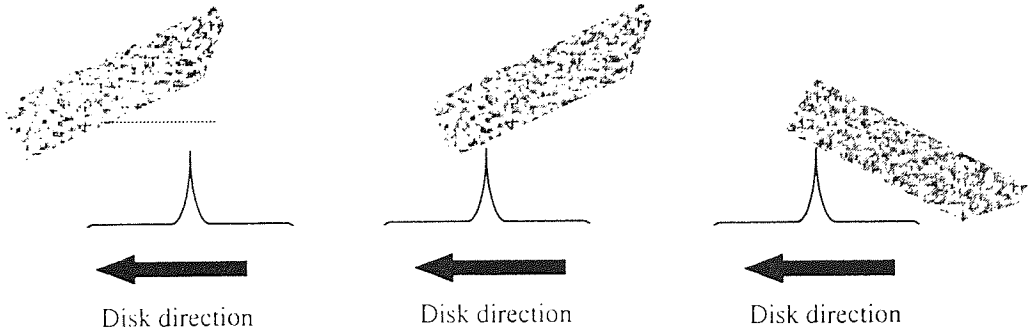

Figure 1.26 Type 1 head-disk collision

Type 2: Asperity height greater than mid-length flying height. Leading edge hits, sending it up and then down as it passes the asperity. This leads to elastic deformation of the asperity, Figure 1.27.

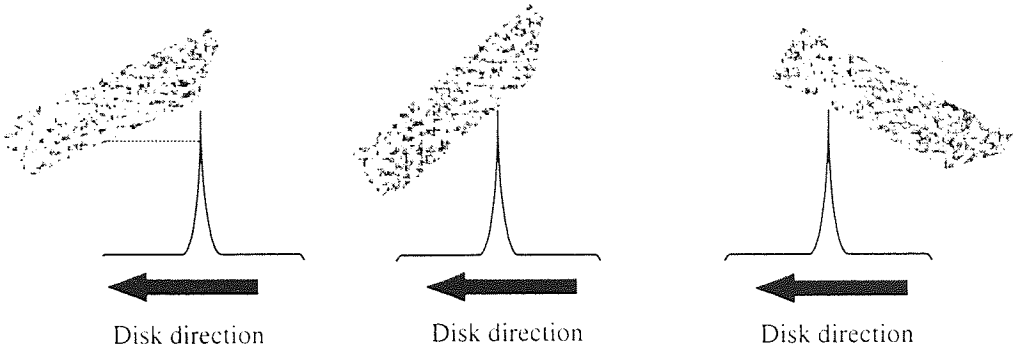

Figure 1.27 Type 2 head-disk collision

Type 3: Asperity height greater than leading edge flying height and downstream asperities are present. Contact fusion causes initial dip of leading of leading edge/raising of trailing edge then downstream asperity prevents negative pitch, Figure 1.28.

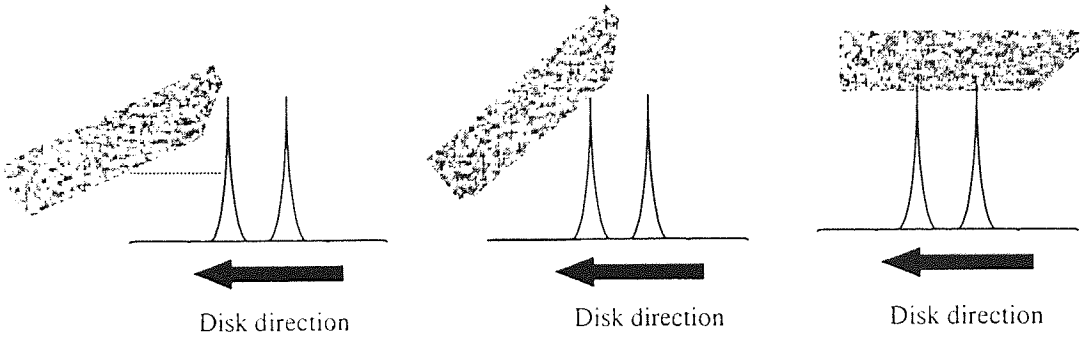

Figure 1.28 Type 3 head-disk collision

Initially on flying the head hit a few asperities (caused by large asperity height or momentary pitch/roll action due to initial flying dynamics). When negative pitch was severe the leading edge hit the disk pushing the alumina particles down semi-elastically and generated local heating. Adhesive transfer of thermally degraded disk-coating binder material occurred, usually onto the head chamfer in the form of smears.

As flying continued debris built up on the head and occasionally transferred back to the disk as partially fused debris piles. These increase the severity of pitch excursions until the disk or head suspension was catastrophically damaged.

Monitoring head dynamics allowed the severity of contacts to be studied, also an estimate of interface failure was given by a sharp increase in pitch excursions.

Li and Menon [121] reported that in proximity recording slider/disk contacts occur at the trailing edge of the slider and that initial contacts and friction forces cause changes in the pitch angle and flying height. The pitch angle starts very small, initial disk interference causes a lifting moment at the trailing edge further decreasing of the angle. As high asperities are worn from disk the pitch again increases reaching its steady state value. Usual proximity pitch angle was between 1-3 milliradians. Hu et al [122] state that having high pitch angle is beneficial since it allowed close contact to disk and gives smaller fly height and contact force.

McMillan et al [123] used AE to study the transition from sliding to flying of sliders. AE signal was found to increase with velocity to some point and then decrease as velocity was further increased.

It was observed that AE signal had a distinct double peak for tri-pad sliders. Further investigation suggested that the first peak occurred when the slider rails contacted the disk at low speed. The second occurred when the slider load was transferred from the rails to the contact pad at the trailing edge. For the standard tri-pad slider, peaks were seen at 1.5 and 3.5m/s, after reaching the second peak the AE signal decreased. For negative pressure sliders, AE signal increased reaching a peak at 2.5m/s and then decreased to the noise floor. A gradual increase was then seen as velocity increases further due to the slider again contacting the disk at higher velocity due to the sub-ambient force. Results indicated that at low velocity most contacts occurred at slider rails, above 4m/s it was the trailing edge region that made contact with disk.

Suzuki and Nishihira [124] report that during proximity recording much direct contact between a tri-pad slider and disk occurs, contacts were again measured by means of an AE sensor attached to the trailing edge of the slider. At high velocities (higher flying heights), the slider flew with less contact to disk. Most of the AE signal was due to air bearing resonance, the amplitude of which depends on the disk material and surface roughness. The slider vibrated more flying over a smooth surface than a textured one of the same material.

Uy [63] reported that the effect of disk roughness was obvious on both slider and disk wear during proximity recording. Smooth disks reduced slider and disk wear, this was attributed to the small amount of slider/disk interference taking place initially.

Chao and Russak [52] reported that the number of intermittent contacts at the interface could be reduced by reducing the waviness and roughness of the disk surface, since this would decrease the amount of fly height variations and subsequent contacts. However, having a low roughness value would detriment stiction performance.

Since slider vibrations were affected by surface topography, flying height and damping could be assumed to be affected also. Fly height fluctuation was measured by changes in Laser Doppler Vibrometer (LDV) measurement. Tested were a textured disk and smooth disk, results show the slider flew slightly higher over the smooth disk.

This behaviour was also reported by Donovan and Bogy [68], super-smooth and smooth disks were tested with proximity tri-pad sliders, with fly height measurements recorded. At high disk velocity no difference was observed, but when velocity fell below 7 m/s, slider fly heights deviated. A maximum difference was reached at 2.5 m/s, where the slider flew 8 nm higher over the super-smooth disk. AE results confirmed that fly height differences were not caused by single asperity contacts but differences in the supporting hydrodynamic film.

To examine slider damping transient motion was measured when in contact with a single protrusion fabricated on both a smooth disk and textured disk. The fly height change was monitored by the LDV at the trailing edge of the slider.

Straight comparison was not appropriate since asperity protrusion heights may have differed, instead the decrement in slider vibration curves after the impact were studied. The conclusion was that a slider flying over smooth disk experienced 20% less damping.

The motion of the air bearing and slider was represented by a spring-mass-dashpot model with 1 degree of freedom. From previous observation the motion of the slider was known to be in underdamped mode and can be described as a function of time by the solution to Equation 1.7, that is

$$x(t) = Ae^{-\zeta\omega t}\sin(\omega\sqrt{1-\zeta^2}\,t) \qquad \textbf{Equation 1.38}$$

where A is initial amplitude, ζ is the damping ratio and ω is angular frequency.

The Root Mean Square (RMS) roughness of x(t) was then calculated by squaring, integrating with respect to time t and dividing by T as below

$$(RMS)^2 = \frac{1}{T}\int_0^T x^2(t)dt \qquad \textbf{Equation 1.39}$$

Solving this provided an expression for RMS in terms of A, ζ, ω and T as shown

$$(RMS)^2 = \frac{A^2}{T}\left(\frac{(1-\zeta^2)}{4\zeta\omega} + \frac{\zeta^2\cos\omega T\sqrt{1-\zeta^2}-1}{4e^{2\zeta\omega T}\zeta\omega} + \frac{\zeta\sqrt{1-\zeta^2}\sin 2\omega T\sqrt{1-\zeta^2}}{4e^{2\zeta\omega T}\zeta\omega}\right) \textbf{Equation 1.40}$$

This equation provided compatible results to the AE values observed experimentally.

Damping ratio was the only variable term in the expression, hence ζ must be less for a smooth disk than textured disk in order to cause the differences in RMS of AE signal observed.

Stationary Contacts

Bhushan and Blackman [125] reported that when two surfaces touch the asperities were first to come into contact. Contact of two surfaces occurs at a small fraction of the nominal area. The applied normal load is carried by the highest asperities which results in extremely high normal pressures at the contacting tips. The real area of contact plays a very important role in the friction and wear.

Archard [126] gave a method for deciding whether the contacts between very smooth surfaces were plastic or elastic.

The plasticity index, ψ, was given in [127] as

$$\psi = \left(\frac{E'}{H}\right)\sqrt{\frac{\sigma}{R}} \qquad \textbf{Equation 1.41}$$

where E' is complex elastic modulus, H is material hardness of the softer material, σ is standard deviation of height distribution and R is the radius of curvature of the asperity.

If $\psi > 1$ surfaces were found to deform plastically, if $\psi < 0.6$ surface deformation was elastic and between these values behaviour was unknown. Usually, deformation at the hard drive interface was elastic [60], wear occurred at lower rates during elastic contacts.

It was assumed that each asperity was covered in tiny micro-asperities, increased load meant that in an elastic model the number of contacting asperities increased and thus contact area remained proportional to load.

It was reported that the exponential asperity distribution function previously used to model surfaces only accounted for the highest 25% of asperities. A new Gaussian model for height distribution was proposed by Onions and Archard [128] as

$$\theta(s) = \frac{1}{2\pi} e^{-\frac{1}{2}s^2} \qquad \textbf{Equation 1.42}$$

This function can be integrated to provide an expression for the probability of finding an asperity between two specified heights, h and (h+Δ h), as

$$f(y) = (2\pi)^{-\frac{1}{2}} e^{-\frac{1}{2}y^2} \qquad \textbf{Equation 1.43}$$

where height was normalised by standard deviation of asperity heights, such that $y = \frac{h}{\sigma}$.

Estimations for the real area of contact can be deduced from this and used in friction/stiction estimation. the disadvantage of this method is that constant asperity radius was assumed which is unrealistic. It was also shown by Polycarpov and Etsion [129] that the method overestimated contact load, area and number of asperities.

The exponential correlation function was defined as

$$C(\beta) = e^{-\frac{\beta}{\beta^*}} \qquad \textbf{Equation 1.44}$$

where β^* was correlation length. Poon and Bhushan [130] used a similar correlation function to generate a random surface with varying asperity radii to improve upon the above model. Contact pressure was found to increase with surface roughness and $1/\beta^*$. Thus, plastic deformation could be avoided by decreasing surface roughness or increasing correlation length. The peak-to-valley value was found to be a significant parameter with respect to contact.

Sharma and Talke [58] illustrated that silicon carbide sliders showed superior stiction and friction behaviour compared to conventional Al_2O_3-TiC sliders. The improvement in tribological behaviour of these sliders was attributed to differences in the real area of contact.

If the peak heights of mating surfaces had Gaussian distribution and asperities were spherical near their summit with constant radius, then real area of elastic contact, A_r, is given by

$$\frac{A_r}{3.2 p_a A_a} \approx \frac{1}{E_c \sqrt{\sigma_p / R_p}} \qquad \textbf{Equation 1.45}$$

where p_a is apparent pressure. A_a is apparent area of contact, R_p is composite radius of asperity peaks, σ_p is standard deviation of peak height distribution and E_c is the composite Young's modulus. R_p , σ_p and E_c are given by the following

$$\frac{1}{R_p} = \frac{1}{R_{pd}} + \frac{1}{R_{ps}} \qquad \textbf{Equation 1.46}$$

$$\sigma_p = \sqrt{\sigma_{pd}^2 + \sigma_{ps}^2} \qquad \textbf{Equation 1.47}$$

$$\frac{1}{E_c} = \frac{1-\upsilon_d^2}{E_d} + \frac{1-\upsilon_s^2}{E_s} \qquad \textbf{Equation 1.48}$$

where subscripts d and s refer to disk and slider respectively and υ is the Poisson ratio of contacting surface.

To obtain an estimate for A_r values were obtained for topographical parameters using an interferometric microscope.

Material	E (GPa)	υ	Hardness (GPa)	σ_p (nm)	1/Rp (mm^{-1})
Al_2O_3-TiC	390	0.21	18	2.32	21.81
SiC	450	0.17	25	0.59	31.54
Rigid disk	100-130	unknown	5-6	5.77	32.6

Table 1.3 Material properties for sliders and commercially available disks

Using these figures, real area of contact for SiC sliders was found to be 9% less than that of Al_2O_3-TiC sliders on the same disk. Since the differences observed in friction and stiction behaviour were greater than 9% it was thought that other factors were also affecting results.

Majumdar and Bhushan [131] extended Equation 1.45 to give predictions for number of contacting asperities, ε, such that

$$\varepsilon \approx \frac{2.64P}{(\sigma_p/R_p)E_c\sqrt{\sigma_p/R_p}} \qquad \textbf{Equation 1.49}$$

where P is the load on the surface.

Chilamakuri and Bhushan [132] claimed that surfaces produced by machining processes such as grinding, shaping and turning and some magnetic disk texturing processes such as sputtering and laser processing were frequently non-Gaussian. Most of the contact models developed

over the past thirty years have assumed Gaussian distribution of surface heights in their analyses. Non-Gaussian surfaces were shown to offer promise for the design of interface roughness to provide low friction, stiction and wear.

Chilamakuri and Bhushan [133] investigated the effect on parked slider contact of laser bump peak radius for the w-type of laser bumps shown in Figure 1.7c). The profile of one such bump is shown in Figure 1.29, where peak radius is indicated by R_f .

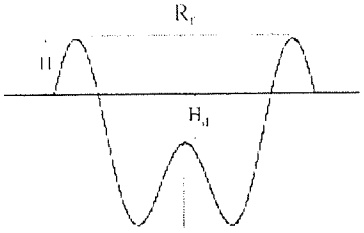

Figure 1.29 Profile of a w-type laser bump

Note peak height - defined as ($H-H_d$) - was held constant during experiments at 25 nm. Contact area and meniscus force was found to decrease with an increase in peak radius.

The problem with modelling surfaces was achieving the broad bandwidth of roughness found in real surfaces. In sampling modelled surfaces are assumed to be perfectly smooth within a finite area. There is also a limitation on the number of data points that can be handled by a computer [134].

1.2.7 Environmental Effect

The continued reduction in the head-disk separation of magnetic data storage systems and the corresponding increase in the frequency of head-disk contacts will place severe stress on the lubricant and overcoat used to protect the surfaces. With decreasing fly heights, environmental conditions such as temperature and humidity have become increasingly important to tribological performance. Contamination - such as gasses and wear debris - also played a significant role on the reliability of the interface. Some examples of how these operating conditions affected tribology are now given.

1.2.7.1 Humidity

Effect on Friction

Friction force decreased in the absence of water vapour. Yang et al [86] showed that flushing the operating environment with dry nitrogen decreased relative humidity and hence friction. Also, it was reported that in moist air (53% RH in this work) the friction coefficient increased rapidly. This increase in friction when the interface is in a humid atmosphere and decrease when a dry gas was introduced into the environment was also reported by Marchon et al [103].

Kaneko, R. and Koshimoto [41] stated that in ambient conditions, friction depends on lubricant thickness, (layers of 0, 5, 9 and 11 nm were tested) with thicker lubricant films giving lowest friction. Note, this was of concern since in future drives the disk lubricant layer could only afford to be one molecular layer thick due to spacing loss. At higher humidity, friction is controlled by the absorbed water layer. Lubricant film can be removed by the condensed water giving thinner film and higher friction.

The effect of the operating environment on the coefficient of friction of unlubricated and lubricated samples was investigated by Bhushan [135]. Silicon samples were lubricated with 2.9 nm thick Z-15 and 2.3 nm thick Z-Dol bonded and solvent washed lubricants. The coefficient of friction in dry environments was lower than that in humid environments. In the humid environment, condensed water from the air competes with the liquid film present on the sample surface and interaction of the liquid film occurs (water for the unlubricated sample and lubricant for the lubricated sample). Adhesion of lubricant to the substrate is weakened and puddles are formed. This is known as de-wetting and results in a poorer lubrication performance, resulting in high friction. The de-wetting effect in a humid environment for Z-Dol was more pronounced than for Z-15.

Cha et al [111] reported that some additional water at the interface meant the shear strength of asperity junctions decreased aiding friction on a disk lubricated with long chain PFPE's. However, at very high humidity the adsorbed water layer could be of comparable thickness to the lubricant layer. This meant the surface tension of adsorbed layers could increase and raise friction. Zhao and Bhushan [39] stated that disk surfaces exposed to humid environments may result in a total liquid film consisting of lubricant and adsorbed water. Since uniformity of liquid film is necessary for constant friction, large variations in friction can be used to signify the presence of this mixed liquid.

For disks lubricated with phosphazene, a decrease in friction with increased relative humidity was observed, this indicated that phosphazene interacted successfully with water. The interaction was thought to be physical mixing since phosphazene molecules are hydrophobic. Surface energy or viscosity could decrease due to this mixing reducing friction.

Effect on Stiction

It has been shown that very high stiction force (of up to 30 grams) can occur under conditions of high humidity due to meniscus effects. In modern drives, the low torque motor may not be powerful enough to overcome such high stiction on drive start-up, especially if more that one interface in the stack experiences this level of force. This could also cause major damage to miniaturised slider components and associated suspensions.

High stiction arose as a result of menisci formation at asperity contacts, as mentioned bonded as opposed to mobile lubricant, limits this formation. Bhushan and Zhao [117] reported the use of two types of PFPE lubricants with alcohol end groups applied to identical disks :-

Lubricant A with end groups HO- ... -OH

Lubricant B with end groups F- ...-OH

A single disk tester was used under different conditions of humidity with an Al_2O_3-TiC slider.

Head and disk materials were exposed to high humidity and the resulting water film thickness was measured by an ellipsometer. The Al_2O_3-TiC slider material had the highest water film thickness due to the Al_2O_3 phase being a good absorber of water and other chemicals.

Lubricant A favoured water adsorption due to the polar group -OH being present at both ends. Lubricant B had this -OH group at one end only which could attach to the carbon overcoat, the other end being non-polar did not favour water adsorption. Hence, less water was absorbed onto disks coated with type B lubricant, which was favourable in humid conditions.

All materials exposed to high humidity reached steady-state adsorption with an equation for water layer thickness given as

$$h = h_1 * RH + h_2 * e^{c(RH-1)} \qquad \textbf{Equation 1.50}$$

where h_1, h_2 and c are experimental constants with values 0.3, 0.5 and 20 respectively and RH is humidity on a scale of 0-1. This model however fails to incorporate temperature, which would also be a factor influencing the resulting layer thickness.

For mobile lubricants, humidity of >50% RH was shown to displace lubricant at some sites and since water has a higher surface tension than the lubricant the meniscus force was accelerated. Mobile lubricant was sensitive to humid environments. Stiction was found to be a function of relative humidity in the range [5-80% RH].

Chun et al [106] tested a DLC overcoated slider flying in proximity contact with a nitrogenated carbon disk in various environments. Contrary to the behaviour reported by Yoon et al [85] no substantial differences between friction in oxygen/non oxygen containing environments was found. However, moisture again was found to increase the adhesive force of stiction, thus higher relative humidity resulted in higher stiction.

Effect on Wear

Yang et al [86] performed CSS tests in ambient and dry conditions using a 50% slider on disks with varying thickness of carbon overcoat. Results were presented with the only failure observed being disk with thin overcoat (5 nm) under dry conditions. This suggested that water vapour could aid wear performance in some instances. Bhushan confirmed this in [42] where disk durability was found to decrease under low humidity or in a vacuum.

Cha et al [111] additionally reported failure in dry conditions using unlubricated disks with Al_2O_3-TiC sliders. This was due to asperities being in solid-solid contact which meant that contacts were dependent only on the high shear strength of asperity junctions and failure occurred readily. As humidity was increased, water bridges were formed at asperity tips, this reduced the amount of solid-solid contact, shear strength and friction. Durability was also improved. However when humidity rose beyond 80% RH, the number of water bridges

increases sharply, the condensed water formed additional junctions and increased total area of contact. The coefficient of friction increased and durability decreased.

For disks lubricated with long chain polymers (e.g. PFPE's), wear behaviour depended on the way water molecules interacted with lubricant. Under dry conditions, there was no condensed water present and the liquid film comprises solely of lubricant. However, some lubricated disks were found to perform best in humid environments, this could be due to the water molecules filling the gaps between the long chains leading to better disk coverage. Water molecules can also increase the mobility of the lubricant and help lubricant replenishment of depleted areas.

Sharma and Talke [58] performed extensive environmental testing was carried out to illustrate the differences between Al_2O_3-TiC and SiC slider material, both standard two rail and negative pressures sliders were studied. Constant speed drag testing was performed at 0.16 m/s under ambient, hot/humid and cold/dry conditions. Results presented have been tabulated for clarity, with failed test shaded in grey.

Test Response	Sub-ambient		Two-rail	
	SiC	Al_2O_3-TiC	SiC	Al_2O_3-TiC
Ambient 23°C/45% RH	No fail in 20K revolutions	No fail in 20K revolutions	No fail even after 20K revolutions.	Fail after 16K revolutions.
Hot/humid 50°C/80% RH	No fail in 20K revolutions	No fail in 20K revolutions	Increase then decrease. No fail in 20K revolutions.	Fail after 3.5K revolutions.
Cold/dry 5°C/10% RH	No fail in 20K revolutions	Fail after 3K revolutions.	Fail after 4K revolutions.	Fail after 1K revolutions.

Table 1.4 Environmental wear test results for Al_2O_3-TiC and SiC slider material

SiC performed the best in tests for both slider types, with the only failure observed under cold/dry conditions. It was found that SiC sliders exhibited high initial friction due to generation and interposition of abrasive wear debris. Following this, a decrease in friction was noted due to compaction of these particles that formed a protective film of hydrated amorphous silica that aided wear performance.

Dry conditions were also found to be the worst environments for wear during proximity recording although long-term friction was relatively stable in cases where no water was introduced. Chun et al [106].

1.2.7.2 Temperature

Effect on Friction

For disk lubricated with phosphazene, decreasing friction with increasing temperature was explained by a decrease in viscosity of the lubricant [111]. The room temperature viscosity of phosphazene was higher than that of long chain polymers, while it's viscosity at 60°C was comparable with room temperature viscosity of long chain polymers. Thus, the same effect was not observed in PFPE lubricated disks, instead friction was found to increase at high temperatures.

Cutiongco et al [31] reported that the structure and sp_3/sp_2 bonding ratio of hydrogenated carbon films strongly affected friction behaviour. In ambient conditions (defined as 22°C), hydrogen atoms are bonded to carbon atoms on the surface of the overcoat by strong covalent bonds. At low sliding speed the temperature increase through friction is small and hydrogen desorption will not occur. Increases in sliding speed results in higher temperatures including flash temperatures at contacting asperities, this exacerbates the local chemical reactions and allows desorption of hydrogen and reduction in coefficient of friction. If flash temperatures exceed the annealing temperature of the hard carbon surface reconstruction occurred accompanied by formation of sp_2 phase. The critical temperature for sp_3 to sp_2 transition depended on the density of hydrogen-terminated bonds on the surface and on the environment (e.g. 400°C for diamond carbon films in ambient, 1100°C in high vacuum). During transition a large proportion of the frictional energy was consumed resulting in decreasing friction coefficient.

Effect on Stiction

Although very little literature was found which reported this affect directly, certain conclusions were drawn. Cha et al [111] reported that during temperature rise from 23°C to 60°C the bulk viscosity of phosphazene lubricant decreased significantly. Since, stiction was reported to be inversely proportional to viscosity by Bhushan [91], this would infer that higher stiction occurred at high temperatures.

It was also reported that the effect of temperature was most significant at low humidity. In the absence of water vapour changes were due to temperature fluctuations alone [111]. A proximity tri-pad sliding on disk with a thin nitrogenated overcoat (<10nm) suffered increasing stiction force followed by catastrophic failure in conditions 55°C/10% RH, as reported by Chao and Russak [52]. With thicker overcoats stiction very gradually increased but interface did not fail in 20K CSS cycles.

Zhao and Talke [27] reported that the effect of temperature on stiction was dependent on the type of media used. With laser textured media the temperature effect was negligible, but where mechanically textured media was used a slight decrease was noted. This was explained by changes in the viscosity of lubricant observed with temperature.

Effect on Wear

During normal operation no slider-disk contact should occur except during the take-off and landing phases during drive start-stops. However, irregularities in surface texture and/or slider flying characteristics mean that occasionally contacts can occur at drive full operating speed. At the interface the majority of frictional energy is transformed into heat. When the normal load, N, is evenly distributed the temperature rise experienced should be in the order of 7-10°C. However, it can occasionally occur that the entire load is carried by one asperity, this leads to high flash temperatures in the order of several hundred degrees. These high temperatures play a significant role in the process of wear.

It was thought useful if a recording head could itself measure the exact temperature increase that head-disk contact induces. An experimental MR head was designed for this purpose by Menon [136], with contact temperatures of over 1000°C recorded. Bair et al [137] also attempted to measure contacting asperity temperatures during operation. During sliding of a sapphire slider at a height of 40 nm (which was larger than disk roughness) hot spots were not expected, but occurred in the presence of surface damage or a single high asperity. Occasional asperity contacts produced hot spots of 500°C for duration's of 30μs. The temperature hot spots created by particles of debris caused slightly lower temperature rise of between 200-500°C.

Chekanov et al [138] reported that the temperature rises that occurred during intermittent contacts could cause cracking of the read-write poles. This was due to thermal expansion/contraction of the head wires causing in-plane fatigue. Cracks could start in the vicinity of the trailing pole tip area where the alumina was thin or at any chipping site and be drawn towards the pole region. Cracks could have depth >100nm and width around 4μm by AFM. Magnetic force microscopy was used to determine the effects of cracking on stray magnetic fields. It was found that only cracking in the gap region affected magnetic field, with gap distortion taking place and creating a flattening of the write field.

Jiang et al [84] reported that debris particles, when acted on by elevated temperatures can be transformed into protective layers, either in the form of compact debris particle layers (for temperatures under 250°C) or smoother glaze layers (for temperatures above 250°C). These layers can explain the reduction in wear from severe to mild during sometimes seen during operation. However, the added material between head and disk gives rise to spacing loss.

Zhao and Talke [27] also observed occasional improvement in hard drive tribological performance with increased temperature This was possibly due to changes in lubricant properties, such as decrease in viscosity aiding wear performance.

Effect on Flying Height

The operating environment inside a disk drive can become very hot especially if many disks are rotating at high speed. Cha et al [139] suggested three main causes of flying height change due to temperature, these were changes in slider crown, air viscosity and mean free path of air.

The deformation of the slider depended on the type of epoxy binder used to attach it to suspension and could increase or decrease the slider crown significantly (by up to 15 nm) this could lead to changes in flying height of up to 5 nm. Note, slider crown is demonstrated in Figure 1.30.

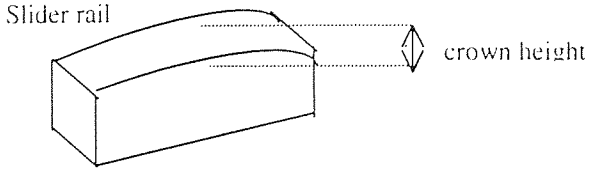

Figure 1.30 Definition of slider crown

The pressure gradient required to raise the slider was related to viscosity. Since air viscosity decreased with temperature this led to decreased load capacity of the slider. Thus, slider flying height decreased with increases in temperature.

The mean-free path of air molecules was approximately 65nm in ambient, when flying height was less than this the actual flying height depended on the mean-free path size. Increases in temperature caused a decrease in the density of air, hence larger mean-free path. This means there will be less air molecules able to flow under the slider, thus flying height will decrease. Similarly, Peng and Hardie [55] reported a decrease in flying height, due to the mean free path increase, was experienced at high altitude.

Note, viscosity and mean-free path effects acted together in an open system (e.g. a spin-stand tester), in a closed or sealed drive air density does not change so neither would mean-free path. Thus, the flying height would only affected by viscosity, that is decrease with temperature.

1.2.7.3 Contamination

Liquid Contaminants

Some common environmental contaminants found in disk drives were silicone oil (used in seals), dioctylphtalate (DOP) and dioctylacetate (DOA) used as plastisisers.

Glass disks were doped with these substances and examined under varying environmental conditions using AFM by Chekanov et al [140]. Under hot/humid conditions haze formed around the droplets of DOP and DOA, this consisted of a mixture of disk lubricant and contaminant material. Haze formed as a result of the smearing action of the head/slider, also friction and stiction force were higher in the hazed region. No such hazing occurred around the silicone oil droplet.

Gaseous Contaminants

Kurokawa [141] reported that various electronic components, gaskets and bearing covers in a disk enclosure can outgas when warmed. If any gas attains a level of vapour pressure that exceeds its level of saturation pressure when compressed underneath the slider, then the vapour liquefies on the slider.

The most likely time at which this liquefaction occurs is when temperature drops following a long run of the drive. This liquefaction continues for as long as saturation pressure is exceeded. If some of the liquid deposited on the slider is blown off by passing air, an equilibrium may be reached between liquefaction and its removal.

In Li and Bhushan [142], Ultra High Vacuum (UHV) environmentally controlled tribotest apparatus was used to monitor gaseous products generated from the head disk interface. The apparatus featured a mass spectrometer with ionisation chamber located in the line of sight of the slider-disk interface. An Al_2O_3-TiC slider was flown over standard Al-Mg and glass disks lubricated with Fomblin Z-Dol and Fomblin AM 2001 lubricants.
Z-Dol lubricant has endgroup -OCF2-CH2-OH while AM 2001 has a piperonyl endgroup, both endgroups were polar. Polar lubricants bonded to the disk surface without any post dipping treatment depending on the cleanliness/chemical reactivity of the overcoat.

During start up lubricant was removed mechanically from the disk by the sliding action of the head. Although most of the lubricant removed was usually found on the slider rails a significant amount disappeared entirely. The lubricant loss mechanism could be evaporation due to high interfacial temperatures or polymer scission producing fragments small enough to be gaseous.

During sliding on Al-Mg disks, decomposition of lubricant took place producing fluorinated compounds. Hydrocarbons were also traced, these emanated from the spindle bearings (since in a control test with no slider present they were also detected). Detection of H_2, $CO+N_2$, CO_2, CFO and CF_3 all began at the time of sliding and continued until the end of sliding. Only H_2 increased with sliding distance, all other compounds decreased slightly for lubricated disks. H_2, $CO+N_2$ and CO_2 evolved from the desorption of organic adsorbates and water from the disk surface. Initially surface groups were removed from the hydrogenated carbon overcoat, reaction with water molecules and/or evolution of hydrogen within the overcoat added to this.

Decreases in the CFO and CF_3 signals were detected after 100 m of sliding along with an increase in H_2, $CO+N_2$, CO_2 and friction coefficient. After some time visible wear tracks were formed. It was thought the change in values preceding this was an indication of lubricant depletion of the track area and direct contact occurring between slider and hydrogenated carbon overcoat.

The disk surface is 'cleaned' when the slider passes by and the fresh surface is exposed to the environment. Water molecules then adsorbed polarly on the fresh overcoat surface. Subsequent sliding may then break the bonds between hydrogen and oxygen atoms causing evolution of hydrogen. The oxygen atoms react with the carbon overcoat producing CO and CO_2 gas. No evolution of CFO and CF_3 was observed during sliding on an unlubricated disk, again indicating that these were lubricant by-products.

It has been suggested that decomposition of lubricant is due to electron mediated process. Electric potential differences of up to 0.1 V have been reported to develop between the slider tracks and reference areas. Shear rates of the lubricant films in these experiments were high and the energy dissipated during sliding may be sufficient to activate the lubricant to decompose. Mechanical degradation was also probable for both types of lubricant.

Pan and Novotny [59] examined slider-disk tribology by means of a tribochamber in which five types of head materials were tested, Al_2O_3-TiC, Mn-Zn ferrite, amorphous silicon, amorphous carbon, ferrite and sapphire. The first two of these represented materials currently in use, the rest were possible future options. Hydrogenated carbon overcoated disks with and without lubricant were used in test.

In a vacuum with Al_2O_3-TiC sliders, formation of C, $CO+N_2$ and CO_2 accompanied increasing stiction. The initial formation was due to desorption of organic adsorbates and water from the disk surface. This then reduced until after 350 m of sliding when the friction coefficient increased suddenly along with the formation of H_2. This was desorption of hydrogen from the carbon overcoat, at this time a wear track becomes visible.

In an ambient environment (oxygen containing) rapid re-absorption of adsorbates prevented the formation of a 'clean' surface and kept the friction coefficient relatively high. With lubricated disks fluorocarbon fragments of varying masses were also detected.

All other slider materials gave longer sliding distance before failure. With lubricated disks and Si slider a large amount of SiF_4 was produced suggesting a tribochemical reaction had occurred. The oxidised slider had reacted with HF (formed by fluorocarbon scission) forming SiF_4 which caused lubricant degradation and catastrophic failure in a vacuum. However, in

ambient as SiO_2 was removed by HF, oxide was continually formed on slider. Thus, durability was maintained.

Slider material, usually Al_2O_3-TiC, can cause break down of PFPE lubricant to form fluorides especially at elevated temperature/humidity. Analysis of disk by mass spectroscopy showed four main peaks - CFO, CF_20, CF_3 and C_2F_5. The first two of these are believed to be lubricant fragments broken down by the slider, the last two were thermally decomposed lubricant fragments. To eliminate this an approached would be to reduce the catalytic activity of the slider by applying a hydrogenated or nitrogenated carbon overcoat to it.

Solid Contaminants

Occasionally, contaminants originated from the actual materials that were used to manufacture sliders and disks [143]. Residual polishing slurries and/or chipped pieces from the sliders were known to adversely affect the reliability of the interface. Six intra-drive particle types were studied, Table 1.5.

Material	Source	Effect at Interface
Diamond abrasive nodules	Used for polishing and cutting sliders	Diamond particles left deep grooves in the disks and sliders.
TiC crystalline grains	One of two components sintered to create slider substrate	TiC particles left grooves in disk and cause scoring to sliders' sputtered alumina.
Alumina grains	As above	Alumina substrate rendered no damage to either surface.
Abrasive alumina nodules	Used in disk texturing	Alumina abrasives left light scores on disk.
Composite Al-TiC	Slider substrate	Al-TiC left disk grooves and slight scoring to sputtered alumina.
Sputtered alumina	Used in thin film head region to encapsulate read-write elements	Sputtered alumina caused disk damage only in the form of light scoring.

Table 1.5 Examples of effects of intra-drive particle contamination

Particles were applied to the interface by rubbing a contaminated cotton swab on the disk. To control the amount of particles added a swab was added to particles and wiped on disk, next a clean cotton swab was wiped over contaminated region of disk and then onto a clean disk - this was repeated until the desired particle dilution was achieved. It was found that different contamination particles had distinct effects on the interface, the end column in Table 1.5 summarises results.

A loose debris particle could become firmly attached to the slider due to the formation of liquid layer - either from liquid or gaseous contamination (see above sections). It could then cause complete drive failure. If the impacted particle is harder than the disk surface or impregnated by material that is harder, then erosive wear may be severe.

After some wear a protruding disk asperity may remove the impacted particle from the slider, this prevents head crash. However, this was found to be rare, it was more common for additional debris to mix with the liquid layer increasing viscosity, which holds the particle firmer still.

The repelling capability of a disk surface to a loose asperity is assessed by Li and Sharma [144]. Three types of spherical particles with different sizes and material properties are used to evaluate the spin-off ratios of disks from various manufacturers and with different lubricant thickness and texture roughness. It was found that the dominant factors determining whether a particle is spun off a disk surface were stiction and the centrifugal force. Particle size and material properties, disk spinning speed, disk radius, surface tension and contact angle also have significant effect. However, lubricant thickness and disk surface roughness have little effect on whether the particle became trapped or not.

Peng and Kirk [145] investigated a system which automatically classified solid contamination particles was proposed. The system uses a Neural Network to classify the source of particles found on a image scan as either rubbing, spherical, cutting, laminar, fatigue or sever sliding. The network uses 9 particle characteristics, including area, roundness and roughness, to compare particle properties with those from a known database. The system would save much time over studying particles 'by-eye', also discrepancies hailing from operator judgement differences would be removed.

Flying Solid Contaminants

Liu et al [146] described the effect of flying particles, which exist at the interface, these can lead to drive failure. Flying particles cause the formation of whiskers on the slider, little has been done to study their effect on the disk. In this experiment, rather than injecting particles into the interface they are actually manufactured there (more akin to the real life situation).

A hardened lump of cured adhesive (sub-millimetre in size) was placed strategically near the ID of the top disk in the stack, which contained two double-sided disks. The slider then hit this and generated loose micron sized particles.

As the disk rotated at high speed particles were dispersed to all parts of the enclosure. However, on examining all sliders and disk surfaces it seemed the top and bottom disk and slider showed most contamination. Whiskers had formed on trailing and side edges of slider, these were broken off in places due to slider/disk impact and had transported to the disk.

A three-stage model explained wear track formation as follows. Particles are generated, some will hit the disk surface and will be stuck on and then be captured by the slider, they will accumulate and whiskers are formed. Particles can then travel anywhere on the disk with the slider. Impact then causes the large mass to collide with the disk at high rotational speed causing severe three-body abrasion.

Most flying particle damage occurs on outer two disk surfaces in stack due to particle dispersion being controlled by air pressure. It is known that the air pressure between a set of co-rotating disks is higher than that between a single rotating disk and a stationary surface, it is known that air flows from high to low pressure carrying with it loose particles.

2 Experimental Apparatus and Method

Experimental results were generated and used in the creation of Mathematical models to explain drive behaviour. Results were obtained by running a hard drive simulator, Section 2.1, initially in ambient environment and then modified conditions.

Several surface analytical methods were used to study head and disk topography and examine chemical composition of surfaces, techniques used are described in Section 2.2.

2.1 Apparatus

Results were gained using a custom-built Accelerated Friction Tester (AFT), which simulated the head-disk interface of a computer's hard drive, Figure 2.1 shows schematic.

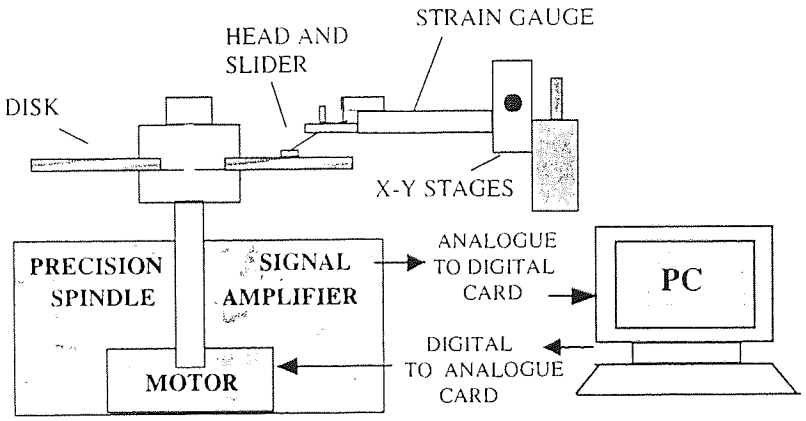

Figure 2.1 AFT set up

The AFT flew a slider, attached to a cantilever arm, over a hard disk rotating at high velocity. The slider was positioned radially and vertically over the disk by means of a precision x-y stage.

Friction was measured by four 130-Ohm strain gauges connected to form a bridge on the cantilever arm. Thus, any lateral force on the slider unbalanced the bridge causing a voltage to appear in the output of a signal-conditioning amplifier (model Vishay 2310). The value of this voltage, proportional to frictional force, was then passed to a PC by means of a Metrabyte DASH8 Analogue to Digital card (ADC) and saved by the acquisition program. Each voltage was then converted into a force (in grams to conform to drive industry standards) by means of

a calibration routine that was carried before each run. Static friction measurements were captured by a peak-hold detector as the maximum lateral force at the slider/disk interface at the instant relative motion takes place.

The PC controlled the motor speed via an Amplicon PC24 Digital to Analogue converter card (DAC). AFT apparatus was situated on a granite slab to minimise vibration during operation. An air bearing motor was used to rotate the spindle again to minimise vibration. A supply of compressed air (at >80 psi) was required to run the bearing; if air pressure fell below this a pressure switch activated halting the run.

Several alterations had to be made to the apparatus at the start of the project, to enable AFT experiments to be carried out in the Magnetic Media Laboratory. A Hydrovane compressor (model 502PURS operating at 10 bar) was purchased to supply compressed air to the bearing. The addition of a filter/regulator unit ensured correct pressure of air was achieved; in fact, 90 psi was used. An air dryer (model TMC21) was also added to the system to vent moisture from the compressed air before supplying it to the bearing. Additionally, the entire AFT apparatus was situated under a Class 100 laminar flow air shower.

2.1.1 Test Definitions

Two main types of experiment were performed Contact Start Stop (CSS) and Drag Tests, both types of tests were carried out initially under ambient and then at various temperatures and humidities.

One CSS cycle involved a disk being accelerated at constant rate to predefined dwell velocity; this was maintained for a set period, at the end of which the disk was decelerated to rest again. A standard CSS comprised of 3.2.3 second ramp-up, dwell and ramp-down cycle was used with dwell velocity 1400 rpm (equivalent to 3.37 m/s at 23 mm from disk centre), Figure 2.2. Note CSS testing was performed over the landing zone of the disk at inner diameter to emulate where take-off/landing would occur in a real drive.

For stiction studies, the disk was ramped to 1 rpm dwell velocity only to be consistent with other literature [98].

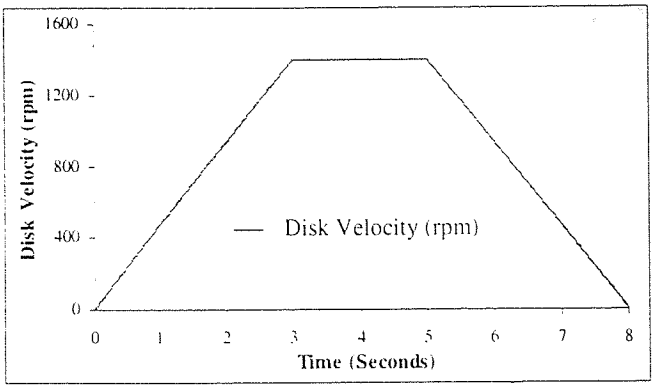

Figure 2.2 Velocity trace over 1 CSS cycle

During CSS cycling dynamic friction readings were taken at a rate of 250 Hz and static friction (stiction) was captured immediately as the disk began to rotate using 2000 Hz.

CSS tests involved many repetitions of the above and simulated a hard drive being turned on and off many times. A standard CSS test comprised of 7000 cycles and took around 18 hours to complete, note an unconstrained pause occurred between some cycles while the data was saved to file. The test represented around 19 year's use of a hard drive, assuming it is turned on and off once daily.

Drag testing involved the disk being rotated at constant velocity for a long period, usually 20 hours, with friction measured frequently throughout. The test was designed to study interaction of slider and disk by accelerating the contact between them. This was achieved by rotating the disk more slowly than normal drive speed; thus ensuring the slider was not flying but dragging on the disk surface. The velocity used for drag testing was 122.24 rpm (0.5 m/s at 39 mm from disk centre), as this was found to be just below slider flying velocity so gave disk contact whilst ensuring that maximum distance was travelled by slider. This test was thought to particularly simulate proximity recording where a significant amount of contact takes place between surfaces. Notice drag testing was conducted over disk data zone, as opposed to landing zone.

2.1.2 Controlling Software 'Aft.bas'

A Qbasic program existed that ran Contact Start Stop (CSS) tests on AFT apparatus and wrote results to floppy disk, this software was written 'in-house' by Xyratex. Since, no information was available on the software; reverse engineering was performed to understand how the program worked [147].

The software controlled motor speed and allowed the user to enter the ramp up, dwell and ramp down times for CSS. Cycles could be repeated any number of times from 5 to 14000. The number of measurements taken per cycle varied with cycle length to allow measurements to be evenly spaced. The force required to overcome static friction (stiction) at the start of each cycle was also recorded from peak hold circuitry. The number of cycles performed and frequency of data recorded was limited by the storage availability on the 1.44-Mb disk.

2.1.2.1 Software Communication and Associated Hardware

Communication between the computer, signal amplifier and motor are illustrated in Figure 2.3, with hardware description following.

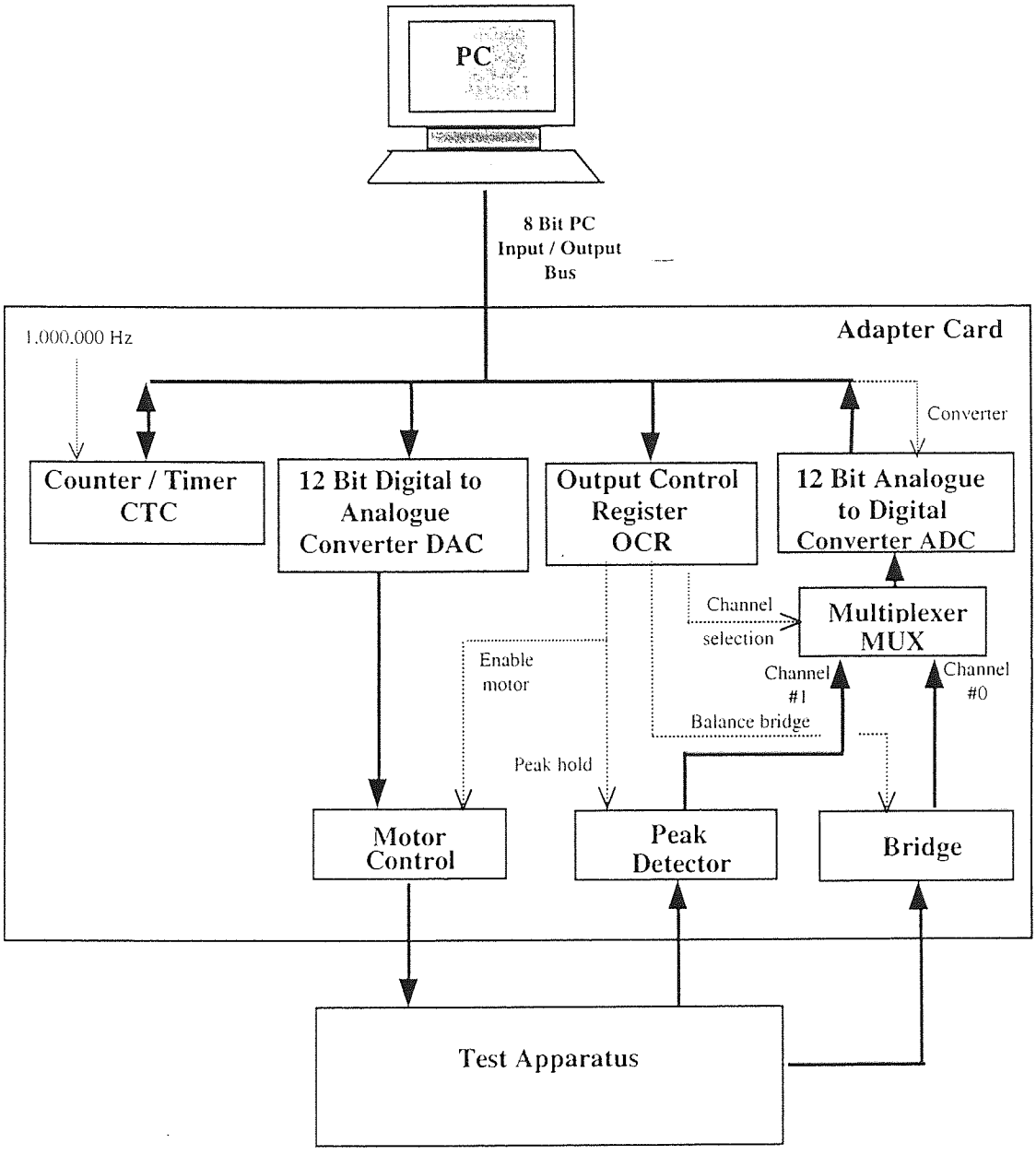

Figure 2.3 Hardware/software communication

(i) Digital To Analogue Converter (DAC) for Motor Speed Control

A 12 bit DAC was used to control the speed of the motor, by converting a digital velocity signal from the PC into an analogue representation of voltage. As the interface bus was only 8 bits wide then 2 addresses are used to set up the DAC as follows

Address 784: least significant 8 bits Address 785: most significant 4 bits

Hence, a 12-bit value was output from the PC (in 2 parts) which was then translated into a voltage and used to control the speed of the motor.

The device was idiosyncratic, in that the greatest motor speed was generated when the device had all bits set to zero, and the motor speed was zero when the device has all bits set to one. Note, the motor has 2048 (i.e. 2^{12}-1) possible speed settings.

(ii) Analogue to Digital Converter (ADC) for Friction/Stiction Storage

The ADC converted analogue voltage signals (representing friction and stiction) into digital representations that could then be read into a PC and be stored. The ADC has 12-bit resolution and again since the PC bus is only 8 bits wide the input from the ADC is in 2 parts as shown,

Address 768: least significant 4 bits Address 769: most significant 8 bits

(iii) Analogue Signal Multiplexer (MUX)

A single ADC unit may be used to convert many different input signals (here two - friction and stiction). Since the ADC may only convert one signal at a time the signal must be converted and presented to the ADC at different times. This staging was achieved using a signal multiplexer as follows:

Friction selected by setting bit 0 of the Output Control Register (OCR) to **0**
Stiction Peak detector selected by setting bit 0 of the OCR to **1**

(iv) Counter Timer Chip (CTC)

The CTC used in timing the frequency of measurements taken in each cycle, when a 16-bit value is loaded into CTC it is decremented at a rate of one bit per millisecond. When the counter reaches 0 it stops and waits until another value is loaded. This counter may be interrogated at any time to determine the amount left in the counter.

(v) Output Control Register (OCR)

The OCR is an 8-bit latch used to control the operation of the above hardware. It was located at address 770 and has the following functions, Table 2.1.

Bit	Function
0	Multiplexer (Set to 0 - Take friction reading/1 - Stiction reading)
1	Unknown
2	Unknown
3	Peak Detector Control (Set to 0 - Clear/1 - Load)
4	Motor Control (Set to 0 - Disable/1 - Enable)
5	Balance Control (Set to 0 - Preserve bridge/1 - Auto-balance bridge)
6	Unknown
7	Unknown

Table 2.1 Output control register

2.1.2.2 *Software Structure*

Software was menu driven with structure as shown in flowchart, Figure 2.4.

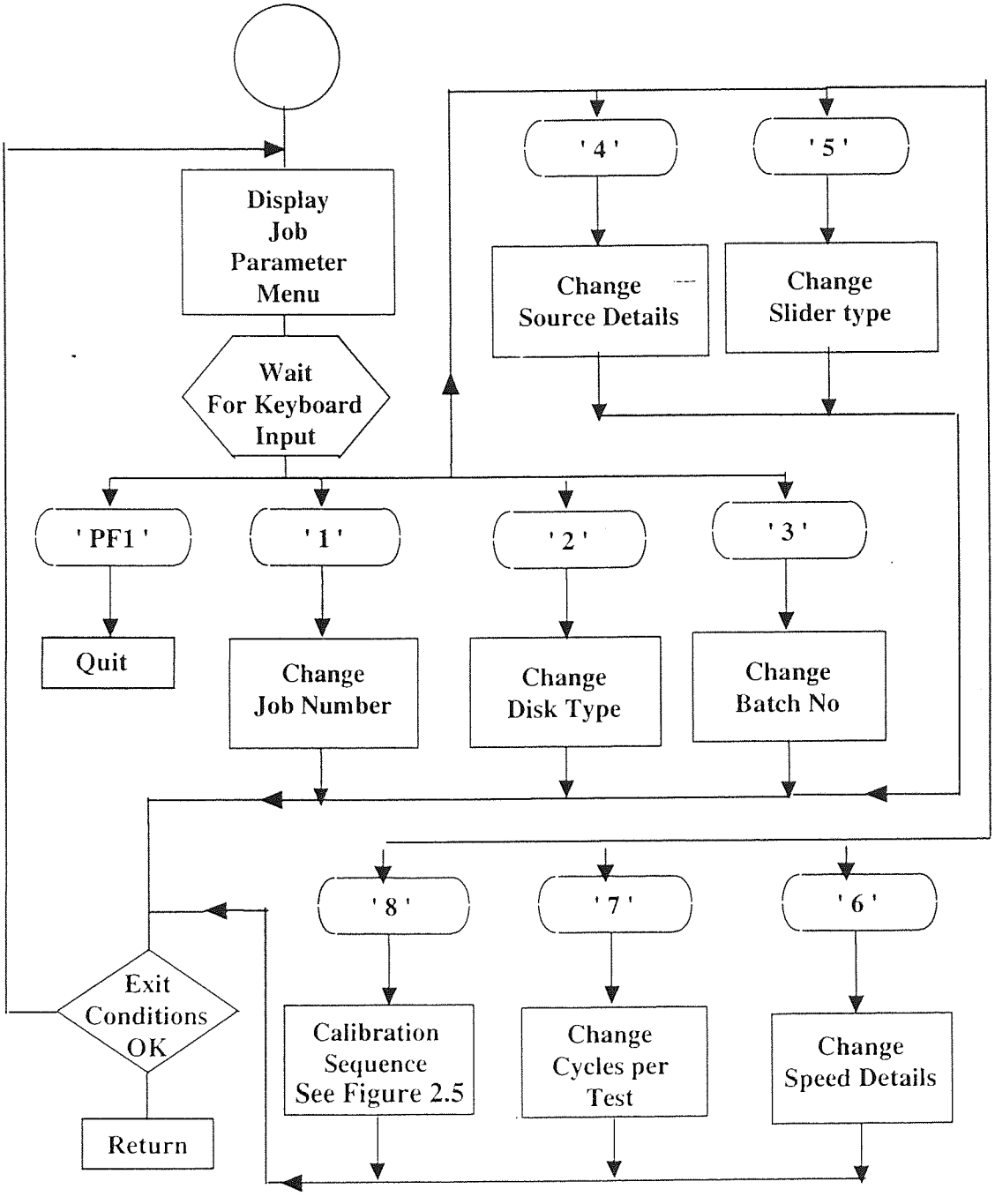

Figure 2.4 Structure of 'Aft.bas'

The calibration routine was performed by applying known force to the cantilever using a force gauge, measuring resulting amplifier signal and generating a linear fit between values, Figure 2.5.

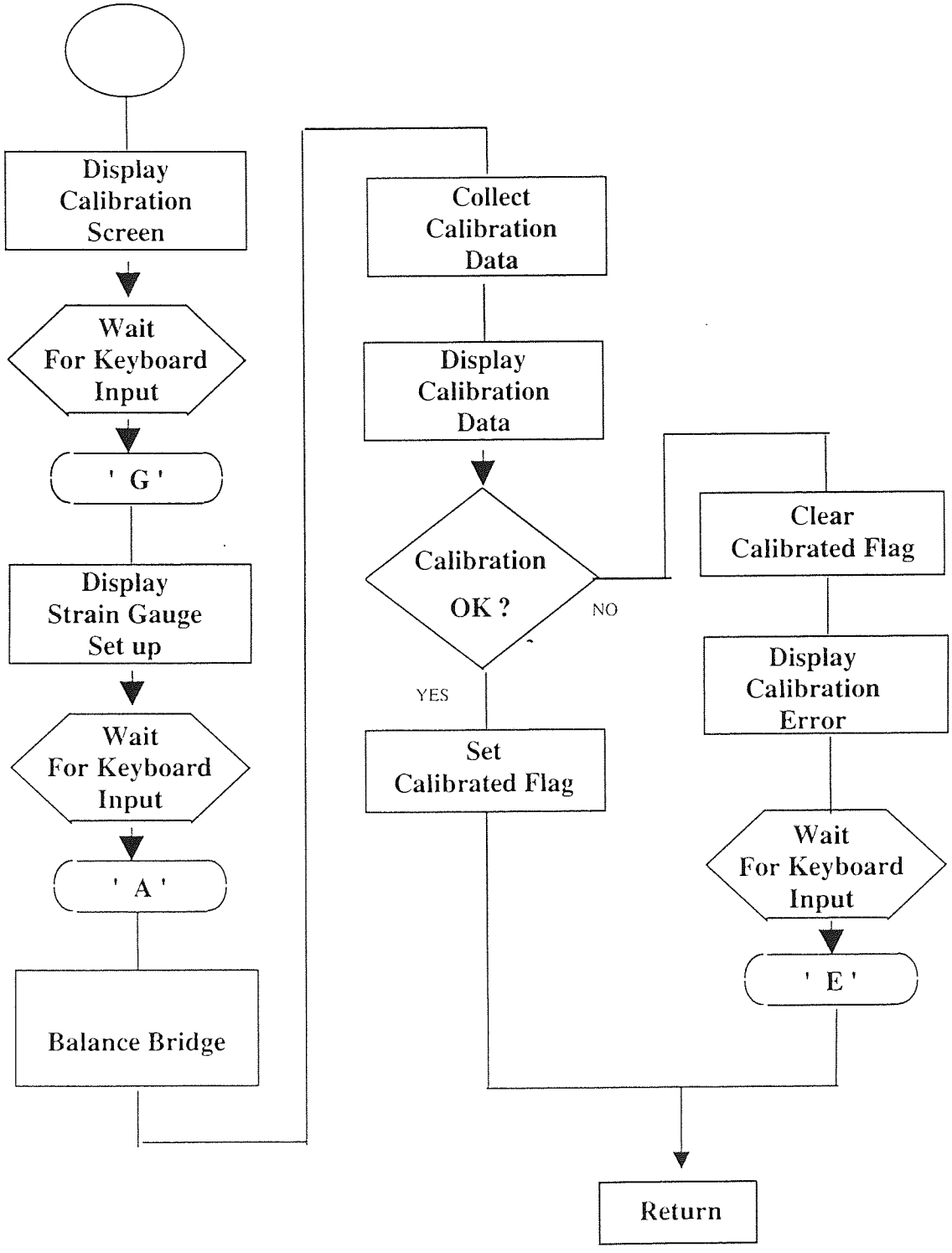

Figure 2.5 Calibration Routine Structure

Once the test was set up, a checklist sequence was performed, if passed the CSS test was run. The checklist sequence is shown in Figure 2.6.

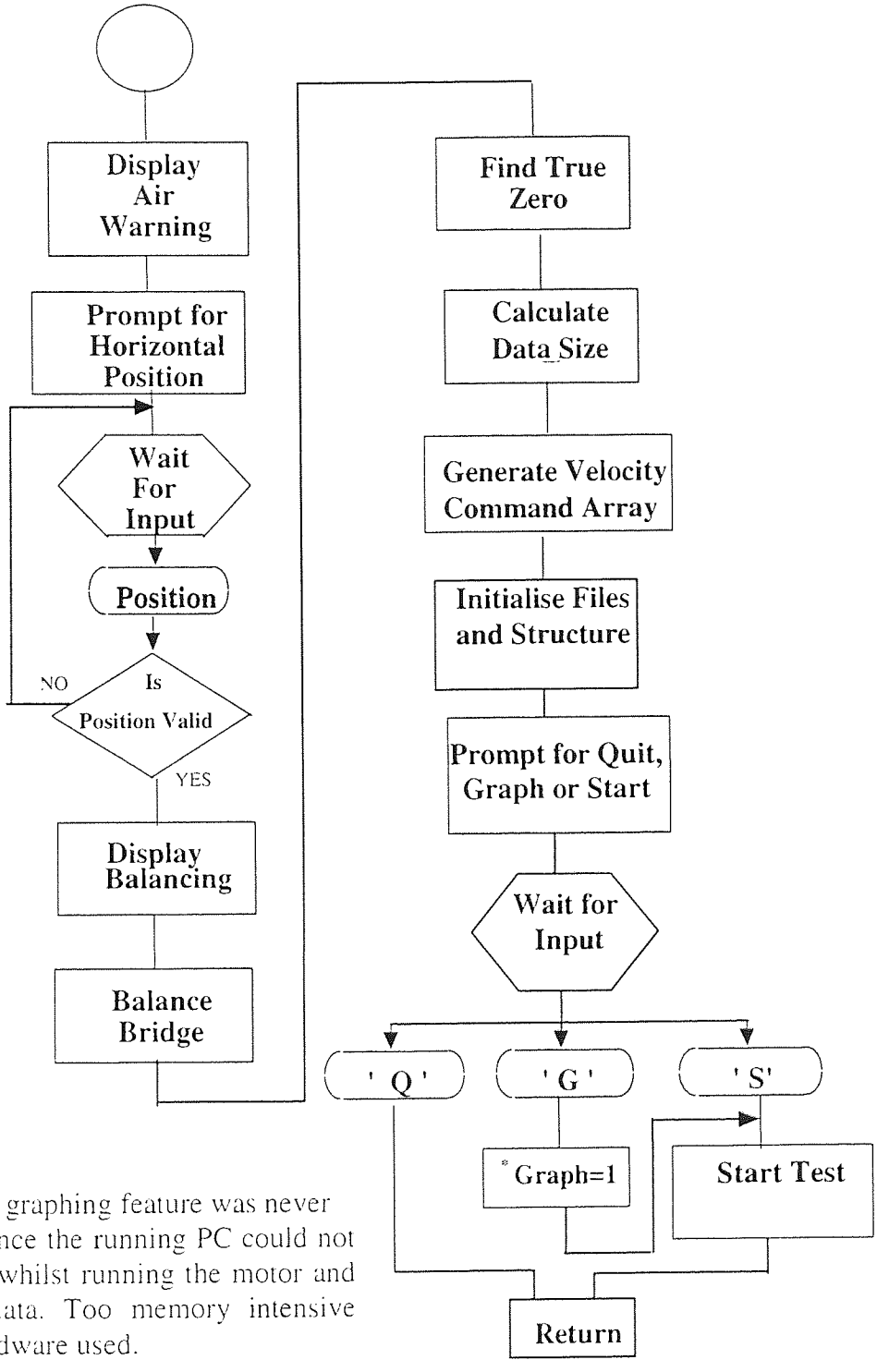

* Note, the graphing feature was never selected since the running PC could not support it whilst running the motor and aquiring data. Too memory intensive for the hardware used.

Figure 2.6 Checklist Sequence

2.1.3 Modifications to Existing Program

Several modifications were made to the Qbasic program 'Aft.bas'.

2.1.3.1 File Type/Storage Directory Change

Execution of the existing program produced three files; one containing the test details (job name, number of cycles, etc.) and files containing friction and stiction readings. Friction files were random binary format, which could only be read by another Qbasic program. This type of file was presumably chosen due to storage limitations of the floppy disk, since this file type required less space than sequential decimal files.

Since more storage space was available on the hard drive than floppy, it was decided to alter the program to enable the user to specify any directory for storage of results. A subroutine was written for this purpose.

Files could then be written in sequential form, and could therefore be imported to other applications for graphing and analysis (e.g. Excel, Matlab). Writing results to the hard drive was also faster and decreased the pause time between CSS cycles.

2.1.3.2 New Output Files

A separate program was written which could read in the entire friction file and produce two additional files; these contained the mean and variance in flying friction over the dwell period in each recorded CSS. The equations used were as follows

$$Mean = \frac{\sum_{i=d_1}^{d_2} F_i}{d_2 - d_1 + 1} = \overline{F} \qquad \textbf{Equation 2.1}$$

$$Variance = \frac{\sum_{i=d_1}^{d_2} \left(F_i - \overline{F}\right)^2}{(d_2 - d_1 + 1) - 1} \qquad \textbf{Equation 2.2}$$

where F_i is friction reading i and $\overline{F}$ is mean friction. Note i runs from d_1 to d_2 readings in the dwell period where the head is in flight, for a standard test reading d_1 occurs at 3 seconds and d_2 at 5 seconds.

A third additional file contained velocity signals to the motor. The velocity signal could then be converted into rotational velocity (rpm) by applying the transformation

$$V_{rpm} = \frac{2047 - V_{signal}}{0.57} \qquad \textbf{Equation 2.3}$$

2.1.3.3 New Calibration Routine

At the start of each test a calibration routine was performed, the existing routine instructed user to apply 0,2,4,6 and 8 grams to the cantilever arm using a force gauge and regressed the resulting amplifier voltage readings to these. Thus, the calibration range/interval was therefore fixed.

Under certain environmental conditions, stiction readings in the order of 30 grams could be experienced . This value would be out of the scope of existing calibration. It was decided that a routine containing generalised equations would allow the user to choose what calibration range should be used depending on the test conditions.

A new Qbasic calibration routine was written to perform least square regression over a customised range and set the number of calibration readings taken [148]. The generalised equations used for slope and intercept terms were

$$Intercept = \frac{\sum Force^2 \sum Voltage - \sum Force * \sum Force * Voltage}{num \sum Force^2 - \left(\sum Force\right)^2} \qquad \textbf{Equation 2.4}$$

$$Slope = \frac{num \sum Force * Voltage - \left(\sum Force * \sum Voltage \right)}{num \sum Force^2 - \left(\sum Force\right)^2} \qquad \textbf{Equation 2.5}$$

where *Force* is the applied force term, *Voltage* is the amplifier voltage reading and *num* is the number of calibration points chosen. Regression coefficient, r, was calculated to check quality of fit, if r was too low (<0.8) the calibration was rejected.

The significance of the slope and error terms was also calculated using a standard T-test, which decided if voltage values are truly dependant on applied force. T-values for slope and intercept were calculated using standard equations, these values were then compared to the appropriate statistical t-table values to decide the significance of regression [149].

$$\text{Intercept t value} = \frac{Intercept}{\sqrt{\frac{\frac{totalerror^2}{num-2}}{\frac{1}{num}+\frac{MeanFrc^2}{\sum(Force-MeanForce)^2}}}} \qquad \textbf{Equation 2.6}$$

$$\text{Slope t value} = \frac{Slope}{\sqrt{\frac{\frac{totalerror^2}{num-2}}{\sum(Force-MeanForce)^2}}} \qquad \textbf{Equation 2.7}$$

where $\text{totalerror}^2 = \sum_{i=1}^{num}(Ave\,\text{Re}ading(Force_i)-(Intercept+Slope*Force_i))^2$

and $\text{MeanForce} = \sum_{i=1}^{num}\frac{Force_i}{num}$

For the calibration to be significant, both intercept and slope t values must be greater than the T-value from statistical table (using n-2 degrees of freedom and 95 % level of significance).

2.1.3.4 Check For Head Crash

It was desirable to know immediately when interface failure had occurred, since little information would be given by running a head/disk that had crashed during early cycle for a long period. In addition, degradation of the interface may occur which would make analysis infeasible.

It was observed that interface failure was often preceded by an increase in the spread of stiction readings. A routine was incorporated into the program to monitor the standard deviation of stiction, halting execution if spread became high. Experimentation into what value to allow was carried out and it seemed that standard deviation <5 grams signified a normal interface, in tests where an obvious crash had occurred standard deviation was usually in excess of this prior to failure.

The form of standard deviation used was

$$\sqrt{\frac{\sum_{i=1}^{Count}(Stiction - MeanStiction)^2}{Count - 1}} \qquad \textbf{Equation 2.8}$$

Zhao and Bhushan [39] reported that a sharp rise in the coefficient of friction (>0.5) may also indicate failure, sometimes such an increase was observed at a 'healthy' interface. To prevent halting an experiment unnecessarily the program was adapted to look for two such rises in succession.

Friction and stiction failure routines used in parallel would trap most problem tests. Note, that it was sometimes desirable to make these routines redundant, i.e. to allow tests to fail and carry on, for example when wear testing or running in extreme environments where high/varied readings were expected.

2.1.3.5 Introduce Pause/Pause Increment

It has been thought that a pause before each cycle may affect stiction. The motor control routine was adapted to allow the user to specify a desired pause length (in seconds) to wait before carrying out each the next cycle, the Qbasic 'sleep' command was used. Code to increase/decrease the pause by some increment with time was also written, with an option allowing the order of different pause lengths to be applied in random order.

2.1.3.6 New Software for Drag Testing

Motor control comprised simply of a motor enable signal sent at the start of execution and disable motor signal at end.

Friction readings needed to be taken regularly over long periods of constant spindle rotation. Sampling frequency was limited such that 10,000 readings were taken during each test, this meant a friction reading was taken every 7.2 seconds for a 20 hour test. Notice, stiction was not measured during drag tests.

2.1.4 Temperature and Humidity Work

AFT testing was carried out under altered environmental conditions, these were produced by a Temperature and Humidity Generator (T/H generator) which was connected to an enclosure housing AFT test apparatus.

The generator works on the principle that air passed over a body of water, takes on moisture from the water. The resulting amount of humidity in the air is related to the temperature of both the air and water. Thus, it was thought possible to generate air at any desired temperature and humidity by altering these two settings.

The generator comprised of a stainless steel box (cubic, with dimensions 50 cm) containing an air heating element and 6 litre tank of water with immersed heating element. Several safety cut out switches were in place to avoid overheating of either air or water. A ball cock connected to a 5-litre top up tank ensured the heating element was never exposed. Also, a float switch was fitted, which activated if the top up water supply failed. The generator was lagged using expanded polystyrene tiles for insulation purposes.

A CAL3200 controller system was used to set the required temperature for both air and water temperature elements, this controller also gave continuous readings of air and water dew-point temperature inside the generator.

Two holes in the sides of the generator allowed air through flow. An electric fan was connected to give circulation using lagged heavy duty aluminium hosing. The air was then blown into the AFT enclosure. The customised enclosure, fabricated from closed-cell polypropylene, was lagged in expandable polystyrene tiles for insulation (enclosure dimensions 30x22x22 cm). The air then circulated through the enclosure and back to the fan again, thus the air in the system was in continuous flow. Figure 2.7 shows schematic.

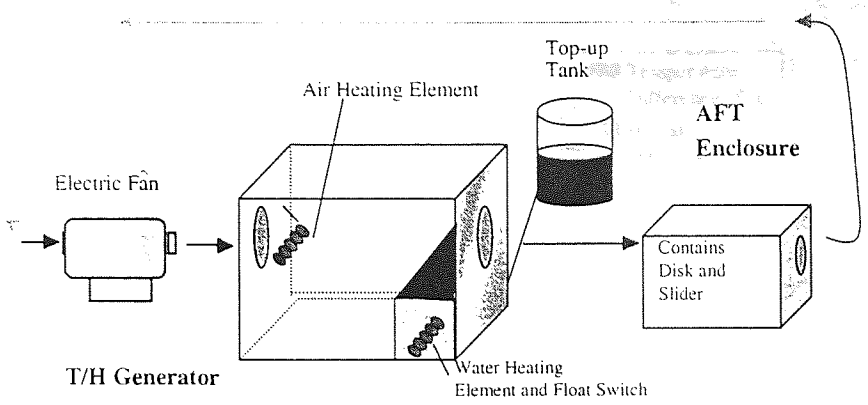

Figure 2.7 Creating environmental conditions

2.1.4.1 Monitoring Conditions inside AFT Enclosure - Temperature and Humidity Probe

The AFT enclosure housed a port where a temperature and humidity probe (model Transmicor 151) could be inserted to monitor the conditions inside. The probe worked on the principal that changing temperature and humidity cause a proportional change in voltage in probe wiring.

Description of Existing Probe Program

Probe measurements were acquired by a C++ program [150], which took voltage readings (one proportional to temperature and one to humidity) via an analogue-to-digital converter card. The program contained linear equations, which converted these voltages into temperature (°C) and humidity (%RH). The existing equations were

$$\text{Temperature} = 2.98 * \text{Voltage}_1 - 29.80 \qquad \textbf{Equation 2.9}$$

$$\text{Humidity} = 1.56 * \text{Voltage}_2 - 42.00 \qquad \textbf{Equation 2.10}$$

The readings were then regularly plotted on screen, sampling rate and test duration were entered by the user at the outset of execution.

Testing Probe Accuracy

Using a professionally calibrated environmental chamber, known conditions were generated, the probe was entered into the chamber and readings taken to test its accuracy. Results of testing in low-ambient conditions are shown in Figure 2.8.

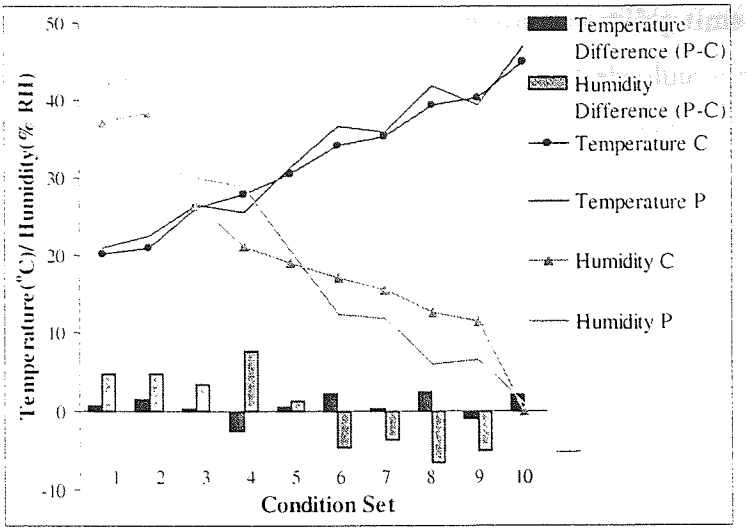

Figure 2.8 Comparing probe and chamber readings (low/ambient conditions)

There were some differences between the readings, especially the humidity, but generally, probe readings were close to known conditions. Next probe readings at high temperature and various humidity settings were studied, Figure 2.9.

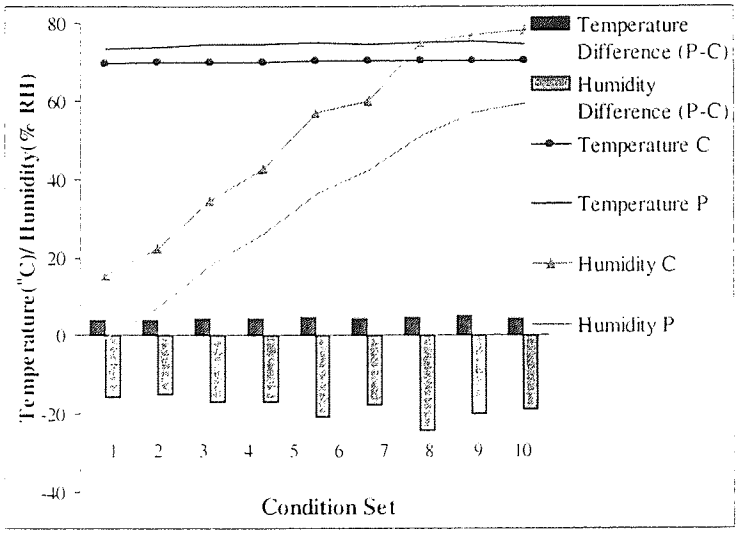

Figure 2.9 Comparing probe and chamber readings (high conditions)

Errors in temperature readings of around 8°C were observed, humidity errors were in the order of 20% RH. It appeared that the probe underestimated temperature and grossly overestimated humidity.

More comprehensive testing of probe readings was carried out, the probe was entered into the chamber under various conditions and readings taken after a settling time of 30 minutes. The differences between chamber and probe readings in terms of absolute error are illustrated in Figure 2.10 and Figure 2.11 for temperature and humidity respectively.

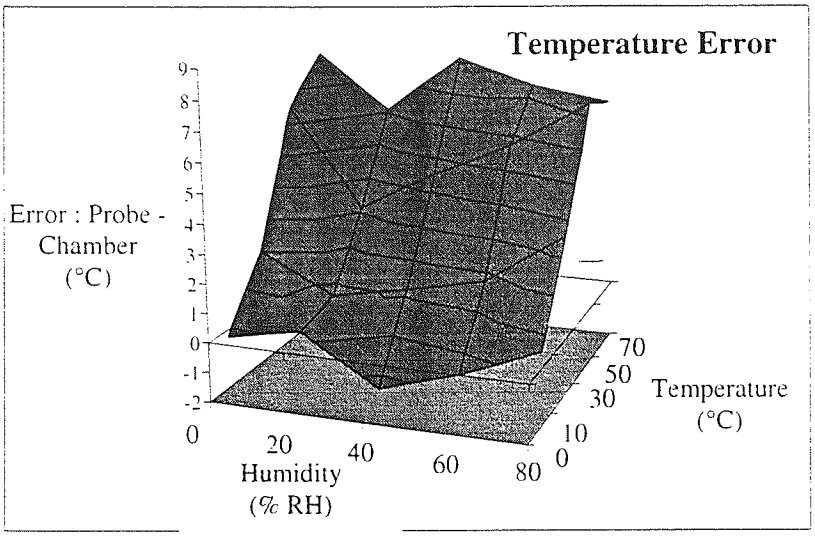

Figure 2.10 Error in temperature over different T/H combinations

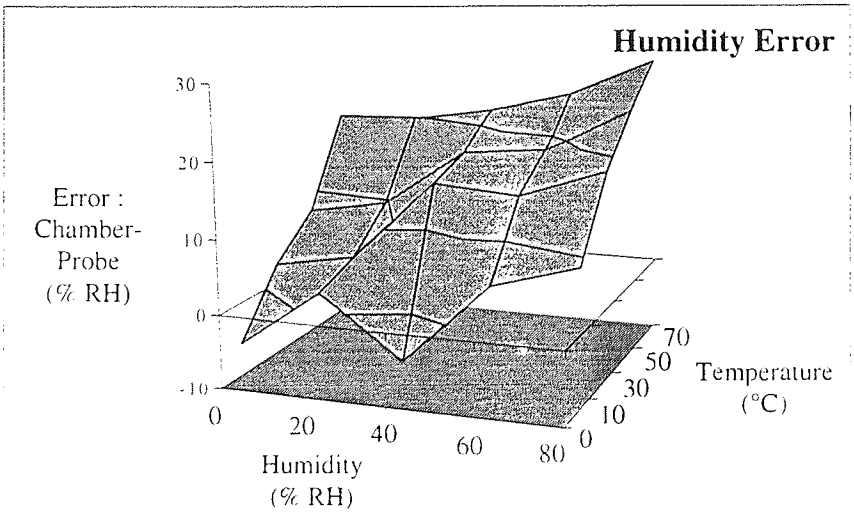

Figure 2.11 Error in humidity over different T/H combinations

Temperature errors increased with chamber temperature setting and were stable for different humidity. Humidity errors were less predictable, although it was clear the highest errors in humidity occurred at extreme high and low end humidity.

Re-calibration of Probe to Chamber

Since accurate environmental indictors were required for modelling of AFT data, it was thought necessary to rectify the error given by the probe program. As different amounts of

error were observed under different environments, it was not appropriate to merely adjust current readings by a correction factor. Complete re-calibration of probe voltages to chamber readings had to be performed to gain the precision desired. Chamber readings and probe voltages used in calibration were mean values taken over a 30 minute period.

Since different orders of error were observed in probe readings at low, medium and high environmental conditions, it was thought best to perform separate calibrations within each of these regimes. Best-fit linear equations for each condition were produced, these are shown in Table 2.2.

Conditions	Range	Linear Equation
Low Temperature and Humidity	0-20°C	T =2.65* $Voltage_1$ - 24.90
	10-30% RH	H = 1.02* $Voltage_2$ - 14.88
Medium Temperature and Humidity	20-50°C	T = 2.69* $Voltage_1$ - 25.00
	30-70% RH	H = 1.84* $Voltage_2$ - 53.42
High Temperature and Humidity	50-80°C	T = 2.73* $Voltage_1$ - 26.25
	70-90% RH	H = 1.27* $Voltage_2$ - 14.63

Table 2.2 New voltage calibration equations

The C++ program was modified using *case* statements to ensure the appropriate equation was used to calculate temperature/humidity depending on environmental conditions being low, medium or high.

Testing New Probe Equations

The program was tested by again placing the probe in the chamber under a variety of conditions, allowing time to settle and taking readings. Results are shown in Figure 2.12 and Figure 2.13.

Re-calibration of the probe gave significant improvement in accuracy of measurements, with temperature accurate to ± 2°C in ambient with overall maximum error 4.5°C. Humidity errors were also reduced, but high errors (in the order of 16% RH) were still evident under hot/humid conditions. It was decided to continue using these probe equations, but to always be aware of possible error in humidity reading in extreme environments.

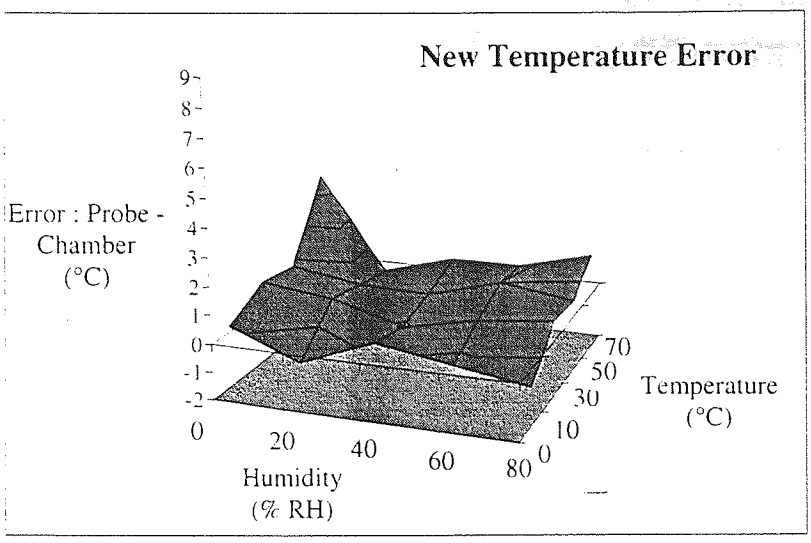

Figure 2.12 Error in temperature over different T/H combinations

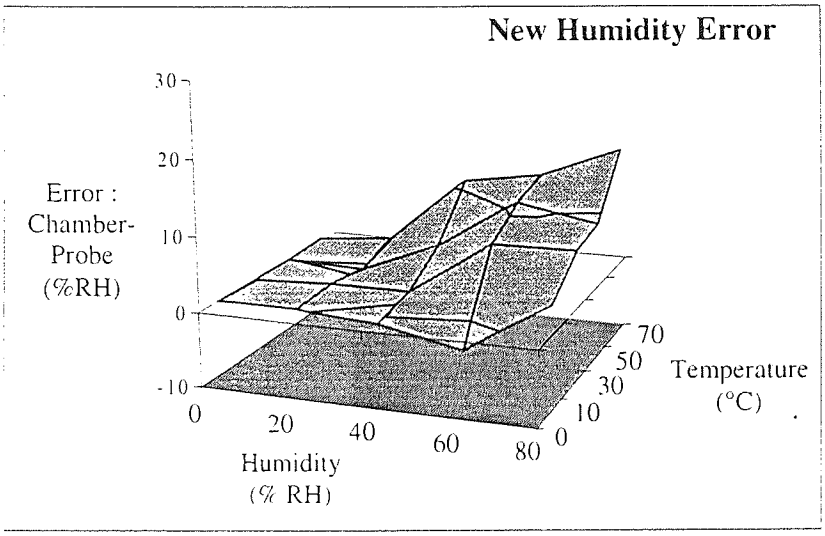

Figure 2.13 Error in humidity over different T/H combinations

Minimum Probe Settling Times

It was thought that in extreme conditions the probe readings may require a longer to settle. To test this theory the probe was entered into the environmental chamber, set at a variety of conditions and it's progress in reading the correct values monitored, Figure 2.14.

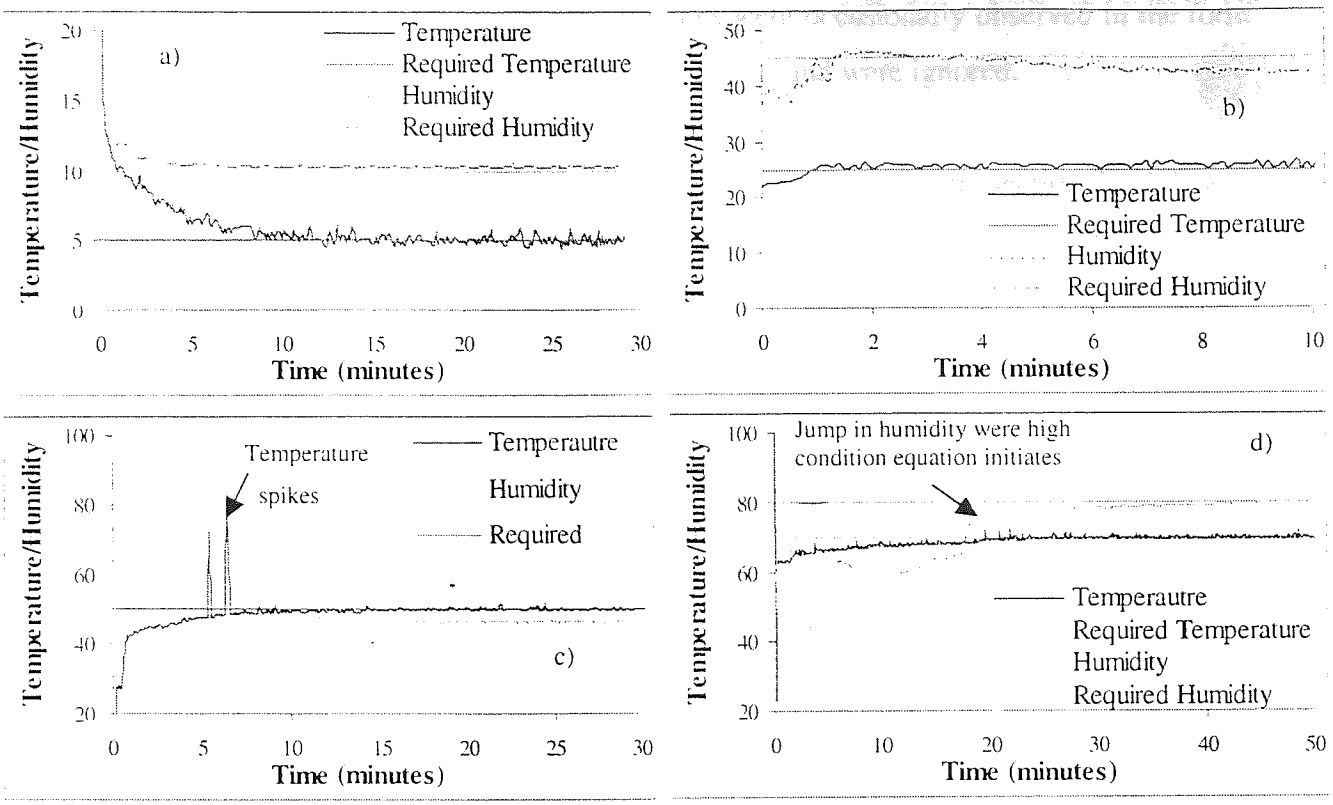

Figure 2.14 Probe arriving at correct reading under a) 5°C/10% RH, b) 25°C/45% RH, c) 50°C/50% RH and d) 70°C/80% RH

At very low temperature/humidity, Figure 2.14a), the probe settled to ±0.5 of the correct reading in less than 10 minutes, this was also true for elevated conditions, Figure 2.14c). Under ambient conditions, Figure 2.14b), the probe almost immediately arrived at correct readings.

Under high temperature and humidity the probe took over 20 minutes to settle, after that time temperature readings were within ±0.5°C and humidity within ±5 % RH of the correct settings, Figure 2.14d). When the probe was entered into a humid environment very high values were observed initially, this was explained by condensation of water on the probe.

These results show settling time was necessary to obtain sensible probe readings, Table 2.3 was produced as a guide of times to allow before using probe readings.

Temperature/Humidity	Time to Settle (minutes)
Low	10
Ambient	2
Elevated	10
High	30

Table 2.3 Guide to settling times

Even after these times, outlying temperature readings were occasionally observed in the form of spikes, Figure 2.14 c), these spikes were not real events and were ignored.

It should be noted that the strain gauge calibration process, described in Section 2.1.3.3, was carried out following the above settling time to eliminate any effect of temperature on strain gauge reading [112].

2.1.4.2 Creating Required AFT Conditions

The T/H generator was set at a variety of temperatures and left to settle as above, resulting temperature in the AFT enclosure was then measured via the newly calibrated probe. Results are shown in Figure 2.15 with linear relationship given in Equation 2.11.

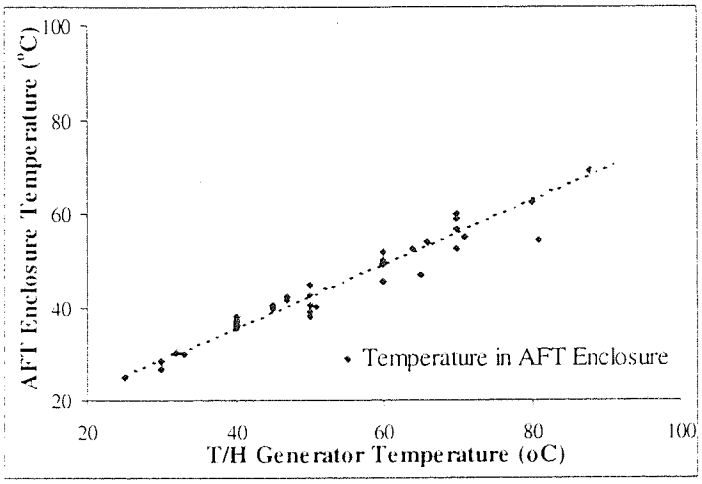

Figure 2.15 Relationship between generator and AFT enclosure temperature

Enclosure temperature = 0.62 * Generator temperature + 8.74 **Equation 2.11**

Despite lagging significant temperature loss took place between generator and AFT enclosure. The loss was thought to be due to unavoidable air leakage in connecting hosing and was amplified at high temperature. In fact, it was found impossible to reach enclosure temperature above 65°C using the existing set-up.

Since high temperature AFT testing was planned, an additional air heating element was fitted inside the generator, this element had separate on-off controller and was used to add heating capacity allowing original element thermostat to control the temperature.

Comparison of the enclosure reaching maximum temperature with/without second element is shown in Figure 2.16. Enclosure temperature of 77°C was now attainable, the second element also gave timing improvement in reaching desired temperature below 65°C.

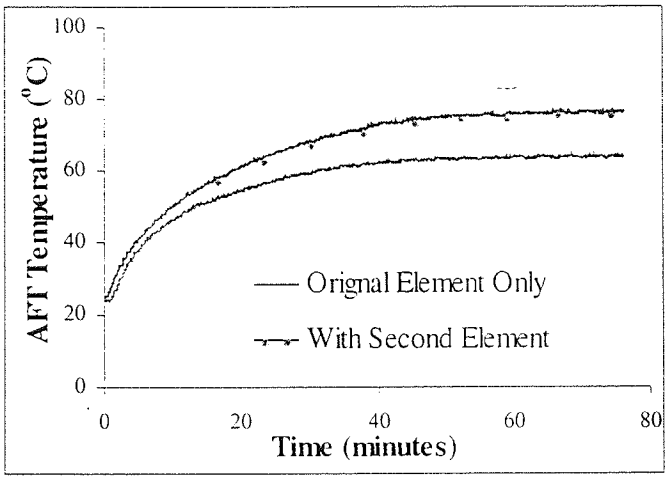

Figure 2.16 Reaching maximum temperature with/without new element

When setting generator an updated form of Equation 2.11 was used to give initial temperature setting, such that $\frac{DesiredEnclosureTemperature - 9.71}{0.65}$.

Required humidity was achieved by first setting temperature, leaving it to settle and then increasing the temperature of the water in the tank gradually. Doing this avoided major condensation and possible flooding in enclosure.

The range of conditions achievable in the enclosure were found to be [ambient-80] °C and [5-90] %RH for temperature and humidity respectively. Note, some combinations were not possible using this apparatus, for example low temperature and low humidity could not be obtained simultaneously.

It was attempted to use aqueous salts to attain very low humidity (<5% RH). The air flow was diverted through a jar of *'Drierite' Anhydrous salts* prior to entering the enclosure. However,

this method of reducing humidity failed due to the volume of air being large and the long duration of tests. Salts became ineffective in less than 1 hour and required drying. In addition, salts were reported to become unproductive when temperature deviated from ambient [151].

2.1.4.1 Stability Testing in AFT Enclosure

Stability testing of enclosure conditions over 18 hours was carried out. It was found that once settled, temperature remained accurate to ± 2°C, humidity was more difficult to control especially at high temperature. Figure 2.17 a) illustrates the increasing variation in humidity at ambient, elevated and high temperature. The source of the variation in humidity was the thermostat controlled water heating element switching on and off, causing periodic fluctuation in humidity. Figure 2.17 b) shows actual humidity recordings at various temperatures, insert shows high temperature forms periodic waves of humidity. Using the equipment supplied there was no way to avoid this fluctuation, care had to be taken when modelling and the use of mean or smoothed humidity values employed.

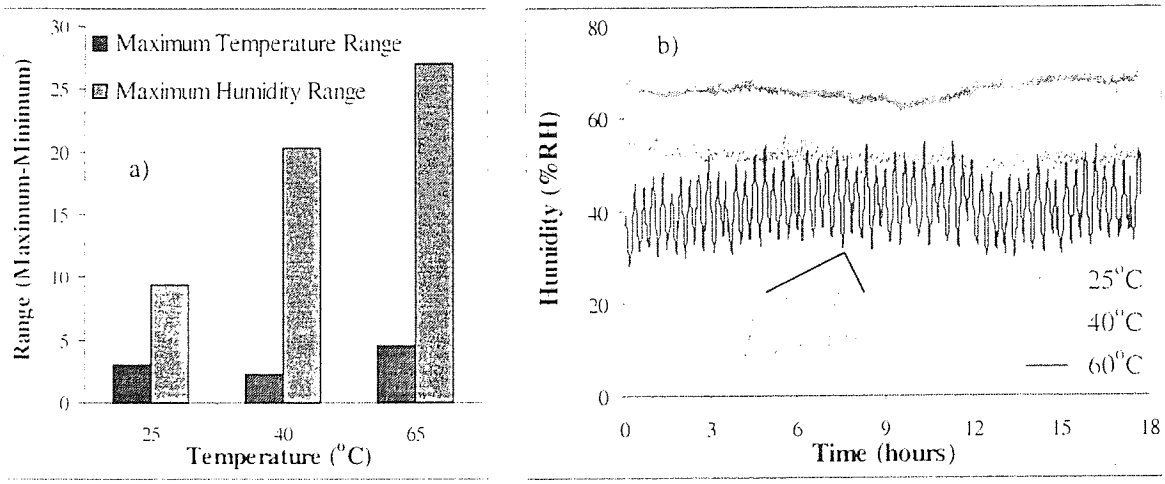

Figure 2.17 a) Maximum range of recorded conditions over 18 hours and b) Increasing instability in humidity at increasing temperature

2.1.5 Slider Types Used

Two slider types were used in this work; negative pressure air bearing sliders (NPAB's) and tri-pad sliders (sometimes known as taildraggers); photographs of these are shown in Figure 2.18 a) and b) respectively.

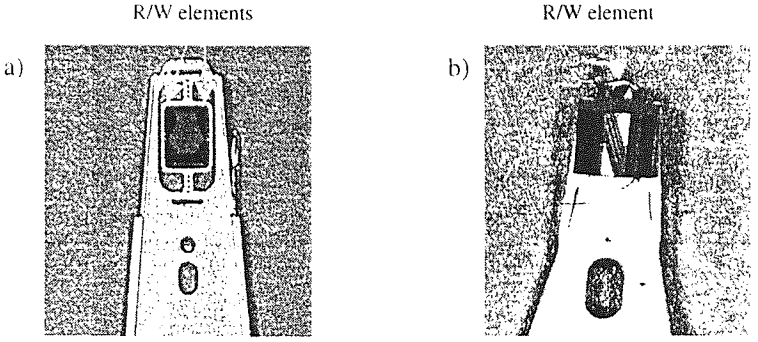

Figure 2.18 Photographs of a) NPAB and b) Tri-pad sliders

Both sliders were fabricated of Al_2O_3-TiC, but the NPAB had sputtered DLC overcoat for wear protection. The NPAB was the more modern slider using inductive write/MR read element technology. The slider had two such elements - situated on the trailing edge of each slider rail, which element was used depended on whether the slider flew on the top or underside of the disk. The tri-pad used a single inductive read/write element, which was situated on the slider contact pad at its trailing edge.

The NPAB slider has specially 'hour glass' shaped cavity bearing that provides a negative, or sub-ambient, force to decease slider fly height. This slider design was reported to yield faster take off and more level flying profile over disk. Both sliders were attached to non-magnetic steel suspension mechanisms - the NPAB to a Type 1950 and tri-pad to Hutchinson type 850 design.

Slider wear had largely been neglected in literature due to the difficulty involved in quantifying wear on very small head areas. However, due to the availability of small area analysis such as Atomic Force Microscopy, 2.2.3, this can now be fully explored.

Missing page(s) from the bound copy

The energy of photoelectrons leaving the sample is determined using a concentric hemispherical analyser. For each element, there will be a characteristic binding energy associated with it i.e. each element will give rise to a characteristic set of peaks in the photoelectron spectrum. The presence of peaks at particular energies therefore indicates the presence of a specific element in the sample under study. Furthermore, the intensity of the peaks is related to the concentration of the element within the sampled region. Thus, peak areas can be used to quantify the composition of the materials surface.

The process is illustrated schematically below, note XPS must be carried out under UHV conditions.

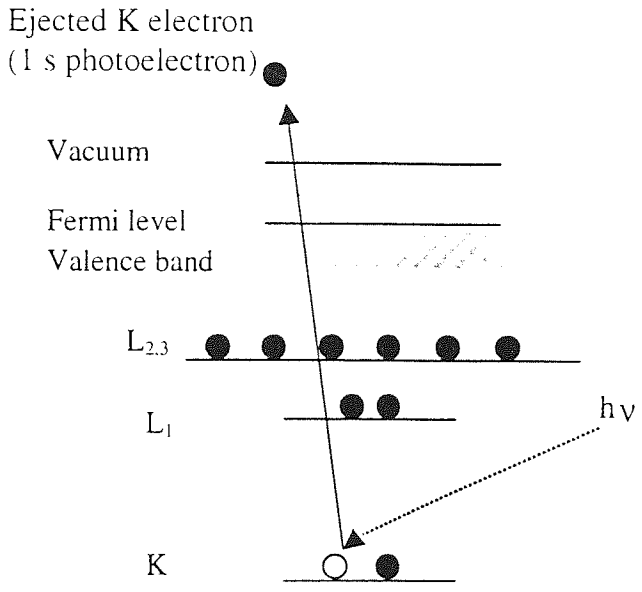

Figure 2.20 Schematic of XPS procedure.

Binding energy, E_b, is calculated using Equation 2.12, where hν is photon energy, E_k electron kinetic energy and ϕ the work function of sample and analyser [153]

$$E_b = h\nu - E_k - \phi \qquad \textbf{Equation 2.12}$$

2.2.1.1 The Instrument and Experimental Set-up

XPS was carried out on heads and disks using a VG ESCALAB 200D instrument. The instrument was controlled by VG ECLIPSE software that also offered spectrum processing. An X-ray source of Mg kα radiation was used in all experiments.

Wide scan XPS spectra were initially collected since little information on sample composition was available. However separate scans for fluorine were always carried out at the start of the experiment, as this element was quickly desorbed by the incident x-rays. Analysed area chosen was 150 μm diameter for sliders and 300 or 600 μm for disks. Where the analysed area was small (150 μm) it was necessary to take a large number of scans (> 100) to attain a reasonably high number of counts and hence improve signal to noise ratio.

Note, XPS was a destructible technique where slider and disks concerned, since slider bodies had to be removed from their suspensions and disks had to be cut up prior to analysis to fit on the XPS stub. Thus, XPS had to be performed once sliders/disks were no longer required [119].

2.2.1.2 Processing Method

The photoelectron spectrum has a rising background with increasing binding energy due to an increase in number of low energy electrons resulting from inelastic scattering processes. The background must be removed to enable quantification. Eclipse software supported the Shirley method of background subtraction, where the intensity of a point above the background is determined by iterative analysis.

The XPS spectra presented were smoothed for ease of peak identification, however, a minimal amount of smoothing was carried out to avoid possible peak distortion. The smoothing method used by Eclipse is that of Proctor and Sherwood which works by fitting a $4^{th}/5^{th}$ order polynomial to spectrum data.

After a peak had been defined and the background subtracted, its area could be found by integration, this area could then be used to quantify the amount of a particular element present in a sample.

Quantification was achieved by using sensitivity factor within the VG Eclipse data processing package.

2.2.2 Scanning Electron Microscopy (SEM)

Analysis of sliders and disks involved using a SEM to examine surface topography and identify any debris and wear. SEM has advantages over its optical counterpart, in that it supports much higher resolution and has larger depth of field.

In SEM a beam of electrons is generated using an electron gun, the beam is then attracted through an anode, condensed by a condenser lens and focused to a very fine point on the sample by an objective lens (both lenses are electromagnetic). Scanning coils are energised to create a varying magnetic field that deflects the beam back and forth in a controlled pattern across the sample.

When the electron beam hits the sample, secondary electrons are produced. These are collected by a secondary detector or a backscatter detector (user option), converted to voltage and amplified. The amplified voltage then is applied to the grid of a Cathode ray tube, causing the intensity of the spot of light to change. The captured image consists of thousands of spots of varying intensity that corresponds to the topography of the sample.

When scanning, vacuum conditions are required to prevent filament burn out and collision of electrons with the gas molecules.

Using the secondary electron detector produces a clear and focused topographical image of the sample. The backscatter electron detector produces an image that can be used to determine the make-up of the sample as each element in the sample appears as a different shade. Backscatter mode was useful when imaging worn sliders to determine the source of debris.

2.2.2.1 The Instrument and Experimental Set-up

A Cambridge Instruments S90B SEM was used to provide primary analysis of sliders and severely damaged disks. Since the SEM required samples to be electrically conductive, it was found necessary to sputter the NPAB sliders before scanning. A thin layer of a conductive material (gold) was sputtered on these sliders prior to analysis.

2.2.3 Atomic Force Microscopy (AFM)

AFM measures features which cannot be seen by conventional profilers and is ideal for analysing very small areas, such as recording head read-write elements [128].

In AFM, a sharp tip mounted on a cantilever is scanned across a sample surface, changes in the position of the tip occur due to sample topography. Tip deflection can be quantified by the measurement of a reflected laser signal on the sectors of a quadrant photodetector. The cantilever is mounted on a piezoelectric ceramic such that any change in the height of the ceramic will change the distance between tip and sample. Feedback circuitry is used to keep force between sample and tip constant by adjusting the piezoelectric ceramic relative to a user defined set point current. The relationship between cantilever deflection, d, and force between tip and sample, F, is given by Hooke's law, with spring constant k,

$$F = -kd \qquad \textbf{Equation 2.13}$$

This force adjustment is used to produce an AFM image. A schematic of AFM is given in Figure 2.21.

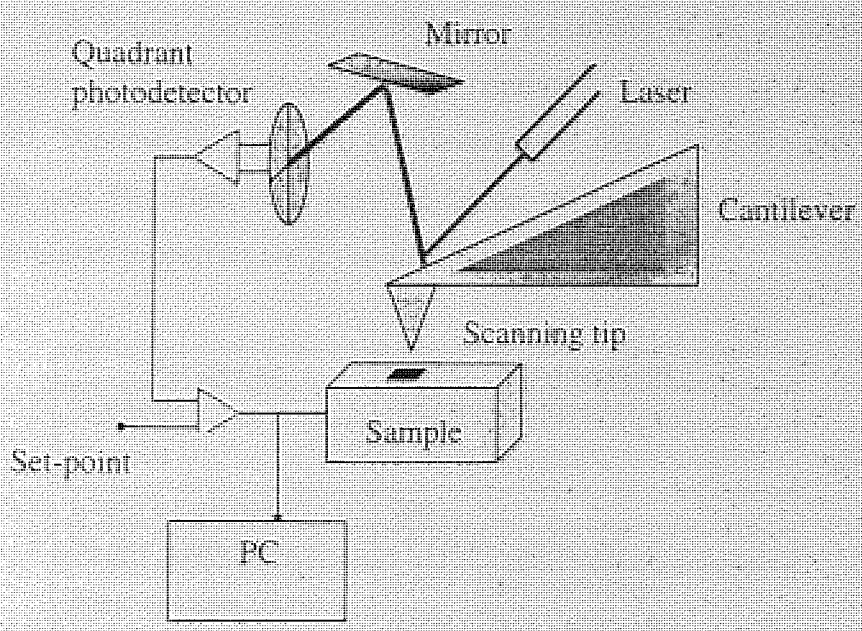

Figure 2.21 Schematic of AFM components

For measurement of lateral (friction force), the left and right photodetector quadrants were used to determine intensity difference whilst scanning the tip orthogonal to the long axis of cantilever beam. Friction force between tip and sample produced a twisting of the cantilever which reflect the laser beam out of plane as defined by the incident beam.

2.2.3.1 The Instrument and Experimental Set-up

The instrument used to perform AFM was a Topometrix Explorer microscope controlled by a PC running Topometrix Spmlab V.3.06.06 software, this was also used for image processing. A scanner with a maximum scan area of 100 x 100μm and a z range of 13.2μm was chosen. Although the instrument was equipped for both contact and non-contact AFM, only the former technique was used where the tip is scanned over the sample in repulsive force mode.

The set point was usually set to 20mA higher than the top-bottom photodiode signal at the instant when the tip is in contact with the sample, this was readjusted if stable feedback was not attained. Stable feedback could be confirmed by carrying out a force calibration, where the tip was pushed into the sample by the z-piezo and the tip deflection measured. Feedback settings were adjusted continuously to minimise the error signal and noise.

Scanning tips had high spring constant to increase the sensitivity of the cantilever to small changes in topography. High tip hardness was also required to preserve tip sharpness whilst scanning in contact. Topometrix type 1520 cantilevers were used, these housed two V-type cantilevers on each unit. However, since only the thinner of these was factory calibrated this only was used. Cantilever properties are given in Table 2.4.

Parameter	Measurement
Geometry	V (Two Cantilevers)
Material	Si_3N_4
L-arm length (μm)	200
W-arm width (μm)	18 (Thin cantilever)
Force constant (N/m)	0.032 (Thin cantilever) 0.064 (Thick cantilever)
Nominal resonant frequency (kHz)	17
Tip geometry	Pyramidal 4μm base, 4μm high
Tip radius (nm)	<50

Table 2.4 Properties of the AFM Cantilevers and Tips Used

Scanning tips used were pyramidal in shape, an SEM image of the type used is shown in Figure 2.22.

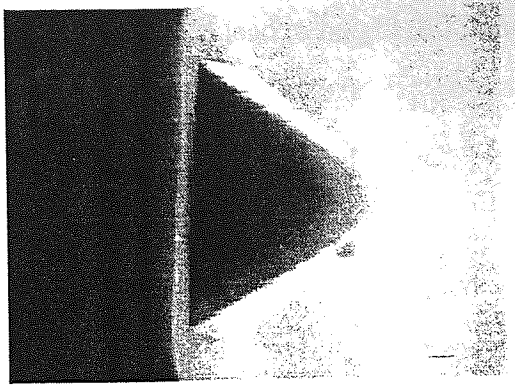

Figure 2.22 SEM of AFM contact scanning tip

Unless otherwise stated, disk and slider trailing edge topographical scans presented in this work were taken at 270°, this is illustrated in Figure 2.23. Slider leading scans were taken at 0° as shown, this was due to large curvature and slope at these regions making scanning at 270° difficult.

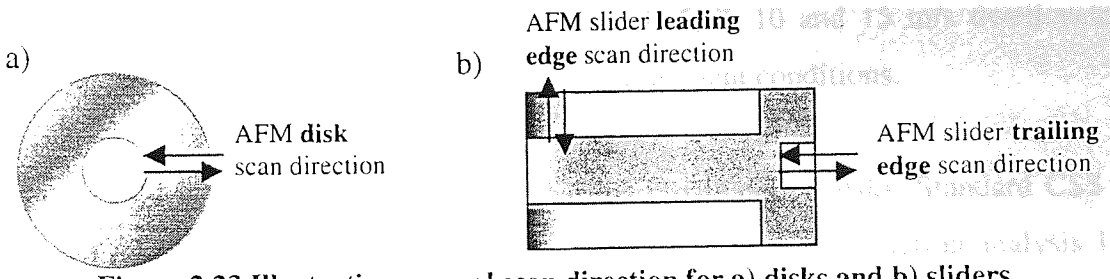

Figure 2.23 Illustrating normal scan direction for a) disks and b) sliders

The left-right signal of the photo-detector could also be collected; giving information on the amount of lateral deflection the tip experiences as it is scanned across the sample. This gives an indication of the relative friction force between the sample and tip. This technique was useful for measuring lubricant distribution across a sample and for distinguishing between two different phases of similar topography.

2.2.3.2 Processing Method

It was usual for topography scans to be processed for feature enhancement, the method used will now be discussed. Firstly, unwanted curvature in the scan was removed using 2nd order

horizontal levelling, the heights in the scan were next normalised and the range of heights in the scan were selected using the histogram command. Scans were usually shaded (light source from left). Li and Wang [154] reported that it was vital to process AFM images identically, since different smoothing/levelling routines could lead to height differences of many nanometers.

2.3 Experiments and Surface Analysis Performed

2.3.1 Contact Start Stop Testing

Primary investigation of CSS behaviour involved standard tests being carried out under ambient conditions. Both NPAB and tri-pad sliders were run in conjunction with crosshatched and graded texture disks. To be consistent with work done previously using the supplied apparatus the standard velocity chosen was 1400 rpm (equivalent to 3.37 m/s at 23 mm from disk centre).

Next investigation into disk dwell velocity was performed, both slider types were used in 1000 CSS tests with crosshatched disks at 1, 2, 3, 4, 5, 7, 10 and 15 m/s dwell velocity, respectively. Again, these tests were performed under ambient conditions.

Extensive environmental work was carried out using crosshatched disks. Standard CSS tests were carried out in 30 different environments with NPAB slider. For stiction analysis 1 rpm tests were performed in 28 environments. For tri-pad slider, standard tests were performed in 11 environments of modified temperature and humidity. CSS tests where environment changed in-situ (known as ramp testing) were also performed with NPAB sliders to determine the affect on friction and stiction.

As mentioned in Section 2.1.3.5, a pause between CSS cycles could have significant effect on stiction. Using both slider types this was investigated in ambient and then elevated environmental conditions. Further pause testing with NPAB only, eliminated the ordering effect from increasing pause length and used extremely long pauses to determine if an equilibrium pause length existed beyond which stiction stabilised.

Using graded texture disks and both slider types, the effect of differing disk texture was studied. Tests were performed at the textured and smooth areas of disks and conclusions drawn.

The effect of disk lubricant and transfer was also investigated. A crosshatched disk was de-lubricated and used in 7K CSS, conflicts with normal behaviour were observed. In a separate test, a crosshatched disk had a thin layer of liquid silicon oil applied at one position only to determined the transfer of material around the disk following CSS testing.

2.3.2 Drag Testing

A number of standard tests were carried out under ambient conditions. Both NPAB and tri-pad sliders were run in conjunction with crosshatched and graded texture disks.

Next investigation into drag velocity was performed, tests were performed at various velocities to identify the required take-off velocity for each slider type. Again, these tests were performed under ambient conditions.

Environmental work was carried out using crosshatched disks. Drag tests were carried out in 10 different environments with NPAB slider. Ramp tests were also performed with NPAB sliders to determine changes in friction.

Using graded texture disks and both slider types, the effect of differing disk texture on friction was studied.

Table 2.5 and 2.6 outline the CSS and drag tests performed on each sample type, respectively.

Table 2.5 Outline of css experiments performed

Disk /Slider Combination		Standard CSS Testing	Dwell Velocity Testing	Environmental CSS Testing		Pause Testing	Texture Effect	Lubricant Effect
				Constant	Ramp			
Standard crosshatched texture	NPAB	10 sets of 7K CSS cycles in ambient.	1000 CSS tests performed at 1, 2, 3, 4, 5, 7, 10 and 15 m/s in ambient.	1400 rpm tests - 30 environments (see section 2.3.2.1).	1400 rpm tests in 2 sets of changing conditions (see Section 3.1.3.2) .	1000 CSS cycles in ambient and 35°C/55% RH. Pause lengths 0, 10, 20 and 30 minutes.	14 K CSS track change experiment.	7K CSS cycles in ambient. Disk de-lubed using IPA.
				1 rpm tests - 28 environments (see Section 2.3.2.1).		40 CSS cycles in 40°C/70% RH. Pause lengths [0-200] minutes - randomised.		500 CSS cycles with disk given added lube-like material in track.
	Tri-pad	5 sets of 7K CSS cycles in ambient.	Tests performed at 1, 2, 3, 4, 5, 7, 10 and 15 m/s in ambient.	1400 rpm tests - 11 environments (see Section 2.3.2.2).	NONE	1000 CSS cycles in ambient and 35°C/55% RH. Pause lengths 0, 10, 20 and 30 minutes.	NONE	NONE
Graded texture	NPAB	2 sets of 7K CSS cycles in ambient.	NONE	NONE	NONE	NONE	7K CSS cycles in ambient at 1400 rpm. Testing at landing and data zones.	NONE
	Tri-pad	1 set of 7K CSS cycles in ambient.	NONE	NONE	NONE	NONE	7K CSS cycles in ambient at 1400 rpm. Testing at landing and data zones.	NONE

Table 2.6 Outline of drag experiments performed

Disk /Slider Combination		Standard Drag Testing	Drag Velocity Testing	Environmental Drag Testing		Texture Effect
				Constant	Ramp	
Standard crosshatched texture	NPAB	5 sets of 20 hour drag tests at 0.5 m/s in ambient.	Tests performed at 0.25, 0.5, 0.75, 1.0 and 1.5 m/s in ambient.	20 hour, 0.5 m/s tests - 29 environments (see section 2.3.2.3).	0.5 m/s tests - 2 environments.	20 hour drag test with track change at 10 hours.
	Tri-pad	2 sets of 20 hour drag tests at 0.5 m/s in ambient..	Tests performed at 0.25, 0.5, 0.75, 1.0 and 1.5 m/s in ambient.	NONE	NONE	NONE
Graded texture	NPAB	2 sets of 20 hour drag tests at 0.5 m/s in ambient.	NONE	NONE	NONE	20 hour drag tests at 0.5 m/s. Testing at landing and data zones.
	Tri-pad	2 sets of 20 hour drag tests at 0.5 m/s in ambient.	NONE	NONE	NONE	20 hour drag tests at 0.5 m/s. Testing at landing and data zones.

Where environmental work was performed, crosshatched disks were tested with sliders under the following constant conditions.

2.3.2.1 CSS Environmental Testing of Crosshatched Disks with NPAB Sliders

Tests were conducted in 30 environments as illustrated in Figure 2.24a). For stiction investigation, 1 rpm tests were conducted in the 28 environments illustrated in Figure 2.24b). Also, shown are the windows for normal drive operation as published by drive manufacturers.

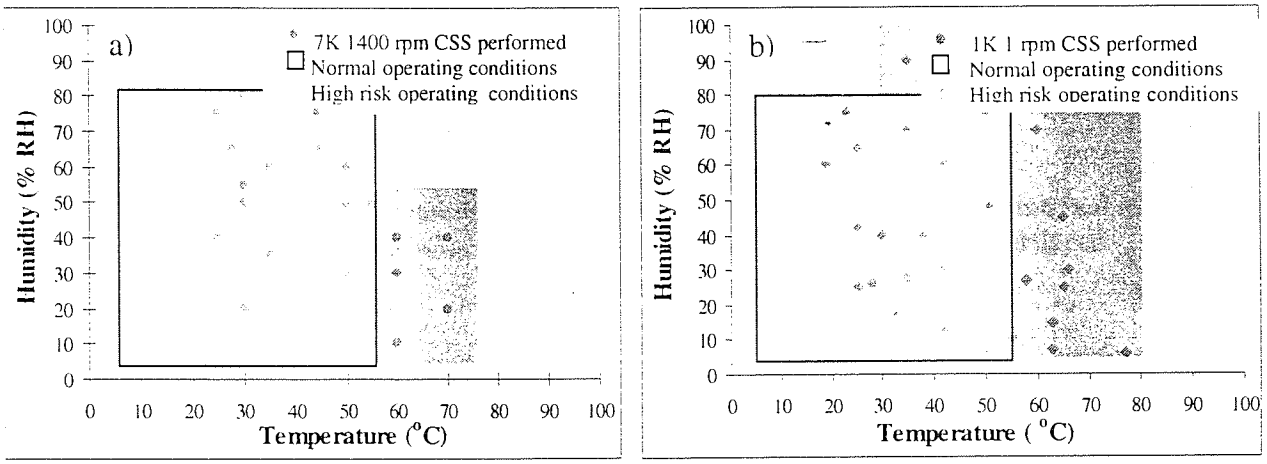

Figure 2.24 Environments chosen to test CSS behaviour with between crosshatched disks and NPAB sliders, with respect to a) friction and b) stiction. Manufacturer expected operating conditions are bordered

2.3.2.2 CSS Environmental Testing of Crosshatched Disks with Tri-pad Sliders

11 environments were chosen in which to perform CSS testing with tri-pad slider, these are shown in Figure 2.25.

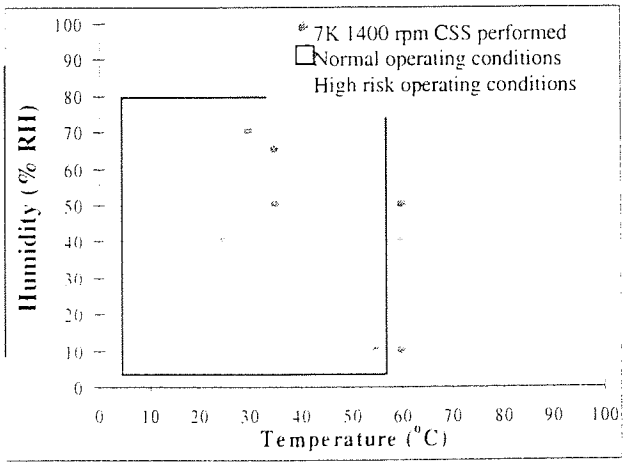

Figure 2.25 Environments chosen to test CSS behaviour with between crosshatched disks and tri-pad sliders. Manufacturer expected operating conditions are bordered

2.3.2.3 Environmental Drag Testing of Crosshatched Disks with NPAB Sliders

29 environments were chosen for drag testing of NPAB sliders in conjunction with crosshatched textured disks, these are shown in Figure 2.26.

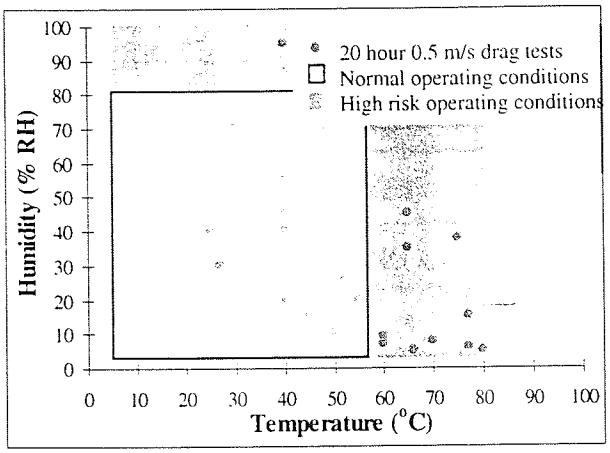

Figure 2.26 Environments chosen to test drag behaviour with between crosshatched disks and NPAB sliders. Manufacturer expected operating conditions are bordered

2.3.2.4 Test Referencing Method

It should be mentioned that tests were named using an amalgamation of the test type and conditions and number of cycles. For example, CT25H40(7K) would denote a 7K CSS test performed in 25°C/40 % RH and DT40H80(20) would denote a 20 hour drag test performed in 40°C/80 % RH. Note, tests which failed were appended with a C. In environmental work, where like test types were being compared it was usually sufficient to reference tests by the temperature/humidity in which the test had been performed.

2.3.3 Surface Analysis Performed

Table 2.7 illustrates a summary of surface analysis performed on each sample. Note some types of analysis were not relevant on certain samples. For example, SEM analysis gave little information on disk samples, unless they were very badly damaged.

Sample Type		SEM	AFM	XPS
Virgin samples	Crosshatched disk	YES	YES	YES
	Graded disk	NO	YES	YES
	NPAB	YES	YES	YES
	Tri-pad	YES	YES	YES
CSS tested Samples	Crosshatched disk	YES	YES	YES
	Graded disk	NO	YES	YES
	NPAB	YES	YES	YES
	Tri-pad	YES	YES	YES
Drag tested Samples	Crosshatched disk	NO	YES	YES
	Graded disk	NO	YES	NO
	NPAB	YES	YES	YES
	Tri-pad	YES	YES	YES
Real drive Samples	Laser textured Disk	NO	YES	NO

Table 2.7 Detailing surface analysis performed on each sample type

3 Experimental and Surface Analysis Results

3.1 AFT Experimental Results

The results of the AFT experiments, as described in Chapter 2, will now be presented. When running both CSS and drag tests it was attempted to always fly the slider at the same disk radius to eliminate variation caused by the tangential component of friction.

However, it was occasionally necessary to change disk testing radius, in those instances friction and stiction results were scaled by

$$\cos[\tan^{-1}(d/r)] \qquad \textbf{Equation 3.1}$$

where $d = d_1, d_2$ at slider positions P_1, P_2 respectively, Figure 3.1.

Since, changes in disk radius were only of the order of 1-2 mm this scaling had only slight effect on results.

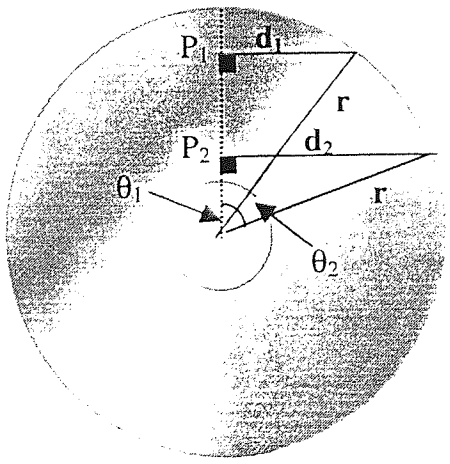

Figure 3.1 Effect of tangential friction component of friction

3.1.1 Friction/stiction over a standard CSS Test

A 7K CSS cycle test was carried out at disk inner diameter as described in section 2.1.1, environmental conditions were considered ambient at 25°C/40% RH. Again it should be noted that friction/stiction was measured in grams to conform to standard drive industry practice.

3.1.1.1 Friction trace over 1 CSS cycle

It was observed that the friction trace over one CSS cycle was essentially symmetrical about a vertical axis and was a function of disk velocity. This was true for both tri-pad and NPAB sliders. The 100th cycle from CSS tests are shown in Figure 3.2 for tri-pad and NPAB sliders.

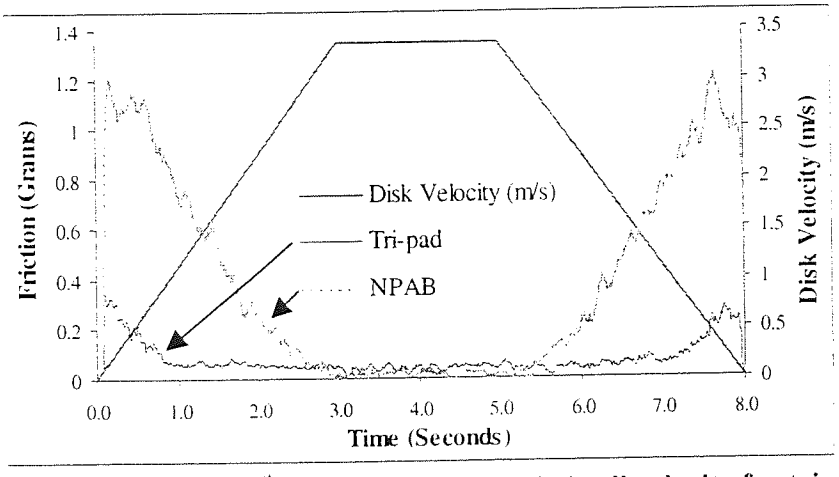

Figure 3.2 Friction trace during 100th CSS cycle at 3.37 m/s dwell velocity for tri-pad and NPAB sliders

Changes in friction trace were observed with increasing cycle number for each slider, with take-off/landing friction peaks increasing with time, this was thought to be due to smoothing of surfaces leading to higher real area of contact during these times, Figure 3.3a) and b). For tri-pad, friction was noticeably higher later in test. Note, it was common for the NPAB slider not to fly correctly on it's first cycle.

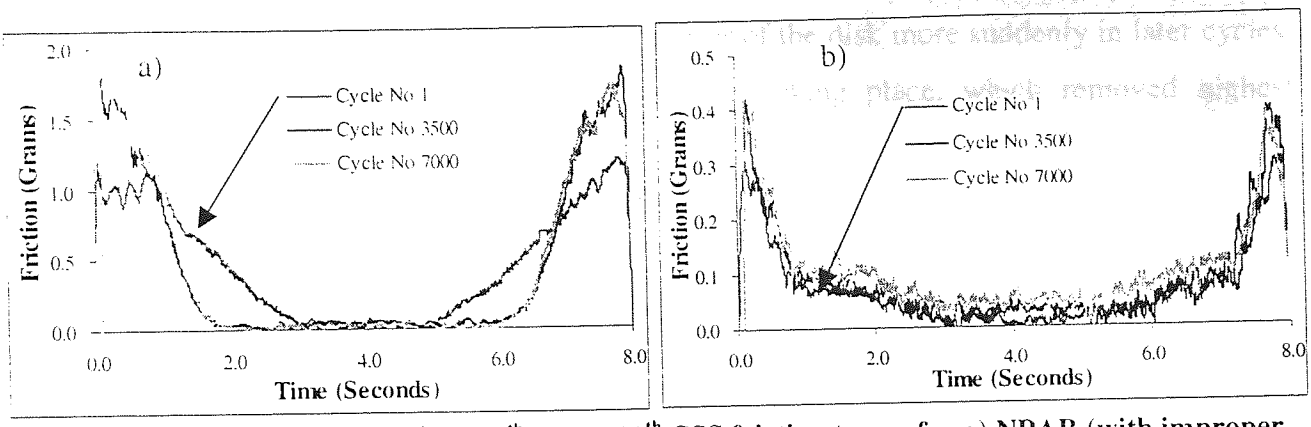

Figure 3.3 T25H40 results. 1st , 3500th and 7000th CSS friction traces for a) NPAB (with improper flying on cycle 1) and b) tri-pad slider

Another example of improper flying of NPAB slider during cycle 1 is shown in Figure 3.4. Note tests displaying this behaviour were not deemed failures, since the slider would usually go on to fly as expected throughout remainder of test.

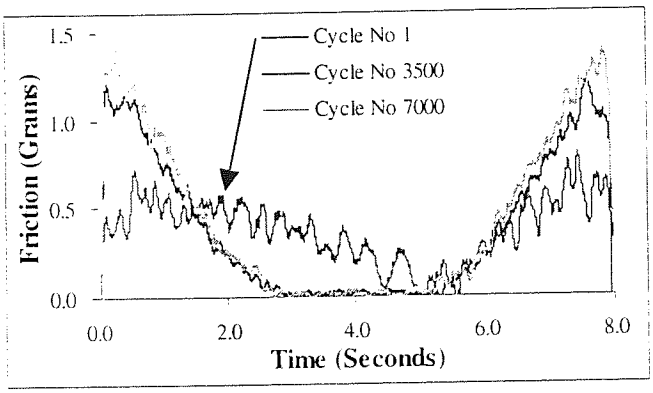

Figure 3.4 T25H35 results. 1st , 3500th and 7000th CSS friction traces for NPAB with improper flying on cycle 1

For both sliders, take-off and landing slopes became steeper with cycle number, indicating faster take-off and landing. Slopes were computed using 200 values (over a period of 0.88 seconds) during take-off and landing phases, results are shown in Figure 3.5, notice the magnitude of slopes increased as test progressed.

Higher slope values indicated that sliders flew clear of the disk more suddenly in later cycles, this could suggest that a smoothing process was taking place, which removed highest asperities.

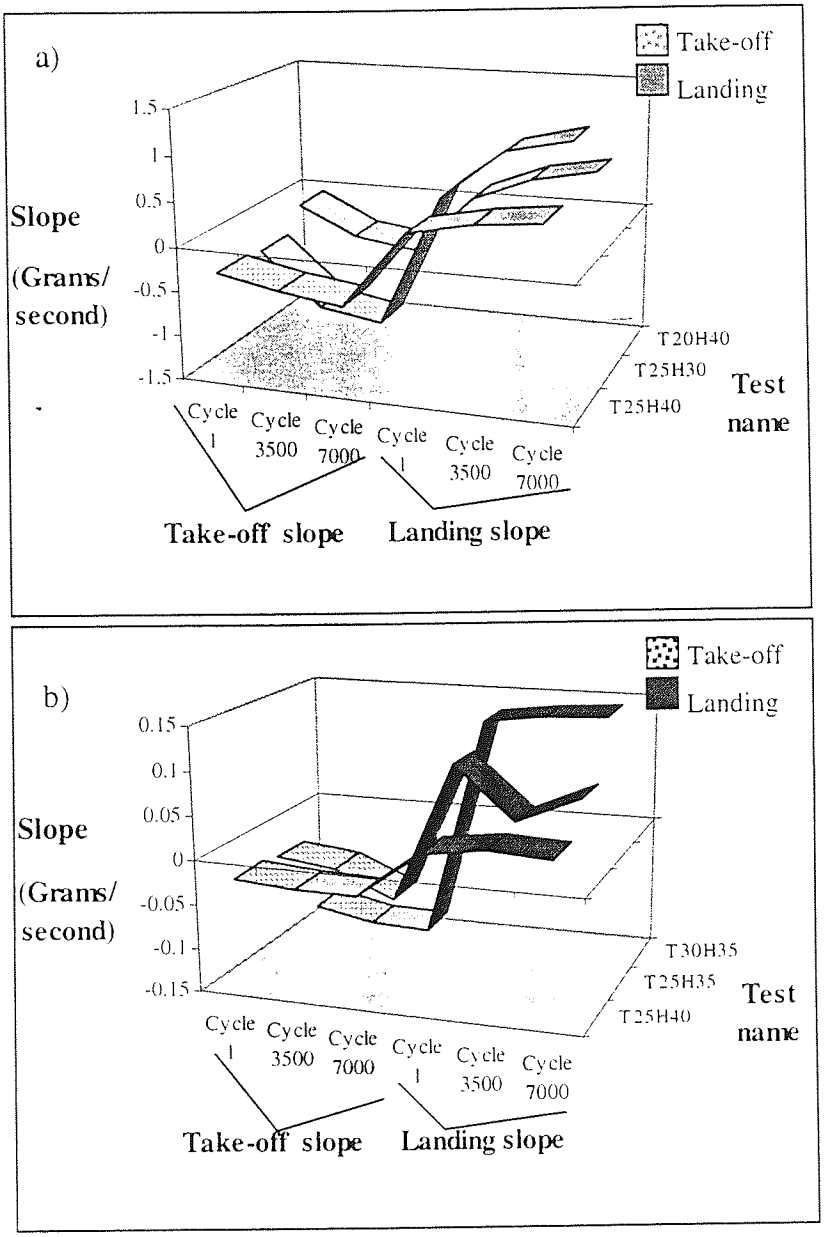

Figure 3.5 Ambient test take-off and landing slopes for a) NPAB and b) tri-pad sliders

Note, where improper flying was experienced during cycle 1, the next recorded cycle (for a standard test cycle 19) was used to compute slopes.

The actual time for surfaces to start to separate, defined as the time of the maximum initial friction peak, was investigated. It was found that surfaces took around 0.1-0.2 seconds to separate for both sliders. To illustrate separation peak, friction during the first second of the 3500th cycle of the NPAB T25H40 test is shown in Figure 3.6.

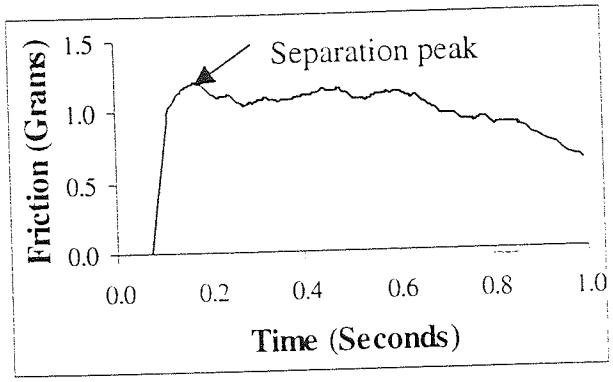

Figure 3.6 Take-off peak for T25H40 NPAB test

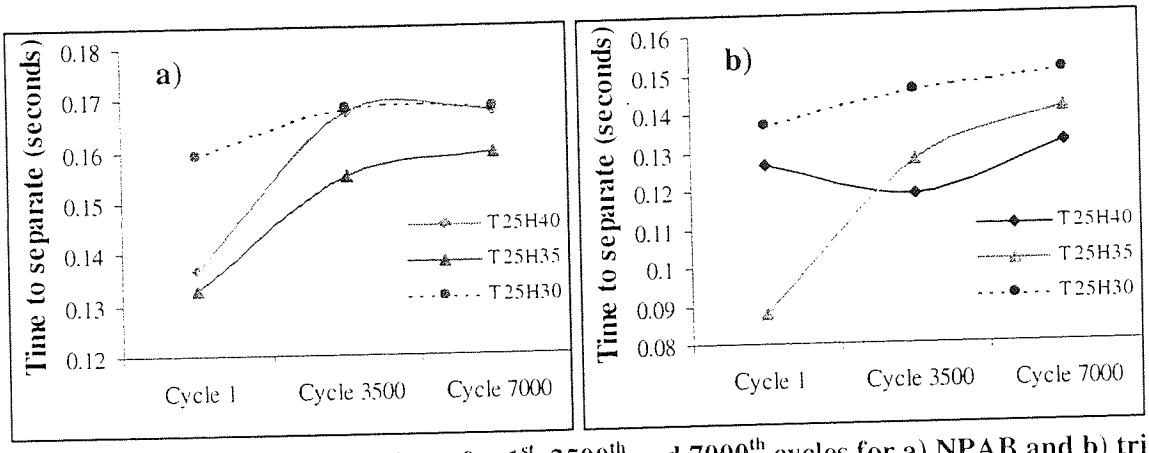

Figure 3.7 Surface separation times for 1st, 3500th and 7000th cycles for a) NPAB and b) tri-pad sliders

For both sliders, separation time increased with cycle number, this was again thought to be due to an increase in real area of contact of surfaces due to smoothing leading to larger areas of meniscus bond formation. Lubricant transfer to slider would also encourage this increase.

3.1.1.2 Mean flying friction over 7K CSS cycles

Mean flying friction was recorded for each test as described in Section 2.1.3.2. For a typical T25H35 7K test with NPAB slider, mean flying friction increased very gradually with cycle number, Figure 3.8. Note, for cycle 1 mean friction was 0.27 grams due to poor flying and is not shown on the graph or included in moving average calculations. The mean value for flying friction over the test was 0.02 grams.

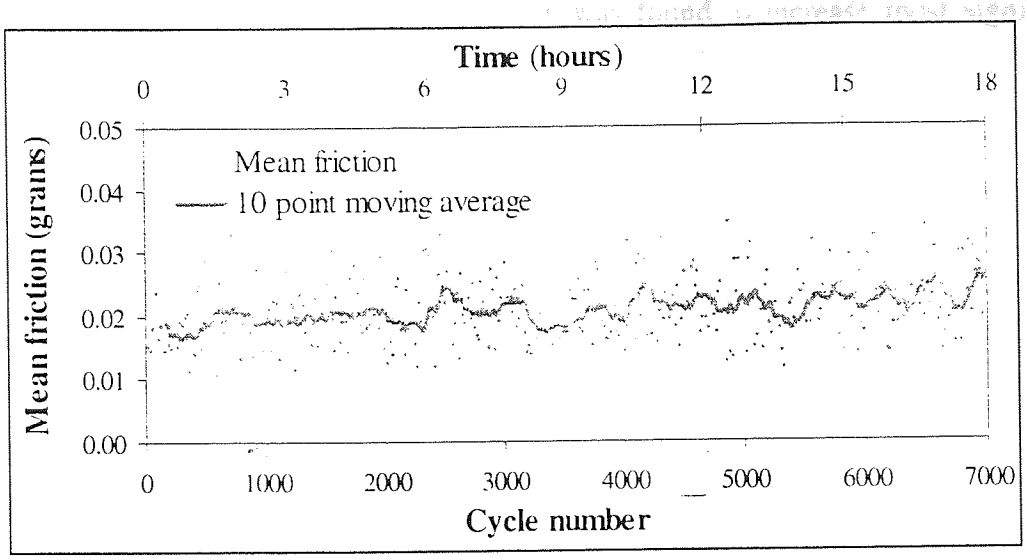

Figure 3.8 Typical flying friction shape using NPAB slider in ambient conditions

Values were distributed evenly around their mean and could be described using a Gaussian model as shown in Figure 3.9. Notice a clear modal value of 0.019 grams was highlighted.

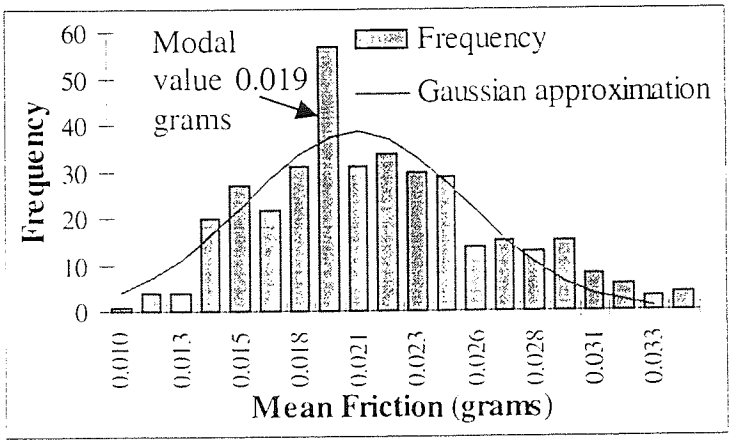

Figure 3.9 Histogram showing NPAB flying friction distribution

For the tri-pad T25H40 test, mean flying friction was found to increase most significantly during the first few hours, Figure 3.10 illustrates.

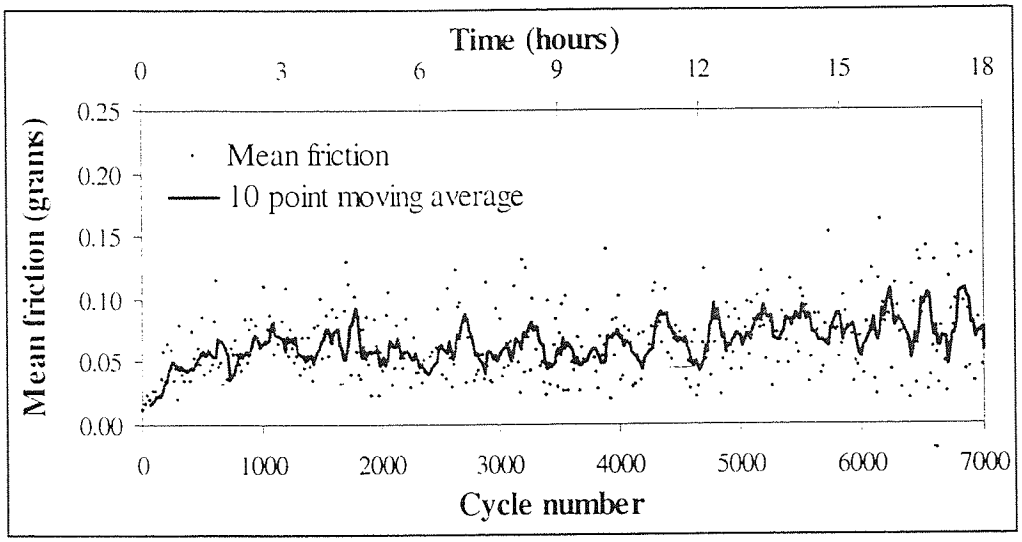

Figure 3.10 Typical flying friction shape using tri-pad slider in ambient conditions

Mean friction during flying was initially low due to the virgin contact pad and disk surfaces being rough, thus any contacts that occurred were of the highest asperities only. Also, initially the slider was free from debris and flew adeptly. As the surfaces smoothed during repeated contact, the highest asperities were worn off both disk track and slider contact pad. Contacts that occurred then had larger surface area and yielded higher friction. This process may also be a source of debris, which further increased friction.

Early values of friction being lower than the mean render the distribution of tri-pad flying friction positively skewed as shown in Figure 3.9.

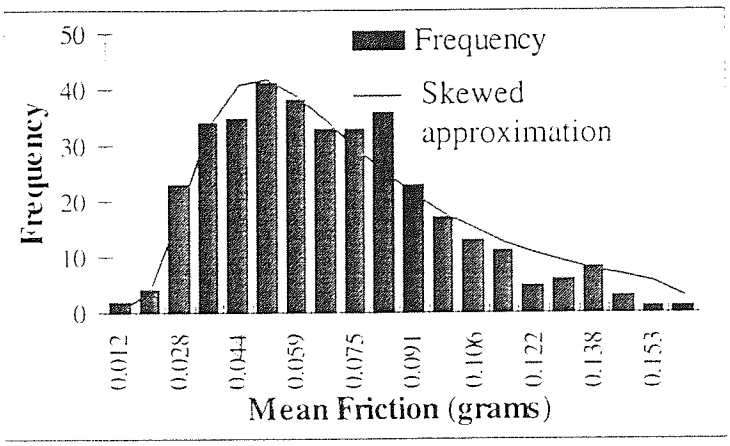

Figure 3.11 Histogram showing tri-pad flying friction distribution

Flying friction values for NPAB were then around half those for the tri-pad slider. This was due to the presence of the contact pad on tri-pad's trailing edge; this third air bearing surface is designed for proximity contact with the disk during flying.

3.1.1.3 Variation in flying friction over 7K CSS cycles

Variance in mean flying friction was recorded for each test as described in Section 2.1.3.2. During flying the amount of variation in friction was of interest, values given during T25H40 tests for NPAB and tri-pad sliders are shown in Figure 3.12. It was clear that for both sliders variation in friction during flying increased linearly with cycle number. Note, best fit linear trendlines are also shown.

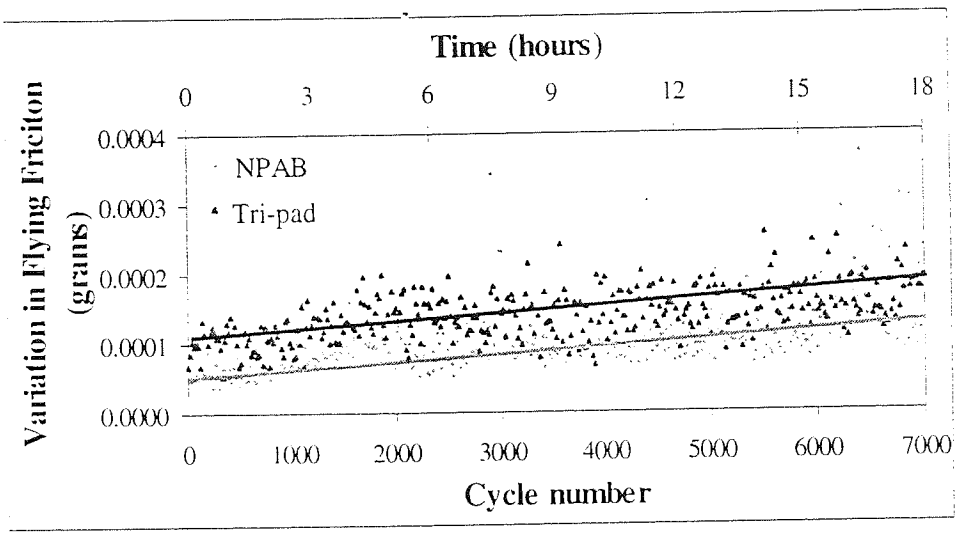

Figure 3.12 Variance in flying friction for NPAB and tri-pad sliders

The NPAB slider gave lowest variation in friction during flying under ambient conditions, although the rate of increase in friction variation was similar for both sliders.

3.1.1.4 Stiction over 7K CSS cycles

Mean stiction over 7K cycles was usually around 3.5 grams for NPAB and 2.5 grams for tri-pad, Figure 3.13a) and b) show stiction plots for each slider type. Notice a lot of spread was present in stiction, with values of up to 30 grams recorded for each slider. Plotting values against disk circumfrential position gave that high values were evenly distributed around the disk, the first 2000 cycles are shown Figure 3.13 c) and d) for each slider. Note, circumfrential position was obtained by integrating the velocity curve of the CSS cycle, see Section 4.1.3.1.

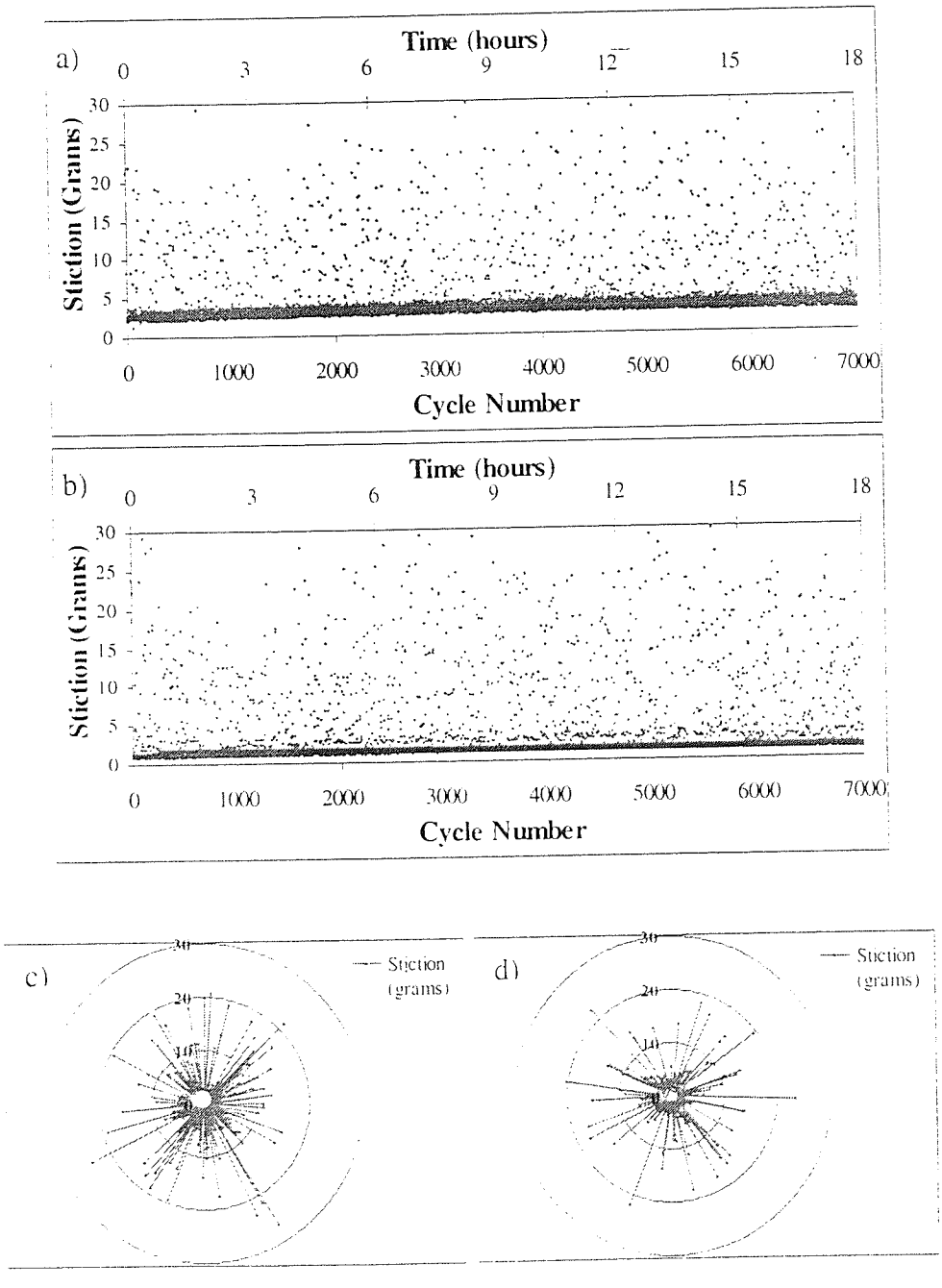

Figure 3.13 Ambient stiction plots for a) NPAB and b) tri-pad and circumfrential stiction plots for c) NPAB and d) tri-pad sliders

A similar rate of increase in stiction was observed over 7K cycles for both slider types. Figure 3.14 shows how mean stiction changed over each 1000 cycles, notice simple logarithmic trend lines again imply that most change occurs between early time groups for both sliders.

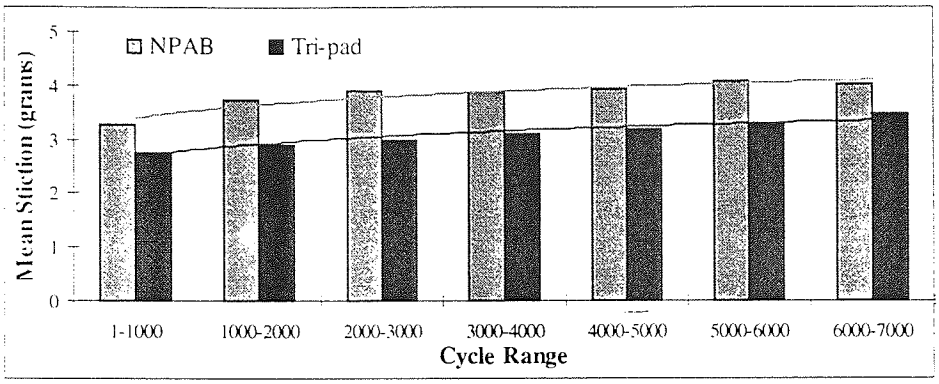

Figure 3.14 Mean stiction values over each 1000 cycle range for both sliders

Distribution of stiction was also similar for both sliders, being highly positively skewed as shown in Figure 3.15. Note logarithmic scale was employed for ease of comparison.

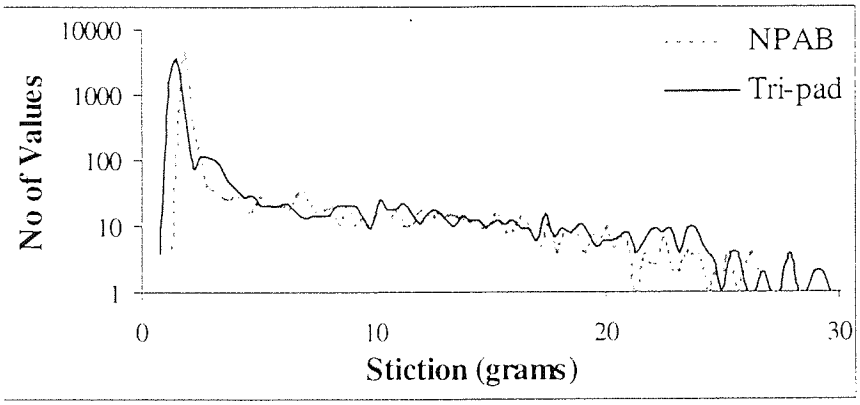

Figure 3.15 Stiction distributions for both slider types

As a measure of distribution of stiction values, the Pearson's coefficient for skew was used where

$$P = \frac{3(\bar{S} - S_{Md})}{\sigma_S} \qquad \textbf{Equation 3.2}$$

with $\bar{S}$ mean stiction, S_{Md} median stiction and σ_S is standard deviation of stiction. For tests shown P=0.89 and 0.87 for NPAB and tri-pad respectively, indicating high positive skew.

3.1.2 Effect of Disk Dwell Velocity

To study the effect of different dwell velocity on friction trace, standard 3, 2, 3 second CSS tests were performed at 1, 2, 3, 4, 5, 7, 10 and 15 m/s dwell time velocity using both types of slider. Tests consisted of 1000 cycles in ambient and a new slider was used for each test.

The NPAB flew at 1 m/s, however the tri-pad slider failed to take-off with contact occurring during dwell time of the cycle. see Figure 3.16. In fact, friction appeared almost independent of disk velocity for the tri-pad, remaining high at around 0.15 grams throughout the cycle.

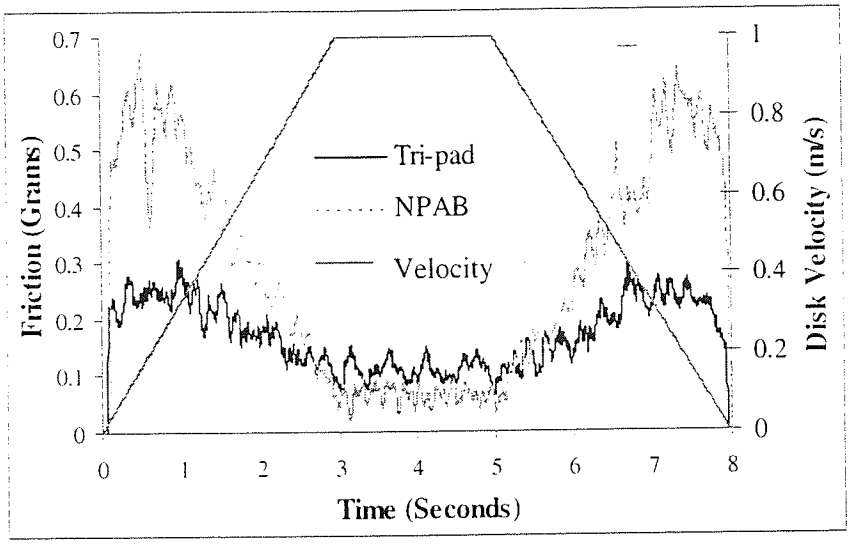

Figure 3.16 Friction traces for both sliders at 1m/s dwell velocity

3.1.2.1 Take-Off and Landing Characteristics

The take-off and dwell friction traces at 2, 3, 4 and 5 m/s are illustrated in Figure 3.17, as expected friction decreases more rapidly as velocity increases. This can be quantified by calculating the slope friction decrease with time during a period of 1 second during the take off phase of each cycle (comprising 225 measurements).

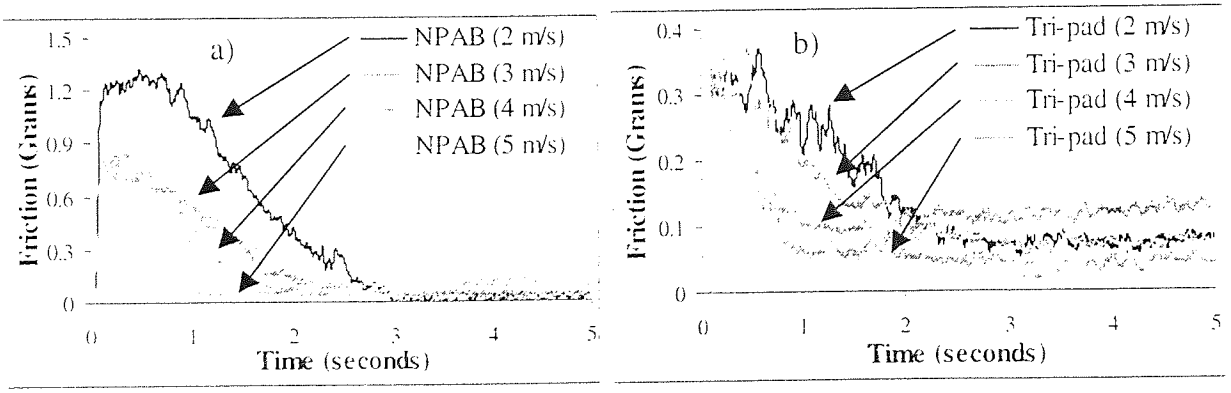

Figure 3.17 Take-off friction slope at 2,3,4 and 5 m/s for a) tri-pad and b) NPAB slider

Table 3.1 illustrates friction slope values for increasing velocity during take-off and landing phases, values are plotted in Figure 3.18.

Linear Velocity	Take-off slope		Landing slope	
	NPAB	Tri-pad	NPAB	Tri-pad
1 m/s	-0.113	0.009	-0.216	0.005
2 m/s	-0.396	-0.164	0.041	0.007
3 m/s	-0.461	-0.289	-0.029	0.065
4 m/s	-0.384	-0.295	0.438	0.292
5 m/s	-0.697	-0.291	0.579	0.382
7 m/s	-0.348	-0.147	0.266	0.256
10 m/s	-1.034	-0.033	1.479	0.514
15 m/s	-1.579	-0.030	1.706	0.053

Table 3.1 Comparing take-off and landing slopes for both sliders

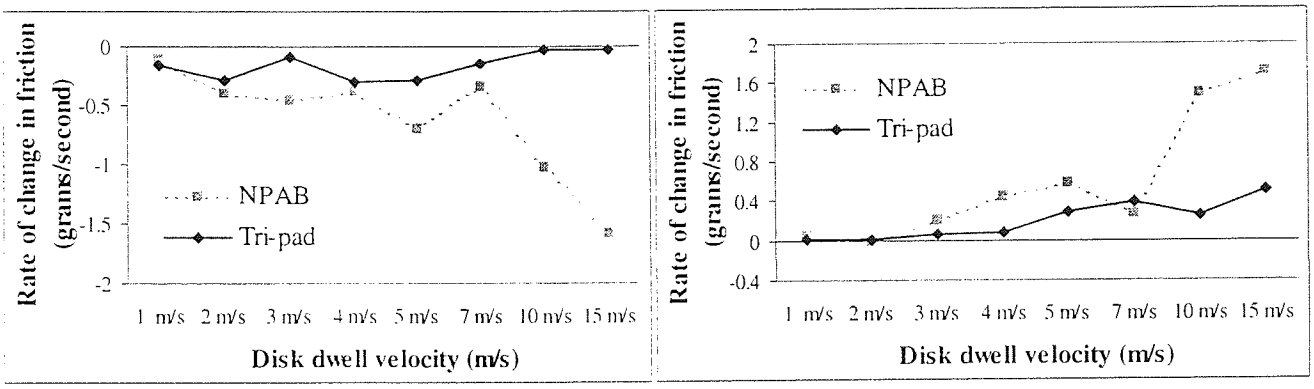

Figure 3.18 Comparing NPAB and tri-pad with respect to a)take-off and b)landing slope

The magnitude of take-off and landing slopes generally increased with disk dwell velocity for both sliders. This was to be expected as the head flew sooner at higher velocity, giving a steeper slope on take-off and the high deceleration rate to rest yielded an abrupt landing slope. The NPAB again reacted more quickly to disk velocity having steeper slopes in almost all cases.

As expected, the time for surfaces to separate decreased with increasing disk velocity, Figure 3.19. Values were measured from the 1000th cycle. Again, the tri-pad slider appeared to separate from disk before NPAB at most velocities.

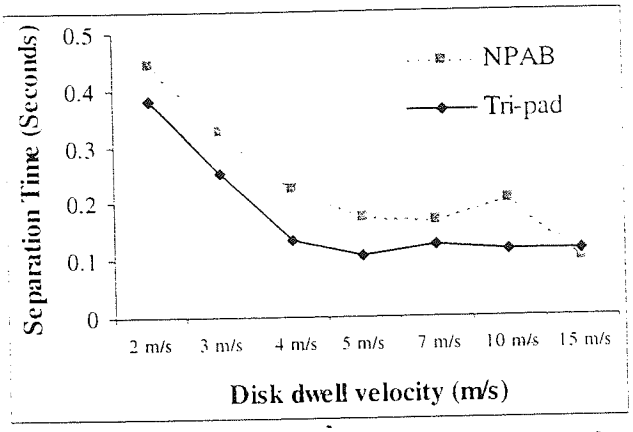

Figure 3.19 Surface separation times with increasing disk velocity for both sliders

During the 15 m/s tests, much fluctuation was observed in friction traces, regions of instability are indicated in Figure 3.20. Since the patterns of variation were similar for both sliders, the source of this was likely to be external vibration of the AFT apparatus. It was decided to limit testing velocity <10 m/s using existing apparatus to prevent unreliable friction results being incorporated into models.

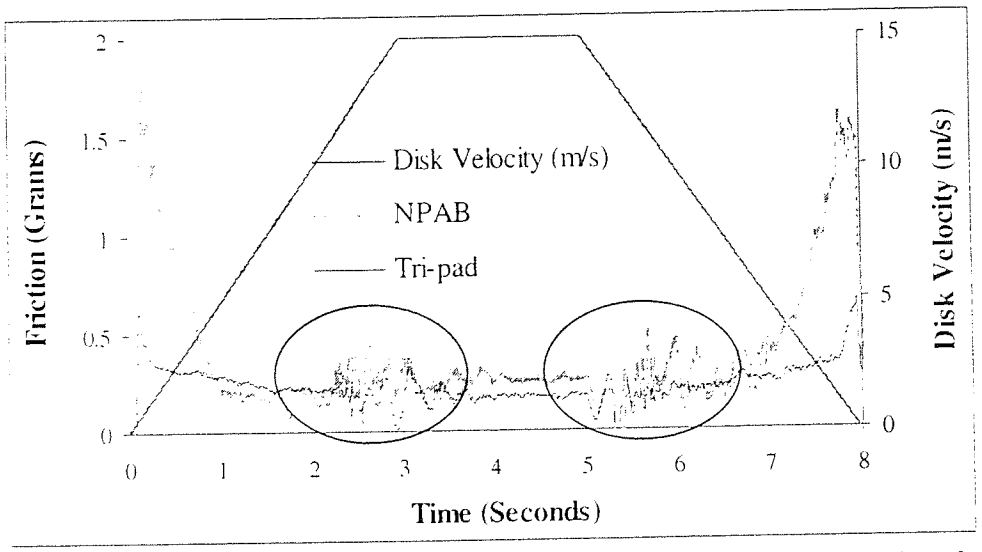

Figure 3.20 Showing large oscillations in friction trace over a CSS cycle for tri-pad and NPAB sliders (worst friction fluctuation periods indicated)

3.1.2.2 *Effect of Disk Dwell Velocity on Mean Flying Friction*

The effect of disk dwell velocity on mean flying friction was studied during the above tests. An additional test was carried out at 0.5 m/s dwell velocity as a control for both sliders. Figure 3.21 illustrates that neither slider flew at this low velocity, as mean flying friction was high (>1 gram).

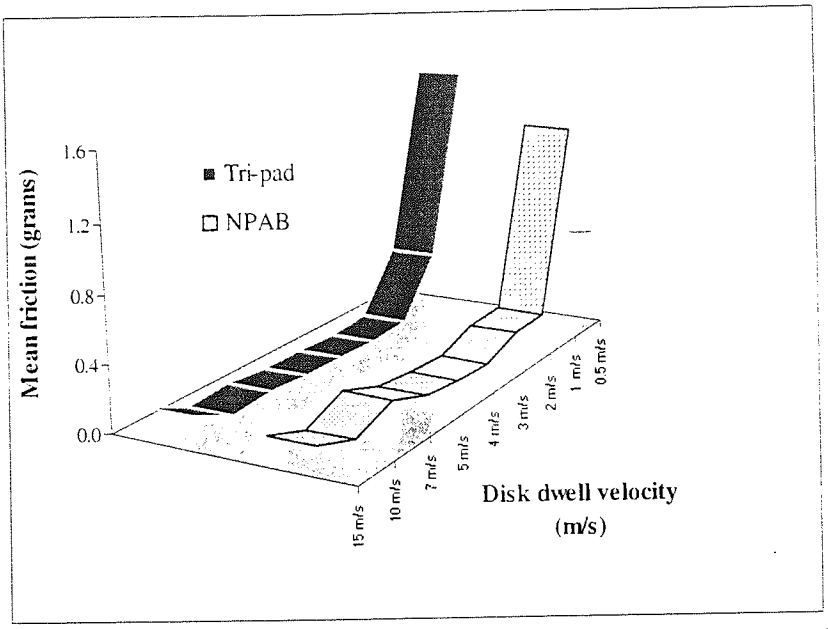

Figure 3.21 Mean flying friction against disk dwell velocity for both sliders (note x-axis scale in reverse order for clarity)

For the NPAB mean flying friction decreased with increasing dwell velocity until 7 m/s, when a sudden increase in friction was observed. This increase could have been caused by the slider's negative pressure force reducing fly height and thus allowing more slider/disk contact to occur.

Tri-pad mean friction decreased until >10 m/s, when system vibration intervened giving rise to high friction.

3.1.2.3 *Effect of Disk Dwell Velocity on Stiction*

Sliders showed contrasting behaviour with respect to stiction at increasing velocity. For the NPAB mean stiction decreased until 4 m/s, further increasing velocity caused an increase in stiction. The tri-pad demonstrated almost the opposite behaviour, whereby stiction increased with velocity until 5 m/s and then decreased again. Minimum, maximum, mean and standard deviation of stiction are shown in Figure 3.22 a) and b).

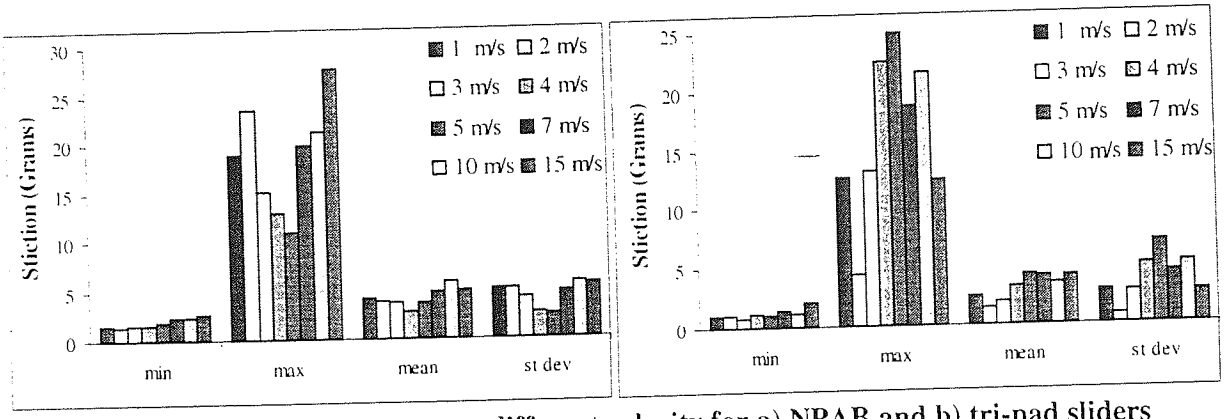

Figure 3.22 Stiction values at different velocity for a) NPAB and b) tri-pad sliders

For both sliders it was clear that the minimum recorded stiction increased with disk velocity, Figure 3.23 shows that higher velocity appears to limit the smallest stiction that was recorded.

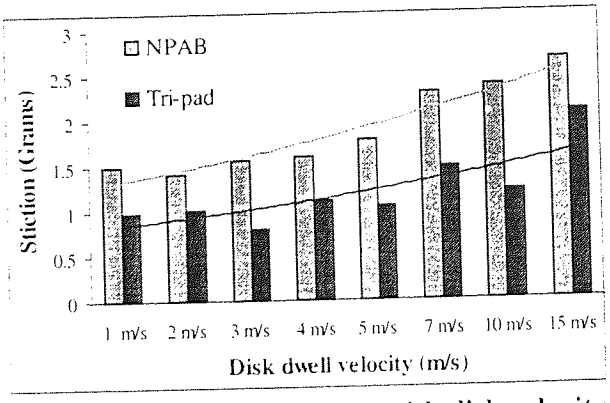

Figure 3.23 Increase in minimum stiction with disk velocity for both sliders

3.1.3 Effect of Environment

CSS tests were run under a variety of conditions using both slider types, results are presented in the following sections.

3.1.3.1 CSS Environmental Testing with NPAB Slider under Constant Conditions

The effects of environment on flying friction were studied, standard tests were conducted in a total of 31 environments as shown in Section 2.3.2.1, Figure 2.2.3 a). Only 27 were successful under the failure criteria (defined in section 3.1.7), these tests will now be analysed. The failed tests will be discussed in section 3.1.7.

The effects of temperature and humidity on flying friction were not initially obvious, Figure 3.24 shows there was large spread in results. In Chapter 4 an improved method of mapping friction results to environment was found.

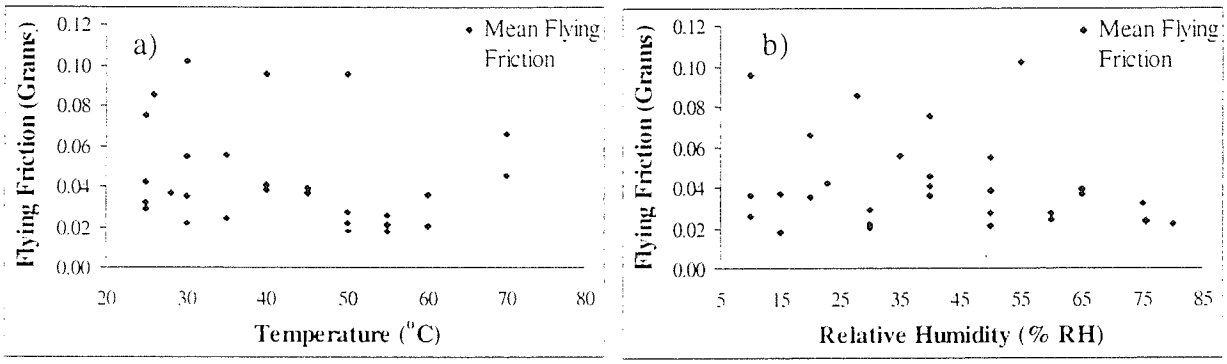

Figure 3.24 Effect of a) temperature and b) humidity on mean flying friction

Since temperature and humidity are not independent, their combined affects were also examined; Figure 3.25 illustrates the mean friction values plotted against both temperature and humidity. Hot/dry environments appeared to yield highest friction, but spread in results had not been eliminated by taking this approach.

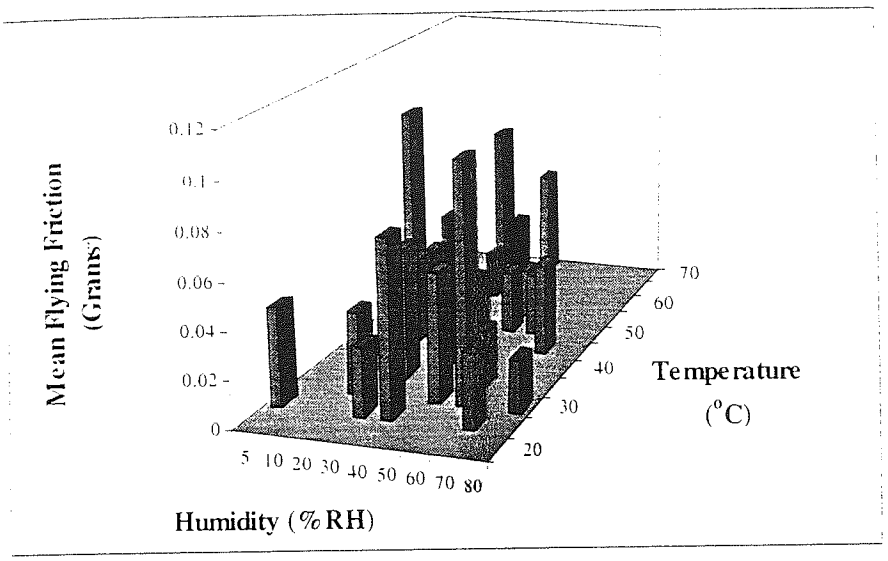

Figure 3.25 Mean flying friction against temperature and humidity

It was noticed that in hot/dry environments the rate of increase of friction was higher than in hot/humid environments, Figure 3.26.

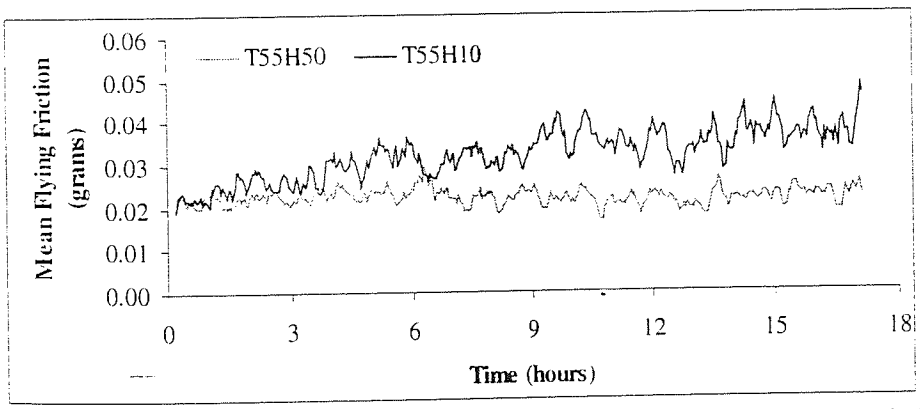

Figure 3.26 Mean flying friction over 7K cycles in 55°C and 10 and 50% RH

When examining the effect of environment on stiction it was decided to perform 1K CSS tests at 1 rpm dwell velocity (equivalent to 0.0024m/s). This velocity was chosen to be consistent with other literature in the field of environmental testing [98]. Shorter test duration, approximately 2 hours, was chosen to allow such high-risk tests to be performed under constant supervision.

The environmental tests performed are illustrated in Figure 2.23 a) and b) of Section 2.3.2.1. Stiction appeared to be unaffected by different humidity under low/ambient temperature. However, high humidity coupled with high temperature led to extremely high stiction, Figure 3.27.

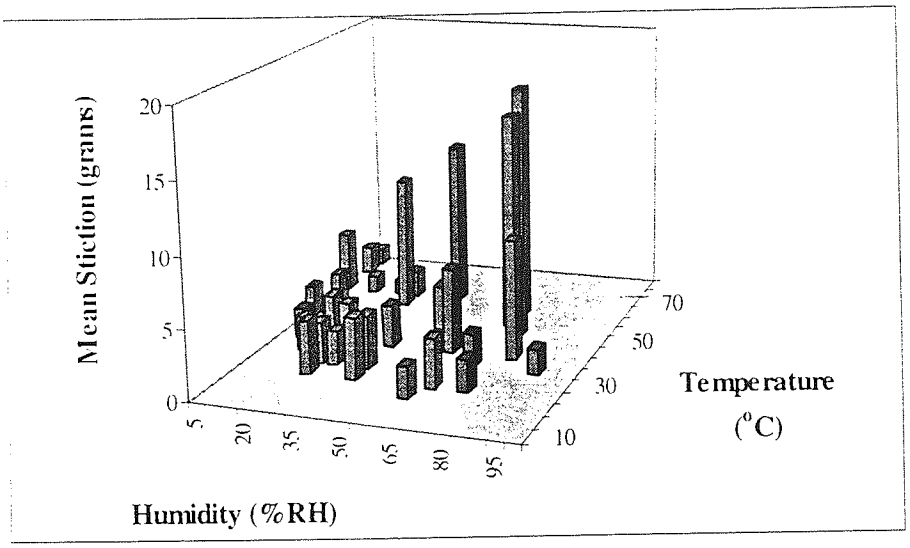

Figure 3.27 Mean stiction against temperature and humidity

3.1.3.2 CSS Environmental Testing with NPAB Slider where In-situ Changes in Humidity Occurred

Where changes in humidity occurred during a test, these were followed closely by stiction values. Figure 3.28 shows that during the first hour of a test in 55°C humidity peaked to 70 % RH and then dropped to 12% RH, stiction values showed large variation but generally followed humidity. Note, a time delay in the order of a few minutes was observed between events.

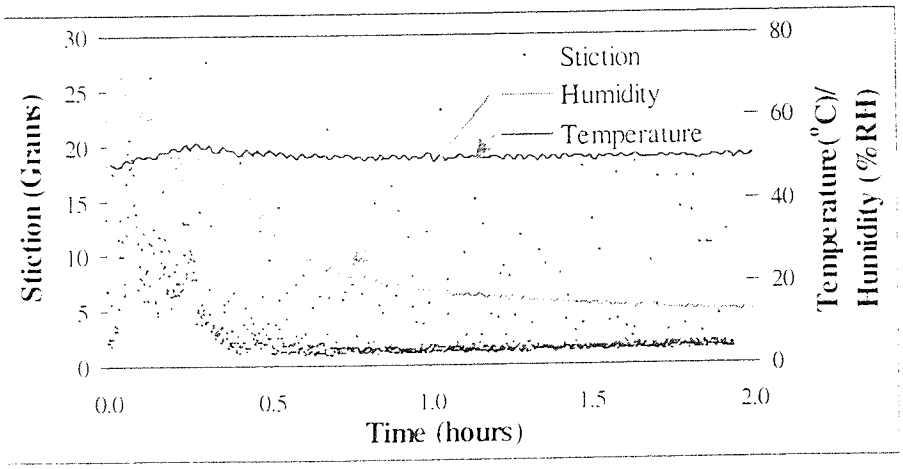

Figure 3.28 Sudden in-situ humidity peak caused peak in stiction values

On examining mean flying friction from a test performed at 30°C/45% RH, a rogue point was observed towards the end of the test. On examining the environmental traces it was clear that a sharp humidity rise had occurred preceding this, Figure 3.29a). Investigation of a CSS friction trace during this very humid period indicated that the slider had failed to fly during cycle 6916, Figure 3.29b). When humidity decreased the slider again flew normally suggesting that recovery of the interface was possible following environmental changes of this type. Later it will be seen that longer duration changes in humidity and dramatic changes in temperature during a test can give irrecoverable interface failure.

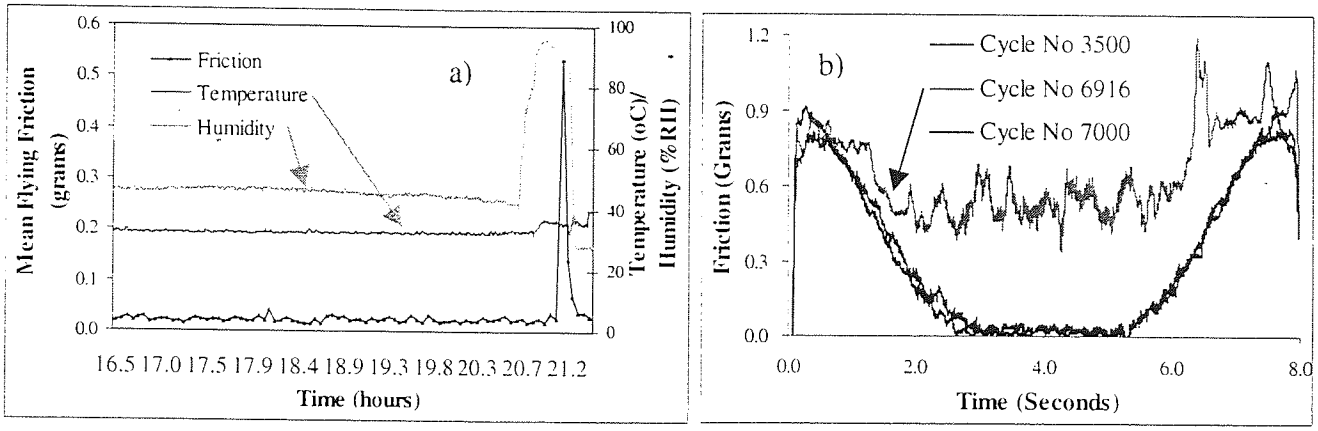

Figure 3.29 a) Sudden in-situ humidity peak caused peak in friction values and b) friction traces before, during and after humid peak

3.1.3.3 CSS Environmental Testing with Tri-pad Slider under Constant Conditions

Only 11 environments were studied using the tri-pad slider, these are shown in Section 2.3.2.2, Figure 2.25. This older type of slider was of less interest with respect to environmental work and the tests performed were used to draw conclusions about friction behaviour only. Thus, the separate 1 rpm stiction tests were not performed for the tri-pad slider.

Generally, friction was higher in high temperature environments, Figure 3.30. It was also noticed that in hot/dry environments friction continued to increase beyond the 4 hour smoothing period observed in 3.1.1.2.

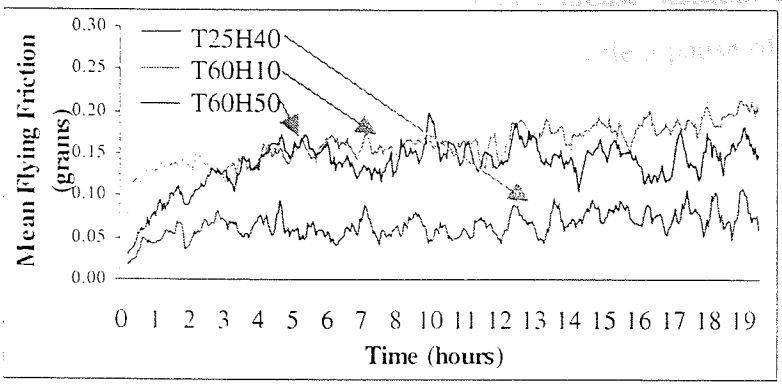

Figure 3.30 Mean flying friction over 7K cycles in 25°C/40% RH and 60°C / 10 % RH and 50% RH

3.1.4 Effect of Pause

It has been suggested that a pause between successive CSS cycles can introduce high stiction at the slider/disk interface due to meniscus effect. Tests were carried out under various conditions to determine what length of pause was required to induce such a response.

Tests consisting of 1000 CSS cycles were carried out with pause lengths of 0, 10, 20 and 30 minutes between cycles were performed in ambient (25°C/40 %RH) and elevated conditions (35°C/55 %RH).

From Figure 3.31, it was clear that in ambient conditions, the pause length had little effect on stiction. However, under more humid conditions increasing pause length led to high stiction. High humidity accelerated the formation of meniscus bonds between slider and disk increasing stiction.

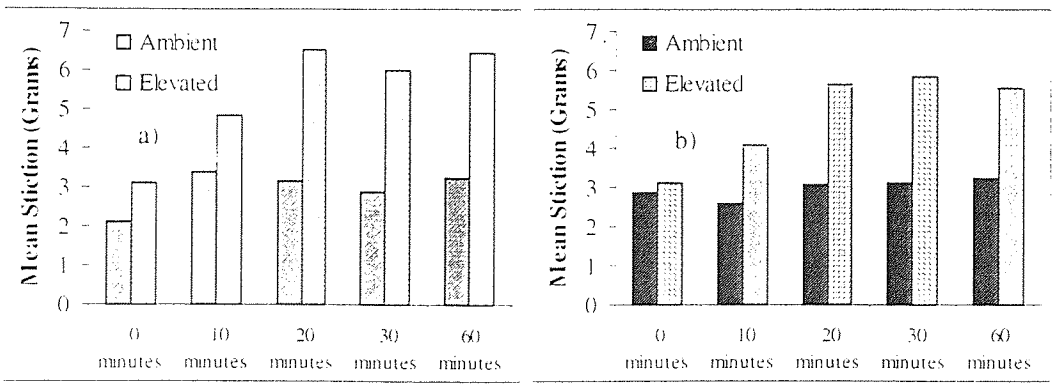

Figure 3.31 Effect of having a pause between cycles in ambient and elevated conditions for a) NPAB and b) tri-pad slider

An additional test was performed using the NPAB to determine if a critical pause length existed beyond which the meniscus effect did not further increase stiction. In conditions of 30°C/70% RH, 40 CSS cycles were performed, between each cycle a pause of different length was applied. The range of pauses studied was [0-200] minutes using 5 minute intervals. In addition, pause lengths were randomised to eliminate any effect of order from the experiment. The test took around 3 days to complete, results are shown in Figure 3.32. Notice a control run was performed under the same conditions with no pause between cycles.

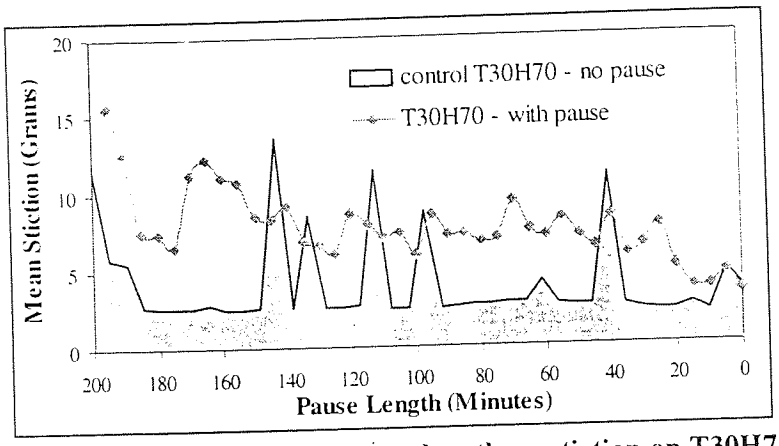

Figure 3.32 Effect of decreasing pause length on stiction on T30H70 NPAB

Stiction increased with pause length up to 25 minutes, whereby values remained fairly steady until a pause of 140 minutes was experienced. Somewhere in this time window meniscus saturation may have occurred. Above 140 minutes stiction appeared to behave erratically again, displacement/transfer of disk lubricant during excessive pause length may have occurred.

By investigating dynamic friction traces for cycles with/without pause, it was clear that the slider had difficulty taking off following a long pause, Figure 3.33. Also, note the separation peak was higher and occurred later following a pause.

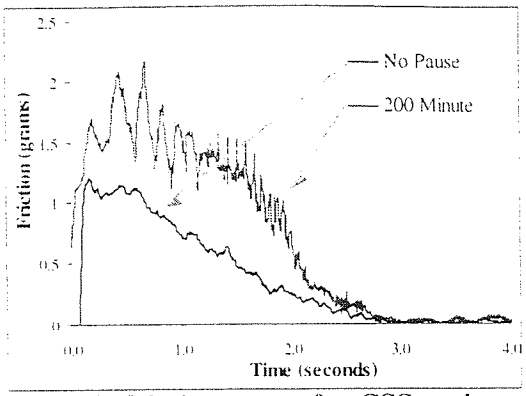

Figure 3.33 Comparing dynamic friction traces for CSS cycles with pauses of 0 and 200 minutes

3.1.5 Effect of Disk Texture

3.1.5.1 Using Crosshatched Disks

Using a NPAB slider, 7K CSS cycles were performed in ambient at disk landing zone (23 mm from disk centre). Following the test the NPAB was raised and moved to a neighbouring track (26 mm from disk centre) and another 7K CSS test performed. Results were scaled appropriately using Equation 3.1 to remove the small difference in tangential component of friction induced by the track change.

Stiction results for the last 500 cycles of first leg of test and first 500 cycles of second leg are shown in Figure 3.34.

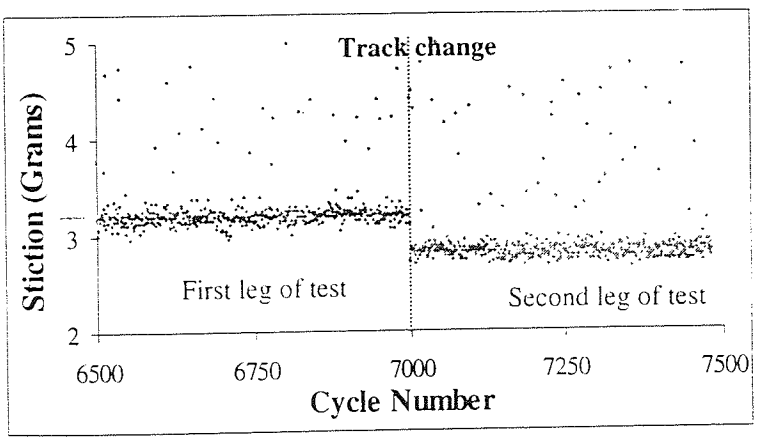

Figure 3.34 Stiction results for track change CSS experiment (Note, stiction values > 5 grams were neglected for this study)

Note following the track change stiction was reduced by around 0.5 grams. This was due to the new, virgin track being rougher than used track. Thus, the new track still had its texture intact, minimising the amount of contact between head and disk during parking and in turn reducing stiction.

This experiment also suggested that a smoothing or burnishing of the original disk track had taken place. Additionally, these results also suggested that the increase observed in stiction during CSS testing was due to smoothing of the disk, rather that slider.

3.1.5.2 Using Graded Texture Disks

Using the graded texture disks the effect of variable disk texture on friction and stiction was studied. NPAB sliders were used in 100 cycle CSS tests in ambient at the textured landing zone and smooth data zone of graded disks. Disk radii chosen for testing were 23 and 39 mm from disk centre and again results were scaled appropriately using Equation 3.1.

The 100th cycles of data and landing zone tests are shown in Figure 3.35. High asperities at landing zone gave head/disk contact for longer during slider take-off while at the data zone lower peak height meant that take-off was a more sudden event. During dwell time friction was higher over the data zone and contained much more variation, this is illustrated in Figure 3.36 a) and b). This behaviour has also been reported by Suzuki and Nishihira [124].

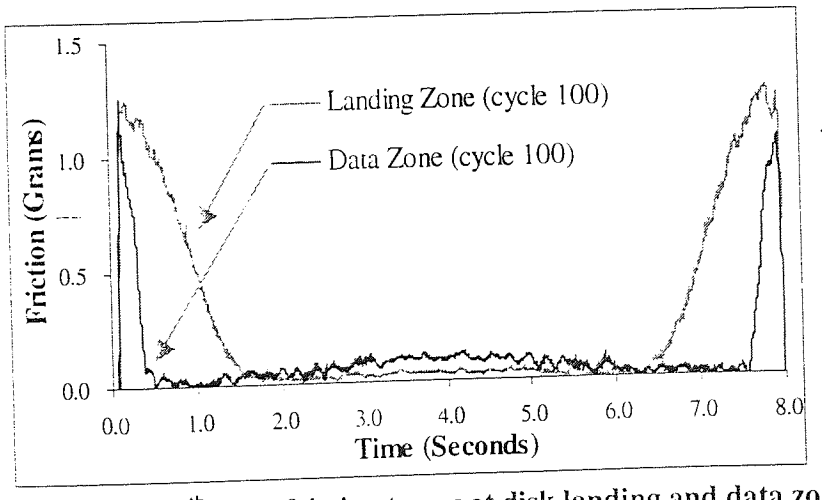

Figure 3.35 100th cycle friction traces at disk landing and data zones

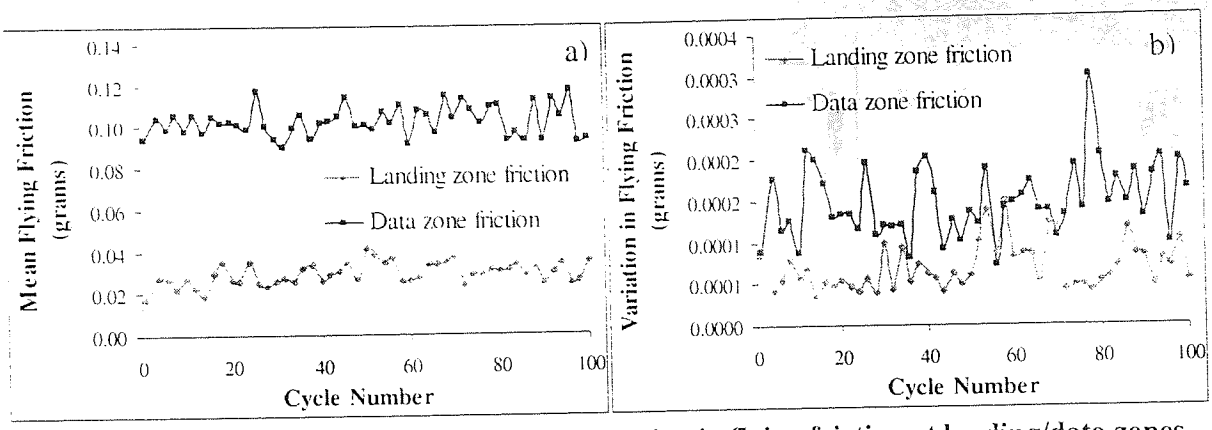

Figure 3.36 a) Mean flying friction and b) variation in flying friction at landing/data zones

Stiction results were as expected, with the smoother area of disk yielding the highest values. Although higher stiction was observed over the smoother region, it was more consistent; implying disk texture was more uniform around disk circumference at the data zone.

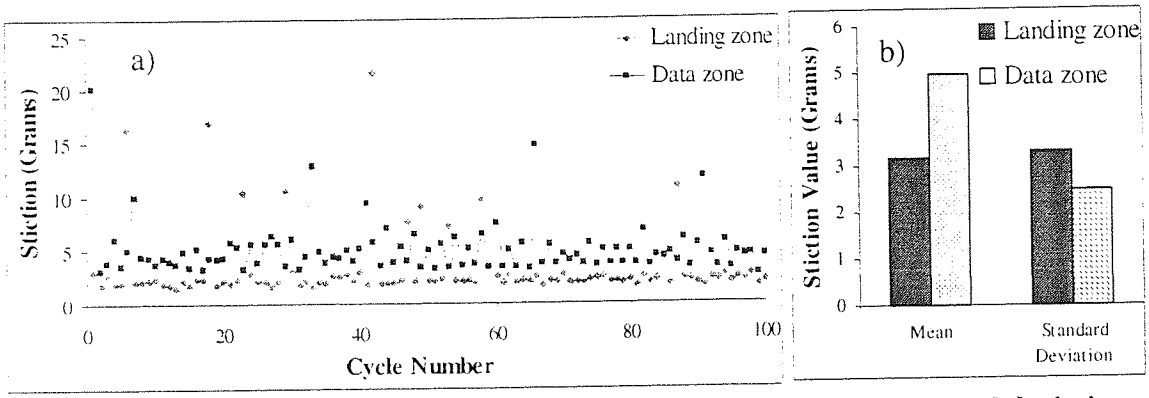

Figure 3.37 a) Stiction over 100 CSS at landing/data zones, b) mean/standard deviation

3.1.6 Effect of Disk Lubricant

3.1.6.1 Lubricant Removal

A crosshatched disk had lubricant removed using IPA solution. Using a NPAB slider a 7K CSS test was performed in ambient. Friction trace results are shown in Figure 3.38. As a control, results from an ambient test using a standard lubricated disk are also shown.

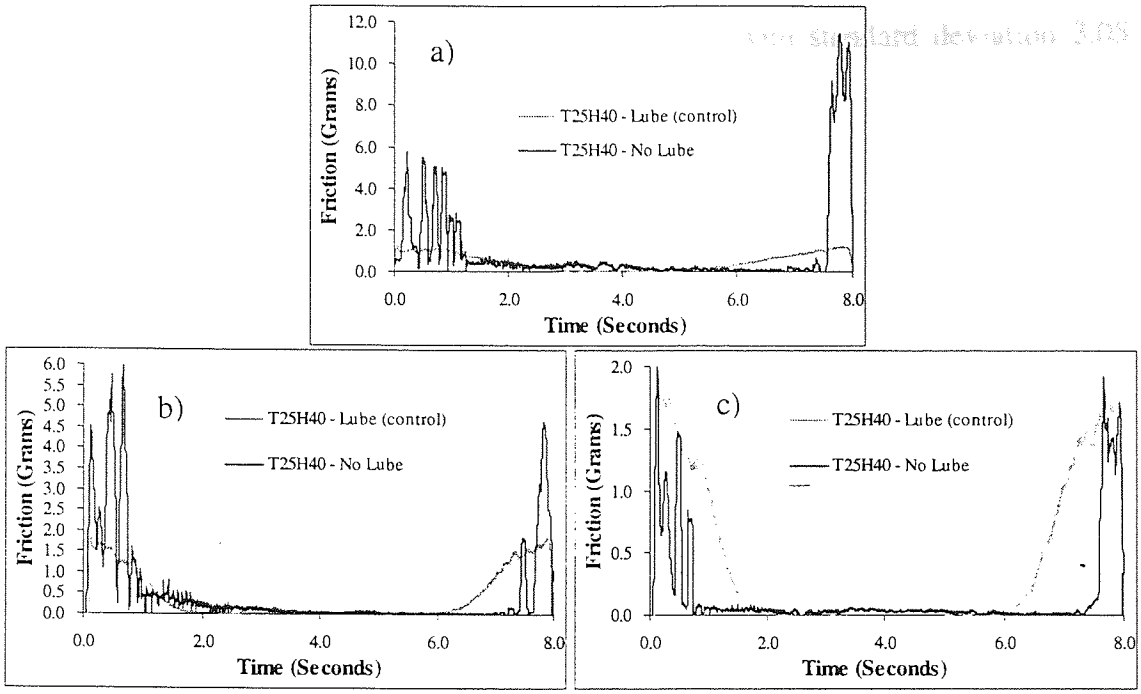

Figure 3.38 Effect of removing disk lubricant, a) 1st, b) 3500th and c) 7000th CSS cycle

Friction was much higher for the disk without lubricant, especially in early cycles of the test. Take-off and landing seemed erratic and very sudden events. Flying friction in early cycles was also higher for the unlubricated disk, Figure 3.39. After around 4 hours however, flying friction was similar to that of a lubricated disk. This implied that some protective layers might have been formed at the interface. Or perhaps that some lubricant held in disk porosity had migrated back to the surface.

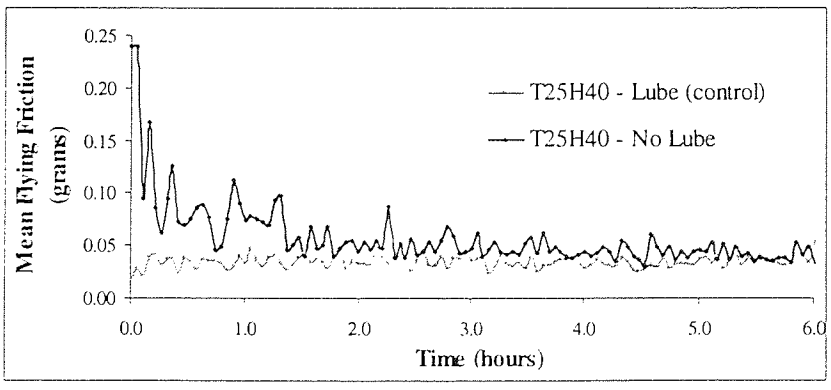

Figure 3.39 Effect of removing disk lubricant on ambient CSS mean flying friction

The unlubricated disk displayed high stiction throughout test, which like friction decreased over the first 4 hours. Mean stiction was 9.06 grams with standard deviation 3.05 grams. Stiction results are shown in Figure 3.40.

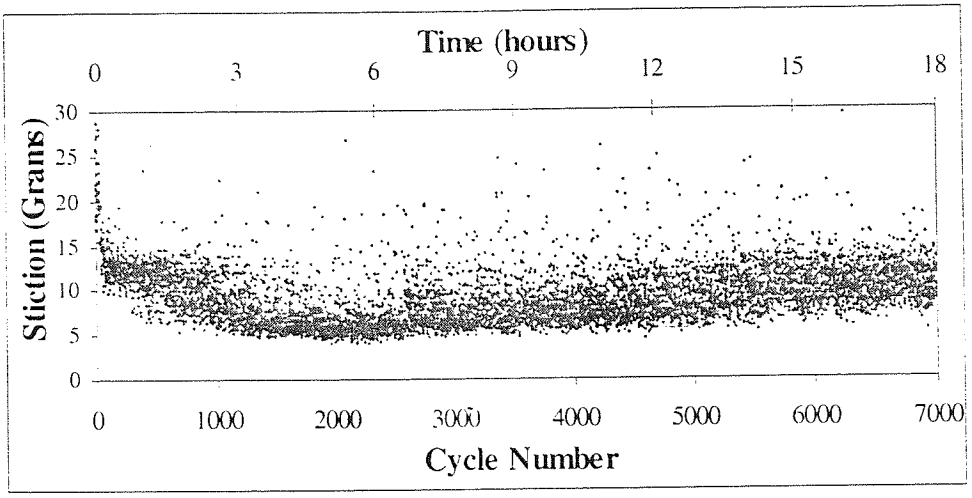

Figure 3.40 Effect of removing disk lubricant on ambient CSS stiction

3.1.6.2 Lubricant Transfer

A thin spot (area approximately 4 mm^2) of silicon oil was applied to one area on a disk track. 500 CSS cycles were conducted in ambient and the affect on stiction noted, Figure 3.41, testing was performed 26 mm from disk centre. Observe the clear cyclic behaviour of stiction as the slider enters and leaves the doped area of disk. It was calculated that the disk performed 8 revolutions during this test. From the graph it was clear that the area of disk affected by doping was larger than one/two slider parking positions originally doped. Clearly, transfer of material to neighbouring disk positions via slider was occurring.

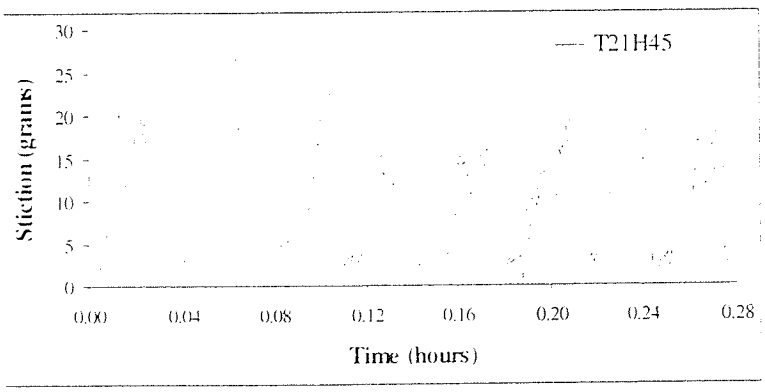

Figure 3.41 Stiction values over 500 CSS cycles at 1 rpm with doped disk

The transfer theory was confirmed by performing a separate stiction test with another doped disk, this test consisted of 1500 cycles and was designed to take only 50 disk revolutions to complete.

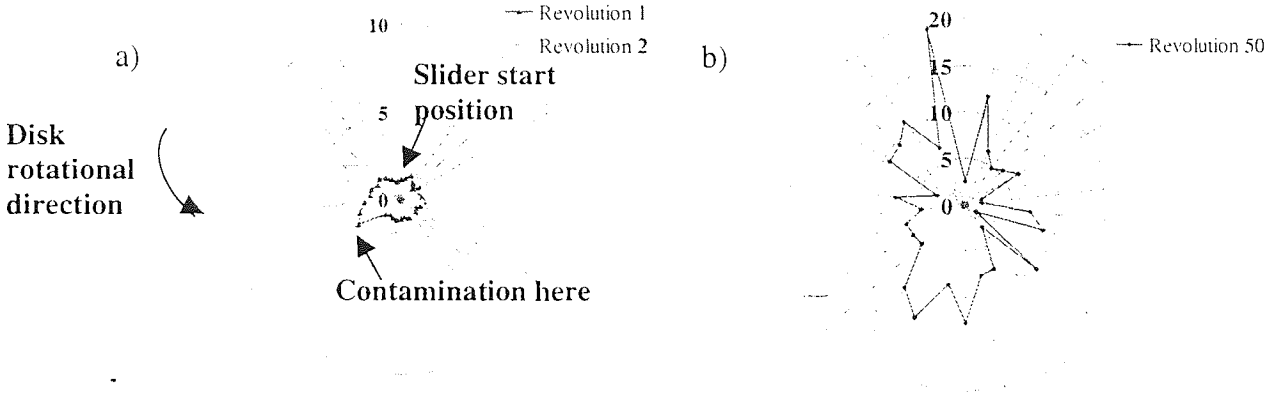

Figure 3.42 Stiction values over a) 1st, 2nd and b) 50th disk revolution using doped disk

Results in Figure 3.42 show stiction on a radial axis plotted against the disk circumfrential position. Circumfrential position was obtained by integrating the velocity curve of the CSS cycle, see Section 4.1.1.1.

During early cycles, the region of disk contamination could be easily identified from stiction plots, Figure 3.42a) and b). However, after 50 cycles stiction was high at almost all disk positions. Post test inspection revealed a continuous ring of silicon oil on disk.

3.1.7 CSS Test Failure

To define failure, a modification of failure criteria for CSS tests as given by Zhao and Bhushan [38,39] was used. That is, a CSS test was deemed a failure if either of the following events occurred:

- Rise in 10 point moving average of stiction to > 4 grams, >3.5 grams for NPAB and tri-pad, respectively or
- Standard deviation of stiction > 5 grams or
- Mean flying friction > 0.25 grams or
- The formation of an obvious disk wear track occurred during testing

Using these criteria, environmental tests described in 3.1.3.1 and 3.1.3.3 for NPAB and tri-pad were classified. Results on failed tests are shown in Figure 3.43 a) and b) respectively.

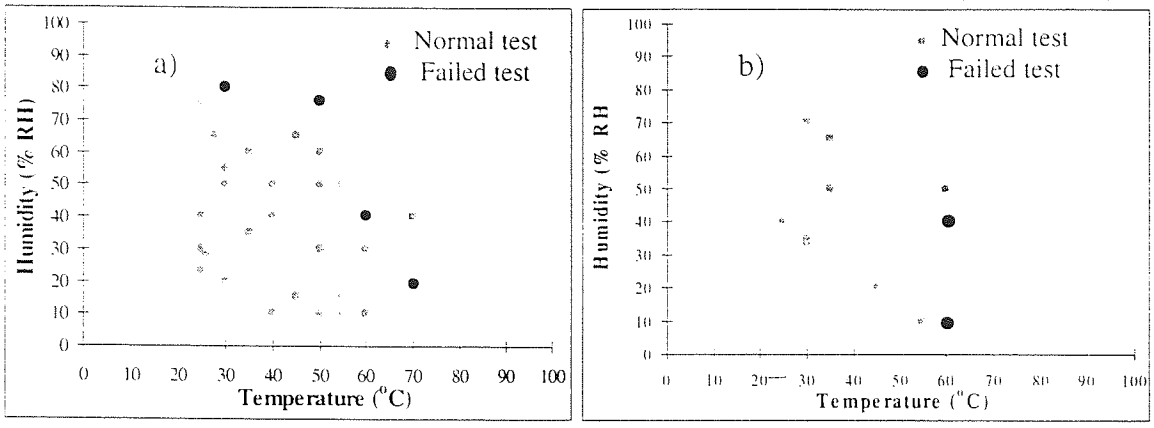

Figure 3.43 Environments in which failure occurred during 7K CSS for a) NPAB and b) tri-pad sliders. Manufacturer expected operating conditions are shaded

3.1.7.1 CSS Tests Displaying High/Increasing Friction

During T60H40C test with NPAB, flying friction was observed to increase around 1 hour into the cycle, Figure 3.44 a). Analysis of friction traces gave that the slider did not fly correctly on cycle 304, Figure 3.44 b). Following this troubled cycle, the slider failed to fly throughout the remainder of the test. It was clear that irreparable damage had been done to the interface.

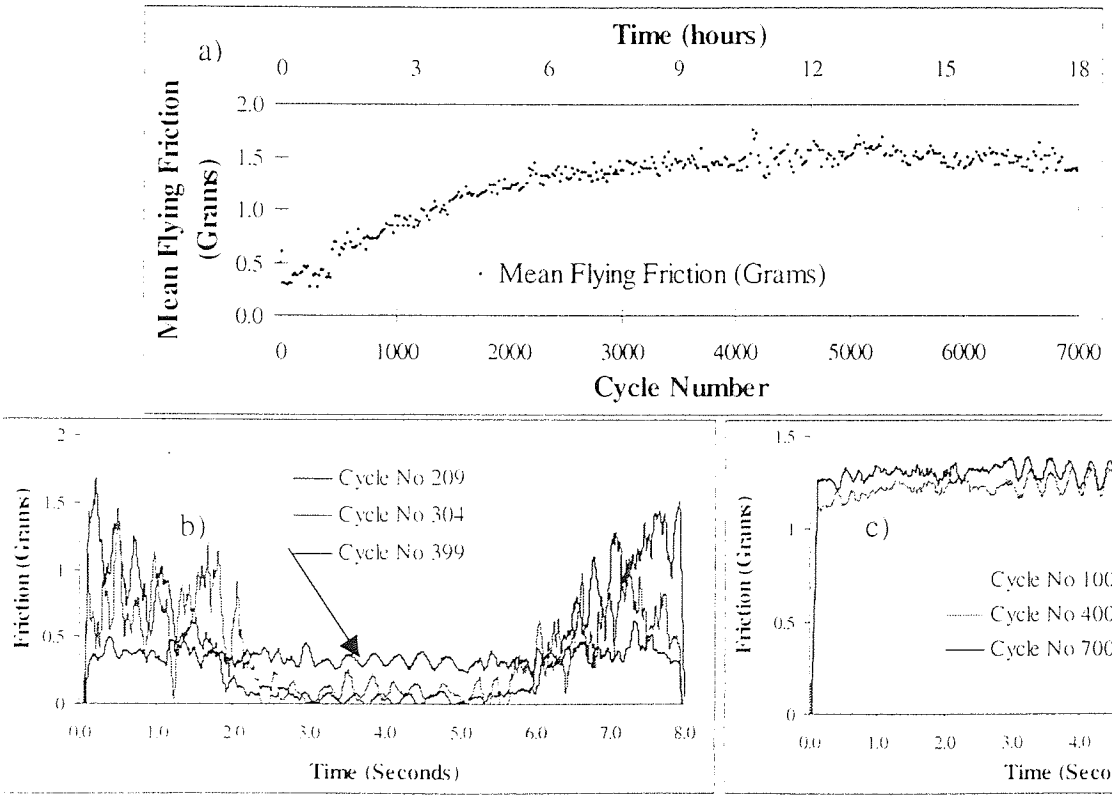

Figure 3.44 a) Mean flying friction for failed T60H40C and friction traces b) around time of failure and c) following failure

During the test T70H20C with NPAB slider, early failure was detected. Analysis of friction traces gave that between the 3000th and 4000th cycles, the interface became damaged and the slider failed to fly correctly, this non-flying continued until the end of the test. Friction traces are shown in Figure 3.45.

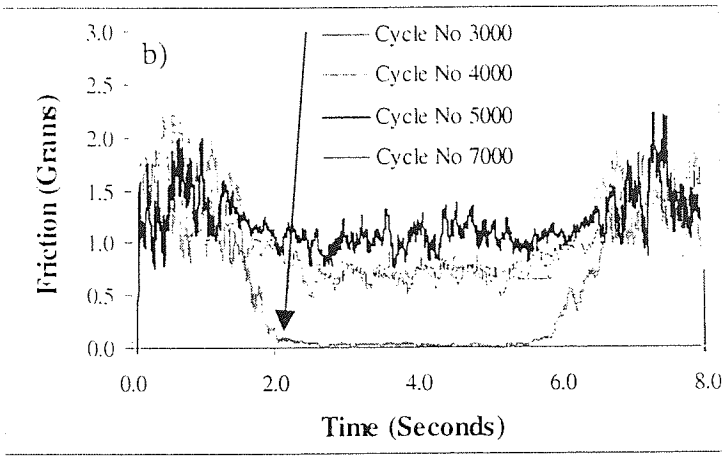

Figure 3.45 Friction traces for failed T70H20C

On examining the mean flying friction values, Figure 3.46 a) a sudden increase in values was observed during cycle 3800, that was approximately 10 hours into the test. Friction trace analysis indicated that slider was taking much longer to take-off than expected preceding increase, Figure 3.46 b). Some slider flaw was expected during the post test surface analysis.

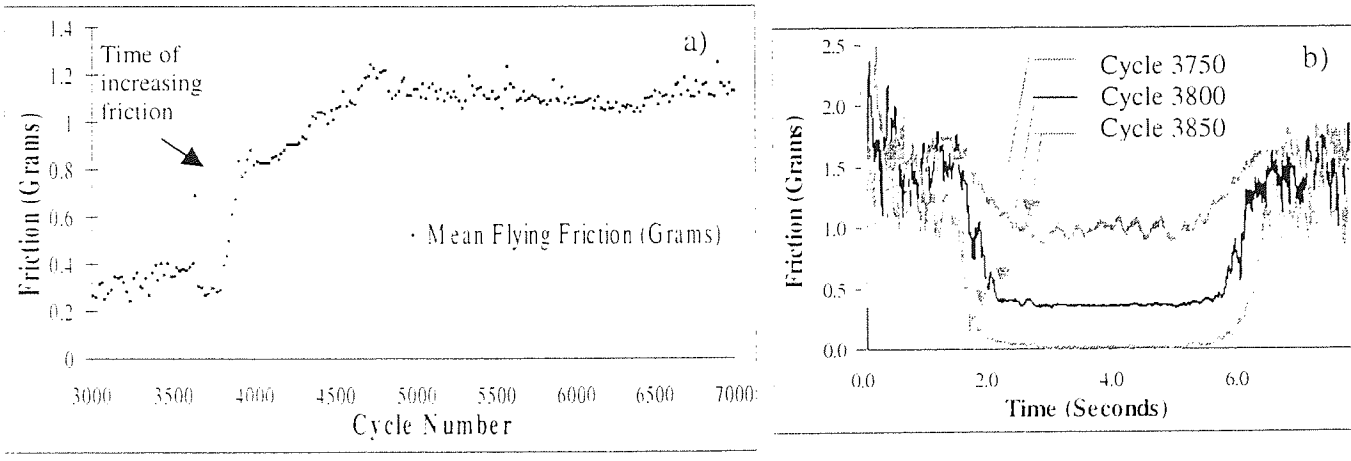

Figure 3.46 a) Mean flying friction for failed T70H20C and b) friction traces around time of failure

For the tri-pad CSS test T60H10C, failure occurred between the 1st and 3500th cycles. By studying the flying friction graph, this failure range was narrowed down, (observed, Figure 3.49a) Figure 3.47a) and b).

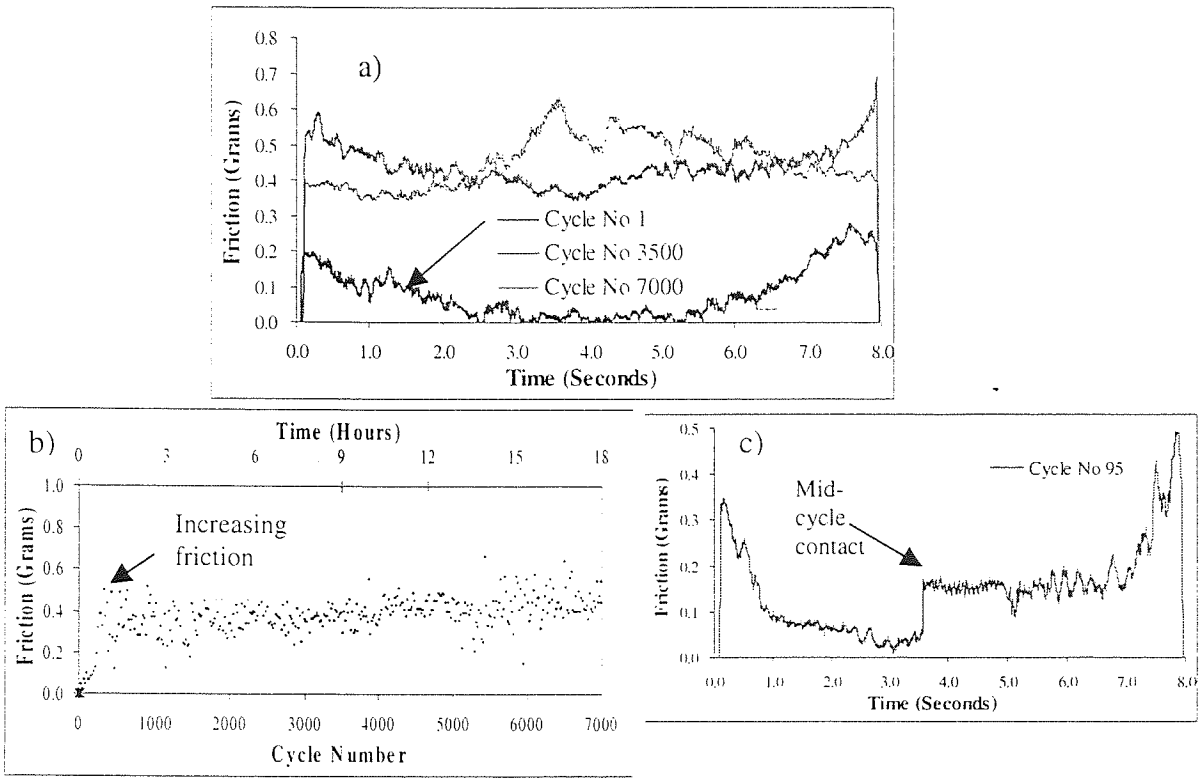

Figure 3.47 a) Friction traces, b) mean flying friction and c) 95th CSS for failed T6H10C

In fact, the 95th cycle friction trace indicated that mid-cycle contact had occurred between slider and disk. Figure 3.47c). During this contact slider damage must have occurred which rendered proper flying impossible for the remainder of the test thus giving high friction.

Stiction was also higher than expected for T60H10C, with values of up to 35 grams recorded.

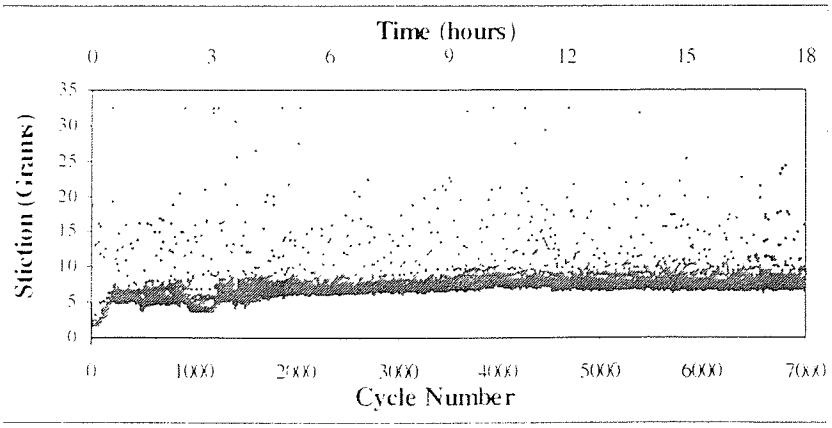

Figure 3.48 Stiction for failed T6H10C

3.1.7.2 *CSS Tests Displaying High/Increasing Stiction*

Around 3 hours into T50H75C test, a sudden jump in stiction was observed, Figure 3.49a). The distribution of values differed from that expected by being bimodal, that is two clear modes were observed representing the most frequently occurring values before and after failure, Figure 3.49b). Stiction distribution was useful to categorise how badly tests had failed.

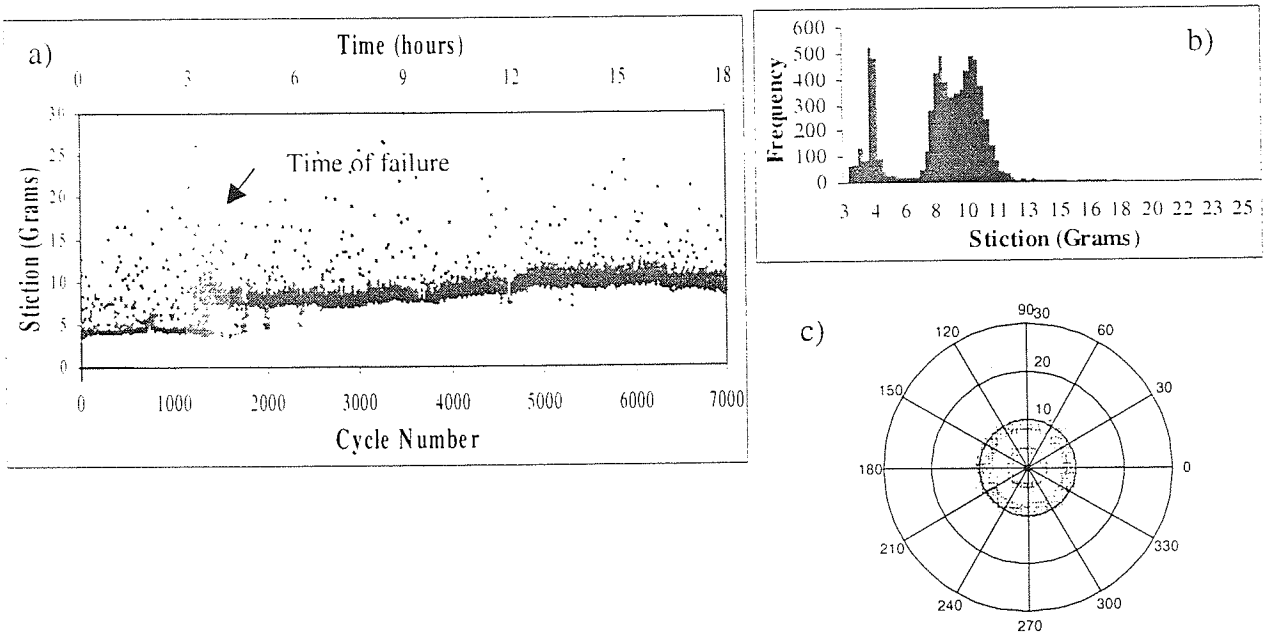

Figure 3.49 Stiction during T50H75C CSS test, a) with time/cycle number, b) stiction distribution and c) with disk circumfrential position around time of failure

Stiction was also studied as a function of disk circumfrential position, Figure 3.49c). Two distinct levels of stiction were seen at all disk positions, implying the problem was with slider rather than disk.

For the tri-pad test T60H40C, stiction behaved erratically initially and grew higher throughout the test. A definite change was observed in stiction around 9 hours beyond which spread increased.

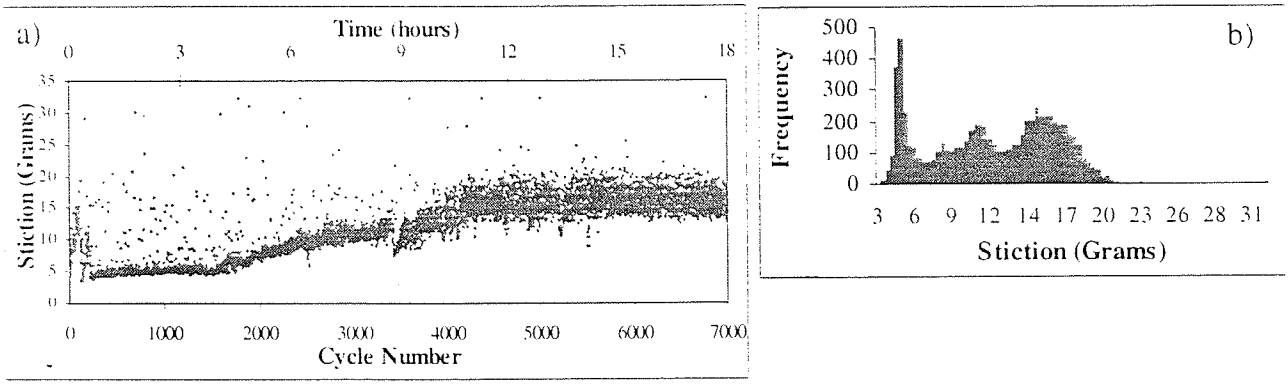

Figure 3.50 Stiction during tri-pad T60H40C CSS test, a) with time/cycle number and b) stiction distribution

Stiction distribution was again multi-modal for the failed test.

3.1.8 Effect of Velocity on Drag Testing

When deciding what velocity to perform drag tests at using test apparatus, experiments were carried out around the velocities reported for drag testing in other literature [38,86]. It was decided that the required velocity was such that the slider was not properly flying but merely dragging on the disk surface. Figure 3.51 shows results for NPAB and tri-pad used in conjunction with crosshatched disks.

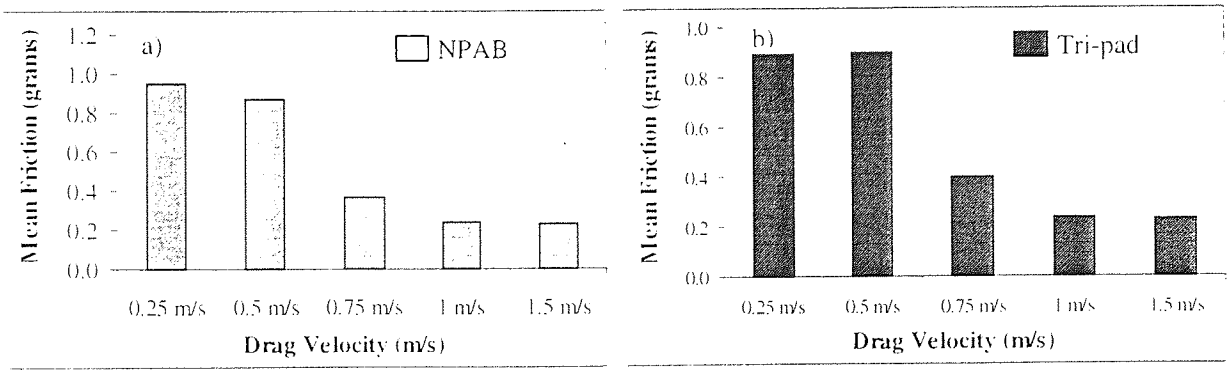

Figure 3.51 Mean friction results of 10 hour drag tests in ambient at 0.25, 0.5, 0.75, 1 and 1.5 m/s for a) NPAB and b) tri-pad

For both sliders, 0.5 m/s appeared to be a good benchmark velocity above which the air bearing force initiated partial flying. Thus, drag testing at this velocity would ensure a large amount of contact occurred between head and disk.

3.1.9 Friction over a Standard Drag Test

Friction increased during standard drag testing as shown in Figure 3.52. This test was performed using a crosshatched disk and NPAB slider. Environmental conditions were constant at 25°C/45% RH throughout the test, right hand axis displays results of environmental monitoring.

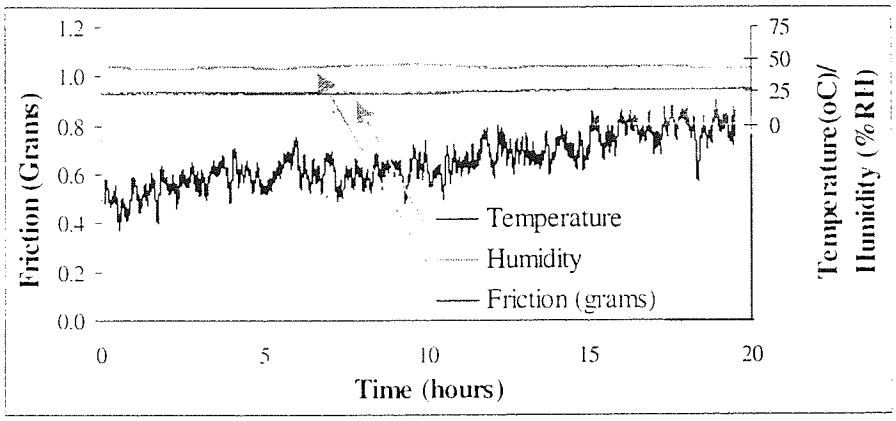

Figure 3.52 Friction over Standard Drag Test T25H45

Drag test results using tri-pad slider were almost identical to that shown above, with similar rate of increase in friction exhibited. For both sliders, mean friction was typically in the range [0.5-1] grams over a 20 hour drag test.

3.1.10 Drag Environmental Testing

3.1.10.1 Drag Environmental Testing with NPAB Slider under Constant Conditions

Standard drag tests were performed in modified environments for 20 hours and friction recorded, see Figure 2.25 in Section 2.3.2.3 for test details. A plot of mean friction against temperature and humidity is shown in Figure 3.53.

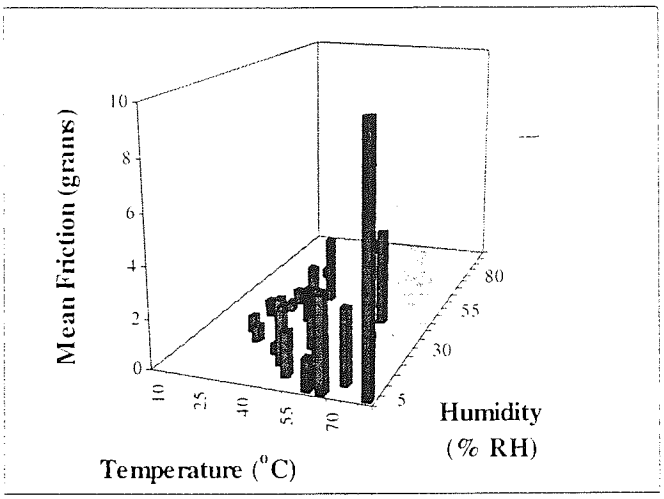

Figure 3.53 Environmental drag test friction against temperature and humidity

High temperature tests displayed the highest friction, especially at low humidity.

3.1.10.2 Drag Environmental Testing with NPAB Slider with In-situ Changes in Conditions

During a 2 hour drag test at 25°C, humidity was increased from 30% RH to 55% RH after 25 minutes. Note it was attempted to hold temperature constant. Almost immediately, friction dropped by around 0.4 grams, Figure 3.54. A slight time delay was observed between events.

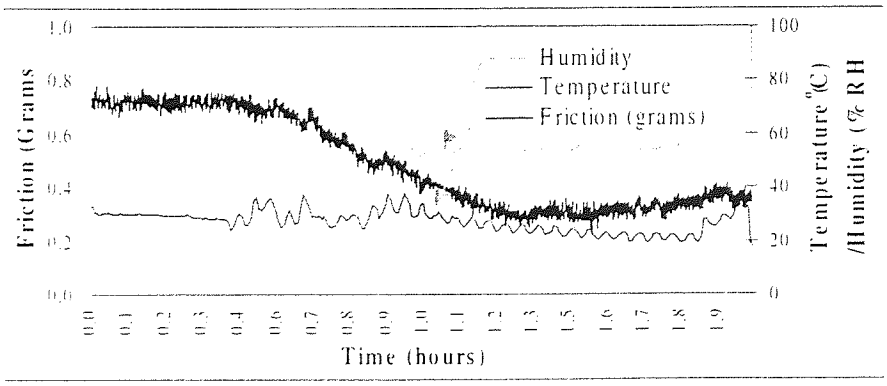

Figure 3.54 Drop in friction follows increase in humidity during drag test

Conversely, a decrease in humidity caused drag test friction to increase. During the last 2 hours of an 18 hour drag test in 40°C, humidity decreased from 70 to 30% RH.

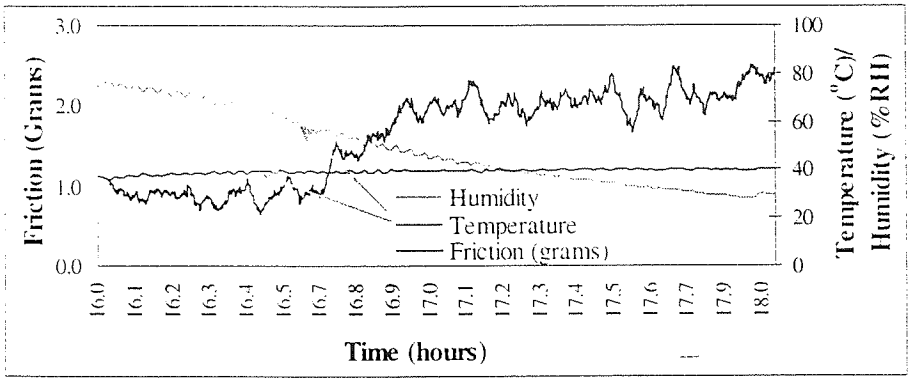

Figure 3.55 Rise in friction follows decrease in humidity during drag test

It could be said that humidity aided friction performance during drag testing. Water molecules between head and disk acted as an extra lubricant.

However, when changes in humidity occurred very suddenly, erratic friction behaviour followed, Figure 3.56 shows friction for a 40°C drag test where humidity was suddenly stepped up by 50 % RH.

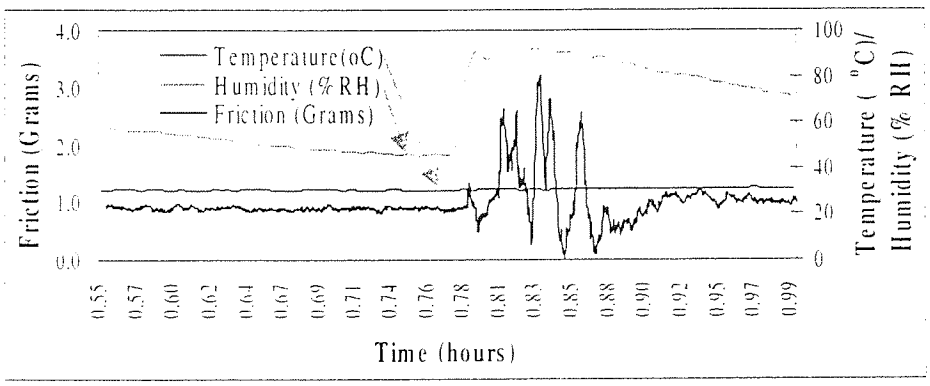

Figure 3.56 Erratic friction follows a sudden increase in humidity during drag test

It was thought that condensation could have occurred at the interface due to such a sharp rise in humidity.

3.1.11 Effect of Disk Texture on Drag Testing

3.1.11.1 Using Crosshatched Texture Disks

Using a NPAB slider, a 20 hour drag test was performed in ambient at disk data zone (35 mm from disk centre). 10 hours into the test the slider was raised and moved to a neighbouring track (33 mm from disk centre) and the test was re-started. Results were again scaled to remove the tangential component of friction.

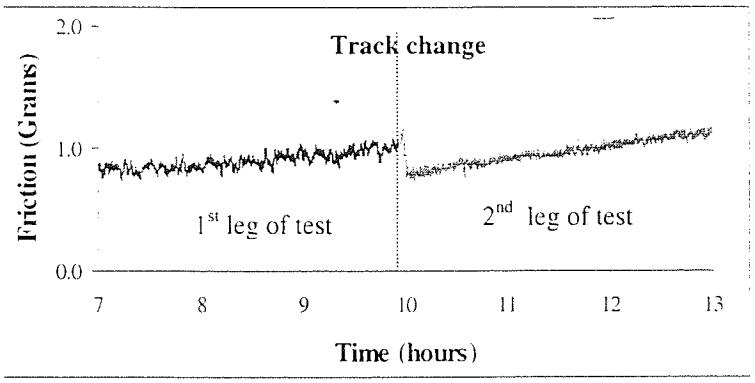

Figure 3.57 Friction results for track change drag experiment

Following the track change, a decrease in friction was observed, Figure 3.57. This again confirmed that smoothing of the disk rather than slider had occurred.

3.1.11.2 Using Graded Texture Disks

Using graded texture disks, the effect of different disk texture on friction was studied. NPAB sliders were used in 15 hour standard drag tests at the textured landing zone and smooth data zone of graded disks. Disk radii chosen for testing were 23 and 39 mm from disk centre and again results were scaled appropriately using Equation 3.1. Friction results are shown in Figure 3.58.

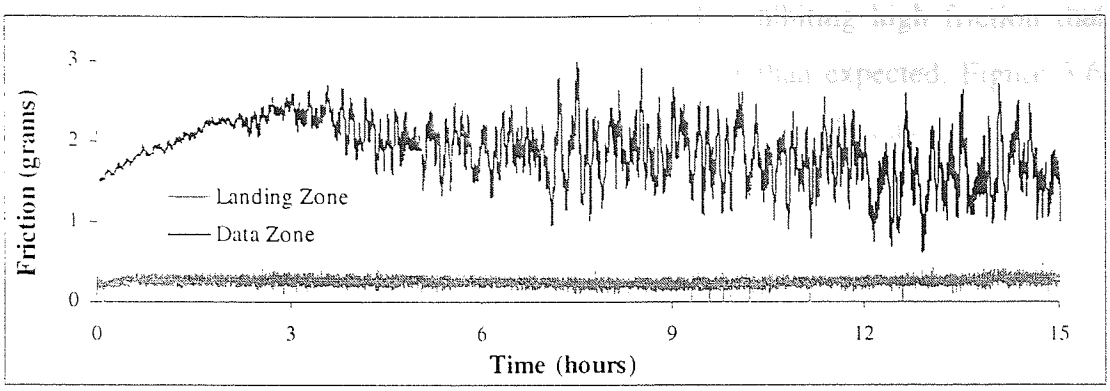

Figure 3.58 Drag test friction at landing/data zones

Differences in friction were given at landing and data zone, both in terms of the magnitude of friction and it's spread. Rougher disk texture gave lower, more constant friction values.

3.1.12 Drag Test Failure

To define failure, a modification of the failure criteria for drag tests as given in [38.53] was used. That is, a drag test was deemed a failure if either of the following events occurred :

- Increase in drag friction above 1 gram or
- The formation of an obvious disk wear track occurred during testing
- Coefficient of friction exceeding twice initial value
- Any sudden reduction in friction (>20%) after a maximum has been established

Failure was common in drag tests and of the 29 environmental drag tests performed only 11 were successful under these rules. Failed drag tests are illustrated in Figure 3.59.

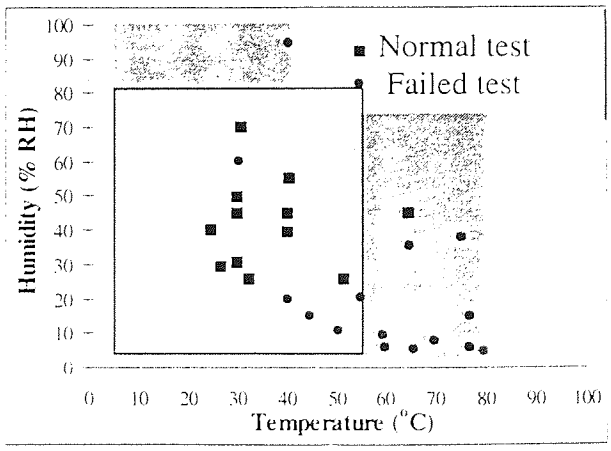

Figure 3.59 Environments in which failure occurred during 20 hour drag tests. Manufacturer expected operating conditions are bordered

All drag tests performed in hot/dry conditions failed, exhibiting high friction that rapidly increased to values almost an order of magnitude higher than expected. Figure 3.60 shows friction traces for some of the drag tests that failed in hot/dry conditions.

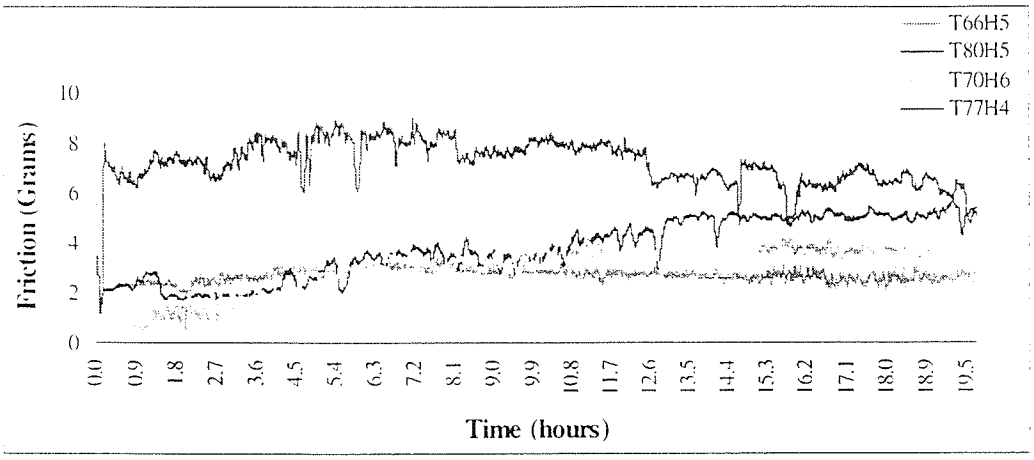

Figure 3.60 Friction over 20 hours for failed hot/dry drag tests

Drag testing ensured head/disk contacts were accelerated, this coupled with the long test duration rendered this test type very damaging to the interface. Even under cooler more humid conditions test failure could occur.

Figure 3.61 shows friction during the failed test T30H60C, note even though the environment was more humid the test displayed very high friction from the start. Friction decreased after 8 hours, but as given by Zhao and Bhushan [38] this can also be an indication of failure.

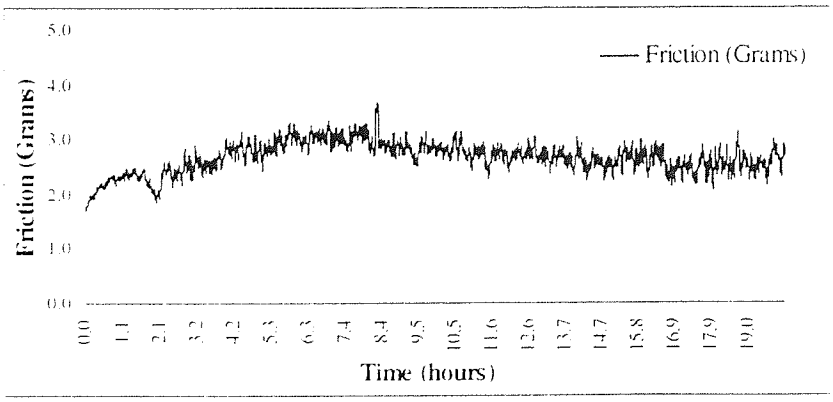

Figure 3.61 Friction during failed T30H60C drag test

3.2 Surface Analysis

To determine the effect of AFT testing on disks and sliders it was necessary to study the topography and chemical composition of virgin surfaces. Once this was ascertained analysis of tested sliders and disks (both CSS and Drag) was performed and comparisons drawn. The physical effects of testing in modified environments were also studied.

Separate investigations were carried out on failed sliders and disks. Analytical techniques identified the nature of damage to surfaces and in some instances indicated the probable cause of drive failure.

In this section, unless otherwise stated all AFM and XPS scans were processed using the methods outlined in Chapter 2, sections 2.3.2 and 2.1.2 respectively.

3.2.1 Virgin Surface Analysis

3.2.1.1 Disk Analysis

SEM Analysis

As previously mentioned SEM was not very useful for imaging disks unless particular features (such as wear tracks) were of interest. For completeness,
Figure 3.62 shows a SEM image of a virgin crosshatched disk.

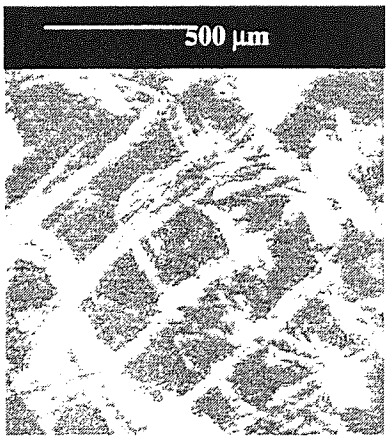

Figure 3.62 SEM image of virgin cross-hatched disk

AFM Analysis

Topographical disk scans were taken perpendicular to disk track direction (i.e. at 270°). Most detailed images were given using this scan direction, Figure 3.63 shows scans of same area of crosshatched disk scanned at 270° and 0°. In addition, scanning at 0° to tracks seemed to introduce noise.

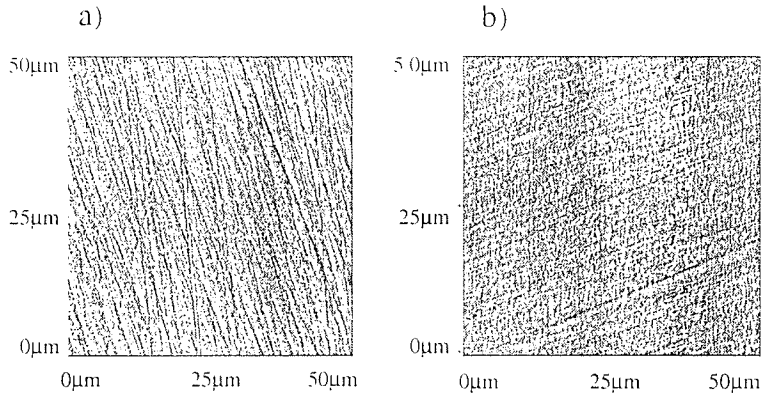

Figure 3.63 Cross-hatched disk scans taken at a) 270° and b) 0°

For the majority of experiments standard crosshatched texture disks were used, Figure 3.64 shows AFM scans at the inner and outer diameter of this disk type.

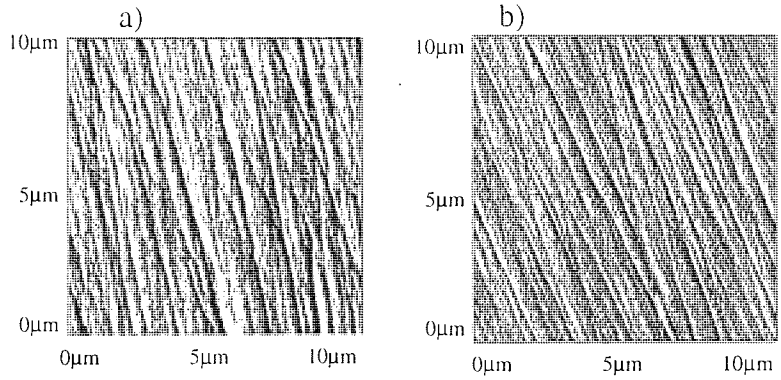

Figure 3.64 AFM disk scans taken at a) inner (20 mm from disk centre) and b) outer (46 mm from disk centre) diameter

When measuring surface roughness of disks, it was found that large area scans (e.g. 100 μm^2) gave least variation in results. Figure 3.65 shows the relative error in root-mean square roughness (R_{rms}) values taken at four distinct locations around disk circumference. Poon and Bhushan [130] also found that quantifying surfaces from small scans (< 80 μm^2) was unreliable. It has been suggested elsewhere that roughness could depend on scan size [130,135].

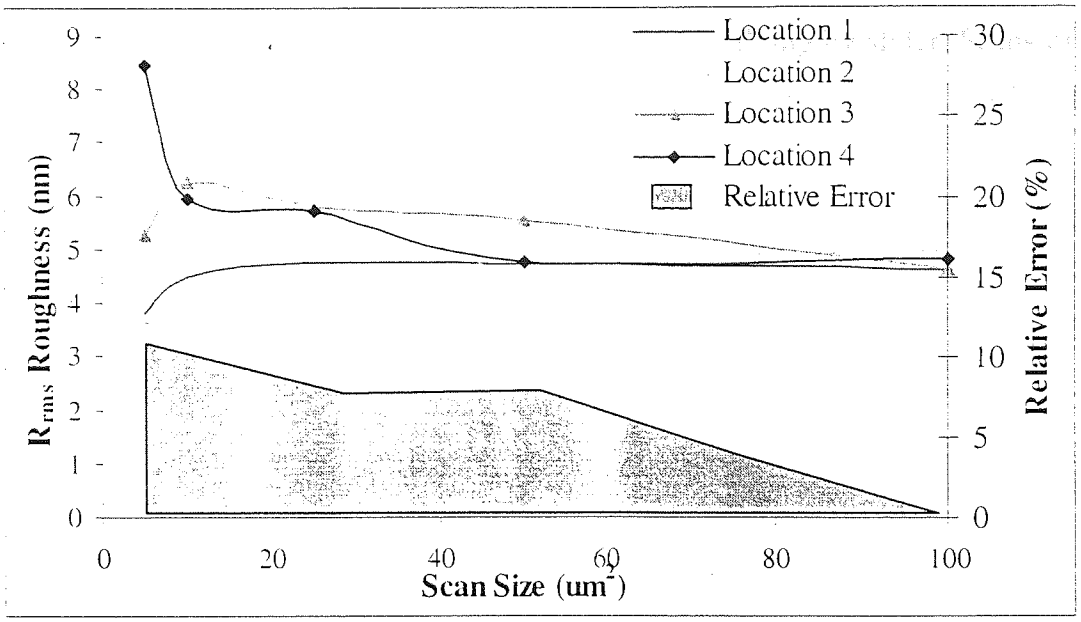

Figure 3.65 R_{rms} roughness values for different scan size at 4 disk locations

Note, $R_{rms} = \sqrt{\sum_i \frac{(h_i - \bar{h})^2}{N}}$ where h_i's are the scan heights and $\bar{h}$ their mean, N is the number of points in the scan. Relative error was defined as the difference between the mean R_{rms} at each scan size and the known roughness (R_{rms}=4.50 nm), divided by known roughness. In this work roughness values were taken from 100 μm^2 scans unless otherwise stated.

AFM analysis gave that disks had almost constant roughness from inner to outer diameter, inner, middle and outer values are given in Table 3.2. Note, middle diameter was taken as being 33 mm from disk centre.

Disk Region	R_a (nm)	R_{rms} (nm)	Height (nm)	Maximum P-V (nm)
Inner	4.33	5.31	21.33	36.56
Middle	4.38	5.84	19.86	38.51
Outer	4.56	5.85	21.41	32.52

Table 3.2 Crosshatched disk roughness parameters

Note, other standard values for measuring surface roughness are defined as average roughness (R_a) with $R_a = \frac{1}{N}\sum_i |\, h_i - \bar{h}\,|$, height is the average height in the scan and maximum P-V is the maximum range of heights in the scan.

Graded texture disks were also analysed using AFM, these disks are textured heavily at the landing zone and are less textured at data zone to allow low flying by slider. Scans of inner, middle and outer disk diameter are shown in Figure 3.66 with parameters given in Table 3.3.

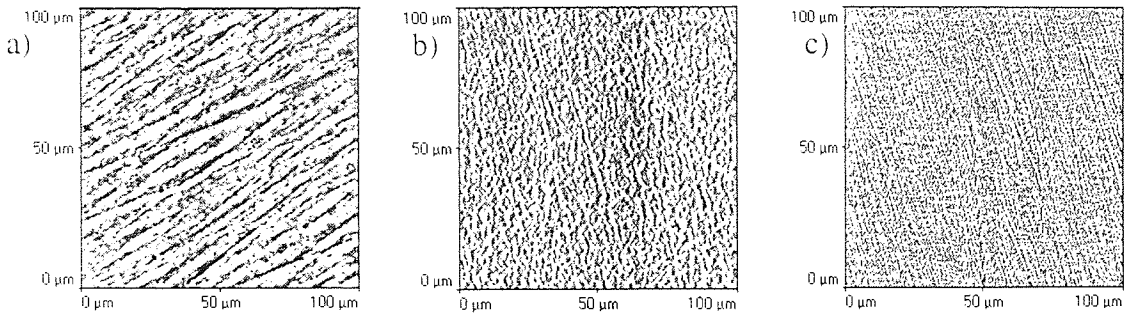

Figure 3.66 AFM scans taken at graded disk a) inner (20 mm from disk centre), b) mid (35 mm from disk centre) and c) outer (44 mm from disk centre) diameter

Disk Region	R_a (nm)	R_{rms} (nm)	Height (nm)	Maximum P-V (nm)
Inner	7.58	8.73	49.12	124.90
Middle	5.21	6.64	22.47	44.95
Outer	2.34	3.02	24.67	31.52

Table 3.3 Graded disk roughness parameters

A laser-textured disk was also analysed using AFM, this disk had been used in a real drive and was used for analysis only. Scans of laser-textured zone at inner and lightly textured zone at outer diameters are shown in Figure 3.67. Roughness values are given in Table 3.4.

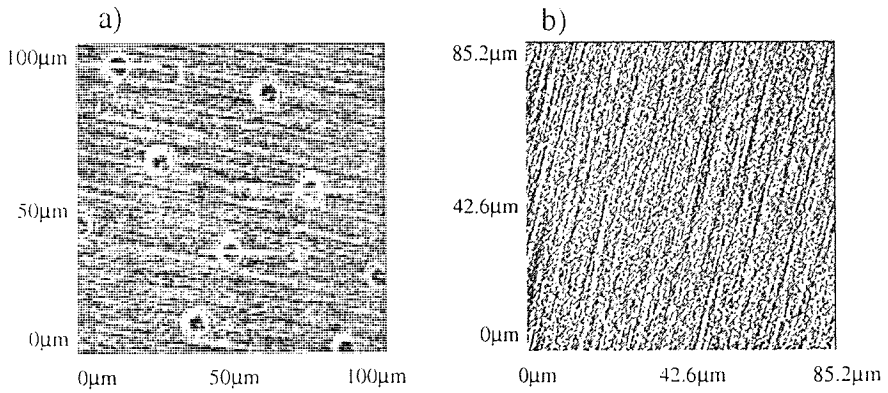

Figure 3.67 AFM scans taken at laser disk a) inner (22 mm from disk centre) and b) outer (45 mm from disk centre) diameter

Disk Region	R_a (nm)	R_{rms} (nm)	Height (nm)	Maximum P-V (nm)
Inner	18.73	23.96	72.01	160.44
Outer*	3.62	4.51	12.99	26.39

Table 3.4 Laser textured disk roughness parameters. *Outer disk surface parameters came from 85.2 μm^2 scan

The laser bumps were found to be the volcano type, three 25 μm line scans across bumps were taken (as shown in Figure 3.67a)), profiles given in Figure 3.68a). Bump recesses were approximately 80 nm below disk surface, with surrounding lip elevated by 80 nm. Fractal analysis was used to identify the highest points on a 50 μm^2 scan of bumps Figure 3.68b). Results confirmed that the highest points on the disk are the raised lips surrounding each bump, Figure 3.68c).

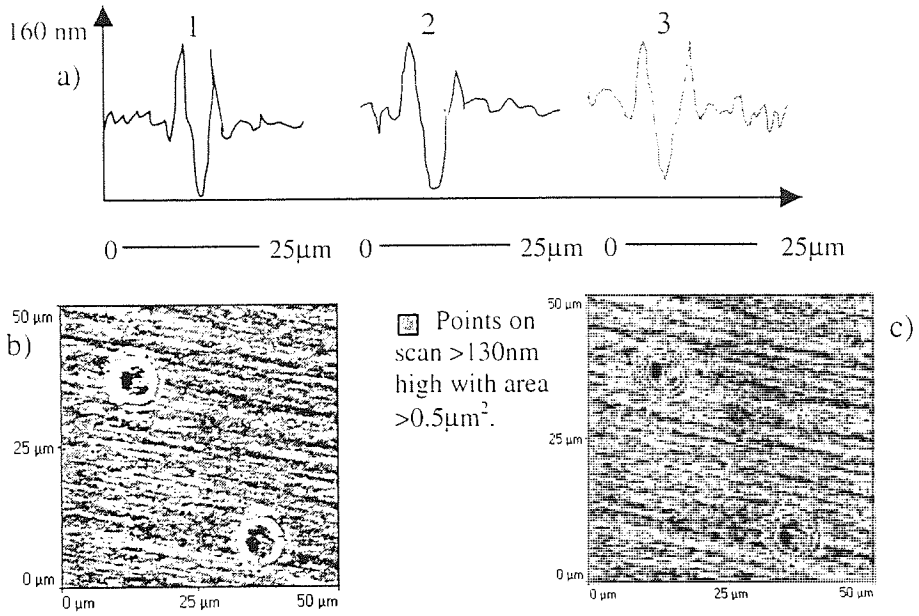

Figure 3.68 a) Line scans illustrating profile of laser bumps and b) Fractal analysis of laser bump scan

XPS Analysis

XPS wide scan analysis was performed on crosshatched and graded texture disk using 600 μm scan size. The presence of the following elements was indicated, Table 3.5, with relative atomic percentages shown.

Element	Atomic Percentage (%)	
	Crosshatched disk	Graded disk
Carbon	52.22	54.32
Oxygen	29.29	23.54
Nitrogen	Not detected	6.25
Fluorine*	18.49	15.89

Table 3.5 XPS Quantification table for virgin disks. *Note Fluorine was collected by separate scans at start of experiments. See section 2.2.1.

For disks, the source of carbon was both the protective disk overcoat and environmental contamination. Oxygen also came from the environment and fluorine from topically applied disk lubricant. Nitrogen was detected on the graded disk sample only, this disk had nitrogenated carbon overcoat.

3.2.1.2 Slider Analysis

SEM Analysis

Photographs of NPAB and tri-pad sliders are shown in Chapter 2 - Figure 2.18. Read/write elements were imaged using backscatter mode SEM, these are shown in Figure 3.69.

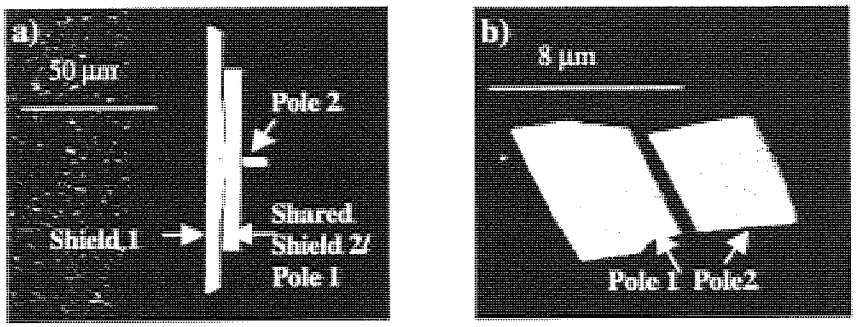

Figure 3.69 Backscattered SEM images of a) NPAB and b) tri-pad read/write elements

The NPAB read/write element consisted of poles between which an inductive write signal could be generated and shields that protect the reading MR element, notice that a merged pole/shield exists. The NPAB has two sets of read/write elements - one on the trailing edge of each slider rail. The tri-pad has a single pair of inductive read/write poles only, these are situated on the contact pad at slider's trailing edge.

Further analysis of entire slider body was performed using secondary mode SEM to give more detail on slider designs and their virgin state. Figure 3.70 illustrates that prior to testing sliders were free from debris and/or staining.

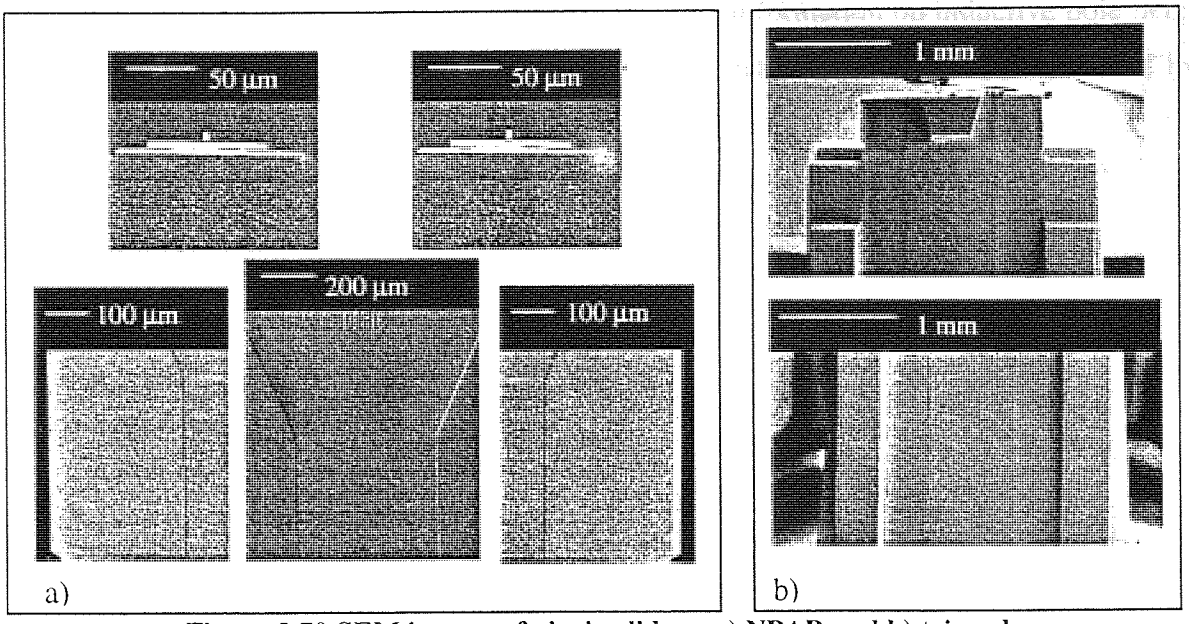

Figure 3.70 SEM images of virgin sliders, a) NPAB and b) tri-pad

AFM Analysis

AFM was used to provide information on the topography of read/write elements, it was found that scanning perpendicular to the pole length (270°) gave most detailed images. Figure 3.71 shows scans of size 24 μm^2 and 15 μm^2 for NPAB and tri-pad respectively.

Of particular interest was the height of read/write elements above surrounding material, since this could be used to categorise severity of slider wear and would have direct effect on signal performance in a real drive. It has been reported that most wear occurs at the extreme trailing edge of slider, since this part of slider would be in closest proximity with the disk during flying. Thus, the difference in height between pole 2 and trailing edge alumina was taken as an indicator of pole wear.

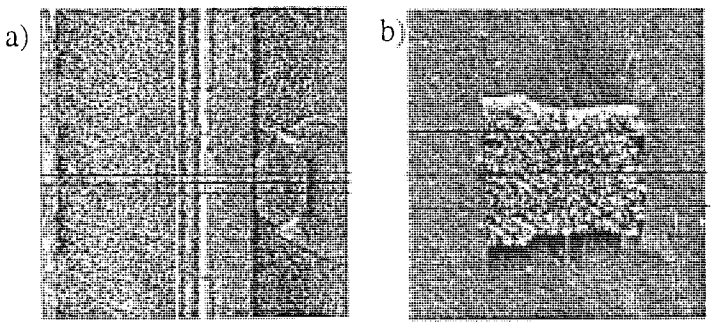

Figure 3.71 AFM scans of a) NPAB and b) tri-pad read/write elements

AFM software supported line analysis, which could give information on inductive pole height above surrounding alumina over a line of any chosen length/orientation. The results of line scans taken at the positions marked in Figure 3.71 are shown in Figure 3.72 below (Line scans were numbered from top to bottom). Notice that the position of the line greatly affected height reading given. Values are given in Table 3.6 together with maximum relative error over the 3 line scans. In fact, for tri-pad slider pole 2 was not significantly higher than contact pad.

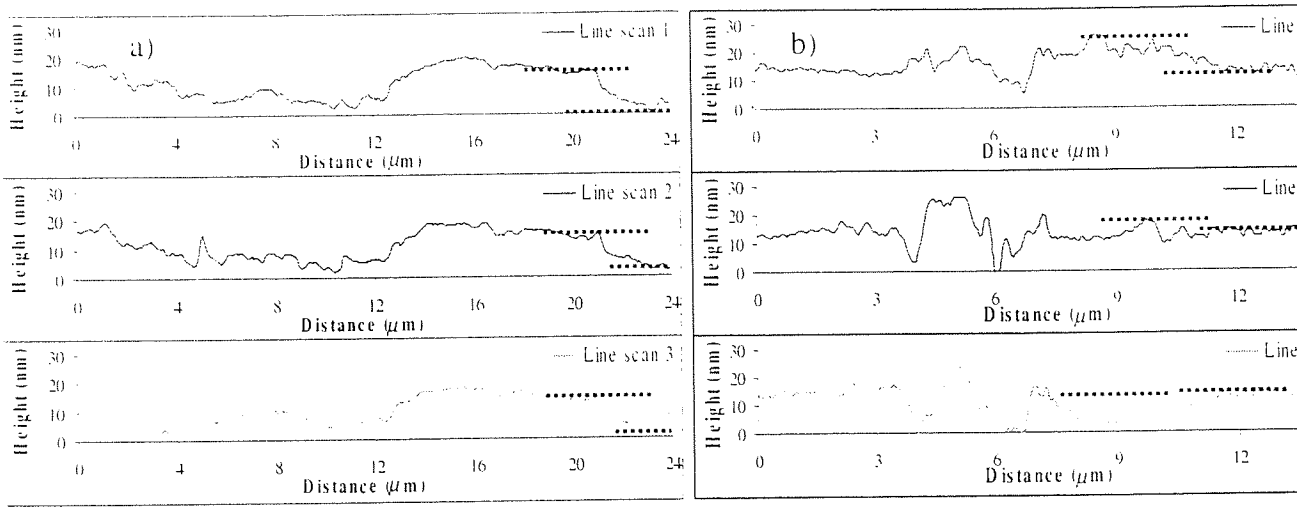

Figure 3.72 Line scan results for a) NPAB and b) tri-pad sliders

Virgin Pole Heights (nm)	Relative pole height (pole 2 - alumina)	
	NPAB	Tri-pad
Line scan 1	11.57	14.83
Line scan 2	8.81	2.90
Line scan 3	8.92	-2.01
Mean Height	9.77	5.24
Relative Error (%)	31.32	837.81

Table 3.6 Virgin pole heights using standard AFM line scans

Since relative error between adjacent line scans could be large, a new model will be proposed in Section 4.4.1.2, which offers improved accuracy in line analysis of read/write elements.

Investigation into the surface roughness of the slider air bearing rails and the contact pad (for tri-pad) showed that these slider surfaces were considerably smoother than the disks. Differences in roughness along the length of slider rails were found to be negligible, the scans presented were taken at approximately mid-rail length, i.e. halfway between trailing and leading edges. NPAB slider cavity region was found to be highly textured, as was tri-pad AB region between slider rails. AFM scans shown in Figure 3.74 with values given in Table 3.7. Note, the terms inner/outer were used to distinguish between slider rails and defines them with respect to normal slider flying position. An illustration given for tri-pad in Figure 3.73.

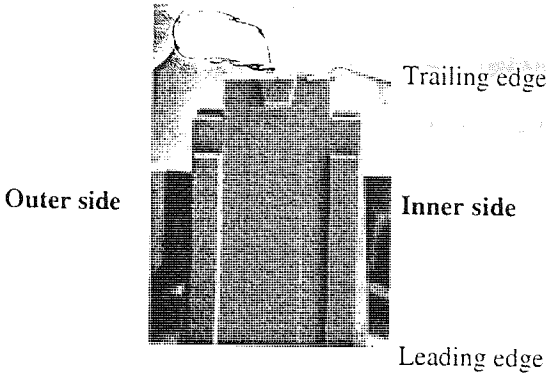

Figure 3.73 Defining slider referencing method

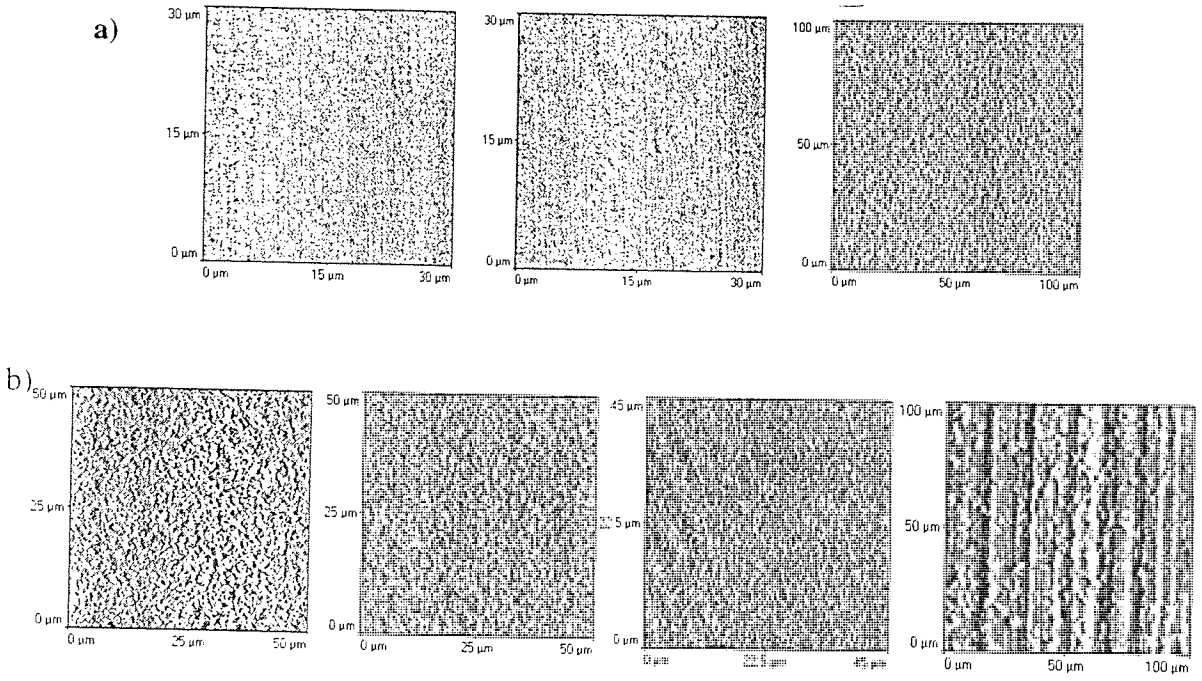

Figure 3.74 AFM scans of slider body, a) NPAB from left to right (i) inner rail, (ii) outer rail and cavity recess and b) tri-pad from left to right (i) inner rail, (ii) outer rail, (iii) contact pad and (iv) AB region

Slider Type		R_a (nm)	R_{rms} (nm)	Height (nm)	Maximum P-V (nm)
NPAB	Inner Rail	2.25	3.21	9.48	26.46
	Outer Rail	2.07	2.95	9.56	25.85
	Recess Cavity	59.71	73.68	188.27	393.07
Tri-pad	Inner Rail	1.72	2.17	6.83	12.62
	Outer Rail	1.84	2.65	6.95	14.25
	Contact Pad	2.13	2.70	9.05	16.79
	AB region	9.80	12.44	29.08	58.86

Table 3.7 Virgin slider surface parameters

XPS Analysis

XPS wide scan analysis was performed on both slider types using 150 μm scan size to determine slider composition. Areas scanned were the extreme trailing edges of the outer slider rail for NPAB and contact pad for tri-pad. The presence of the following elements was detected, Table 3.8, with relative atomic percentages shown.

Element	Atomic Percentage (%)		
	NPAB		Tri-pad
	Original Unetched	Etched	
Oxygen	7.62	28.98	31.23
Titanium	Not detected	4.554	1.936
Carbon	88.81	31.84	34.94
Aluminium	3.56	34.61	31.89

Table 3.8 XPS Quantification table for virgin sliders

Notice, for the NPAB carbon was mainly detected, this was due to NPAB having a sputtered carbon overcoat for wear protection. Etching the sample for 30 minutes with energetic Ar ions removed this (approximately 18 nm thickness was etched away). Both sliders were confirmed to be fabricated from Al_2O_3-TiC.

3.2.2 Ambient CSS Tests Surface Analysis

Disks and sliders that had experienced 7K CSS cycles were examined to determine the effect of testing. In this section, only surfaces which had not experienced failure during tests (defined by failure criteria Section 3.1.7) were analysed.

Disks usually exhibited a light wear track - consisting of one ring for each slider rail (plus one for the contact pad in the case of a tri-pad slider). These wear rings were only visible under very bright light or, if more subtle, by passing the disk under humid air whereby the track became visible momentarily (known as haze testing). This technique is documented elsewhere [116,143]. Due to their shallow nature it was impossible to measure the depth of these tracks using Talysurf profiling.

3.2.2.1 Disk Analysis

AFM Analysis

Locating the track area for AFM analysis proved problematic, since the area of the disk was very large compared to the width of these wear tracks. Scratches were made either side of the track following haze testing and these were used as guides for scanning. Since the maximum AFM scan was only 100 μm^2 only small sections of the wear tracks could be imaged at any time.

A scan was taken inside one of the slider rings on a crosshatched disk, Figure 3.75a). This disk had been run in conjunction with a NPAB slider. Original disk texture had been flattened slightly and clusters of debris particles were evident. A scan to the outer diameter of the same disk revealed many small debris particles, even thought the slider had never flown over this area, Figure 3.75 b). No such particles were seen to inner diameter of wear track. This suggested that during AFT operation small particles of debris could be carried outwards by centrifugal force and deposited on other areas of disk.

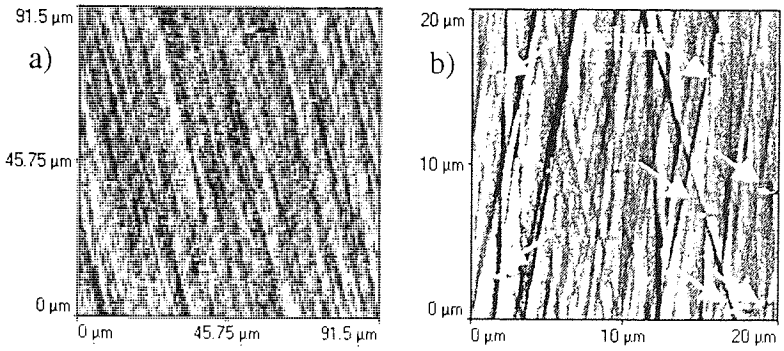

Figure 3.75 a) Large AFM scan in wear track and b) smaller scan outside wear track - arrows indicate small debris particles

The wear track was slightly smoother than surrounding disk but had higher average height - this suggested material had been deposited upon it by slider. The region of disk outside the wear track had become marginally rougher than a virgin disk and had higher maximum P-V value due to transported debris. Table 3.9 shows AFM scan values.

Disk Region	R_a (nm)	R_{rms} (nm)	Height (nm)	Maximum P-V (nm)
Wear track	3.61	4.49	26.14	58.53
Outside wear track	3.95	4.71	23.78	51.84

Table 3.9 Ambient 7KCSS tested crosshatched disk wear track roughness parameters. Wear track surface parameters came from 91.5 μm^2 scan

Further analysis of the small transported debris showed that it was mainly spherical, suggesting it could have been formed by rolling action between disk and slider. When scanning in contact mode debris appeared slightly mobile and could be displaced by AFM scanning tip, this implied the particles could have composed of disk lubricant, transferred to slider and then back to disk. Typical debris diameter was <0.5 μm, with height ranging from 10-30 nm, note this height agrees with the increase in maximum P-V value observed above.

Scoring was often noticed on tested disks, barely visible on topography scans scores could be identified using lateral force mode AFM. Figure 3.76 shows 0° AFM topography and lateral force scans of disk score. Score depth was around 6 nm, lateral force shows higher friction is associated with scored region (lighter shade). Notice lateral force scan also identifies disk tracks, a vertical line scan taken down centre of Figure 3.76b) gives track width as 10 μm which would indicate track density of around 2540 per inch for this disk type.

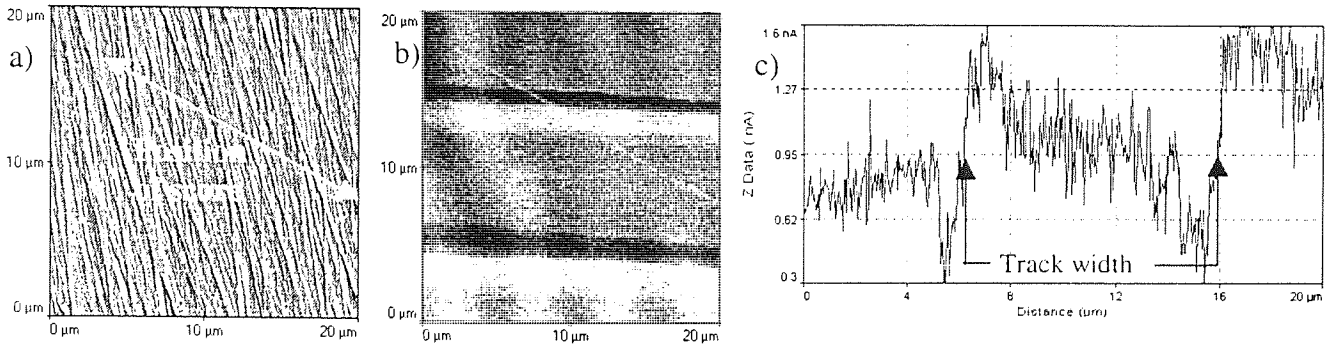

Figure 3.76 7K CSS disk a) topography scan and b) lateral force scan and c) vertical line scan of lateral force

A used graded texture disk was analysed in the wear track region, this disk also had been tested with a NPAB slider, Figure 3.77. Roughness values are given in Table 3.10.

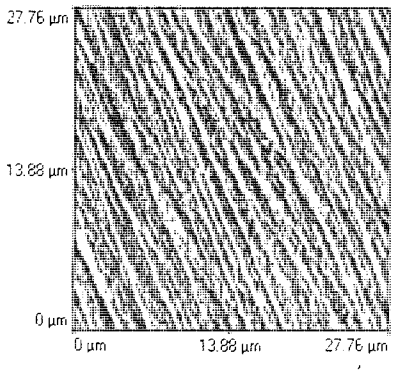

Figure 3.77 AFM scan of wear track on graded disk

Disk Region	R_a (nm)	R_{rms} (nm)	Height (nm)	Maximum P-V (nm)
Wear track	7.22	9.49	46.17	117.81
Outside wear track	9.17	11.65	50.22	104.90

Table 3.10 Ambient 7KCSS tested graded disk wear track roughness parameters

Again the disk had been smoothed in the wear track region, with the surrounding area remaining virtually unaltered.

XPS analysis

XPS analysis was carried out on disk wear tracks, quantification given in Table 3.11. No extra elements appeared in the table where the NPAB slider was concerned, confirming that slider material was not transferred to disk during normal testing. However, disks used with the tri-pad slider had aluminium present in the wear track, since magnetic layer elements were not detected it was assumed that the source of this was slider material and not disk substrate.

Element	Atomic Percentage (%)		
	Crosshatched disk		Graded disk (NPAB only)
	with NPAB	with Tri-pad	
Carbon	75.39	66.25	62.20
Oxygen	17.29	21.54	23.04
Nitrogen	None	None	5.46
Fluorine*	7.32	11.27	9.29
Aluminium	None	0.94	None

Table 3.11 XPS Quantification table for Ambient 7K CSS disks. *Note again fluorine was collected by separated scans at start of experiments. See section 2.2.1

3.2.2.2 Slider Analysis

SEM analysis

SEM analysis of tested sliders showed that read/write elements had collected some small debris particles following a standard test. Larger debris was concentrated around the slider's leading edge and usually took the form of light coloured streaks in the direction of slider travel. Note, the tapered leading edge of a slider rail will now be termed the chamfer as labelled.

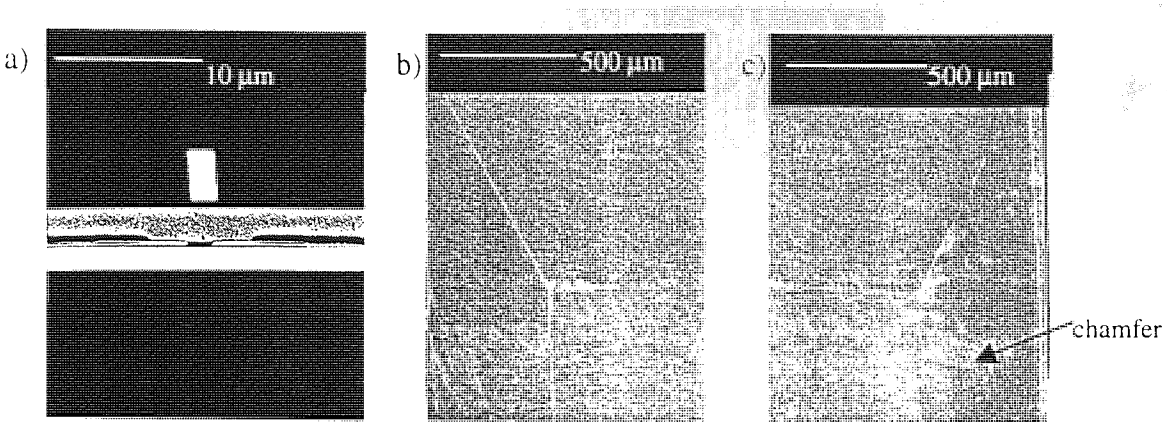

Figure 3.78 Ambient 7K CSS tested NPAB slider a) outer rail read/write element and b) outer and c) inner leading edge

AFM Analysis

When examining NPAB read/write elements using AFM, large amounts of debris were observed on element poles and shields, Figure 3.79 shows the outer rail elements on a slider used with crosshatched disk. Debris was usually greatest on outer rail element, actually appearing in read-gap area. Slight cracking was also observed around inductive element. In addition, poles and shields appear to have been recessed, this will be investigated in Section 4.4.1.2 .

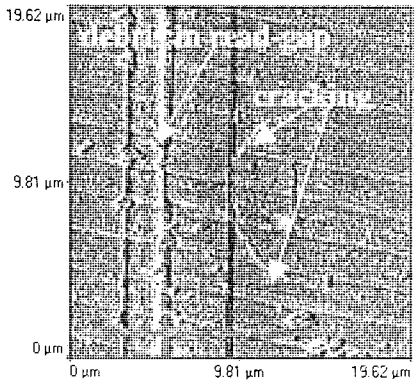

Figure 3.79 Outer read/write elements on ambient 7K CSS NPAB

After testing, the slider rail was no longer equal in terms of roughness, with trailing edge being smoother with lower P-V suggesting burnishing had taken place there (with R_{rms}=2.41 nm and P-V=18 nm). At the leading edge, slider rail was much rougher containing debris. The worst site for debris was found to be the chamfer (with R_{rms}=10.65 nm and P-V=341.56 nm).

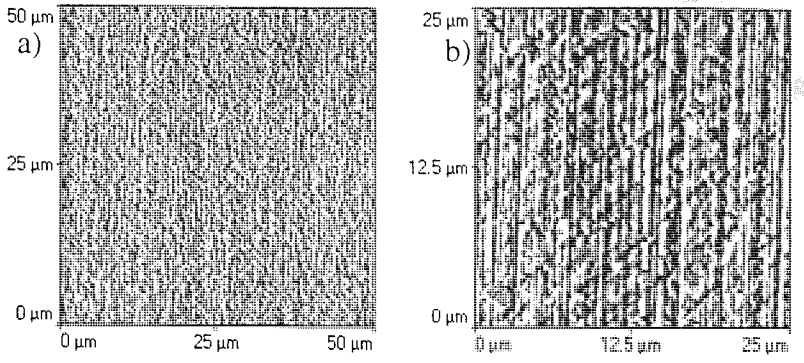

Figure 3.80 NPAB outer rail scans at a) trailing edge and b) leading edge

For tri-pad slider CSS testing had serious implications for the read/write element, with wear being severe. Usually, it was impossible to obtain an image of element on a used slider following 7K cycles.

Figure 3.81a) shows a large scan of a 7K CSS tri-pad slider contact pad (including read/write element position marked), the element is not visible under mass of debris. Figure 3.81b) and c) show element is still visible after 1K CSS and 100 CSS respectively.

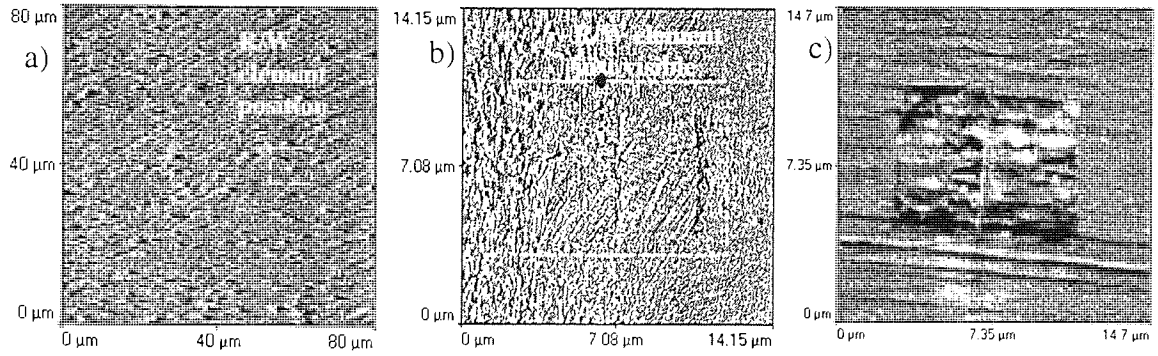

Figure 3.81 Scan of ambient a) 7K CSS and b) 1K CSS and c) 100 CSS tri-pad contact pad

Again the worst site for debris was slider chamfers, with the outer rail revealing most debris, Figure 3.82

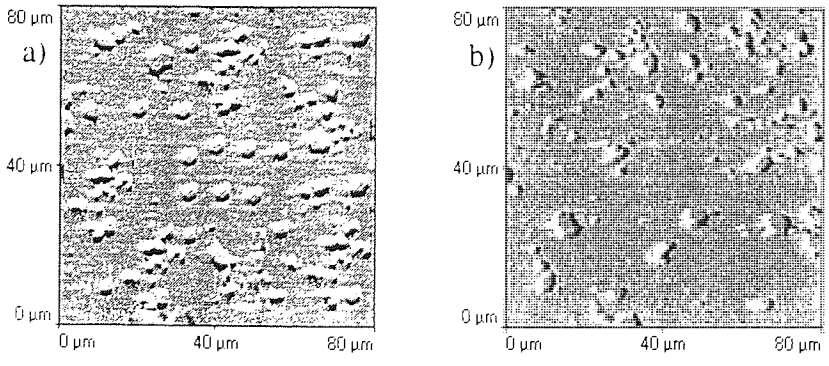

Figure 3.82 Tri-pad leading edge chamfer scans of a) outer and b) inner rail

During all scanning of sliders debris was found to be soft and mobile, again suggesting it was composed of disk lubricant.

XPS analysis

XPS analysis detected fluorine on trailing and leading edges of both slider types, this was likely disk lubricant, transferred to slider during contacts.

Element	Atomic Percentage (%)			
	NPAB		Tri-pad	
	Trailing Edge	Leading Edge	Contact Pad	Leading Edge
Oxygen	4.88	13.16	35.79	19.87
Titanium	None	None	2.27	1.48
Carbon	91.95	73.49	30.77	59.00
Silicon	2.74	6.97	None	None
Aluminium	None	1.90	19.41	17.92
Fluorine	0.432	4.47	11.42	1.71

Table 3.12 XPS Quantification table for 7K CSS tested sliders

Notice, for NPAB lubricant transfer was greater on leading edge of slider, this was most likely transferred during parking. Lubricant transfer was greatest on tri-pad contact pad, this was likely due to the close proximity of contact pad to disk during flying period.

3.2.3 Modified Environment CSS Tests Surface Analysis

Surface analysis was carried out for the environmental CSS tests. The 1 rpm tested surfaces were not analysed since normal flying did not occur during these tests.

For the majority of tests, surfaces were similar to those of ambient tests. Specific tests which caused surface topography to differ from that expected will now be discussed with tests grouped by environment.

3.2.3.1 Ambient Temperature/Low Humidity Tests

Following an ambient/dry test little disk damage was observed making the track difficult to locate using AFM. Damage was in the form of smoothing of track or slight scoring. Figure 3.83a) shows a large scan of T25H30 disk wear track and Figure 3.83b) and c) shows a small 0° scan of a T30H20 wear track and corresponding lateral force scan.

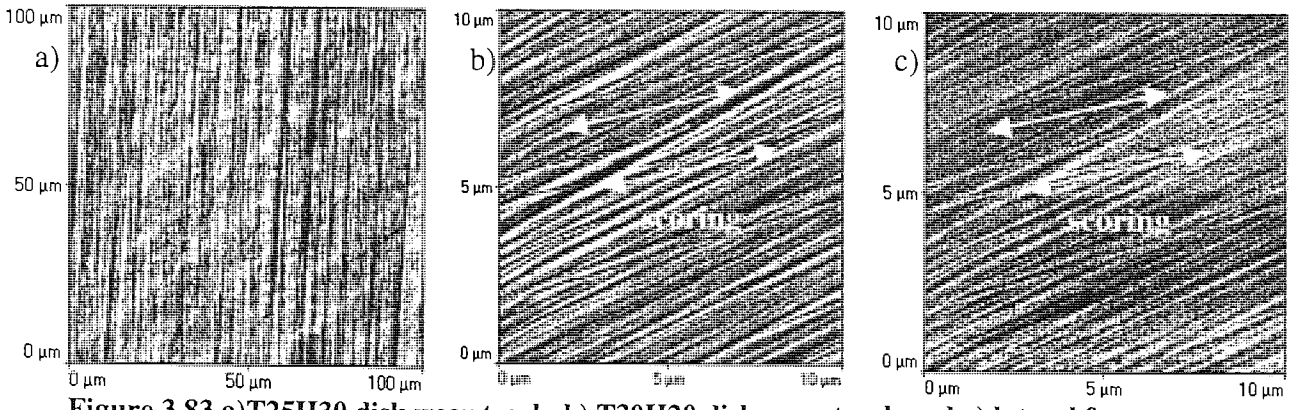

Figure 3.83 a)T25H30 disk wear track, b) T30H20 disk wear track and c) lateral force scan corresponding to b)

For the T25H30 test, disk wear track was slightly smoother than surrounding disk (R_a=3.78 nm and R_{rms}=4.41 nm) with lower mean height of 21.01 nm and maximum P-V of 31.51 nm. T30H20 disk displayed scores in direction of slider travel (up to 60 nm deep) as marked on scan, note scores also showed as lines of high friction on lateral force scan, Figure 3.83c).

Least slider body damage seemed to occur under ambient/dry conditions, SEM analysis of low humidity test NPAB (T30H20) is given in Figure 3.84a). Although no debris was observed around read/write elements a light coloured build up was observed at the trailing edge side of shared pole/shield, Figure 3.84b). This build up was common among tests performed under low humidity.

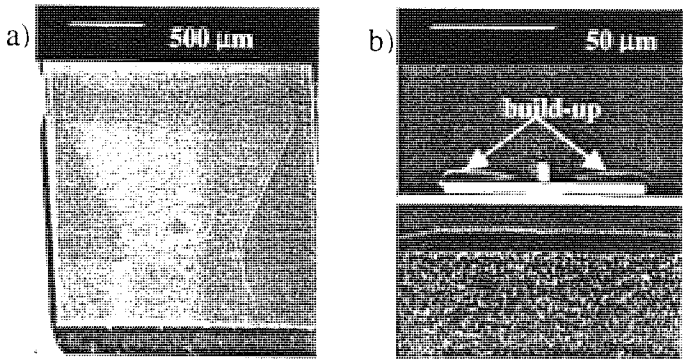

Figure 3.84 SEM of T30H20 NPAB a) slider body and b) outer rail read/write elements

AFM scans of outer/inner rail chamfer are shown in Figure 3.85a), surfaces were smoother than before (with R_a=1.19, R_{rms}=1.57), but P-V was greater at 75.32 nm which could indicate that debris had accumulated.

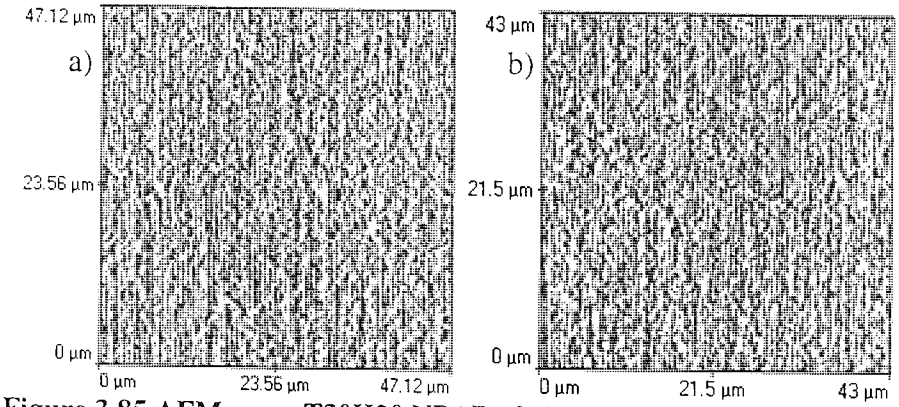

Figure 3.85 AFM scans T30H20 NPAB of a) outer and b) inner chamfer

AFM scans of outer and inner rail read/write elements are shown in Figure 3.86 a) and b), notice poles were almost obscured by stain. When scanning it was noticed that stain was not mobile, nor displaced by scanning tip. Stain height above alumina was given by line analysis as 30 nm, stain was found to be smoother than surrounding material by around 3 nm R_{rms}.

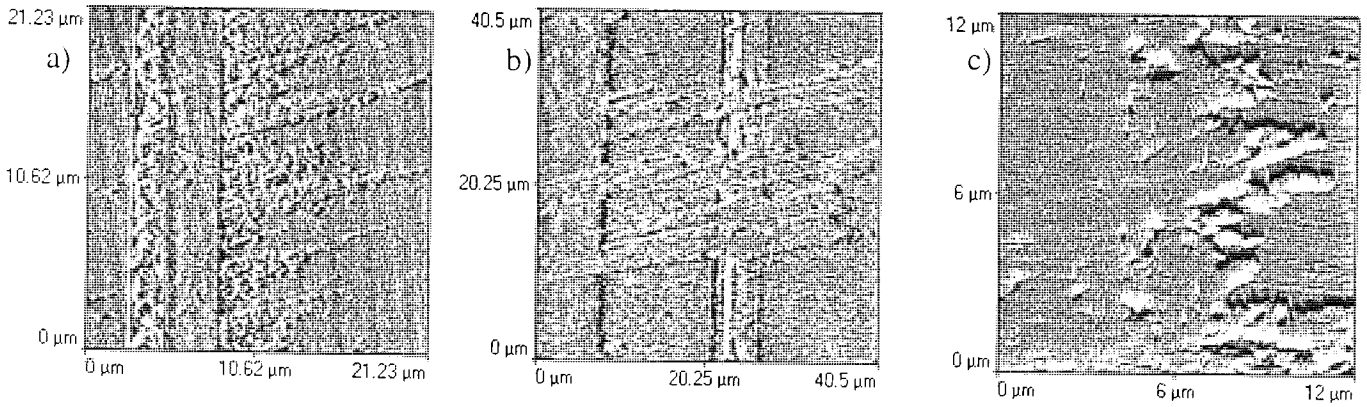

Figure 3.86 AFM Scan of T30H20 NPAB read/write elements a) outer, b) inner and c) zoom in on stain on inner element

For the T40H10 test, stain completely obscured read/write elements, unshaded AFM image shown in Figure 3.87. Again stain height was found to be around 30 nm.

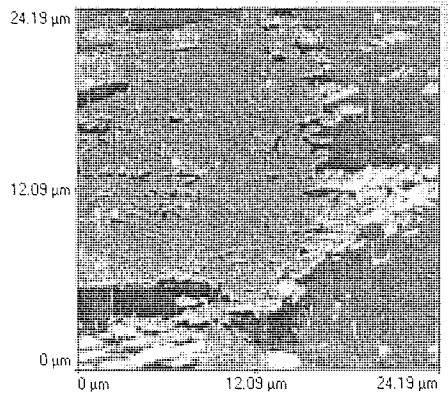

Figure 3.87 AFM image of stain on T40H10 NPAB

XPS results for slider leading edge and disk were similar to those for ambient tested surfaces. Trailing edge stain was composed of carbon and fluorine from disk/slider overcoat and lubricant.

3.2.3.2 High Temperature/Low Humidity

Following the T60H10 test, the boundary between the disk wear track and off-track region was identified using AFM, Figure 3.88. This wear track was more severe than previously seen, with line scans across track indicating grooving of 400-500 nm maximum P-V.

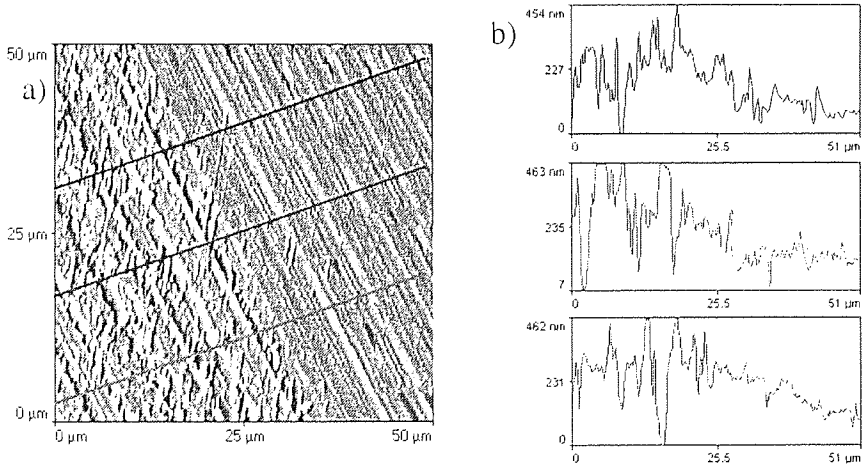

Figure 3.88 a) Boundary between track and off-track region on used graded texture disk and b) corresponding line analysis

Stain frequently occurred over read/write elements following hot/dry tests, Figure 3.89 a) illustrates staining on NPAB from T50H10. Once more this stain was found to be around 30 nm high. Another common feature was grooving over elements, NPAB from T60H10 is shown in Figure 3.89 b). This grooving was mostly found to be in the direction of slider travel with depth of up to 200 nm. Possible cause of grooving could be a hard wear particle impacted in disk surface.

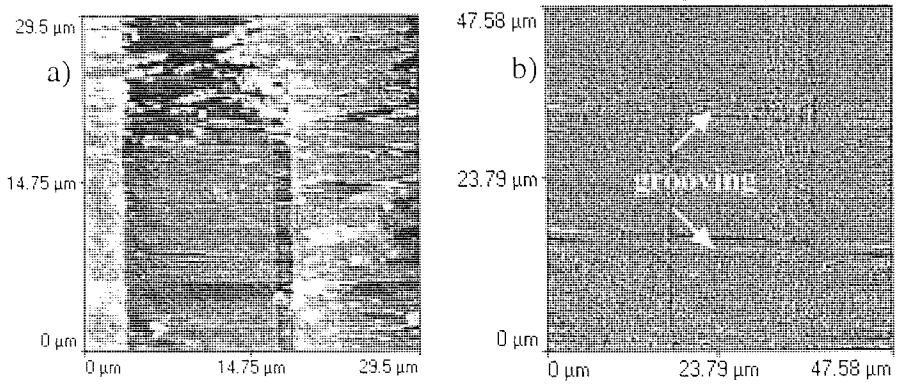

Figure 3.89 AFM of a) T50H10 outer read/write element, b) T60H10 inner read/write element

Testing at extremely high temperatures often caused the formation of large circular features on disk and slider. Examples from T77H10 test is illustrated, with disk scan shown in Figure 3.90 a) (scan was taken at 0°).

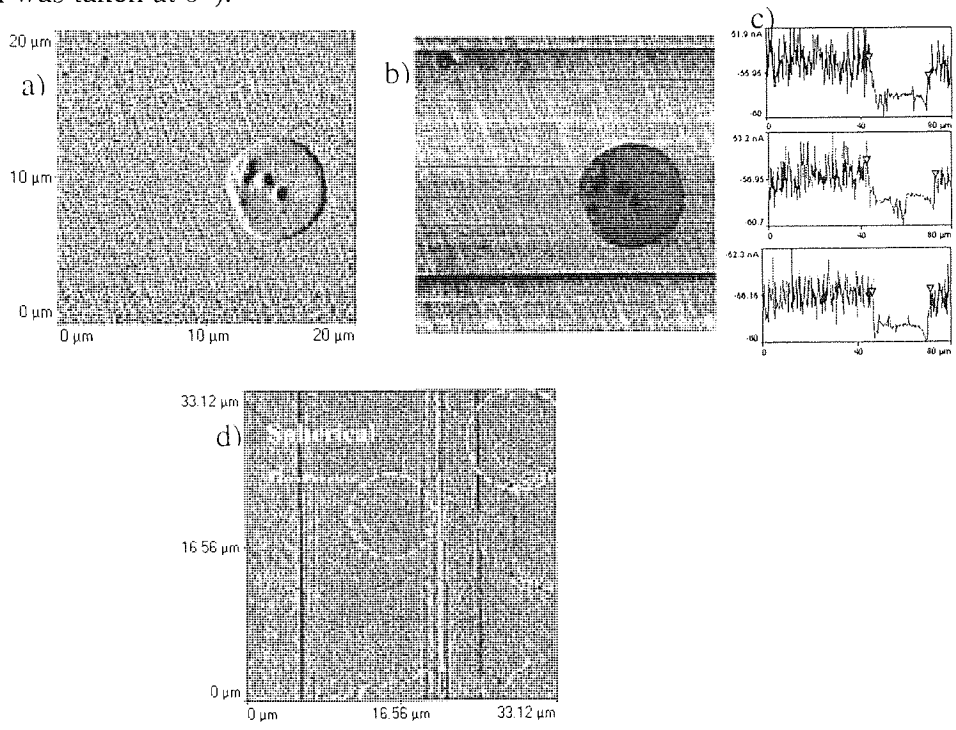

Figure 3.90 Scan of T77H10 disk circular feature a) topography, b) lateral force, c) line scan of lateral force and d) similar features observed on slider

The feature had maximum height 75.35 nm. Corresponding lateral force image shown in Figure 3.90 b) suggests this feature has lower friction associated with it than surrounding region - line scans shown in Figure 3.90 c). This implied the feature could be composed of disk lubricant. Figure 3.90 d) shows a topography scan corresponding to the slider, notice similar spherical shapes just visible on the trailing edge, these were measured as 14 nm high with diameter 5-7 nm.

XPS results were again similar to ambient tests for sliders. For disks, chromium was often detected in wear track region (0.1-0.4 %), this was thought to come from the disk magnetic layer indicating wear of the carbon overcoat.

3.2.3.3 High Temperature/High Humidity Tests

Following the T50H60 test, the disk was found to have a wear track comprised of many debris particles distributed evenly around the disk circumference. Figure 3.91 a) shows an AFM scan in the wear track region. The disk track was rougher than the surrounding disk due to the presence of these particles (R_a=6.78 nm and R_{rms}=8.31 nm). Fractal analysis was performed on this scan and all points between 52-58 nm were identified. Thus, it can be said that most debris particles were in this height range Figure 3.91 b).

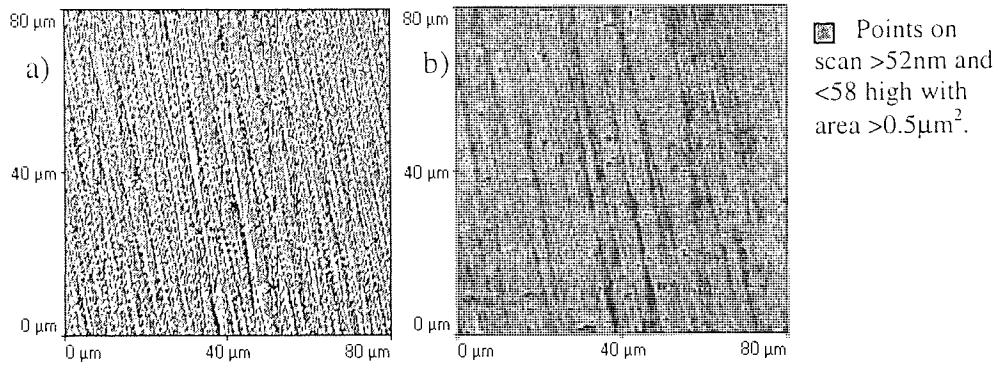

Figure 3.91 a) Disk damage following T50H60 test and b) fractal analysis

The T50H50 disk displayed similar particles in the wear track Figure 3.92 shows a topography (scan direction 0°) and lateral force in the track. Note debris particles were lighter in shade on the lateral force scan, indicating they had different friction associated with them than surrounding area.

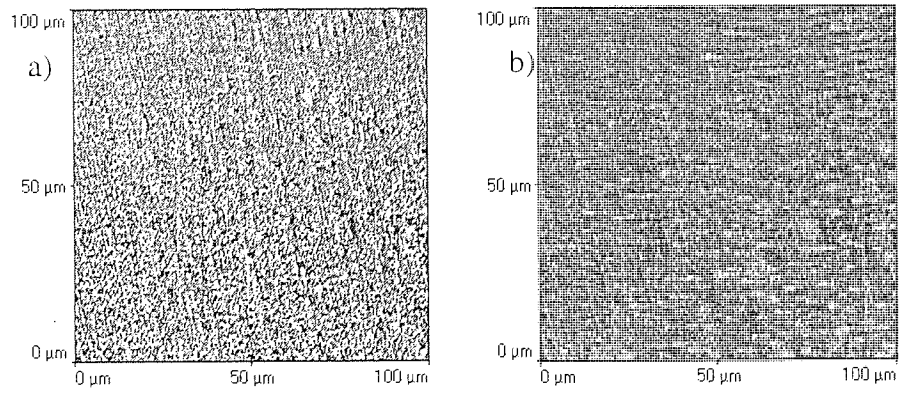

Figure 3.92 T50H50 Disk wear track a) topography and b) lateral force scans

The T50H60 NPAB slider's read/write elements showed some damage in the form of spherical debris particles and scoring over the poles/shields. Slider leading edge surface displayed a lot of damage. In fact, all of the sliders that had experienced hot/humid conditions displayed severe debris over their leading edges. SEM images shown Figure 3.93.

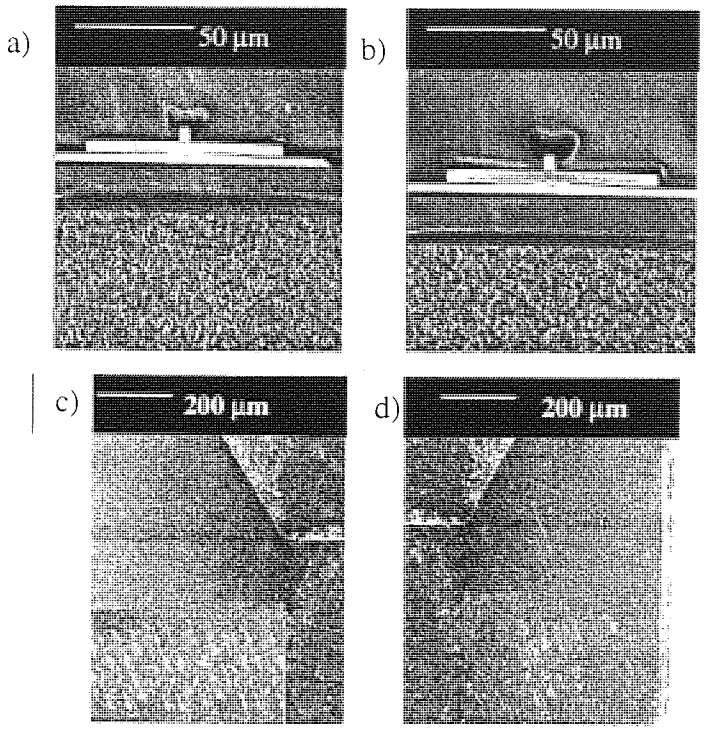

Figure 3.93 SEM of T50H60 NPAB a) outer, b) inner read/write elements, c) outer and d) inner leading edge chamfers.

AFM analysis of the above slider's inner chamfer only was possible as debris on outer rail was too high for scanning, Figure 3.94. This debris greatly increased surface roughness (R_a=291.54 nm, R_{rms}=345.21 nm) with maximum P-V 1129.22 nm.

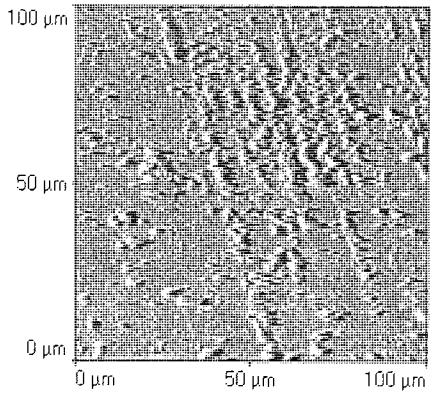

Figure 3.94 Scan of T50H60 NPAB inner chamfer

The outer read/write element and chamfers of a slightly less damaged slider, from test T45H65 were analysed, AFM images shown Figure 3.95.

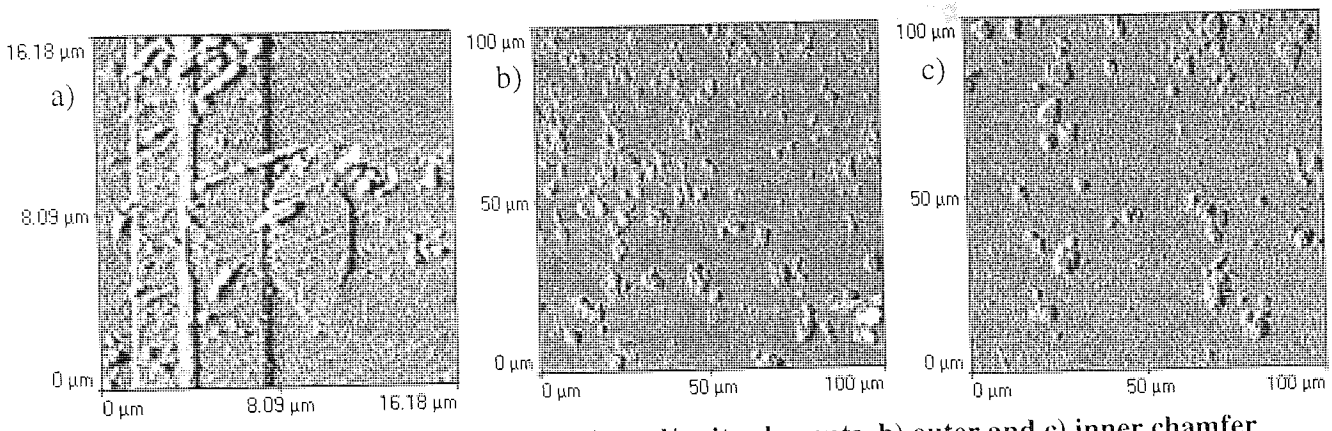

Figure 3.95 AFM of T45H65 NPAB a) read/write elements, b) outer and c) inner chamfer

Read/write elements were still visible above alumina but had significant debris coverage of height up to 15 nm. Very high debris was observed on the chamfers of this slider, with line analysis giving heights of up to 1.5 µm. Again outer slider rail displayed most damage. XPS indicated higher fluorine on slider than expected (up to 9% on leading edge), disk results were similar to ambient.

3.2.4 Long Pause in Elevated Conditions following CSS test

A CSS pause test was carried out in 30°C/75% RH as described in Section 3.1.4. Following the test, conditions were allowed to return to ambient and the slider was then parked on the disk for approximately 24 hours.

On trying to remove the slider from the disk it was found that severe adhesion had occurred, in fact an upward force in excess of that required to remove the slider from it's suspension was required to separate the two surfaces. SEM analysis was performed on the disk surface, revealing a definite footprint left by slider, Figure 3.96. Crosshatch texturing of disk was still visible behind the footprint.

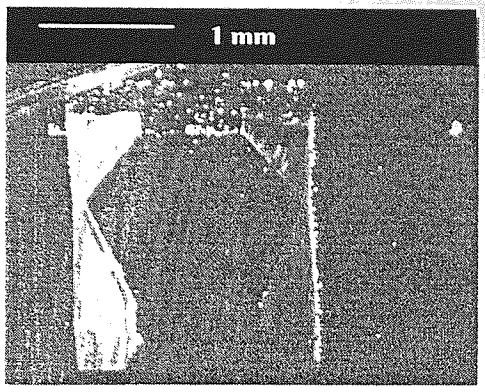

Figure 3.96 Slider footprint on disk surface

AFM analysis suggested the footprint was formed from debris transported from slider to disk. Figure 3.97 shows the topography and lateral force scans of right hand edge of footprint. Lateral force scan shows lower friction (darker areas) is associated with debris pile than surrounding area, this suggests debris contains lubricant material.

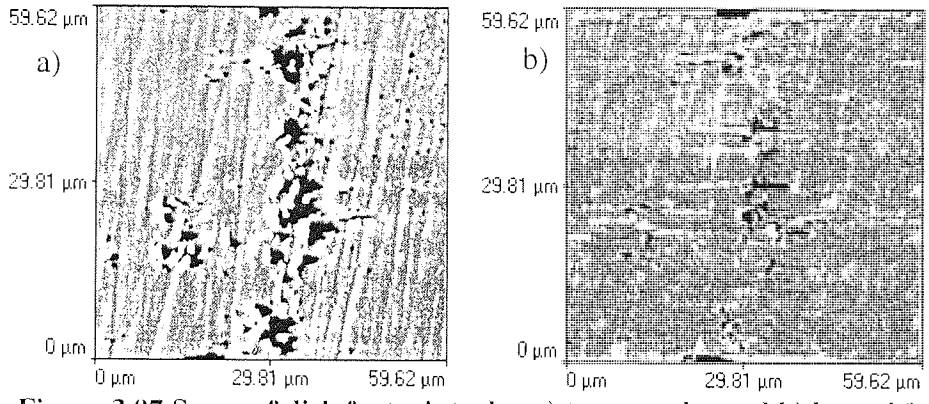

Figure 3.97 Scans of disk footprint edge a) topography and b) lateral force

AFM analysis of slider's trailing and leading edges are shown in Figure 3.98, read/write elements were no longer visible. Rectangular debris in Figure 3.98a) was around 11 nm high and could be formed from broken up poles/shields. Massive debris was observed on leading edge rails, Figure 3.98b), this was measured up to 1500 nm high (1.5 µm).

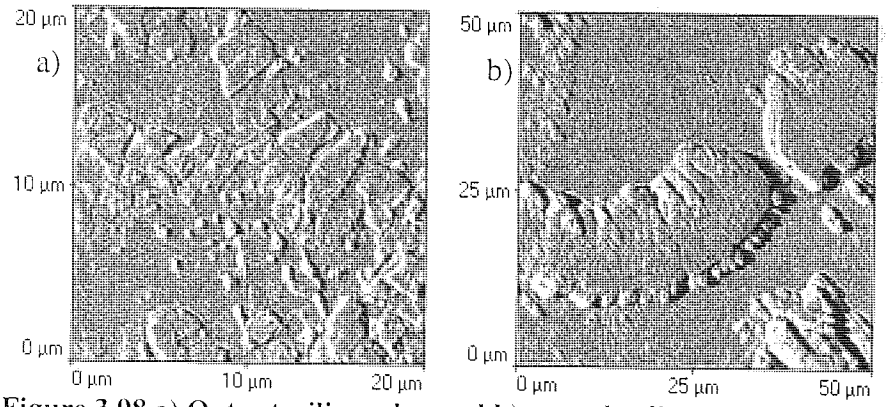

Figure 3.98 a) Outer trailing edge and b) outer leading edge rail scan

XPS on the disk revealed expected materials but also silicone (0.5%), silicone was also found on slider trailing edge (1.6%). The binding energy associated with it (101.5 eV) suggested it was siloxane, Kurokawa [141] reported that the heat in operating drives caused outgassing of siloxane from silicone gaskets. Slider XPS analysis showed higher than expected amount of aluminium and titanium (9.85 % and 1.49 % respectively), this suggested that the protective carbon overcoat could have been removed in places.

3.2.5 Analysis of Failed CSS Tests

Tests classed as failures by failure criteria will now be analysed.

3.2.5.1 Tests Displaying High/Increasing Friction

The T60H40C test failed exhibiting very high friction after 2 hours. Examination of disk revealed a clearly visible wear track, SEM shown in Figure 3.99.

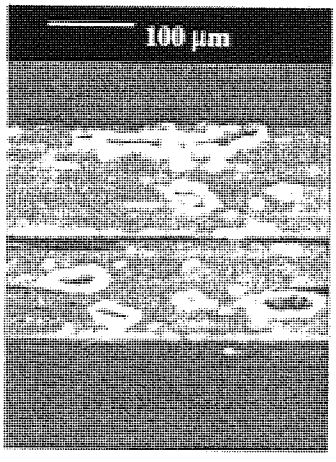

Figure 3.99 SEM images of failed T60H40 disk wear track

Figure 3.100 shows a 100 μm^2 AFM scan taken in the disk wear track, line analysis is included. Disk wear track roughness was R_a= 18.46 nm, R_{rms}=23.25 nm with P-V=87.37 nm.

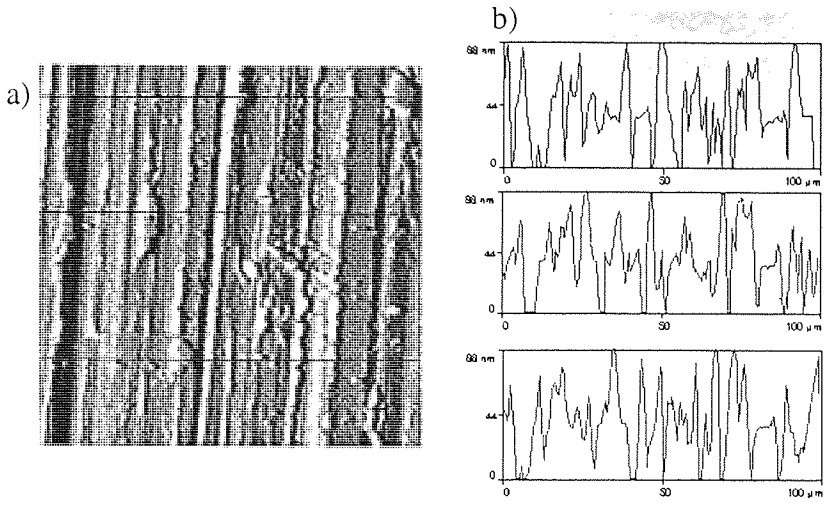

Figure 3.100 T60H40C a) disk scan and b) line analysis

Corresponding NPAB slider showed most severe damage at the trailing edge. The outer pole/shield was chipped and huge debris was observed down slider inner edge. SEM images shown Figure 3.101. Slider trailing edge damage was too severe for AFM analysis.

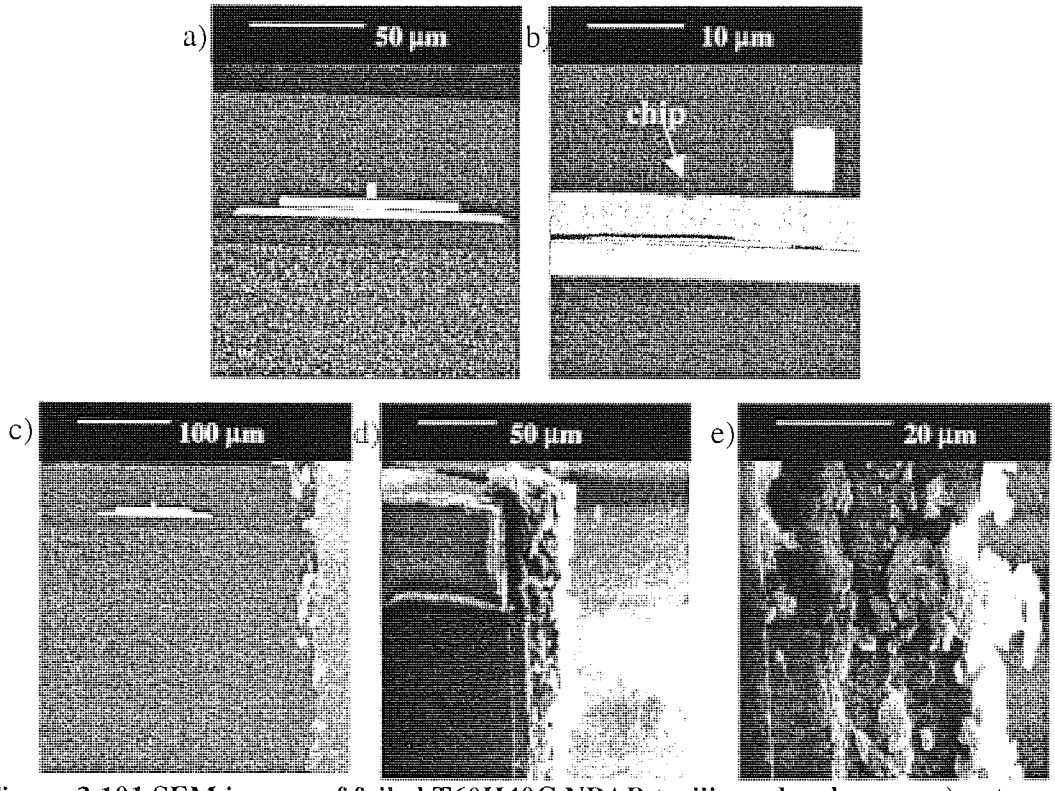

Figure 3.101 SEM images of failed T60H40C NPAB trailing edge damage a) outer read/write element, b) zoom-in on chip, c) debris to inner side of rail, d) and e) zoom in on debris

Analysis of the slider's leading edge showed some debris, Figure 3.102, but no more than would be expected on a normal 7K tested slider.

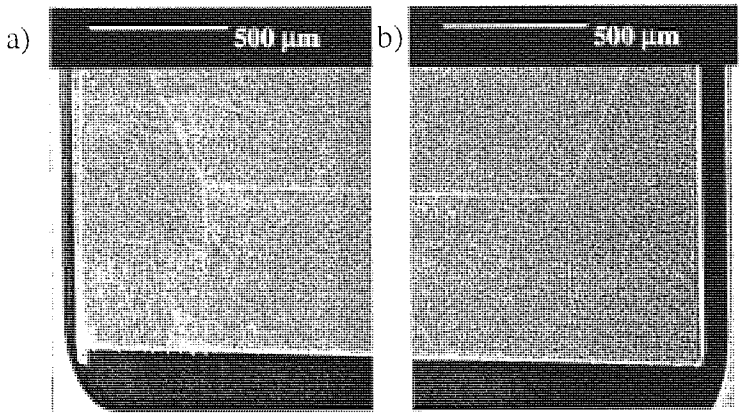

Figure 3.102 SEM images of failed T60H40C NPAB leading edge damage at a) outer and b) inner rail

XPS detected chromium on disk and slider surfaces implying wear of the disk carbon overcoat had occurred exposing magnetic layer material.

Another high friction tests was T70H20C, following testing an obvious wear track was observed on the disk, AFM scan in Figure 3.103. Pits were seen in the track, pit depth of up to 60 nm was measured.

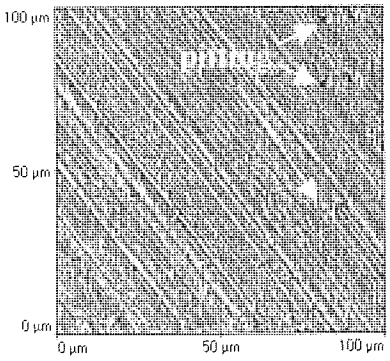

Figure 3.103 AFM image of failed T70H20C disk wear track

Again damage was limited to trailing edge of slider, with part of outer rail actually chipped away, SEM shown in Figure 3.104.

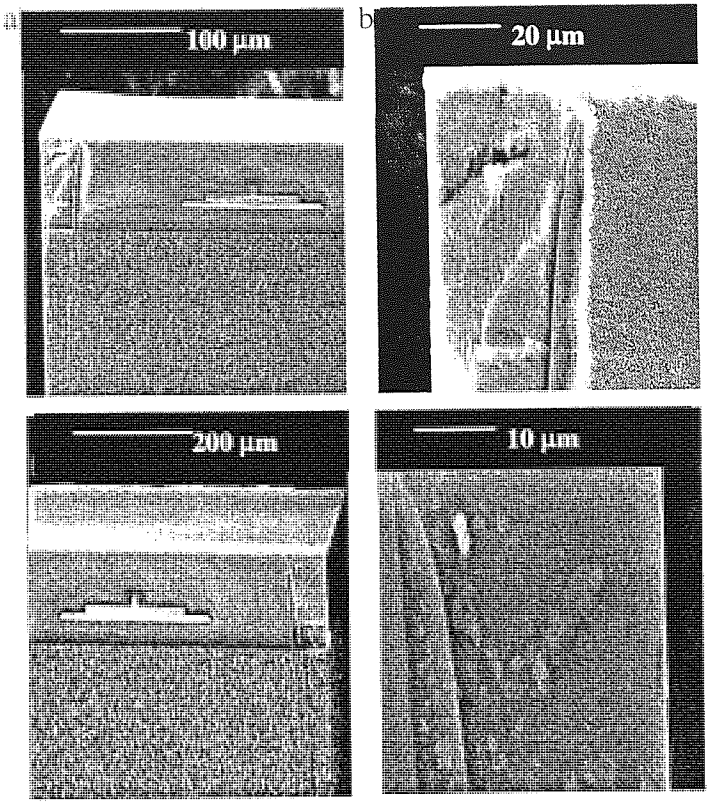

Figure 3.104 SEM images of failed T70H20C NPAB trailing edge damage a) outer read/write element, b) zoom-in on crack, c) debris to inner side of rail and d) zoom in on debris

For the tri-pad test T60H10C which failed around 1 hour into a test, massive debris was observed on the slider contact pad. Line analysis gave this debris to be > 500 nm in height, Figure 3.105 shows AFM scan of debris.

c)

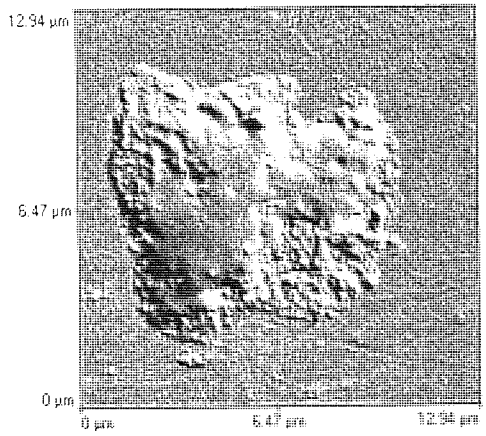

Figure 3.105 T60H10C tri-pad contact pad

3.2.5.2 Tests Displaying High/Increasing High Stiction

During test T50H75C very high stiction was recorded, SEM analysis revealed undamaged trailing edge but an abundance of debris on leading edge rail and chamfers, Figure 3.106. Chamfer damage was too severe for AFM analysis.

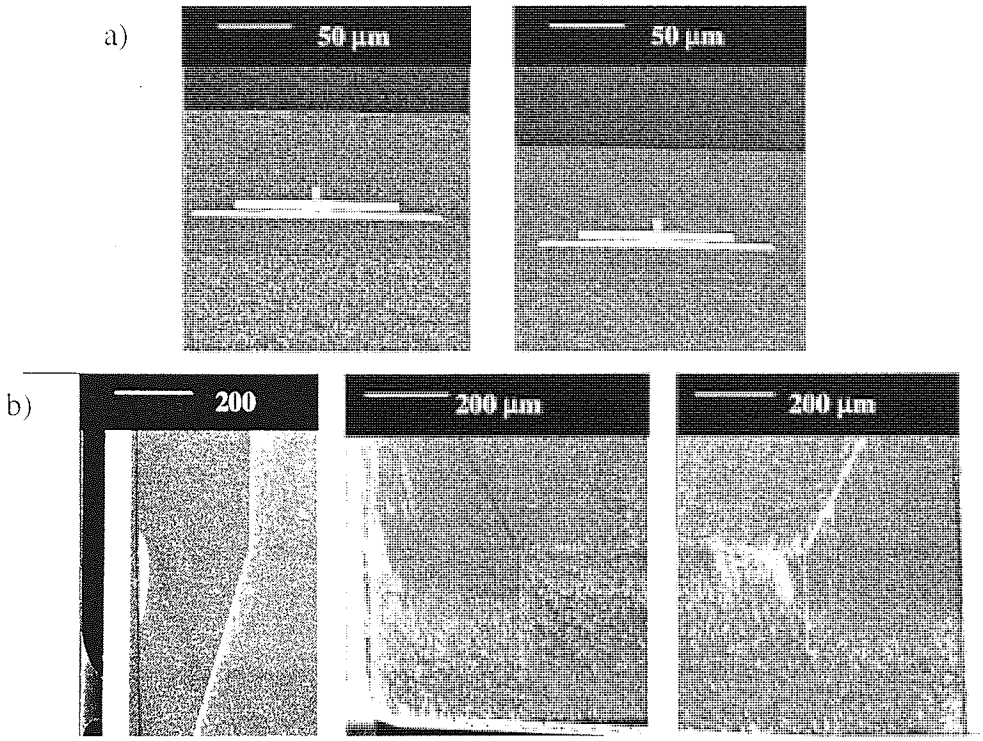

Figure 3.106 SEM of T50H75C NPAB a) trailing edge, from left to right, i) inner, ii) outer elements and b) leading edge, from left to right, i) damaged rail, ii) outer and iii) inner chamfers

Similarly, the test T30H80 exhibited higher stiction than expected. Leading edge SEM scans are shown in Figure 3.107.

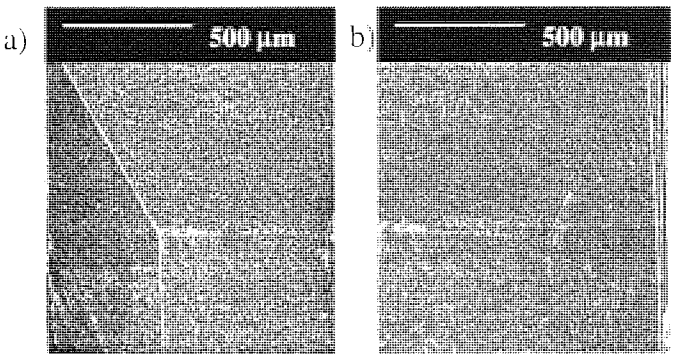

Figure 3.107 SEM scans of T30H80 NPAB a) outer leading edge and b) inner leading edge

Again damage was confined to leading edge rails and chamfer, AFM scans of chamfers shown in Figure 3.108. Debris height was up to 300 nm on both chamfers increasing R_{rms} roughness to 40 nm and 29 nm for outer and inner chamfer, respectively.

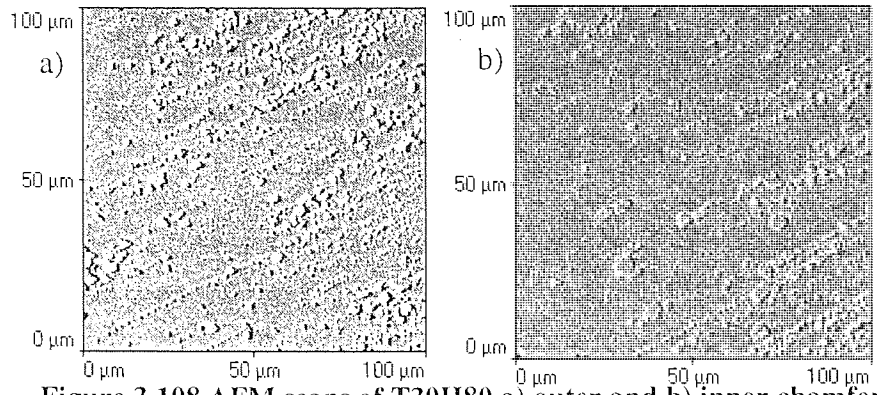

Figure 3.108 AFM scans of T30H80 a) outer and b) inner chamfers

3.2.6 Ambient Drag Tests Surface Analysis

Drag testing was found to be very damaging to disk and slider even under ambient conditions. Following drag testing, disks frequently revealed deep wear scars, SEM of disk wear track after 20 hours drag test in ambient is shown in Figure 3.109.

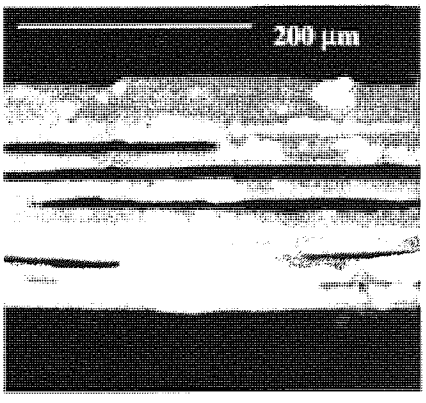

Figure 3.109 Wear scar on T25H40 drag test disk

The main location of slider damage following drag testing was around read/write elements and trailing edge rails. Elements were found to be worn almost flat and covered in debris. AFM images shown in Figure 3.110.

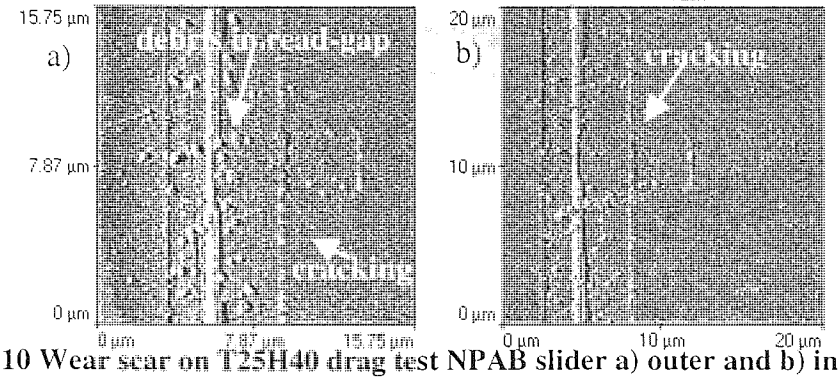

Figure 3.110 Wear scar on T25H40 drag test NPAB slider a) outer and b) inner read/write elements

XPS detected chromium on both slider and disk surfaces following testing, implying disk carbon overcoat had been removed.

3.2.7 Modified Environment Drag Test Surface Analysis

As for CSS testing, hot/dry conditions encouraged the formation of stain around read/write elements during drag testing. The slider body was found to be almost free from debris, with any damage being in the form of whiskering off chamfer leading edge, Figure 3.111.

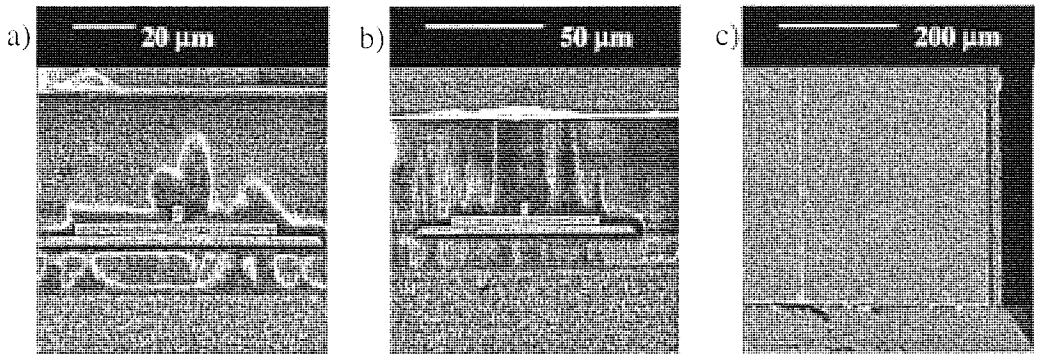

Figure 3.111 SEM of stain around a) outer, b) inner read/write elements and c) inner chamfer of T60H10 drag tested NPAB

Again most loose debris was observed on sliders tested in humid conditions, Figure 3.112 shows slider from T30H70 test. Debris on chamfers was larger than before, but much fewer particles were seen (usually less than 10 particles per slider).

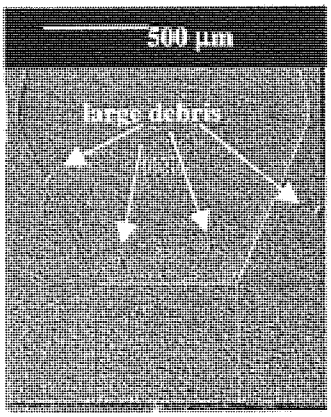

Figure 3.112 T30H70 drag test NPAB slider body

Humid environments aided drag performance, with water molecules acting as an extra lubricant at the interface. Wear tracks were narrower and shallower under humid conditions, Figure 3.113 shows the disk wear track from T30H70 drag test. Notice, a few large debris particles were also present in and around the track.

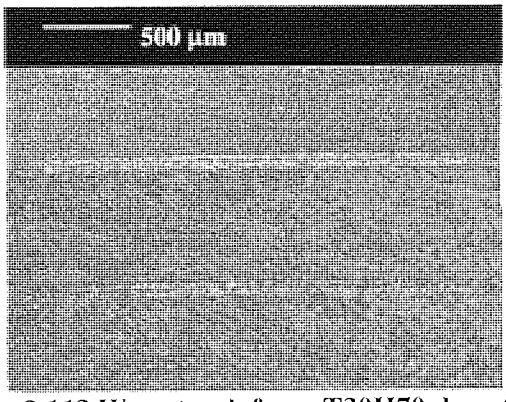

Figure 3.113 Wear track from T30H70 drag test disk

3.2.8 Analysis of Failed Drag Tests

All of the drag tests performed under very hot/dry conditions failed displaying extremely high friction. Disks had hazy appearance following testing with wear tracks visible and sliders were covered in debris. For T80H5 drag test, disk overcoat could be seen to be removed in large flakes or laminae, SEM shown in Figure 3.114a).

Analysis of slider showed huge debris on outer rail trailing edge, Figure 3.114b) and c). Debris was composed of disk magnetic materials, carbon overcoat and lubricant.

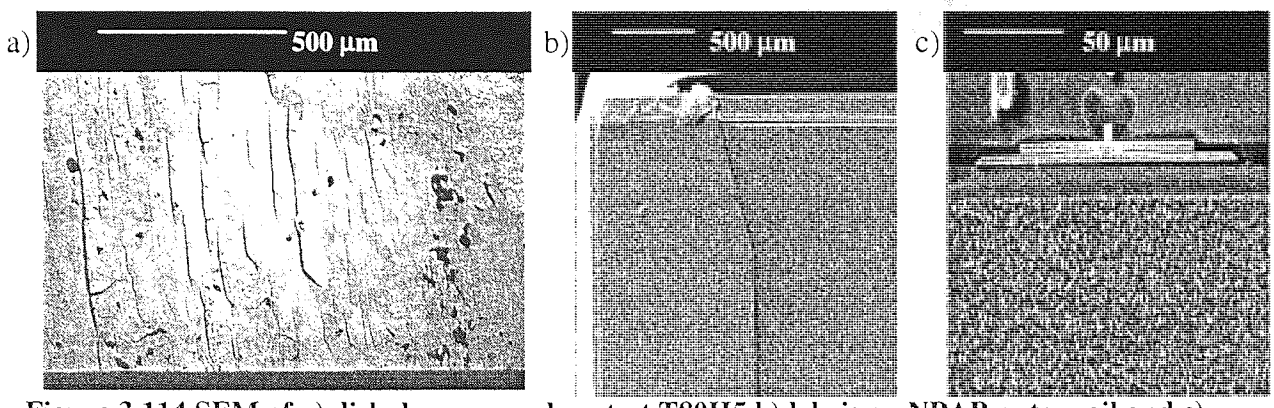

Figure 3.114 SEM of a) disk damage on drag test T80H5 b)debris on NPAB outer rail and c) zoom in on b)

AFM analysis of the NPAB used in T70H6 test revealed some 'bone' shaped features on the trailing edge side of read/write element, scan shown in Figure 3.115. XPS of this area detected fluorine indicating these features could stem from disk lubricant. 'Bones' were 2 µm in diameter at widest part and up to 200 nm high.

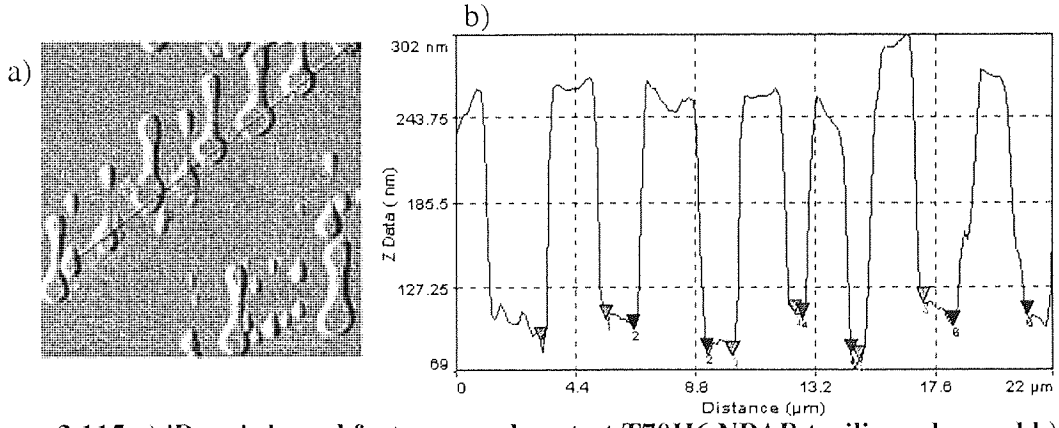

Figure 3.115 a) 'Bone' shaped features on drag test T70H6 NPAB trailing edge and b) line analysis

For the failed T77H4 drag test, analysis of slider revealed spherical shapes on trailing edge. These were soft and could be flattened by AFT scanning tip, Figure 3.16a) shows how small scan (50 μm^2) scan flattened features and showed up in large scan in Figure 3.16b). The soft nature of shapes again indicated the material was disk lubricant transferred from slider.

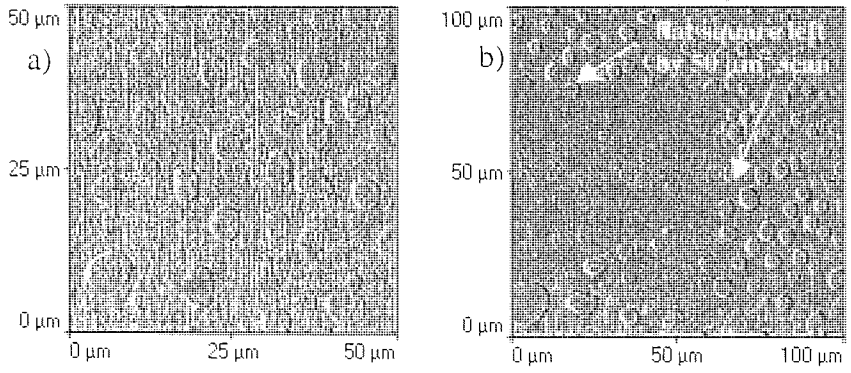

Figure 3.116 Spherical features on drag test T77H4 NPAB trailing edge a) 50 µm^2 and b) 100 µm^2 scans

Under hot/dry conditions lubricant breakdown occurred, this explains the complete interface failure observed in all tests under these conditions. Disk lubricant reformed into spheres on slider surface and was therefore not protecting surfaces as it should. Major damage was therefore allowed to occur to both surfaces.

Figure 3.117 shows cracking of NPAB read shields during drag test T66H5 and corresponding optical microscope image of the disk wear track.

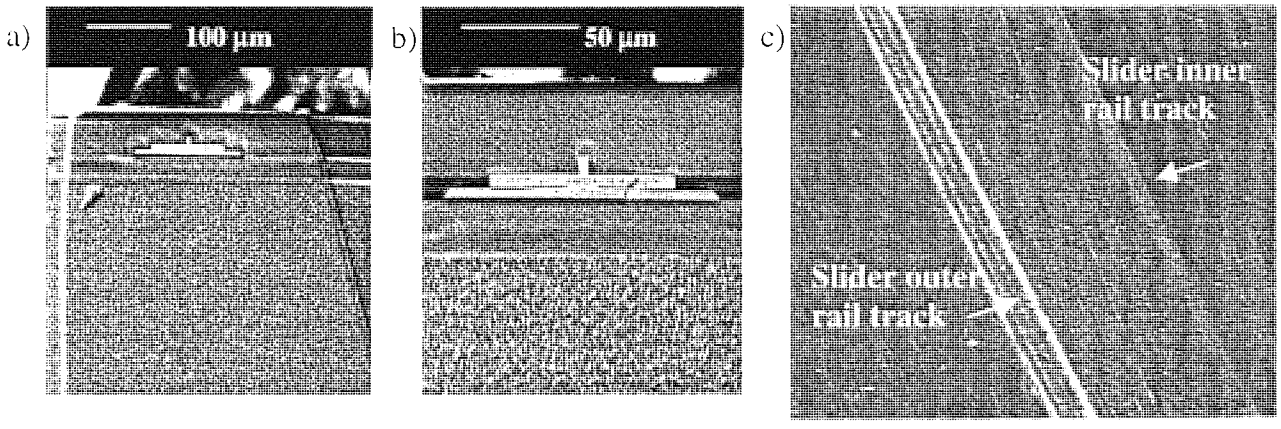

Figure 3.117 T66H5 NPAB outer trailing edge showing crack over read shields a) large scale, b) zoom-in and c) disk wear track

XPS of the slider leading edge showed presence of disk magnetic materials, carbon overcoat and lubricant. Large aluminium peak (5.1%) was also detected, perhaps indicating that disk had been worn through to substrate level.

4 Modelling Chapter

In this chapter results from AFT experiments, Section 3.1, were further examined with models for friction and stiction proposed. Parameters studied were time, disk velocity and testing environment.

Slider fly height was also examined, with dynamic estimates for each slider given. These estimates allowed comparison between NPAB and tri-pad slider and possible explanation of the contrasting friction behaviour observed.

Detailed slider debris analysis was performed with explanation given for slider debris position. Additionally, a quantification method for debris was proposed. Finally, contact analysis was performed between disk and slider with results once more supporting original friction/stiction results.

4.1 Models for Friction/Stiction Behaviour

4.1.1 Friction Trace Model over 1 CSS with Respect to Disk Velocity

When modelling friction against disk velocity, linear velocity (m/s) was used to avoid changes in relative velocity between disk and slider caused by altering disk testing radius. The simple conversion equation is shown below, where r was the distance from the disk centre to track.

$$Vel_{linear} = \frac{Vel_{rotational} * 2\pi r}{60 * 1000} \qquad \textbf{Equation 4.1}$$

It was observed that the friction trace over a typical cycle was essentially symmetrical about a vertical axis and followed the typical Stribeck curve shape. Friction was related to disk velocity in the cases of both sliders, see Figure 4.1

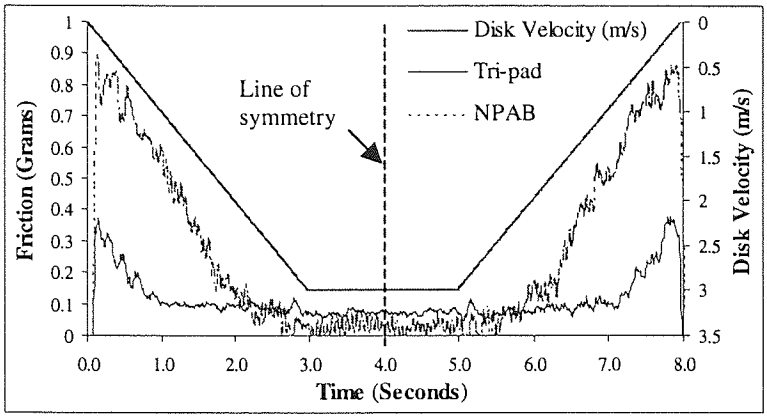

Figure 4.1 Friction traces during a typical CSS at 3 m/s for NPAB and tri-pad sliders. Note, velocity scale is inverted to highlight relationship

A 6th order polynomial of the form $f(t) = \sum_{i=0}^{6} c_i v(t)^i$, where v(t) is velocity at time t, was originally used to describe the friction trace.

An example, for a 3m/s NPAB cycle is shown in Figure 4.2. Although this type of model gave good fit, modelling the coefficients (c_i with i=1,2..7) to obtain an estimate of friction trace for general velocity case proved problematic.

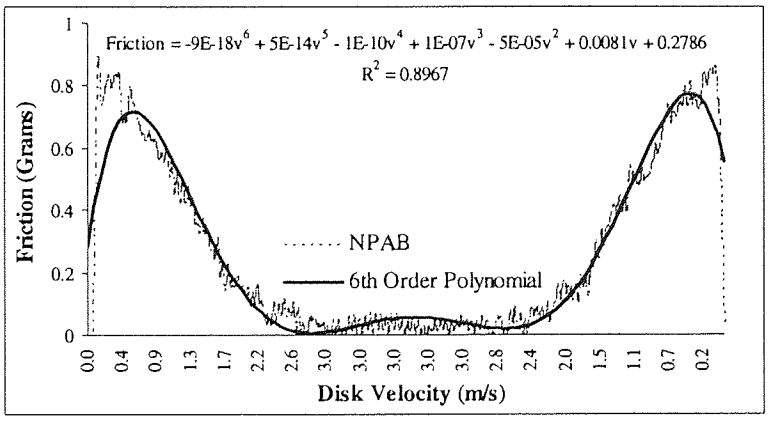

Figure 4.2 6th order polynomial of typical friction trace against disk velocity for NPAB

Introducing the Cubic Model

It was decided to use the near symmetrical property of the friction trace to produce a 3rd order (or cubic) model for friction with respect to disk velocity, thus reducing the number of model coefficients to 4.

The original 'bathtub' shape traces were reflected about their line of symmetry at the mid-point in the cycle, to give simplified graphs, Figure 4.3 below. The figure again shows the friction trace during 3 m/s CSS tests and shows the take-off and landing phases of the cycle against disk velocity.

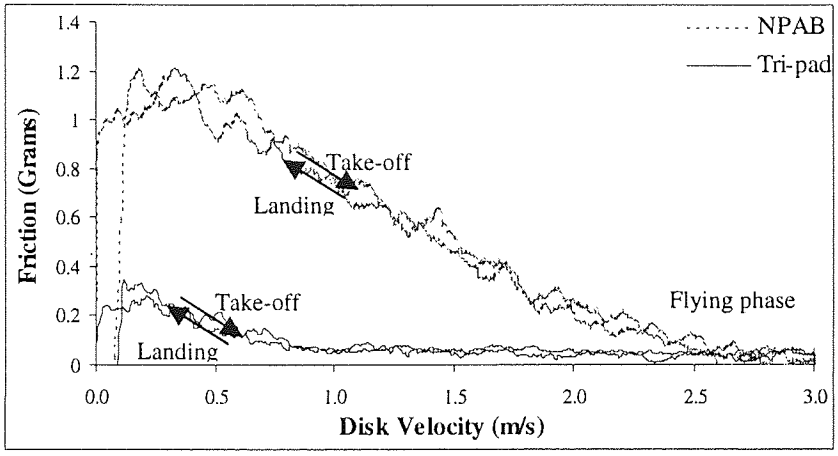

Figure 4.3 Take-off and landing phases of cycles against disk velocity for 3m/s CSS

This technique was repeated for tests at dwell velocities 2, 3, 4, 5, 7, and 10 m/s and cubic models were applied. A selection of these are shown in Figure 4.4, notice that for dwell velocity above 4m/s the cubic model did not accurately describe the behaviour of the tri-pad slider. Thus, this technique was only pursued for the NPAB since R^2 values given were all in excess of 0.8 indicating the cubic model gave good fit.

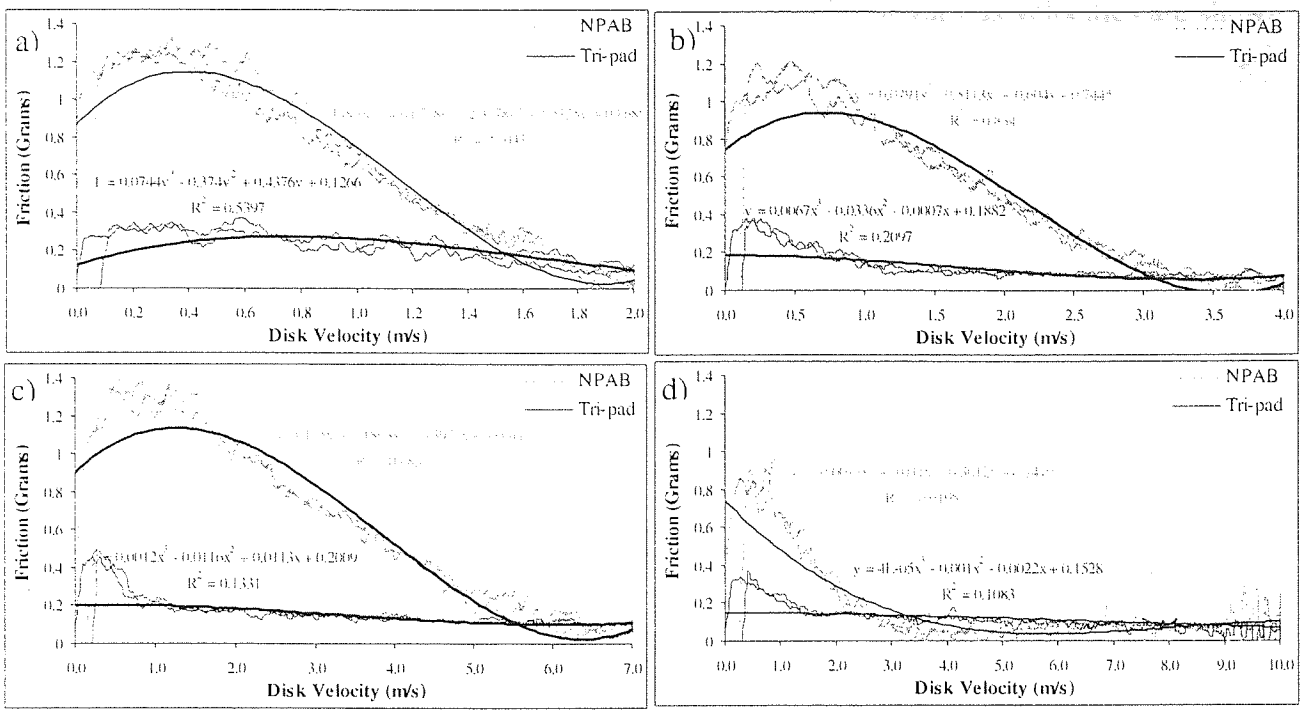

Figure 4.4 Cubic models for CSS at a) 2, b) 4, c) 7 and d) 10 m/s for NPAB and tri-pad

The cubic model for each dwell velocity for the NPAB slider could be represented by

$$f_i(t) = \sum_{j=0}^{3} C_{i,(j+1)}\, v_i(t)^{(3-j)} \qquad \textbf{Equation 4.2}$$

for i=1 to 6 (corresponding to tests at 2,3,4,5,7,10 and 15 m/s) and t=0 to end of cycle.

$$\text{Where } C = \begin{pmatrix} 0.9884 & -3.4477 & 2.6969 & 0.586 \\ 0.1645 & -0.7972 & 0.7813 & 0.4425 \\ 0.0598 & -0.3733 & 0.4615 & 0.3863 \\ 0.0293 & -0.2121 & 0.2382 & 0.5145 \\ 0.0221 & -0.2579 & 0.6339 & 0.6954 \\ -0.0006 & 0.0204 & -0.1944 & 0.5975 \\ -0.00004 & 0.0091 & -0.1825 & 1.1091 \end{pmatrix}$$

and $\underline{v}_i(t)$ is the vector containing disk velocity at time t for each test.

Cubic model estimates of NPAB friction during a CSS cycle for various velocities are shown in Figure 4.5.

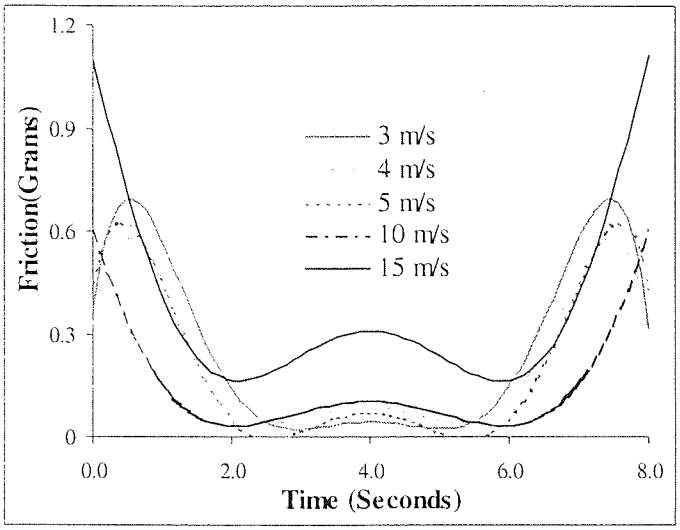

Figure 4.5 Estimated NPAB friction traces at 3, 4, 5, 10 and 15 m/s

The model agreed with previous results, in that take-off and landing slopes increased with dwell velocity. Also, at high velocity (>10m/s) a large jump in flying friction was observed, this agreed with the tests performed at 10 and 15 m/s where average flying friction was 0.09 and 0.29 grams, respectively in real tests.

Estimating Coefficients of Cubic Model

When coefficients of each model were plotted, trends were noticed with increasing dwell velocity, Figure 4.6.

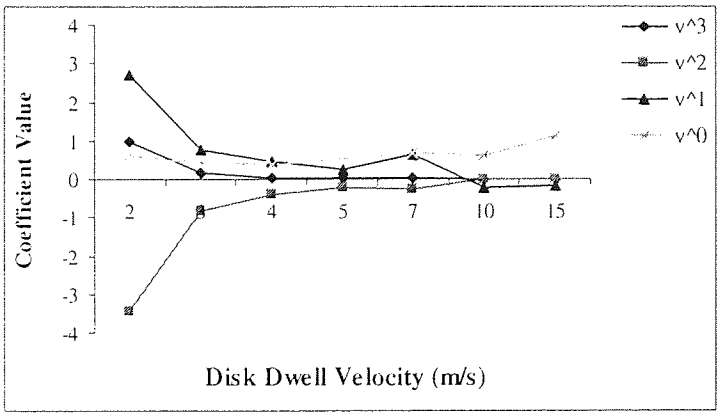

Figure 4.6 Trends in cubic model coefficients with dwell velocity

In fact, simple curve fits could be applied to each order term to explain how that term changed in the cubic model with increasing disk dwell velocity, Figure 4.7.

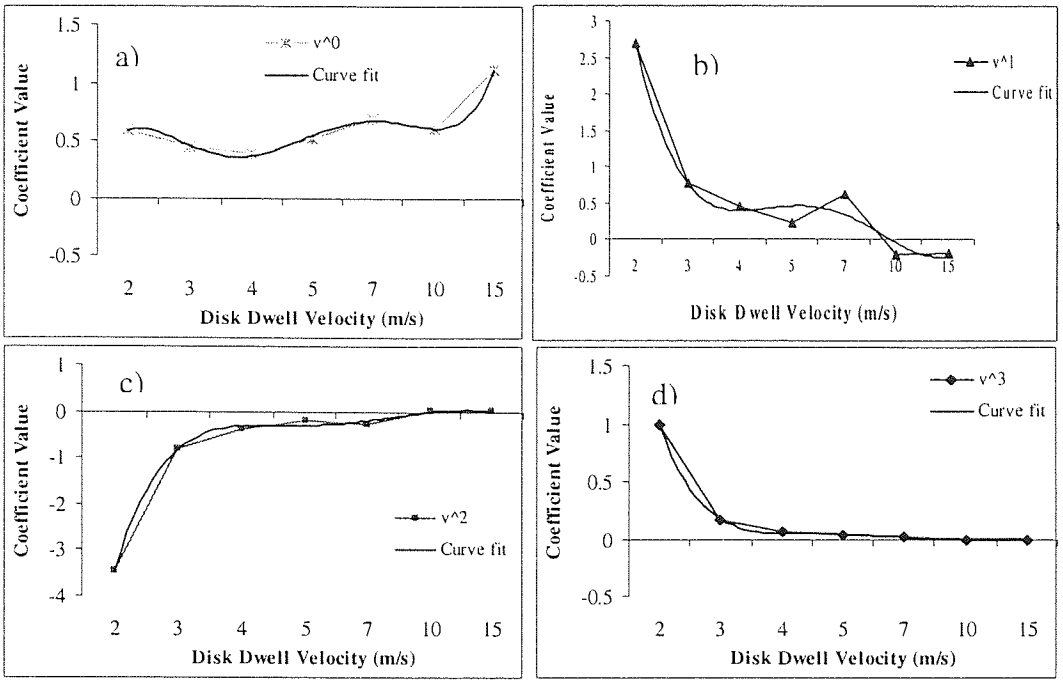

Figure 4.7 Curve fits for cubic model a) constant, b) v, c) v^2 and d) v^3 terms at different disk velocity

The four modelled curves were given by

$$p_i = \sum_{j=0}^{6} (D^T)_{i,(j+1)} (V_d)_{(j+1),i}^{(6-j)} \quad \text{for i=1 to 4} \qquad \textbf{Equation 4.3}$$

where

$$D = \begin{pmatrix} -0.00043 & 0.00114 & -0.00030 & 0.00003 \\ 0.01712 & -0.04675 & 0.01526 & -0.00045 \\ -0.25732 & 0.71855 & -0.28488 & -0.00857 \\ 1.80938 & -5.18388 & 2.43394 & 0.16954 \\ -5.97646 & 17.62236 & -9.49149 & -0.82682 \\ 7.49695 & -22.97718 & 13.96944 & 1.63992 \end{pmatrix}$$

and $V_d = \begin{pmatrix} 2 & 3 & 4 & 5 & 7 & 10 & 15 \\ 2 & 3 & 4 & 5 & 7 & 10 & 15 \\ 2 & 3 & 4 & 5 & 7 & 10 & 15 \\ 2 & 3 & 4 & 5 & 7 & 10 & 15 \\ 2 & 3 & 4 & 5 & 7 & 10 & 15 \end{pmatrix}$

Thus, it was thought possible to use the equations to provide coefficients of the cubic model for any chosen dwell velocity in the range [2-15] m/s by substituting Equation 4.3 into Equation 4.2 to give

$$\underline{f}_i(t) = \sum_{k=3}^{0} \sum_{j=1}^{4} \sum_{i=0}^{6} \left[(D^T)_{j,(i+1)} (V_d)_{(i+1),j}^{(6-i)} \right]^T v_i(t)^k \qquad \textbf{Equation 4.4}$$

However, when this was attempted for a CSS cycle with dwell velocity 3.37 m/s the friction predicted gave the graph below.

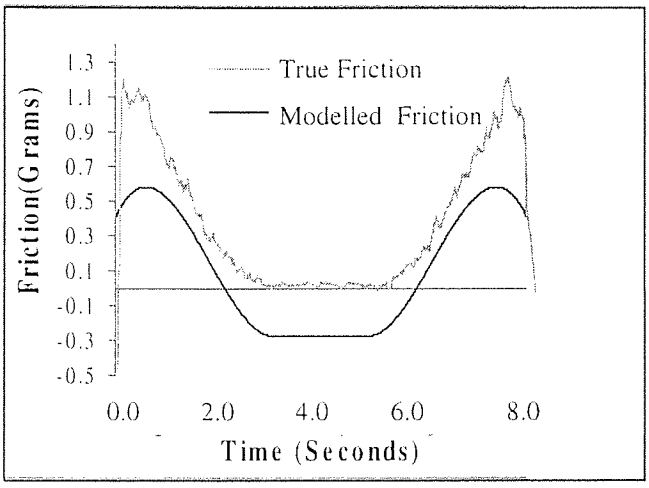

Figure 4.8 Cubic model friction estimate for 3.37 m/s cycle

Although the model was the correct shape, the values predicted were 0.4 grams lower than the true readings throughout the cycle. However, the model could be used to estimate take-off and landing slopes.

The error in values occurred due to the cubic model underestimating the value of the constant coefficient c_o. Rather than using the formulae for this term, it was decided to simply interpolate between known values of c_o from the data set. In this case interpolation was performed between the known constants for 3 and 4 m/s tests giving $c_o = 1.11$.

The modelled flying friction was now slightly higher than actual friction, but a definite improvement was observed, Figure 4.9.

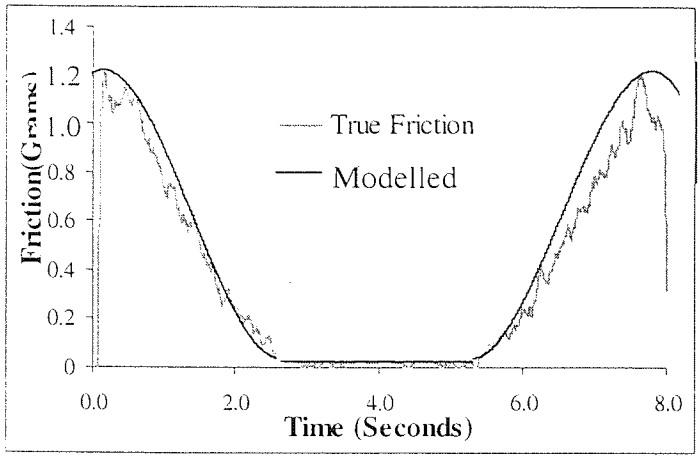

Figure 4.9 Showing improved cubic model fit for 3.37 m/s CSS trace

4.1.1.1 Modelling Disk Velocity Over a CSS Cycle

To use Equation 4.4 to predict the friction trace, the disk velocity vector, $\underline{v}_i(t)$ must be known for any chosen dwell velocity. A general model for disk velocity during a variable length CSS cycle will now be given.

Parameter definition :

T_{up} Ramp-up time (seconds)

T_{dwell} Dwell time (seconds)

T_{down} Ramp-down time (seconds)

V_d Maximum disk velocity at T_{dwell} (m/s)

α Disk acceleration factor (m/s^2), for the AFT system with α **=0.335** m/s^2

$\frac{dx}{dt}$ Disk Velocity at time t (m/s)

$\frac{d^2x}{dt^2}$ Disk acceleration at time t (m/s^2)

k_1, k_2 , k_3 are constants

Since the acceleration/deceleration factor of the AFT apparatus was known to be constant throughout the ramp up/down phase of a CSS test and zero over the dwell phase, separate differential equations were formed for velocity in each of the cycle phases as shown below.

During Ramp-up Phase ($t < T_{up}$) :

$$\frac{d^2x}{dt^2} = \alpha V_d$$

Integrating both sides with respect to t gave $\frac{dx}{dt} = \alpha V_d t + k_1$

Applying Initial Condition $\left.\frac{dx}{dt}\right|_{t=0} = 0$, gave $k_1 = 0$

Hence,

$$\frac{dx}{dt} = \alpha V_d t \qquad \textbf{Equation 4.5}$$

During Dwell Phase ($T_{up} < t < (T_{up} + T_{dwell})$) :

$$\frac{d^2x}{dt^2} = 0$$

Integrating both sides with respect to t gave $\frac{dx}{dt} = k_2$

Applying Initial Condition $\left.\frac{dx}{dt}\right|_{t=up} = V_d$, gave $k_2 = V_d$

Hence,

$$\frac{dx}{dt} = V_d \qquad \textbf{Equation 4.6}$$

During Ramp-down Phase ($(T_{up}+T_{dwell}) < t < (T_{up} + T_{dwell} + T_{down})$) :

$$\frac{d^2x}{dt^2} = -\alpha V_d$$

Integrating both sides with respect to t gave $\frac{dx}{dt} = -\alpha V_d t + k_3$

Applying Initial Condition $\left.\frac{dx}{dt}\right|_{t=(T_{up}+T_{dwell})} = V_d$, gave $k_3 = V_d + \alpha V_d (T_{up}+ T_{dwell})$

Hence,

$$\frac{dx}{dt} = V_d (1 - \alpha (t - T_{up} - T_{dwell})) \qquad \textbf{Equation 4.7}$$

The formulae were validated by comparing with true velocity data from a 3.37 m/s standard CSS cycle. It was observed that true and modelled traces were indistinguishable with $R^2>0.999$.

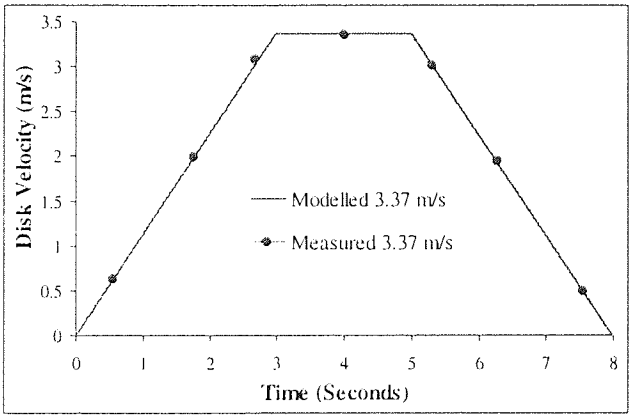

Figure 4.10 True and modelled velocity traces for 3.37 m/s CSS

Velocity vectors for CSS cycles at 2, 3, 4, 5, 7 and 10 m/s were calculated, Figure 4.11.

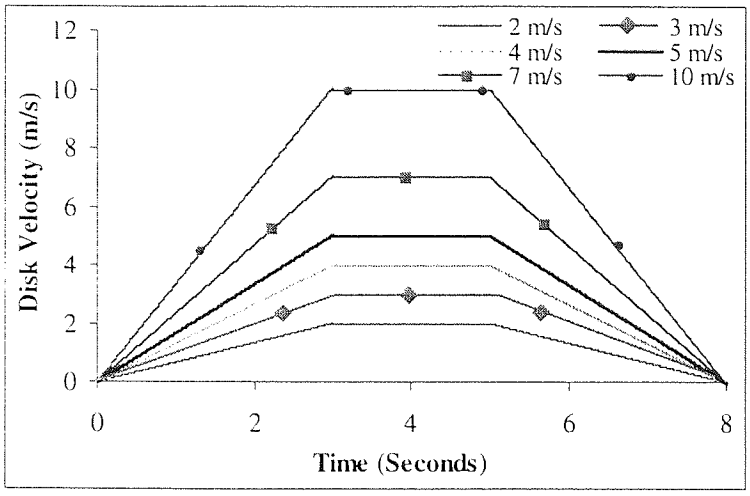

Figure 4.11 Generated velocity vectors for CSS cycles

The predicted velocity vectors, $\underline{v}(t)$, could then be used in Equation 4.4 to provide friction trace estimates.

4.1.1.2 Modelling Slider Separation Time with Respect to Acceleration

Equation 1.33 was applied to model the time to separate disk and slider at various disk accelerations. As expected, separation times decreased with increasing disk acceleration for both sliders. Figure 4.12 shows that the model could be used to provide estimates for both slider types.

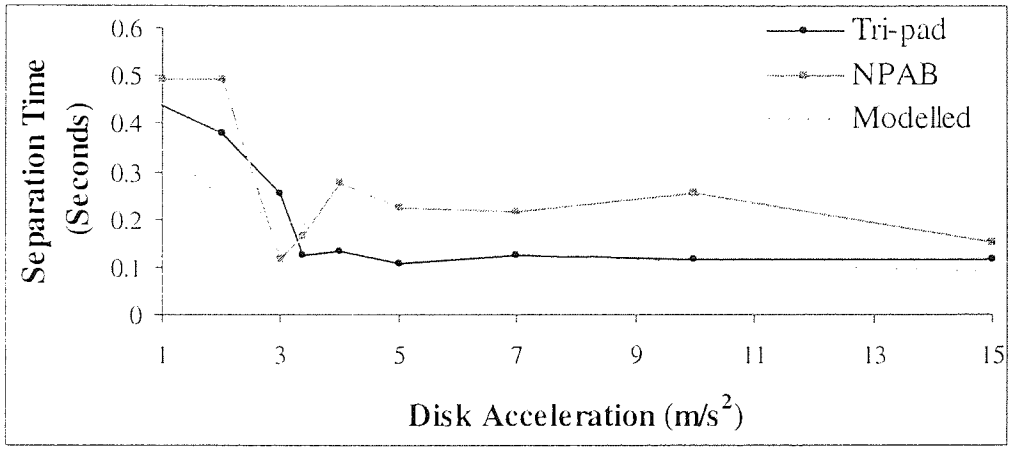

Figure 4.12 Separation times for NPAP and tri-pad at increasing disk acceleration

4.1.2 Mean Flying Friction Model

4.1.2.1 Tri-pad Slider

To describe how mean flying friction changed over a 7K CSS test the Gompertz model was employed, graph shown in Figure 4.13a). This model accurately described the decreasing growth rate in friction with time, Figure 4.13b) shows model derivative trace over the test duration.

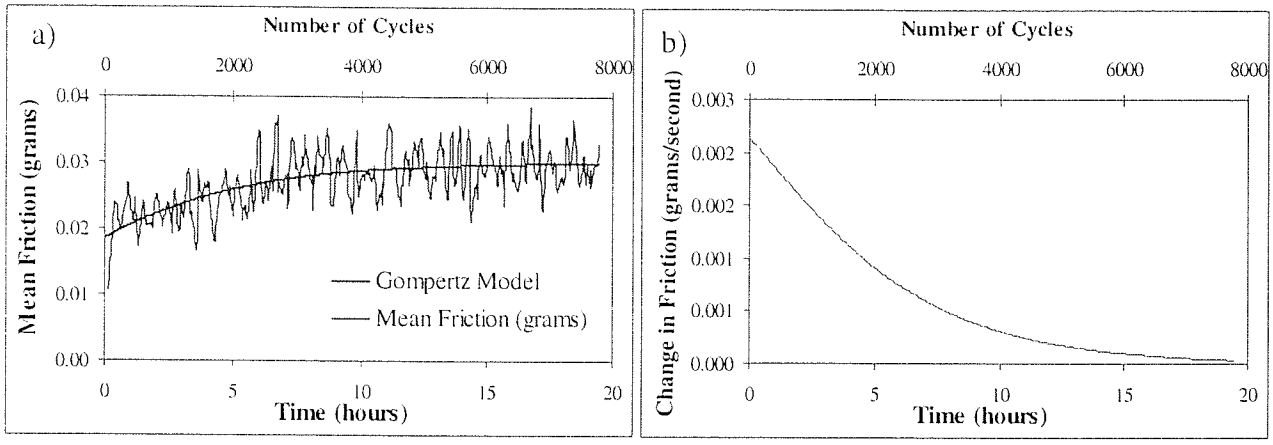

Figure 4.13 Gompertz model for mean flying friction during T25H35 test with tri-pad slider. Model parameters l=0.237, g=0.115 with f(0)=0.019

The general form of the equation was

$$f(t) = f(0)e^{\frac{r}{l}(1-e^{-lt})} \qquad \textbf{Equation 4.8}$$

The parameter r affected the rate of increase in mean friction, with highest values yielding the highest slope. In section 4.1.4.3, the relationship of this parameter with environment will be studied.

4.1.2.2 NPAB Slider

For the NPAB friction increased linearly throughout CSS testing with no such levelling observed, Section 3.1.1.2.

4.1.3 CSS Stiction Model

As shown in Figure 4.14, stiction increased almost linearly throughout CSS testing for both sliders. The rate of increase was small at around 0.1 gram/hour in ambient conditions for both sliders, thus mean stiction can be simply estimated by using

$$\text{Stiction}(t) = \text{Stiction}_{initial} + 0.1 * t \qquad \textbf{Equation 4.9}$$

Where stiction is measured in grams and t is time in hours.

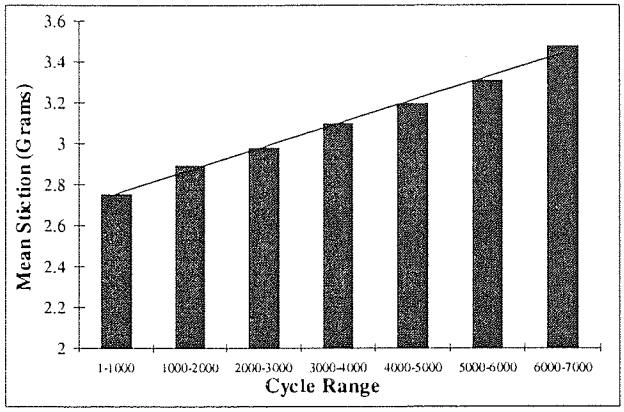

Figure 4.14 Linear increase in stiction over ambient 7K CSS with NPAB

It was also useful to map stiction as a function of disk parking position. As shown in Figure 4.15, this method could identify particular areas of disk where a problem may commonly occur and highlight disk damage. Note, in the example below the shaded area of disk contained very varied stiction readings (up to 40 grams was recorded). This indicated some possible damage of that region was present.

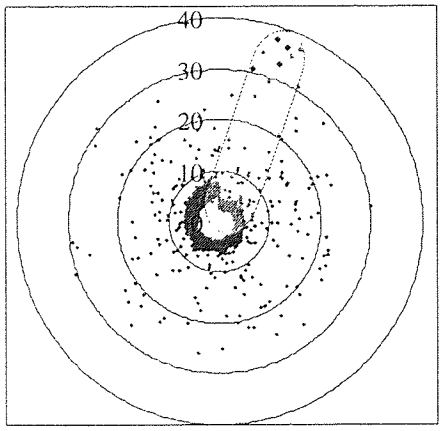

Figure 4.15 Disk analysis by means of stiction map

The method used to identify the position is outlined below.

4.1.3.1 Calculating the Distance Travelled by Slider over 1 CSS

During Ramp-up Phase ($t < T_{up}$) :

Disk velocity at time t was given as $\frac{dx}{dt} = \alpha V_d t$, integrating both sides with respect to t gave an expression for distance travelled at time t. By applying the initial condition x(0)=0 it was given that during ramp up

$$x(t) = \frac{\alpha V_d t^2}{2} \qquad \textbf{Equation 4.10}$$

To get the total distance travelled during the ramp up period, Equation 4.11 must be solved over the interval $0< t < T_{up}$, therefore the distance travelled was

$$x_{up} = \frac{\alpha V_d T_{up}^2}{2} \qquad \textbf{Equation 4.11}$$

Since the CSS cycle type used in this work was always symmetrical (i.e. $T_{up}=T_{down}$) the quantity x_{up} was equal to the distance travelled during disk ramp down.

During Dwell Phase ($T_{up} < t < (T_{up} + T_{dwell})$) :

During disk dwell time, the distance travelled was defined as x_{dwell} where

$$x_{dwell} = V_d T_{dwell} \qquad \textbf{Equation 4.12}$$

Thus, the distance travelled over 1 complete CSS cycle, X, was

$$X = V_d T_{dwell} + \frac{2(\alpha V_d T_{up}^2)}{2} \qquad \textbf{Equation 4.13}$$

Substituting values into Equation 4.14 for the standard CSS test, gave X=16.9m. That is, during every 3,2,3 CSS test at 3.37 m/s the slider covered 16.9m distance. Since testing radius, r, was known (23 mm from disk centre), the number of disk revolutions occurring during 1 CSS was computed using

$$revs = \frac{V_d T_{dwell} + \frac{2(\alpha V_d T_{up}^2)}{2}}{2\pi r} \qquad \textbf{Equation 4.14}$$

During each standard CSS 116.95 disk revolutions occurred and the slider parked at a position of $1/95$ revolutions from its position in the previous cycle. Thus, the sliders parking position changed by 0.066 radians in an anti-clockwise direction each cycle. These radial values were generated by a simple subroutine and then used as the x-axis values to polar plots.

This technique can provide extra information on interface failure and even provide locate disk defects.

4.1.4 Environmental Modelling

Returning to Section 3.1.3, initial experimental CSS results were disappointing, with no obvious trends observed with changes in environment. It was decided to abandon the use of relative humidity as a measure of the moisture content of air at the interface, an explanation of why this was done follows.

4.1.4.1 New Humidity Measurement Proposed to Replace Relative Humidity

Relative humidity (RH) is a measure of the wetness of air, or the concentration of water vapour in the air. RH is expressed as a percentage, with dry air having relative humidity of 0% and saturated air having relative humidity of 100%.

RH measures water vapour, but relative to the temperature of air. In other words, it is a measure of the actual amount of water vapour in the air compared to the total amount of vapour the air could hold at its current temperature. Warm air can hold more water vapour

than cold. RH is given by the ratio of water vapour pressure in the air to saturation pressure at a particular temperature, Equation 4.15.

$$RH = 100\left(\frac{e_a}{e_s}\right) \qquad \textbf{Equation 4.15}$$

where e_a is the vapour pressure of air (in kPa) and e_s is saturation pressure of air (in kPa) at temperature T.

The saturation pressure of air is given by Equation 4.16; Figure 4.16 shows the saturation pressure of air at temperatures in the range [0-100] °C. Clearly, the saturation pressure increases rapidly at high temperature.

$$e_s = 0.61365e^{\frac{17.502T}{240.97+T}} \qquad \textbf{Equation 4.16}$$

where and T is temperature in °C.

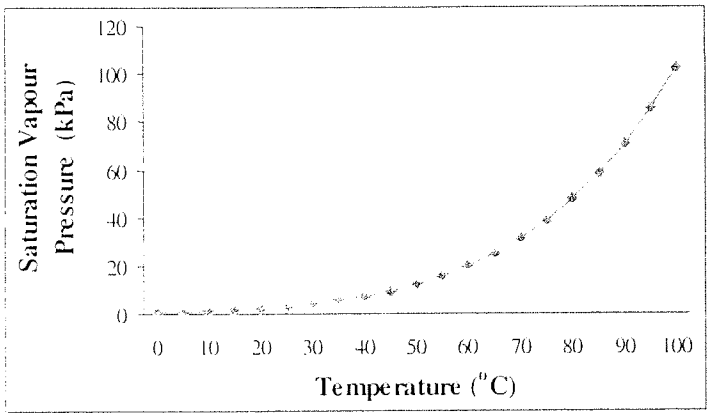

Figure 4.16 Showing saturation pressure of air with temperature

It was thought that modelling results from tests that had been performed in significantly different temperatures was inappropriate using RH, since warm air could hold much more moisture than cool. Note it was still acceptable to use RH as a measure of humidity when comparing tests where temperature was similar. Several other units of measurement for humidity were investigated as follows.

Water Vapour Pressure

The vapour pressure of air was calculated at various conditions using Equations 4.15 and 4.16, Figure 4.17. Note at high temperatures a small increase in relative humidity, produced a large increase in vapour pressure values.

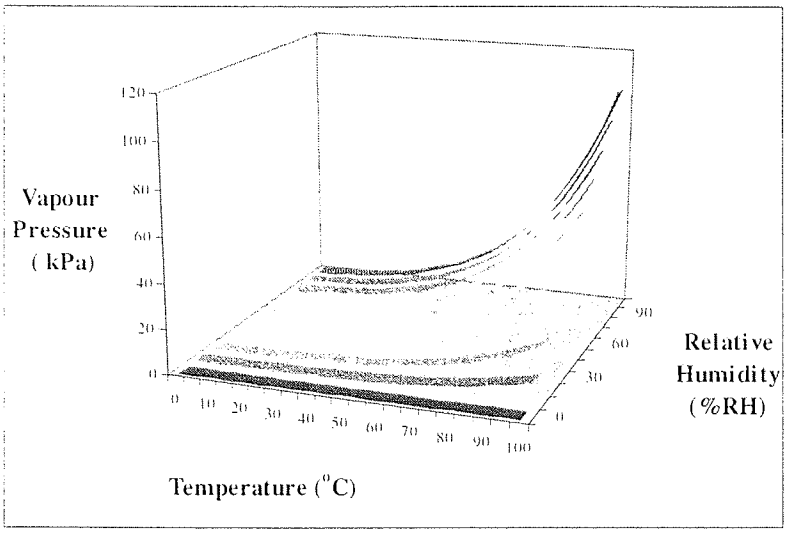

Figure 4.17 Water vapour pressure of air at various temperature/humidity

4.1.4.2 CSS Stiction Modelling using Water Vapour Pressure

For the environmental tests performed, see Figure 2.3 b), the effect of vapour pressure on mean stiction were studied, Figure 4.18a). The poor relationship with relative humidity was shown for completeness in Figure 4.18b).

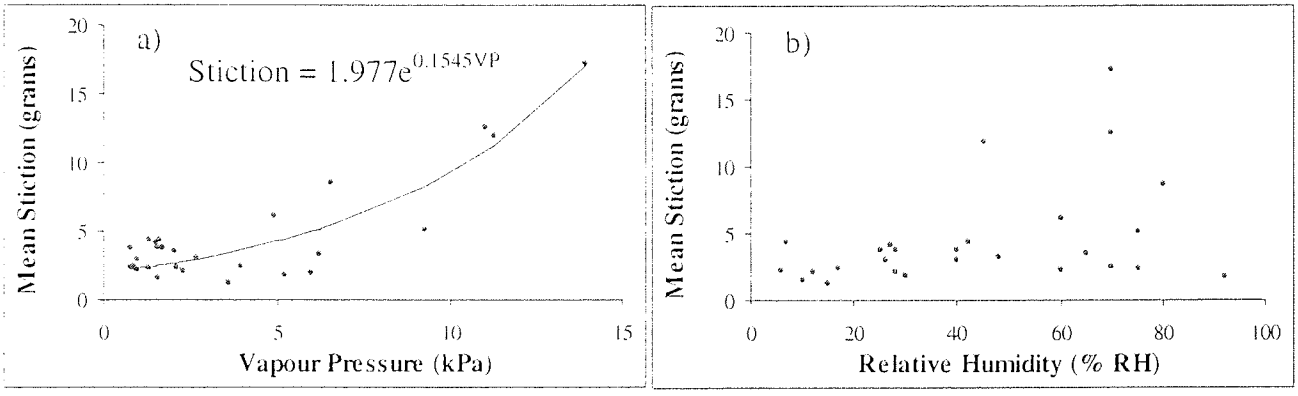

Figure 4.18 Effect of a) vapour pressure and b) relative humidity on mean stiction

Results were encouraging with mean stiction clearly related to water vapour pressure. The best-fit exponential equation could be used to map mean stiction estimates to temperature and relative humidity as before, Figure 4.19.

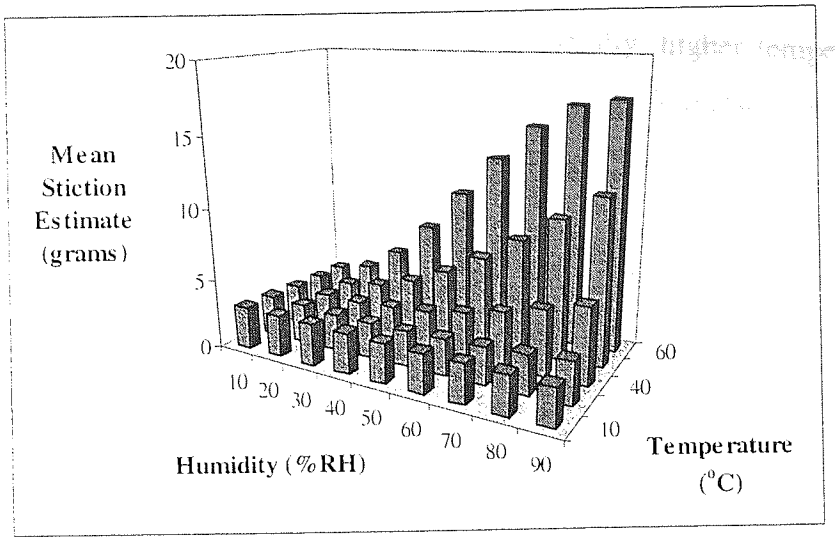

Figure 4.19 Exponential mean stiction model results against temperature and humidity

Modelled results now reflected the real-life situation, in that increasing relative humidity has most impact on stiction at high temperatures, with most damaging conditions being high temperature and high humidity. Further investigation of vapour pressure as a modelling parameter for stiction is made in Section 4.5.1.

4.1.4.3 CSS Friction Modelling using Water Vapour Pressure

The Gompertz model for flying friction, Equation 4.6, was applied to each of the environmental tests shown in Figure 2.3 a). The model was rejected in the event of the correlation coefficient $R^2<0.8$. In such tests the parameter 'r' would have reduced significance on burnishing rate and should not be included here. Where appropriate, 'r' was studied as a function of temperature and water vapour pressure to describe how these affected the rate of increase in friction during the early hours of a CSS test, Figure 4.20.

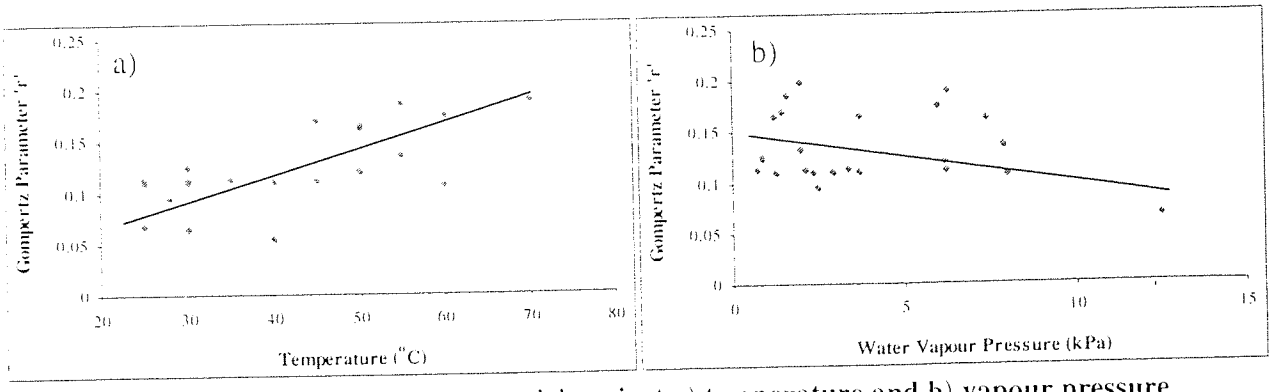

Figure 4.20 Gompertz parameter 'r' against a) temperature and b) vapour pressure

Although large spread was present in results, generally, higher temperatures ensured more rapid increase in flying friction at the start of testing. Conversely, higher vapour pressure reduced the rate of this initial increase. Thus, where friction was concerned higher humidity could be advantageous to friction at the interface.

4.1.4.4 Drag Friction Modelling using Water Vapour Pressure

Under Stable Conditions

Drag tests conducted in low vapour pressure always showed highest friction. A critical value of VP=2 kPa was established below which friction grew dramatically with time, Figure 4.21.

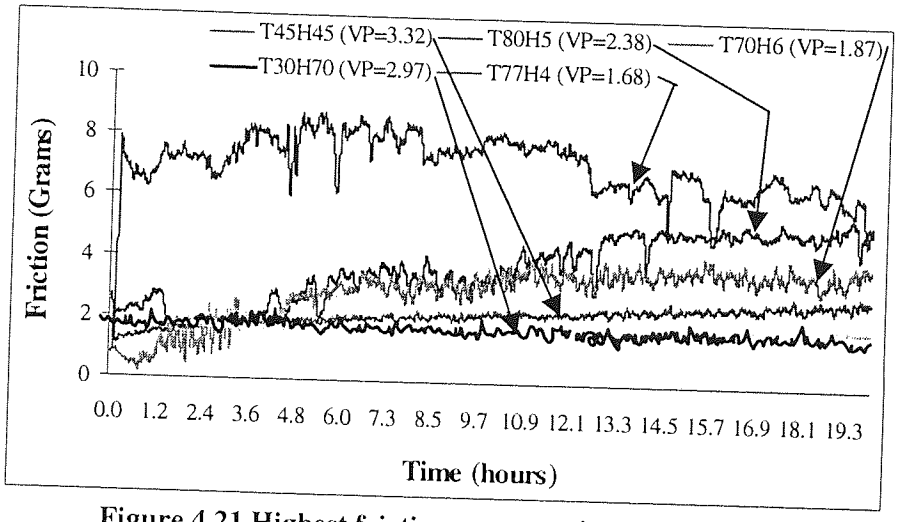

Figure 4.21 Highest friction was associated with VP<2 kPa

Under Varying Conditions

For the test shown in Figure 3.54, friction was inversely related to vapour pressure as shown in Figure 4.22. Notice the time delay between the increase in humidity and decrease in friction.

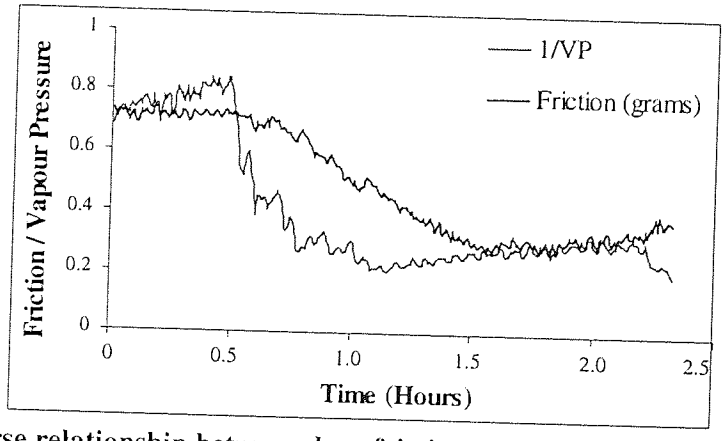

Figure 4.22 Inverse relationship between drag friction and vapour pressure (40°C/60% RH test)

The relationship was not always so well matched, Figure 4.23, shows another example of sudden humidity change on friction. 1/VP values were low due to the humidity being very high during this test (90% RH at 40°C), thus scaling values $\frac{5.5}{VP}$ would provide a better approximation for friction in this instance.

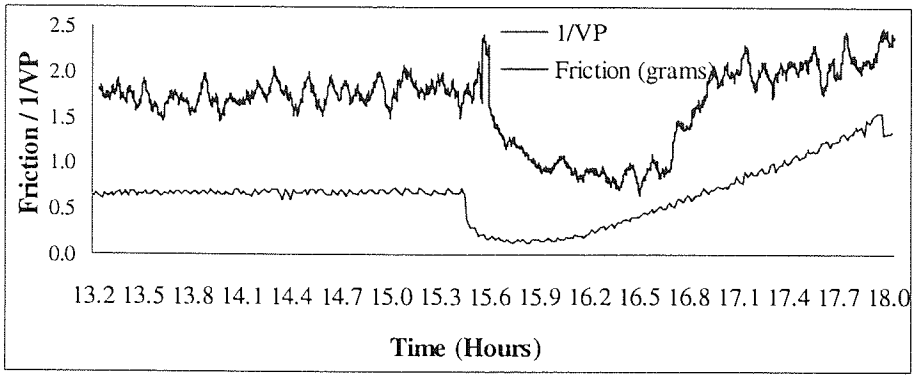

Figure 4.23 Inverse relationship between drag friction and vapour pressure (40°C/90% RH test)

By backwards time shifting 1/VP values by 5 minutes and plotting friction against $\varsigma/_{VP}$, where ς is a scaling factor (where appropriate), it can be seen that for both examples very clear relationships were observed, Figure 4.24.

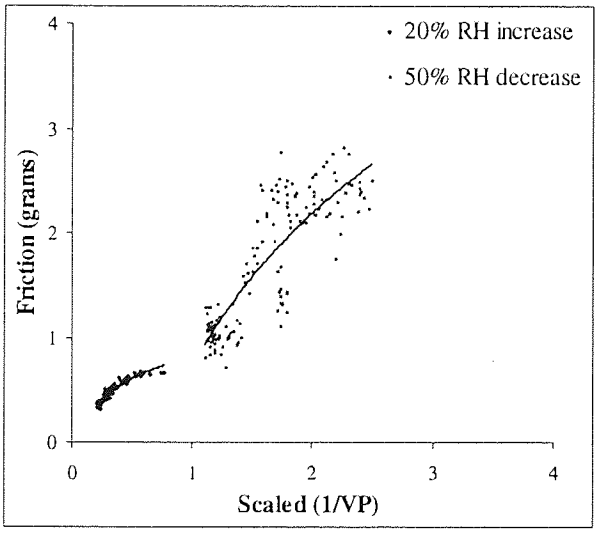

Figure 4.24 Clear proportionality between inverse vapour pressure and friction

It was found that ς was related to the amount of change in humidity occurring, with largest changes requiring larger scaling factors. That is, the most dramatic changes in environment had most pronounced affect on friction as expected.

4.1.4.5 Drag Friction Analysis using Dew Point Temperature

Dew point temperature was also studied as alternative gauge of humidity. If a volume of air is cooled; eventually enough energy will be removed to allow condensation to occur. The temperature where condensation begins is known as the dew point temperature. In terms of relative humidity, as the air is cooled relative humidity increases, when relative humidity reaches 100% dew point temperature has been reached. Dew point temperature is related to water vapour pressure as

$$\frac{116.9 + 273.3\ln(VP)}{16.78 - \ln(VP)} \qquad \textbf{Equation 4.17}$$

Unlike relative humidity if dew point increases, it is only because the amount of moisture increases. If relative humidity changes it can be because of changes in temperature or humidity.

Dew point can never be higher than the temperature, at saturation, i.e. 100% relative humidity the temperature and dew point are the same. Returning to the drag test illustrated in Figure 3.56, a sudden increase in humidity led to erratic friction behaviour. Adding dew point to this graph showed that immediately prior to erratic friction, temperature and dew point met, i.e. condensation would definitely have occurred at this time, Figure 4.25.

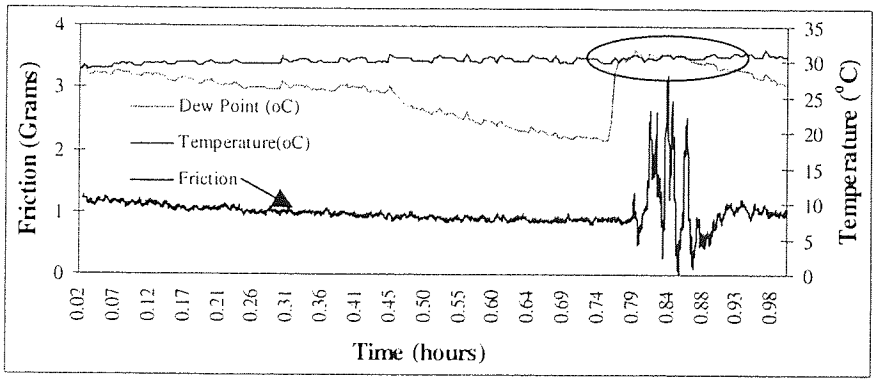

Figure 4.25 Dew point temperature reaching air temperature during drag test

In a separate test, dew point was very close to air temperature and similar friction behaviour was observed, Figure 4.26.

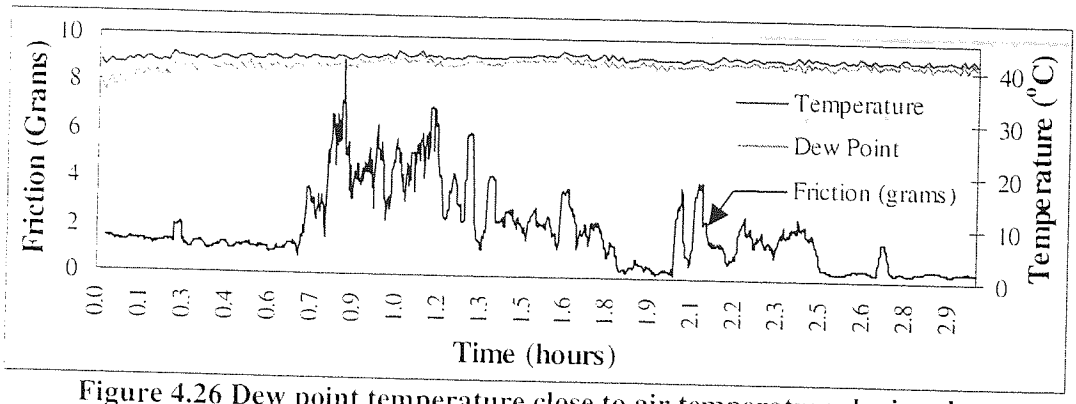

Figure 4.26 Dew point temperature close to air temperature during drag test

Although high humidity has been shown to reduce friction during drag testing, it was found beneficial to monitor dew point temperature and ensure it remained less than air temperature. Dew point could occasionally explain erratic friction behaviour.

4.2 Fly Height Modelling with Extension to Friction Estimation

4.2.1 Velocity Based Model

In order to achieve higher areal density low slider fly height is required, Section 1.1, however there needs to be a compromise to minimise slider contact with disk Thus, it was important to study fly height in this project.

A relationship was deduced between flying friction and velocity for the NPAB slider as shown, Figure 4.27a). By ignoring the low velocity point (1 m/s) on this graph, when slider was not flying completely, a linear trendline was applied to data. Note intercept was set to zero to reflect real situation, Figure 4.27 b) containing Equation 4.18.

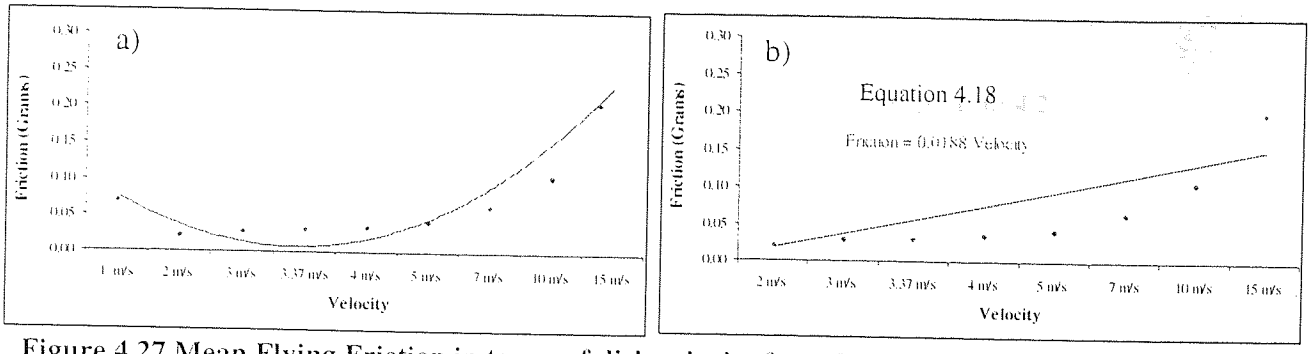

Figure 4.27 Mean Flying Friction in terms of disk velocity for velocity a) [1-15] and b) [2-15] m/s for NPAB slider.

Khurdoshov and Talke [110] expressed a similar linear relationship, except detection of surface interaction was achieved by acoustic emission signal (AE), in fact root-mean-square of AE signal was used. Relationship between V_{rms} (mV) and disk velocity, V (m/s) was found to be linear, such that

$$V_{rms} = 91V \qquad \textbf{Equation 4.19}$$

It was also stated that V_{rms} signal was related to disk velocity and slider fly height, FH (nm) as

$$V_{rms} \propto \frac{V}{FH} \qquad \textbf{Equation 4.20}$$

By equating like terms (V) in Equations 4.18 and 4.19 and substituting into Equation 4.20, it was given that

$$4840.426\,F = \frac{kV}{FH} \qquad \textbf{Equation 4.21}$$

where k was a constant of proportionality.

The known flight height for the NPAB slider was 63 nm during normal flying operation, using this the value of the constant is k=3049.47

Thus, NPAB slider fly height was estimated by

$$FH = \frac{V}{1.59F} \qquad \textbf{Equation 4.22}$$

Similarly, relationships were deduced between fly height and friction for the tri-pad slider as follows. Linear fit shown is in Figure 4.28.

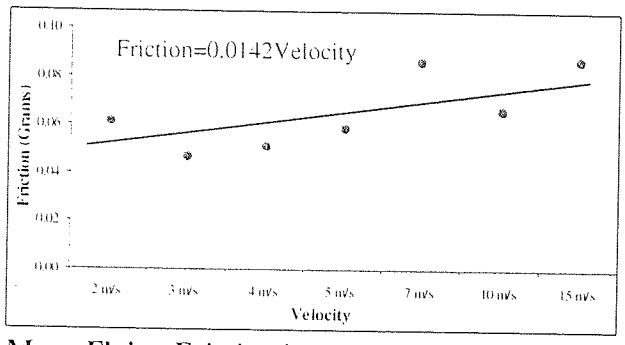

Figure 4.28 Mean Flying Friction in terms of disk velocity for tri-pad slider

A relationship was formed as above, such that

$$FH = \frac{V}{1.67F} \qquad \textbf{Equation 4.23}$$

Using experimental mean friction values and velocity, fly height profiles were drawn for each slider type, Figure 4.29 a) and b). The predicted values agreed with intuition, in that flying height was low when disk velocity low and airflow was insufficient to support slider. As disk velocity increases so does fly height, this continues until the sub-ambient force begins to pull slider down to disk at high velocity in the case of NPAB. There was no such force for the tri-pad so fly height continues to increase with velocity.

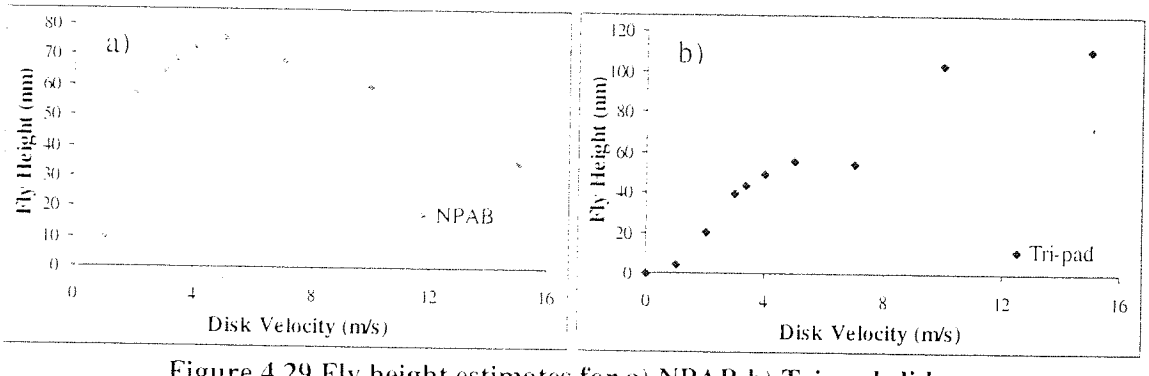

Figure 4.29 Fly height estimates for a) NPAB b) Tri-pad slider

Equation 4.22 was also used to estimate flying height dynamically during the ramp-up and dwell phase of a CSS cycle for various dwell velocity, results are shown for NPAB slider, Figure 4.30 a), and b).

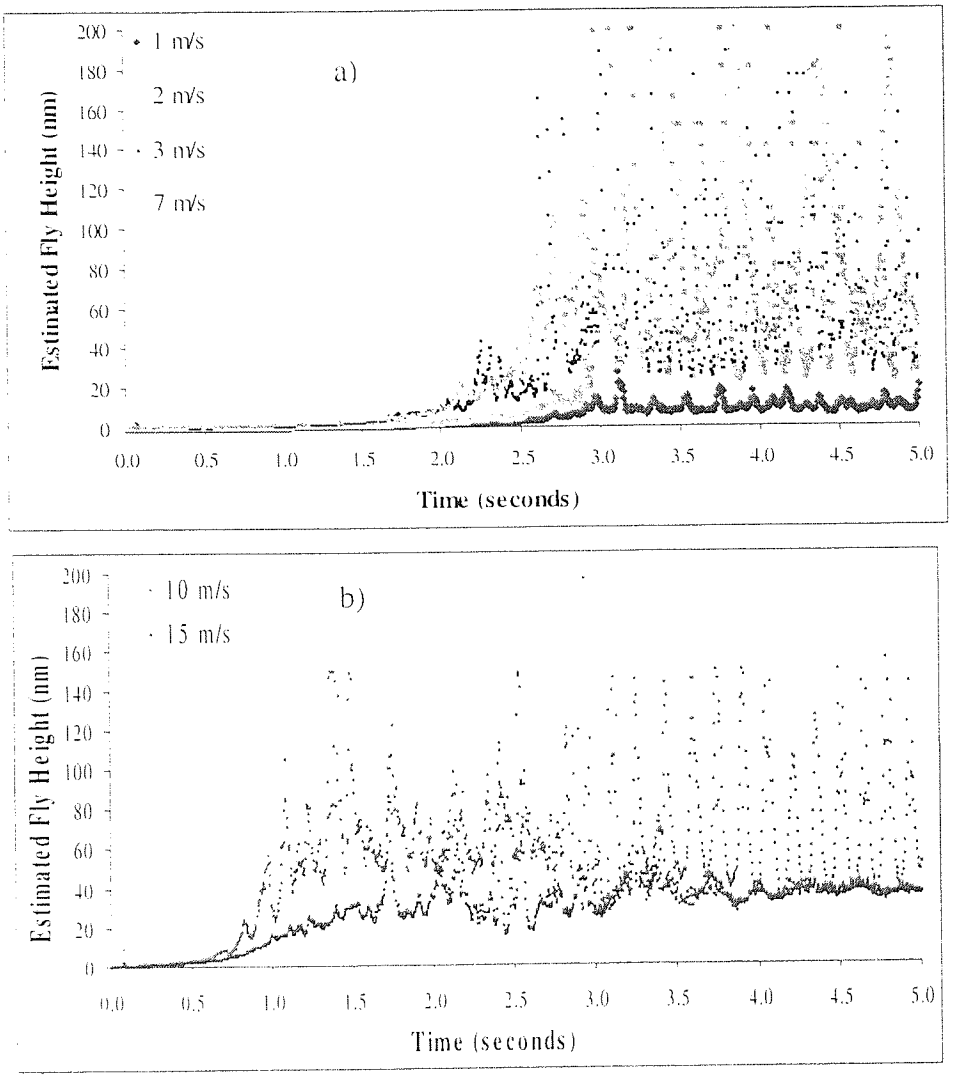

Figure 4.30 Dynamic fly height estimation for NPAB at a) low/medium and b)high dwell velocity

Results were as expected for dwell velocity ≤7 m/s with flying height increasing to dwell time and then levelling off. For higher dwell velocity erratic flying behaviour was observed but as expected mean flying height was lower since subambient force had initiated. That is, sufficient pressure had built up in the recessed region to oppose the air bearing force and decrease fly height.

For the tri-pad slider the estimated fly height increased and levelled-off as the cycle entered its dwell phase. Less spread was observed for this type of slider, this was due to original friction values containing less spread, Figure 4.31 a) and b) illustrate. Note in Figure b) increase not reduction in fly height occurs at high velocity due to the absence of a negative pressure air bearing in this type of slider.

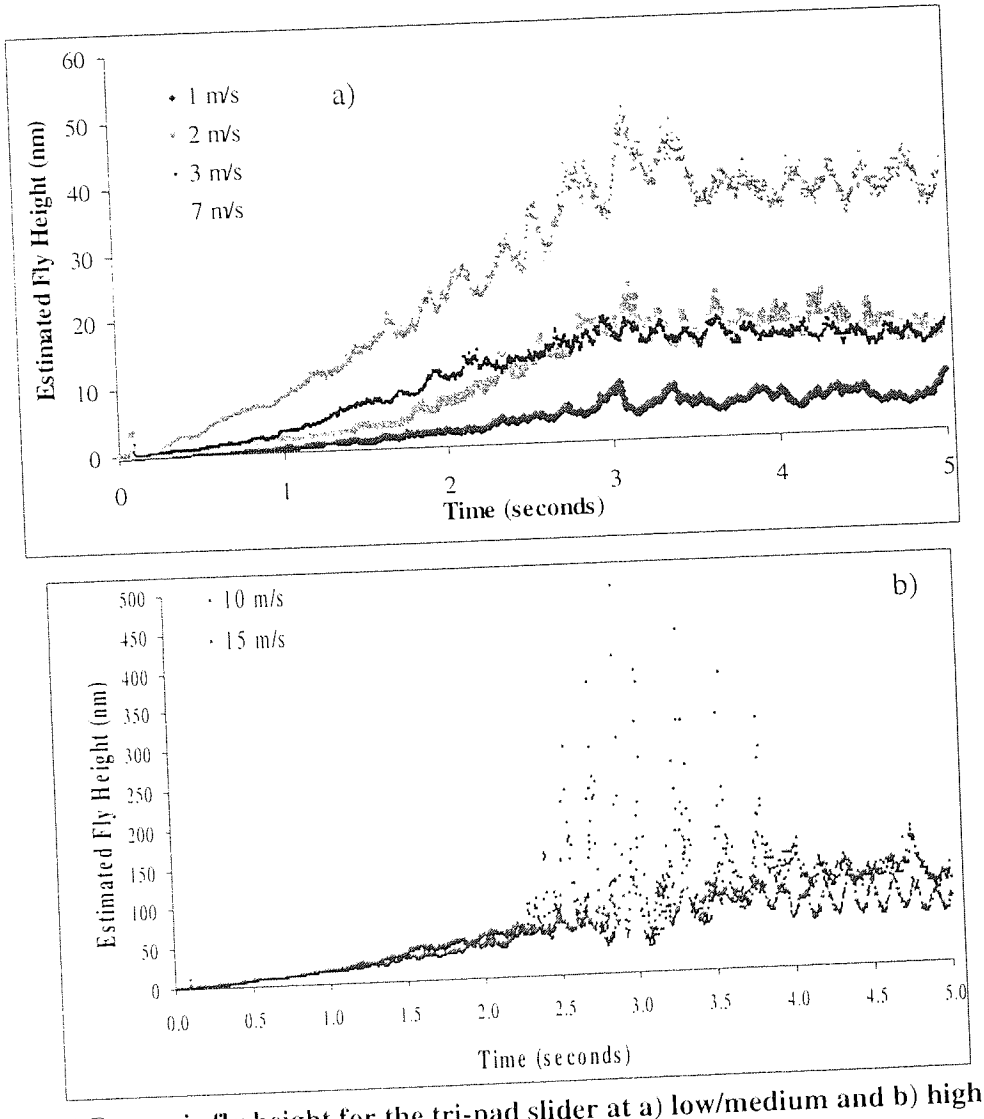

Figure 4.31 Dynamic fly height for the tri-pad slider at a) low/medium and b) high dwell velocity

When comparing dynamic flying heights for both slider types it appeared that in the very first second of disk start up the tri-pad slider flew higher than the NPAB. Figure 4.32 a) shows true values and Figure 4.32 b) modelled values for clarity.

The NPAB slider reached its maximum flying height in 2 seconds as opposed to the 4 seconds taken by the tri-pad. Logistic equations were used to model data as shown with parameter values given in Table 4.1 below. The faster take-off observed with the NPAB slider was due

to the contact location shift occurring sooner. The shorter rails on this type of slider meant that load transferring from the leading to trailing edge occurred sooner [122].

$$FH = \frac{a}{(1 + b * e^{-ct})}$$

Equation 4.24

Parameter	NPAB	Tri-pad
a	80.78	78.43
b	82593.88	61.46
c	5.85	2.10

Table 4.1 Logistic Parameters

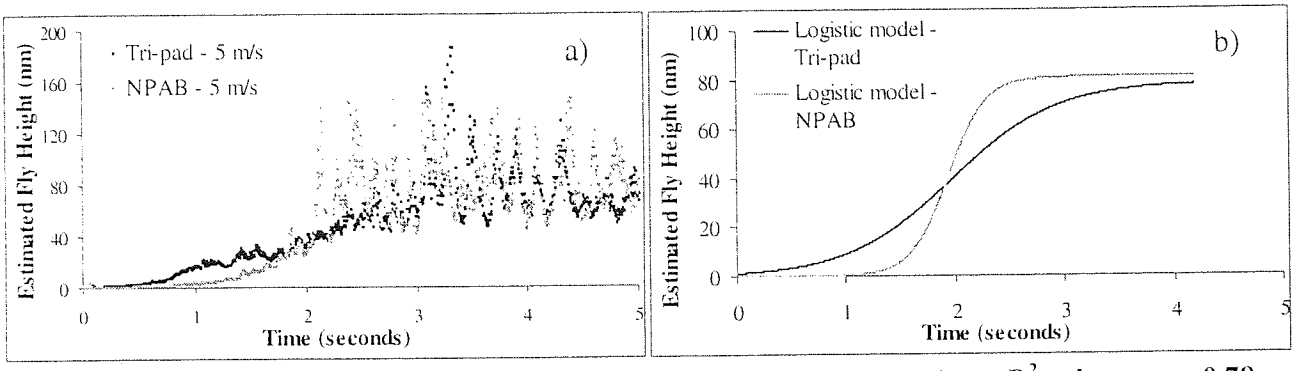

Figure 4.32 a) Actual fly height data and b) Logistically modelled data (note R^2 values were 0.78 and 0.72 for NPAB and tri-pad respectively)

4.2.1.1 Using Velocity Based Model for Fly Height Prediction

Returning to Figure 4.29, models were used to predict fly height in terms of disk velocity, Figure 4.33 shows equations that fit the fly height estimates FH_1 and FH_2 respectively.

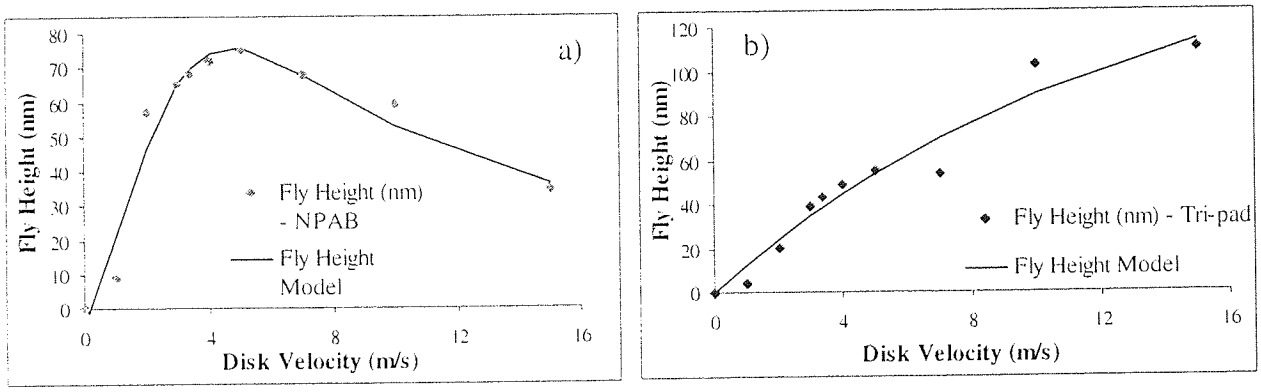

Figure 4.33 Fly height models for a) NPAB b) Tri-pad slider

The equations of the solid lines in above figures were

$$FH_1 = \frac{-4.37 + 23.22V}{1 - 0.14V + 0.047V^2} \quad FH_2 = 162.37(1 - e^{-0.081V})$$ **Equation 4.25** and **Equation 4.26**

Using Equation 4.25 and 4.26, fly height over a CSS cycle at any chosen velocity could be estimated, Figure 4.34 a), b), c) and d).

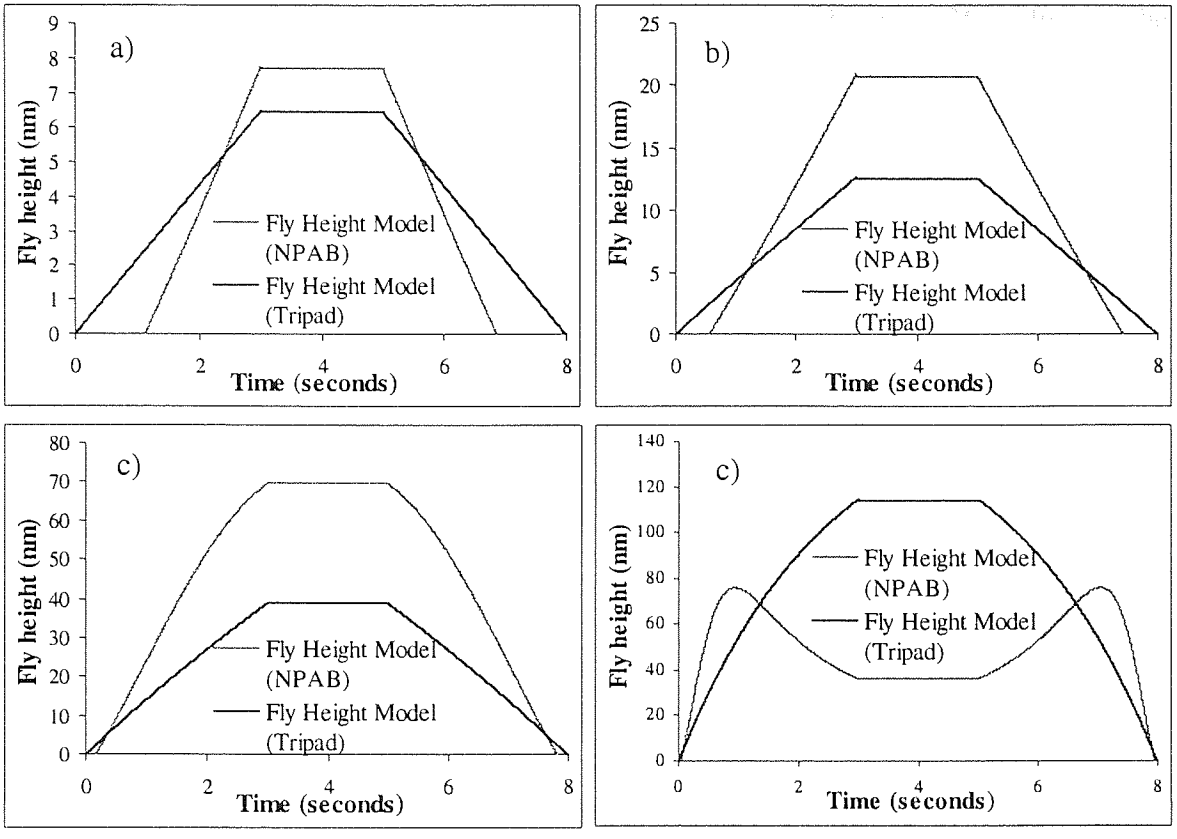

Figure 4.34 Flying height in terms of time for 4 dwell velocity, a) 0.5 m/s, b) 1 m/s, c) 3.37 m/s and d) 15 m/s.

Equation 4.25 was used to determine exactly when the NPAB's suction force initiated, Figure 4.35 illustrates that this occured between 5 and 5.5 m/s.

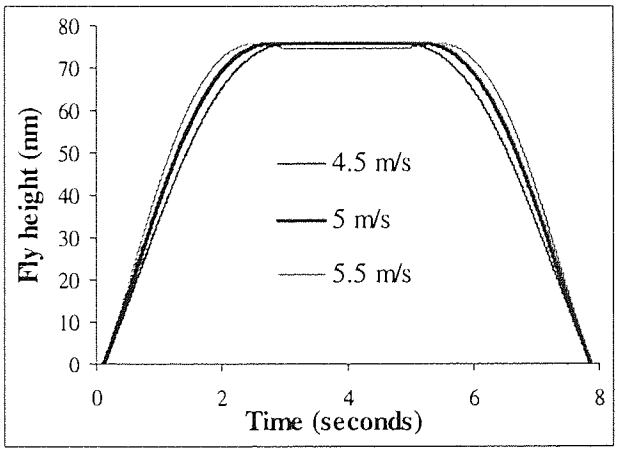

Figure 4.35 Showing negative pressure air bearing force initiates > 5 m/s

If this result is accurate, it would mean that the NPAB's suction force did not come into effect during the standard CSS test.

4.2.1.2 Using Velocity Based Model to Study Fly height Variation with Disk Radius

The difference in linear velocity experienced between slider/disk at disk inner/outer diameter was studied. The difference was greatest at high rotational velocity, Figure 4.36 a). In fact, the change in linear velocity with radius grew linearly with rotational velocity as shown in Figure 4.36 b). Differing linear velocity would definitely lead to differences in slider fly height.

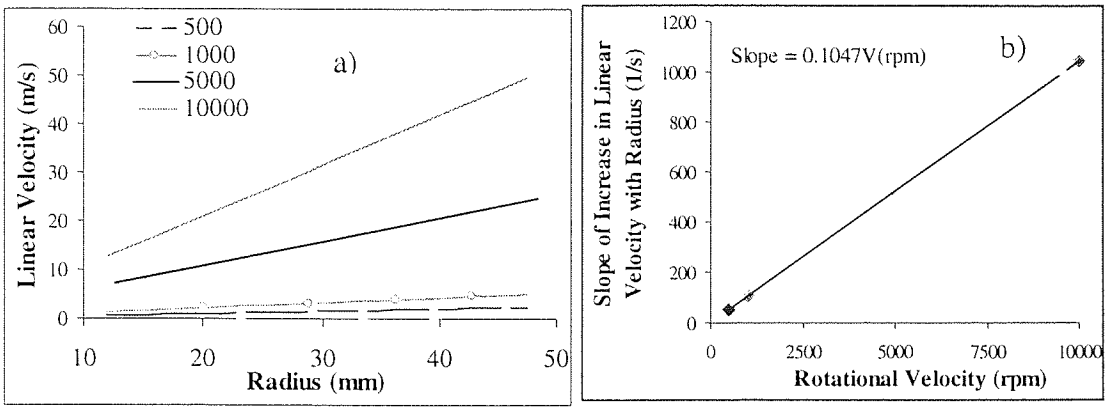

Figure 4.36 a) Increase in linear velocity at increasing disk radius and b) slope of increase in linear velocity with disk radius was linearly related to rotational velocity

Fly height variation with disk radius was studied using linear velocity equations from the above analysis, Equation 4.25 and 4.26 for NPAB and tri-pad respectively. This was performed for rotational disk velocity 500, 1000, 2000 and 5000 rpm, Figure 4.37 below.

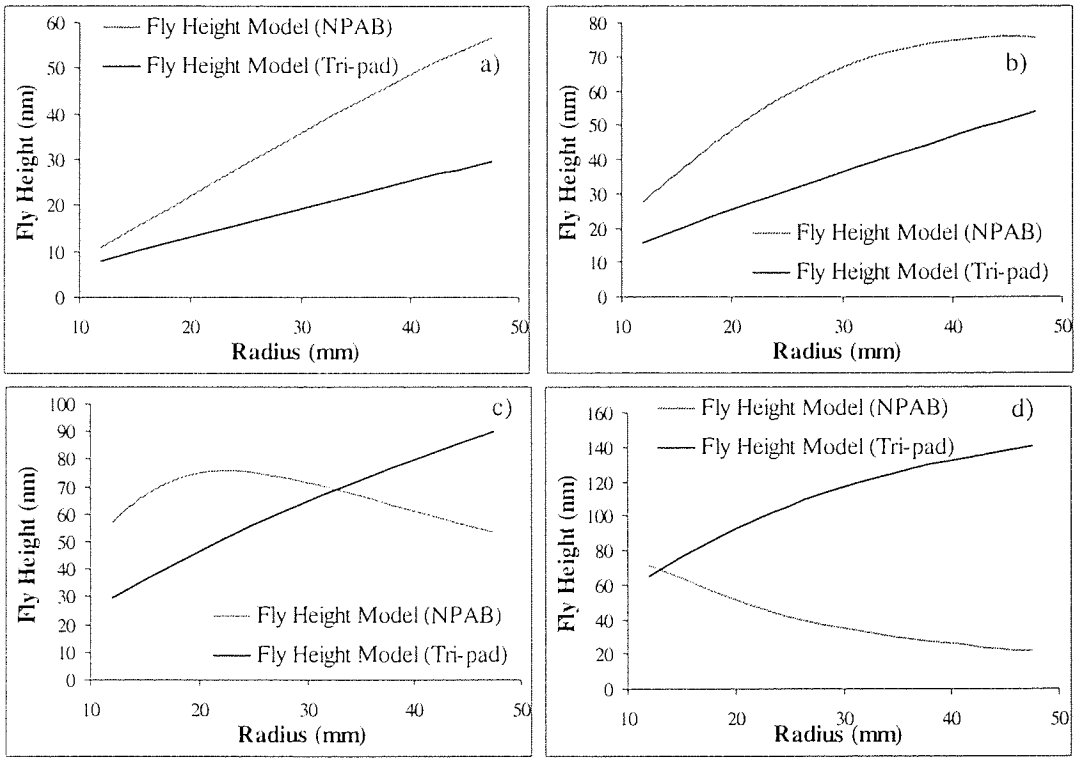

Figure 4.37 Relationship between fly height and disk radius for both slider types at disk rotational velocity a) 500, b) 1000, c) 2000 and d) 5000 respectively

At low disk velocity, Figure 4.37 a) the NPAB flew higher than the tri-pad and would probably clear the majority of disk asperities. The tri-pad slider flew below disk P-V at 1000 rpm, Figure 4.37 b) and much contact would take place at any disk radius. The NPAB had a more level flying trace from inner to outer diameter at 2000 rpm, Figure 4.37 c).

It was clear that at 5000 rpm the tri-pad slider flew extremely high, especially at outer diameter. This would lead to large signal spacing loss. This type of slider could be said to be unsuitable for use at such high disk velocity. The NPAB negative force ensured this slider did not fly too high, if anything the slider may fly too low giving problems of contact that would be increased by the high speed of impact of asperities.

Comparing the range in fly heights (maximum - minimum) for both sliders over a larger range of velocity (50-10,000 rpm), the NPAB had the most level flying profile, Figure 4.38. Although the tri-pad slider fly height range decreases beyond 5000 rpm, the actual fly height values remained very high, it was merely the difference between them that lessened.

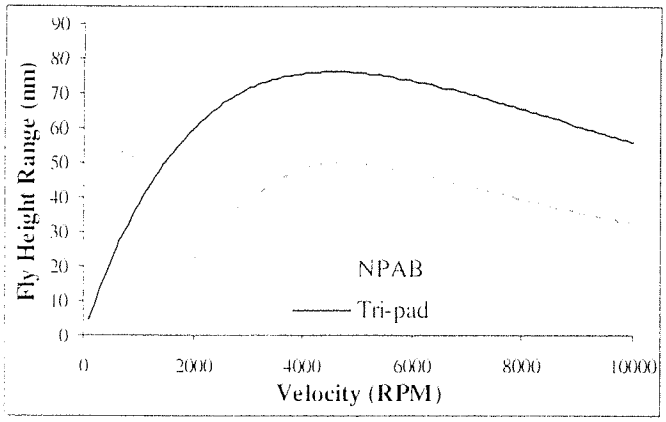

Figure 4.38 Fly height range (max-min) with disk radius for velocity [50-10000] rpm

The maximum peak observed for the NPAB at around 1000 rpm occurs because the slider's negative force was not effective (linear velocity was < 5 m/s), producing large differences in fly height at inner/outer disk radii. The table below illustrates the corresponding linear velocities at this speed, Table 4.2.

Radius (mm)	Linear Velocity (m/s)
12.000	1.257
15.227	1.595
18.455	1.933
21.682	2.271
24.909	2.608
28.136	2.946
31.364	3.284
34.591	3.622
37.818	3.960
41.045	4.298
44.273	4.636
47.5	4.974

Table 4.2 Linear velocity with radius at 1000 rpm

4.2.1.3 Using Velocity Based Model to Estimate Friction Trace

Using Equation 4.22 and 4.23, estimates for friction during CSS were deduced using fly height values. Figure 4.39 shows results of this for CSS traces 1.5, 3.37 and 7 m/s dwell velocity, respectively.

It was observed that the model collapsed for the tri-pad slider, this was due to estimation of fly height values being too high during take-off period, rendering take-off friction very small. An alternative model will be discussed for this type of slider in Section 4.2.2.

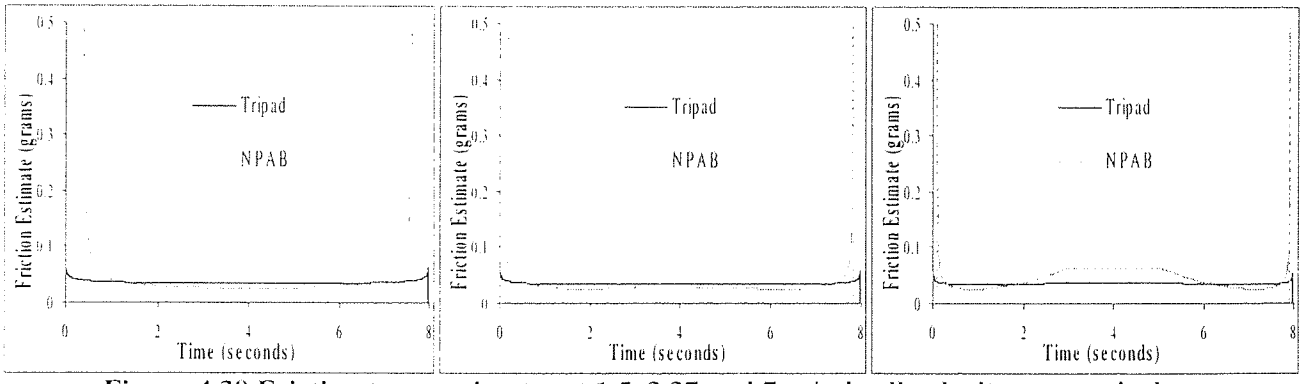

Figure 4.39 Friction trace estimates at 1.5, 3.37 and 7 m/s dwell velocity, respectively.

For the NPAB, modelled friction seemed realistic, with the slider taking-off sooner at higher velocity and friction increasing during dwell phase of 7 m/s test due to negative pressure force decreasing fly height.

4.2.2 Disk Roughness Based Model for Tri-pad Slider

It has been reported that for the tri-pad slider, fly height was greater over smooth disks and at high velocity. Table 4.3 and Figure 4.40. illustrate slider fly height (in nm) over 5 different aluminium disks and at 5 different velocities as reported in [68]. Disks differed in terms of roughness only. Fly height measurements were taken using a multi-channel laser interferometer. Measurements were taken at a point on the slider's contact pad just forward of the trailing edge. AE technique was also used to confirm contact between slider and disk during testing.

Linear Velocity (m/s)	Disk Surface Parameters :				
	R_a	**2.47**	**2.04**	**1.73**	**1.20**	**0.9**
	R_p	**8.39**	**6.26**	**6.66**	**4.47**	**N/A**
	R_{rms}	**3.07**	**2.54**	**2.20**	**1.52**	**1.25**
1	18	32	40	52	60
5	24	39	46	59	70
7.5	29	41	50	61	76
10	31	44	52	69	79
15	38	52	60	74	90

Table 4.3 Flying height values (nm) for 5 disks of different roughness at velocity [1-15] m/s

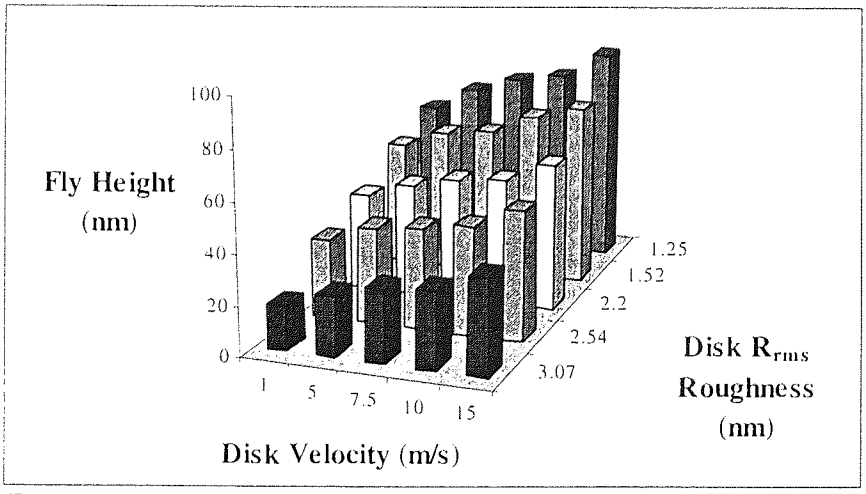

Figure 4.40 Flying height values (nm) for 5 disks of different roughness at velocity in [1-15] m/s

4.2.2.1 Neural Network Sensitivity Analysis to Build Model

It was decided to use the fly heights tabulated above to build an alternative model for fly height for the tri-pad slider during AFT testing.

A Neural Network Tool (NNT) was created using disk roughness parameters (R_a, R_{rms} and R_p) as inputs. For the desired outputs total flying height for each disk (summed over all velocity) and rate of increase in fly height with velocity were used.

The NNT was successfully trained and found to give low mean square error (<0.001) after 200 iterations, Figure 4.41. Figure 4.42 a) and b) show how closely the trained network matched the total fly height and slope respectively.

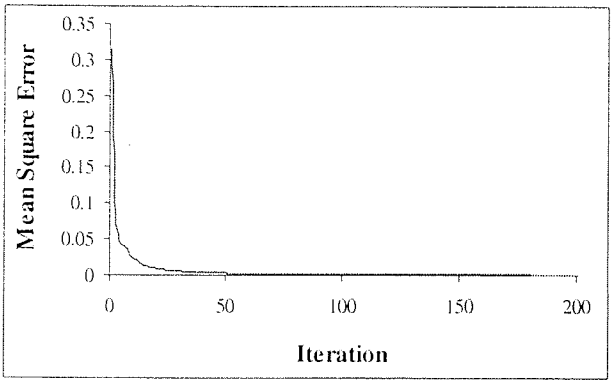

Figure 4.41 Error approaching 0 as network trains

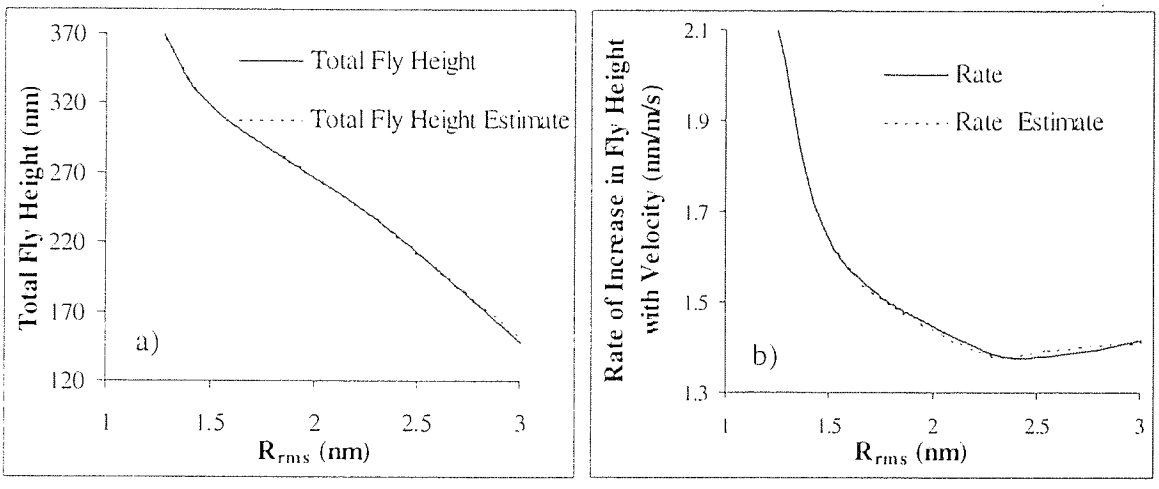

Figure 4.42 NNT output estimates for a) total fly height and b) rate of increase in fly height respectively

The R^2 values between estimate and true values was >0.999 in both cases.

Sensitivity analysis was carried out. This is where each parameter was varied between its mean +/- a user defined number of standard deviations with the effect on the output recorded. The NNT output was computed for a defined number of steps above and below the mean, the process was repeated for each input. Variation of each output with respect to the variation in each input was deduced.

It was found that the parameter R_a had the most impact on fly height when varied about +/- 3σ about it's mean using 200 steps, Figure 4.43 and Figure 4.44 illustrate.

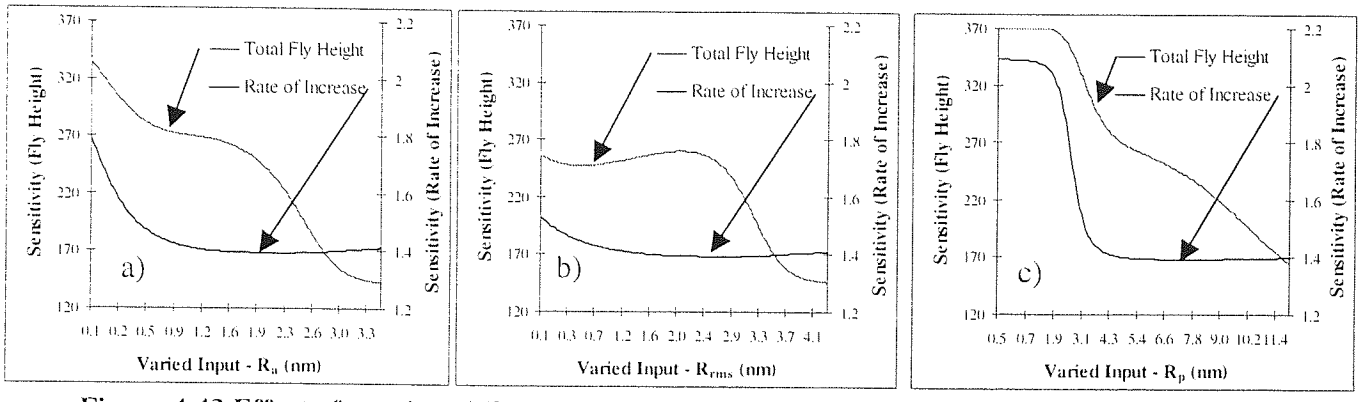

Figure 4.43 Effect of varying a) R_a, b) R_{rms} and c) R_p about it's mean on total/increase in fly height

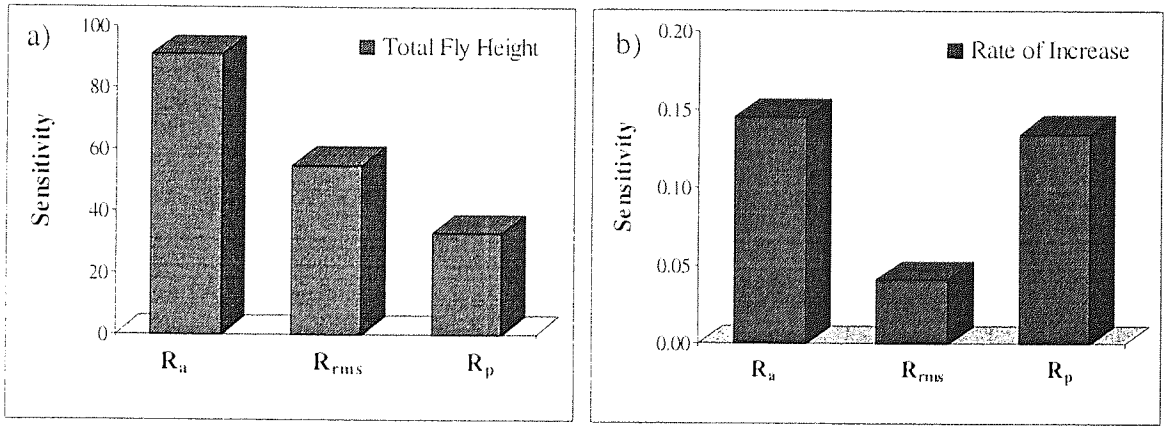

Figure 4.44 Sensitivity factors for each surface characterisation parameter. R_a had most impact on a) total fly height and b) rate of increase

Since the most significant parameter for disk roughness was found to be R_a, it was chosen for modelling purposes. From Table 4.3, flying height was proportional to velocity and inversely proportional to disk roughness, this was again confirmed in Figure 4.45.

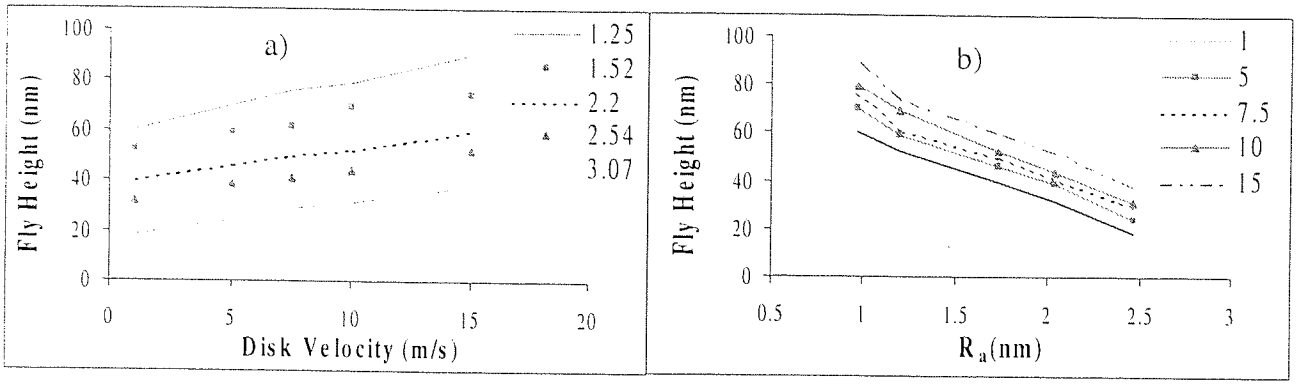

Figure 4.45 Fly height a) proportional to disk velocity and b) inversely proportional to disk roughness

Thus, it can be said that fly height (FH)

$$FH \propto \frac{V}{R_a} \qquad \textbf{Equation 4.27}$$

Re-plotting fly height values against $\frac{V}{R_a}$ a relationship was given as shown in Figure 4.46, the equation used to model values was

$$FH = 38.02 + 2.97\left(\frac{V}{R_a}\right) - \frac{2.74}{\left(V/R_a\right)^2} \qquad \textbf{Equation 4.28}$$

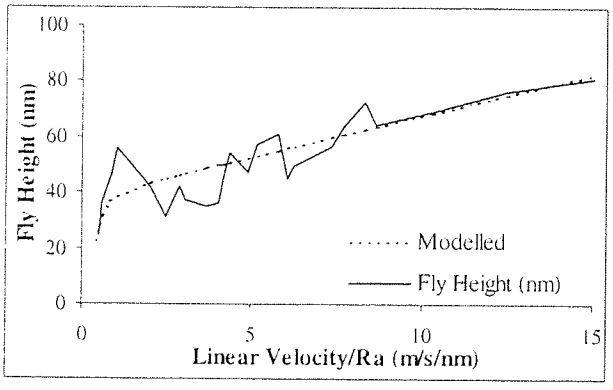

Figure 4.46 Relationship between fly height and linear velocity/Ra

Using Equation 4.28, a plot of fly height against linear velocity and disk roughness was produced, this is shown in Figure 4.47. Notice disk roughness was translated back into the R_{rms} to allow comparison with Figure 4.40.

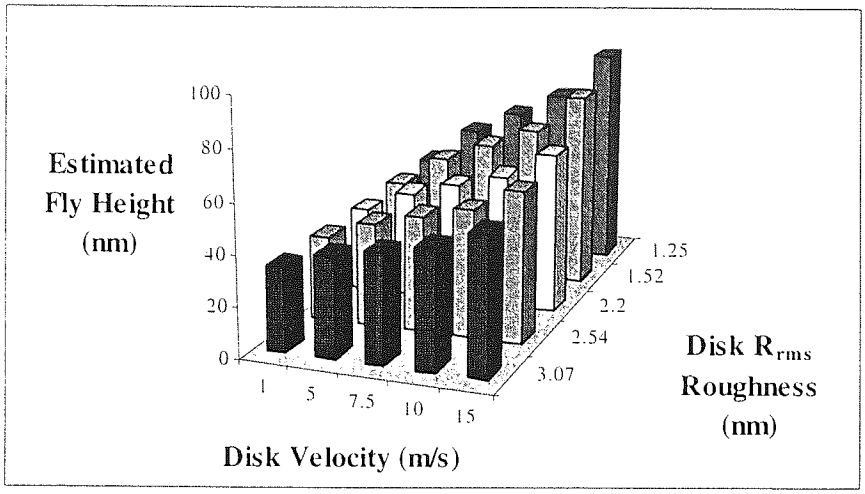

Figure 4.47 Fly height against linear velocity and disk roughness

Notice similarity between Figure 4.40 and 4.42, in fact, R^2=0.65 between true and estimated data sets.

By substituting values for velocity during standard CSS cycle into Equation 4.28 and using disk inner diameter roughness, R_a=4.33 nm, a trace of estimated tri-pad fly height was constructed, Figure 4.48.

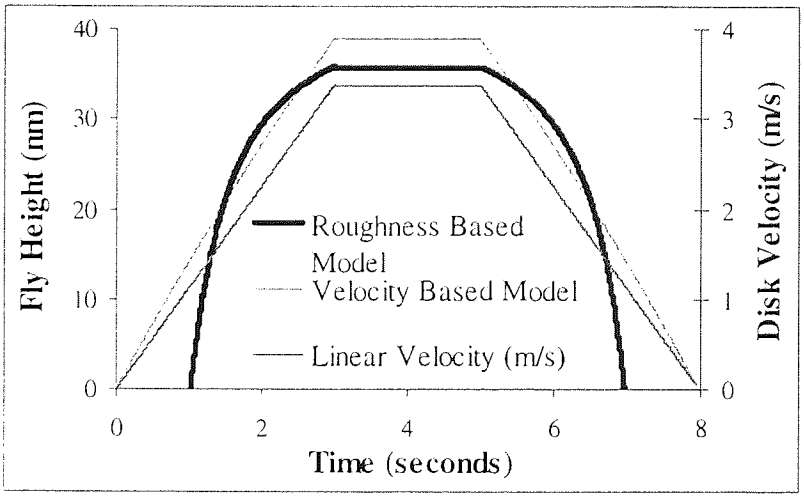

Figure 4.48 Modelled fly height and linear velocity against time during 1 CSS

The model predicted flying height of 35.82 nm during dwell phase of cycle, this was 8.32% lower than that predicted by the velocity based model (Section 4.2.1). Notice the model failed to predict positive fly height <1 second and >7 seconds into cycle, this was due to the negative end term of Equation 4.28 being large for small V. Generally, the model could not be used to predict fly height below a velocity of 1.2 m/s at this disk roughness.

Examining predicted flying height values at different dwell velocity, the following graphs were obtained, Figure 4.49.

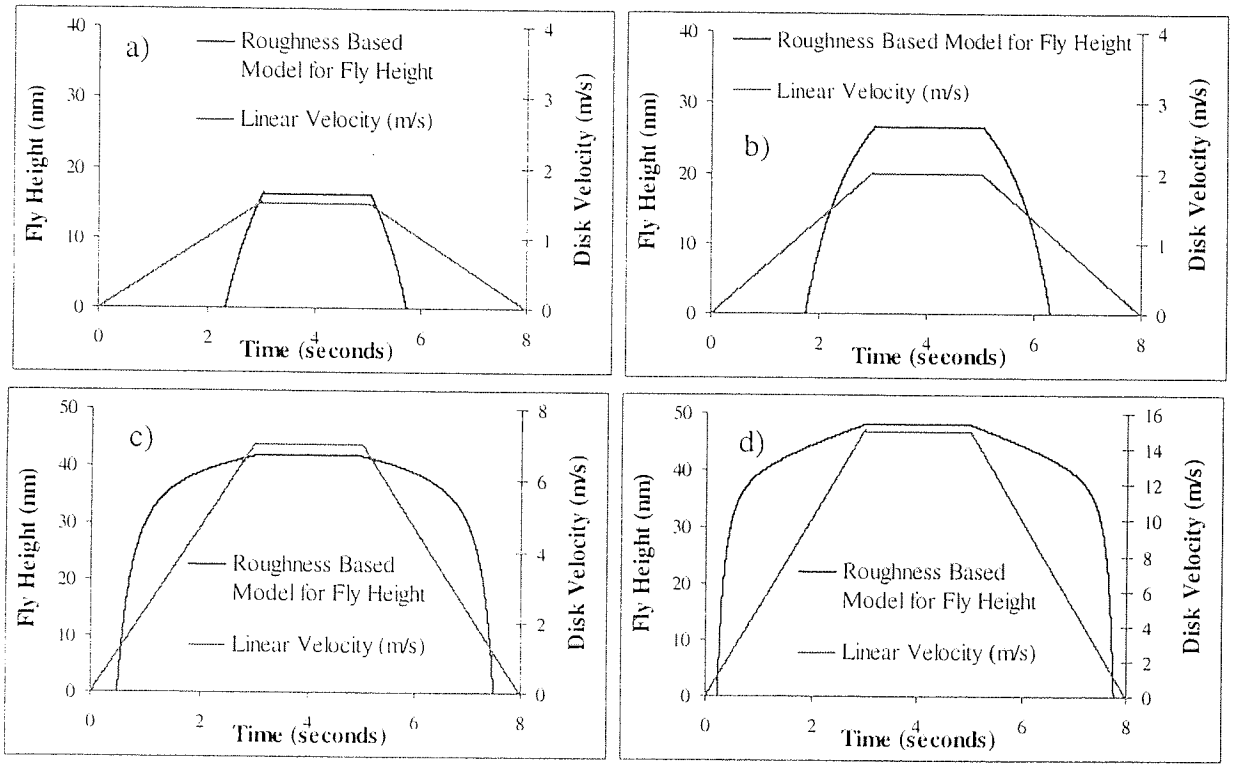

Figure 4.49 Estimated fly heights at a)1.5, b) 2, c)7 and c)15 m/s using roughness model

4.2.2.2 Using Disk Roughness Based Model to Estimate Friction

Estimates of mean flying friction were deduced for a range of dwell velocities, Figure 4.50.

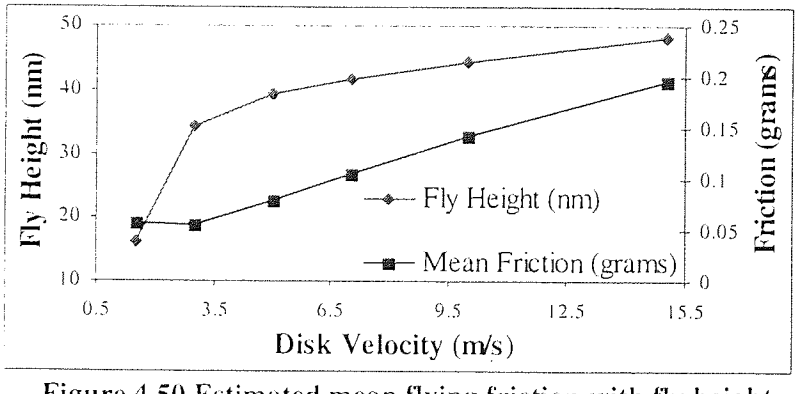

Figure 4.50 Estimated mean flying friction with fly height

Notice the fly heights predicted here were much lower than for velocity model, this difference was amplified at high velocity.

Equation 4.23 was also used to provide estimates for dynamic friction trace over 1 CSS, Figure 4.51 shows estimated traces for 1.5, 3.37 and 7 m/s dwell velocity.

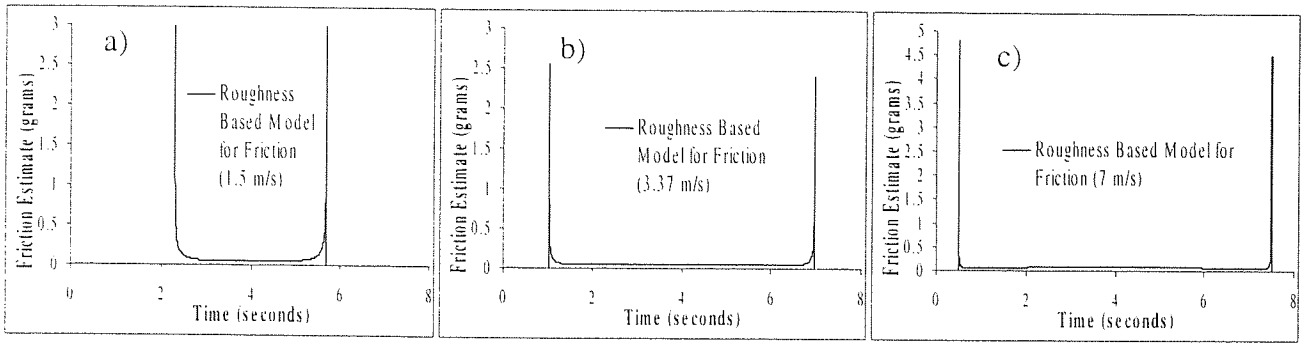

Figure 4.51 Friction trace estimates at a) 1.5, b) 3.37 and c) 7 m/s dwell velocity, respectively

Notice the modelled friction follows intuition in that the take-off occurs sooner for high velocity cycles and take-off peak magnitude grows with velocity. However, again the model failed for low velocity.

Flying height values, and hence mean flying friction, were deduced for various disk roughness. In this section of work it was assumed that dwell velocity was 3.37 m/s, Figure 4.52.

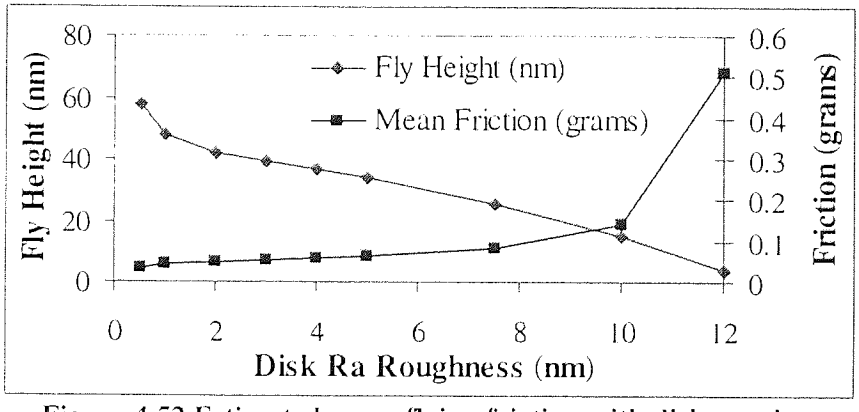

Figure 4.52 Estimated mean flying friction with disk roughness

Dynamic friction trace estimates were produced for different disk roughness, see Figure 4.53.

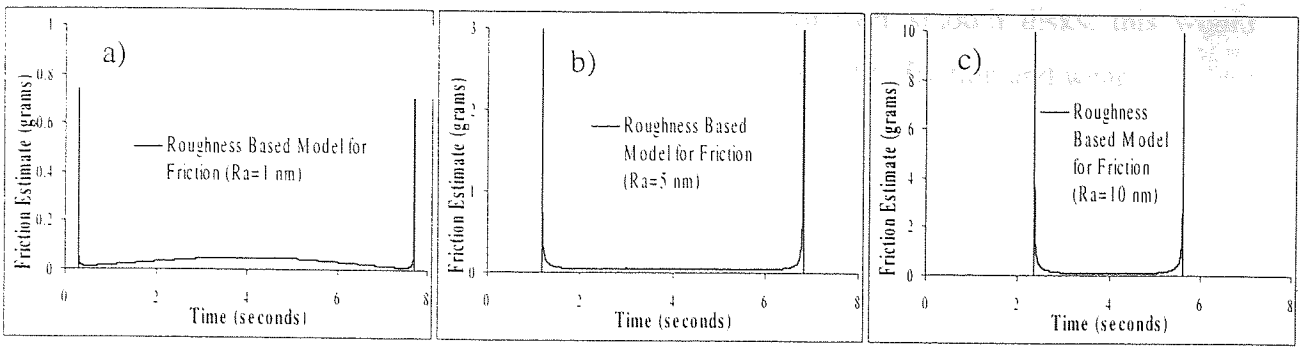

Figure 4.53 CSS friction trace estimates for disks with R_a a) 1 nm, b) 5 nm and c) 10 nm

The model supported the notion that the time at which friction suddenly decreased (i.e. the time when the slider is completely flying) will be earlier for smooth disks than rough. Obviously, this was due to smooth disks containing lower asperities than rough, meaning the slider flew clear of the disk sooner. Also, it is recognised that in practice disk roughness would affect the air flow between slider and disk and thus affect slider fly height.

However, the model greatly overestimated the dynamic friction peak on take-off/landing, and gave a value of 2.43 grams for take-off from a disk with R_a=4.33 nm at 3.37 m/s (the actual value observed in experiments was around 0.4 grams). This overestimate was amplified at high disk R_a.

By comparing the friction curves in Figure 4.51 and Figure 4.53 it seemed that low velocity yielded a similar friction trace to high disk roughness. That is, there was very late take-off and disk much longer duration contact between slider and disk, this supports the recent trend towards using high velocity drives and very smooth disks in the drive industry.

Figure 4.54 compares the estimated trace from a rough disk/slow cycle and a smooth disk/fast cycle.

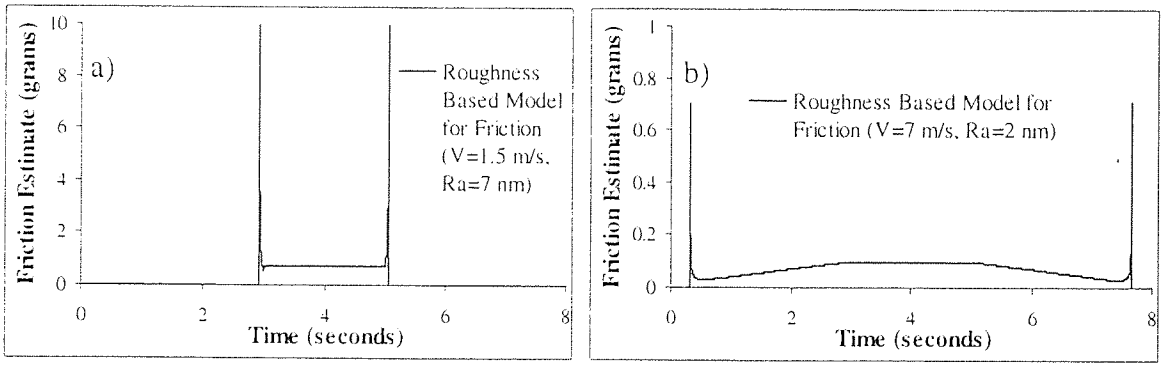

Figure 4.54 CSS friction trace estimates for a) rough/slow cycle and b) smooth/fast cycle

Bogy also reported that the slider flew with higher pitch over smooth disks, this would decrease the possible contacts, again and advantage with respect to friction and wear.

4.2.2.3 Using Disk Roughness Based Model to Study Fly height Variation with Disk Radius

It was decided to study how fly height varied with disk radius using the roughness-based model. Figure 4.55 shows the estimated fly height for tri-pad sliders at velocity 500, 1000, 2000 and 5000 rpm. Note velocity model fly height results are included for comparison.

Again R_a=4.33 nm was used to simulated a crosshatched disk and roughness was assumed to be constant at all disk radii. The model was then adapted to examine how the slider flew over a disk having graded texture. The simulated grading used was R_a=4.5 nm at disk inner diameter and R_a=2.5 nm at outer.

Again the roughness-based models provided no information for low velocity (<1 m/s), for example at disk inner radius during the 500 rpm test.

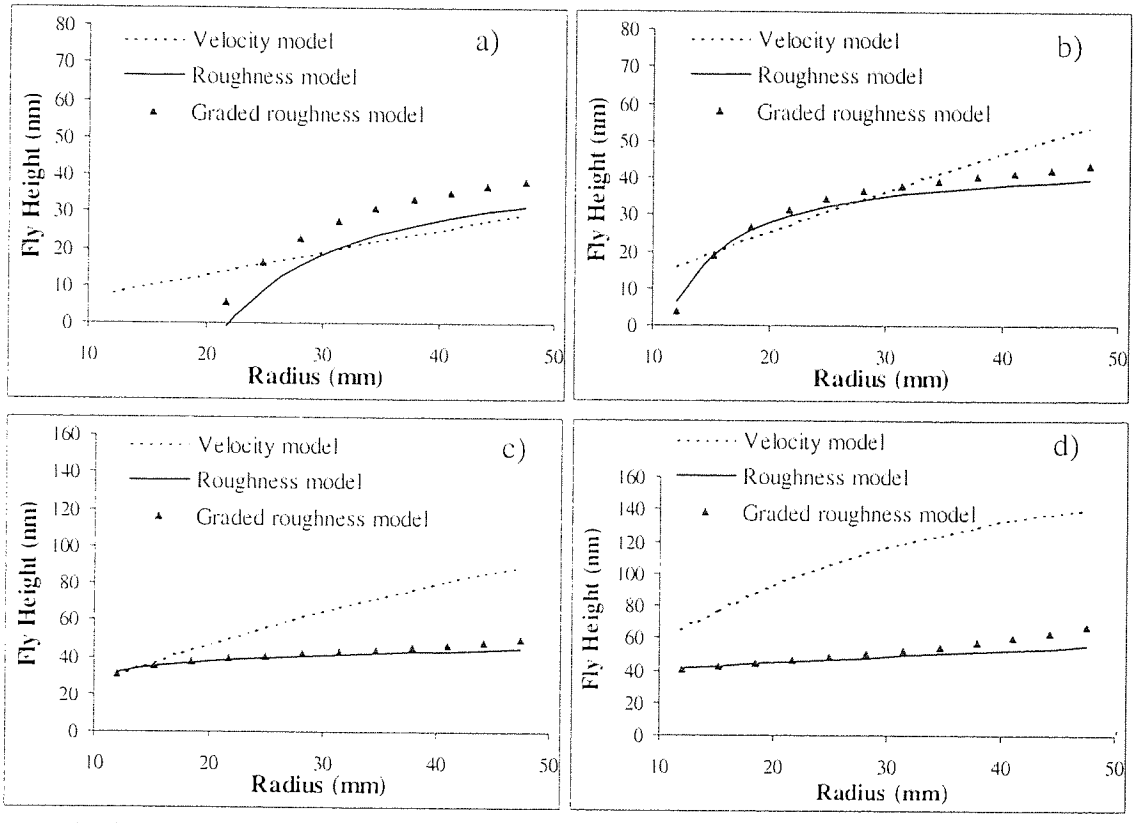

Figure 4.55 Relationship between fly height and disk radius for velocity and roughness models at disk rotational velocity a) 500, b) 1000, c) 2000 and d) 5000 respectively

The roughness models predicted a more level flying profile with lower value than were previously predicted. Note the effect of slight grading (losing only 2 nm R_a across disk radius) does not affect flying trend significantly.

Fly height range studies implied most variation occurred at low velocity (<1000 rpm), however this was due to negative fly heights, incorrectly predicted by model and should be neglected, Figure 4.56.

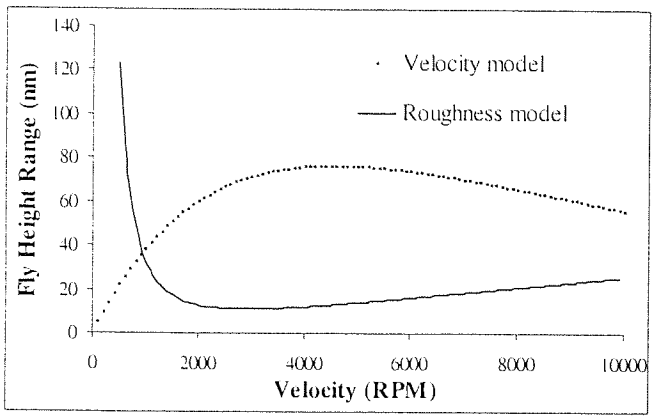

Figure 4.56 Fly height range (max-min) with disk radius for velocity [50-10000] rpm

If fly height estimated were required for this type of slider, it would be advisable to take a value that was bounded on the extreme models.

An estimate of how the slider flew with radius over a laser-textured disk was formed, Figure 4.57.

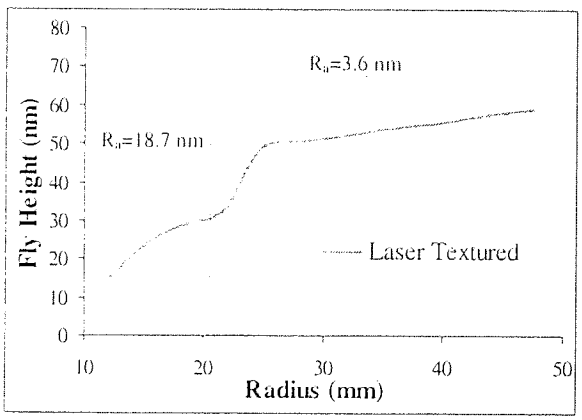

Figure 4.57 Fly height over laser textured disk spinning at 5000 rpm.

Notice a sharp fly height increase of 20 nm was observed in the region where texture change occurs.

4.2.3 Comparison of Friction Estimates Provided by Velocity and Roughness Models

Using the velocity based model for NPAB and roughness based model for tri-pad; friction was studied as a function of fly height. The results were as shown in Figure 4.58a) and b). Again, note that the roughness model did not provide any useful information below 10 nm.

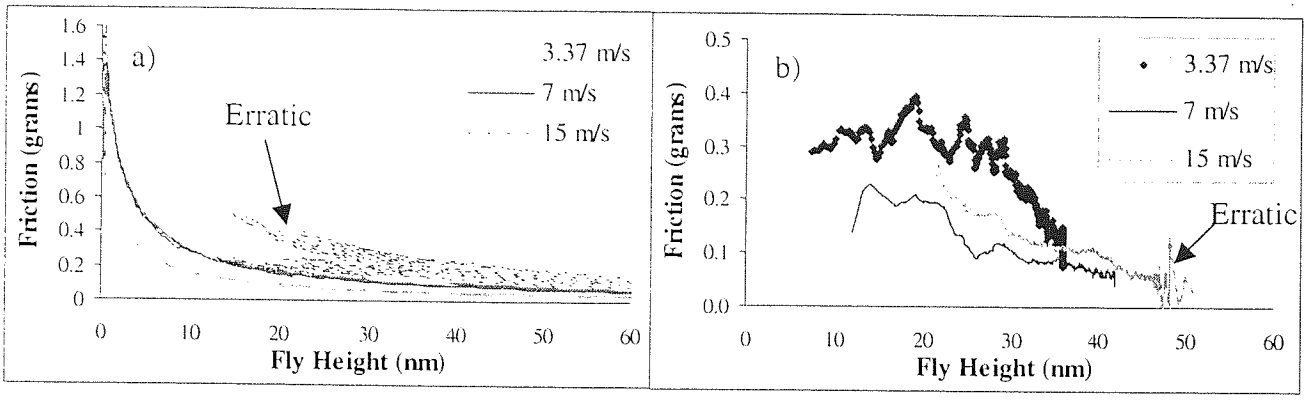

Figure 4.58 Friction in terms of fly height for a) NPAB and b) tri-pad slider

Each slider experienced different friction readings at the same fly heights for different dwell velocities. For example, at 10 nm the NPAB experienced friction of 0.17 and 0.34 grams for 3.37 and 7 m/s dwell velocity, respectively. This shows that other factors, such as the speed of asperity contact and proportion of slider load supported by air bearing, must influence friction.

For the NPAB erratic behaviour was observed at 15 m/s, this was explained by external vibration of AFT rig causing occasional contact and was especially noticeable during the slider's low flying phase (where negative pressure force would be initiated), Figure 4.58 a).

For the NPAB take-off occurred sharply above fly height of 20 nm (friction was below 0.1 gram), for tri-pad take-off was a less sudden event with fly height of 37 nm necessary before 0.1 gram recorded.

The main difference between sliders was due to the contact pad on the tri-pad; this gave proximity contact with disk as slider pitch increased. Therefore, although the tri-pad was deemed to be flying it could still be in partial contact with the disk. The exception to this was at extremely high velocity (>10 m/s) when tri-pad flying height would exceed disk P-V height and slider would fly free of disk, however AFT apparatus vibration could then occur causing erratic behaviour, see Figure 4.58b).

4.3 Slider Damage Location Analysis

4.3.1 Trailing/Leading Edge Comparisons

Generally, high friction experienced during a CSS test indicated slider trailing edge damage; high stiction usually indicated that leading edge damage would be evident following testing.

Through SEM/AFM examination of both negative pressure air bearing and tri-pad sliders, it was found that the most common collection site for debris was on the leading edges of the slider rails, Figure 3.17.

The debris was usually found to be concentrated on the chamfers and was thought to have come from the disk surface during the ramp up/down and parking phases of the CSS cycles. That is, at the instances in the cycle when disk velocity is low, sufficient pressure will not have built up at the air bearing regions to enforce pitch change and enable flight to take place. During these times, the chamfers will actually drag on the disk collecting/depositing debris.

4.3.1.1 Using Scion Image for Particle Counting and Area Analysis

To accurately quantify the amount of debris on tested surfaces, the software package *Scion Image* was employed. This image analysis package allowed graphical files to be analysed in various ways. The most useful feature was the ability to count and measure areas of raised height on an image. Figure 4.59a) shows a test image that was used to demonstrate the particle count feature, with the procedure described below.

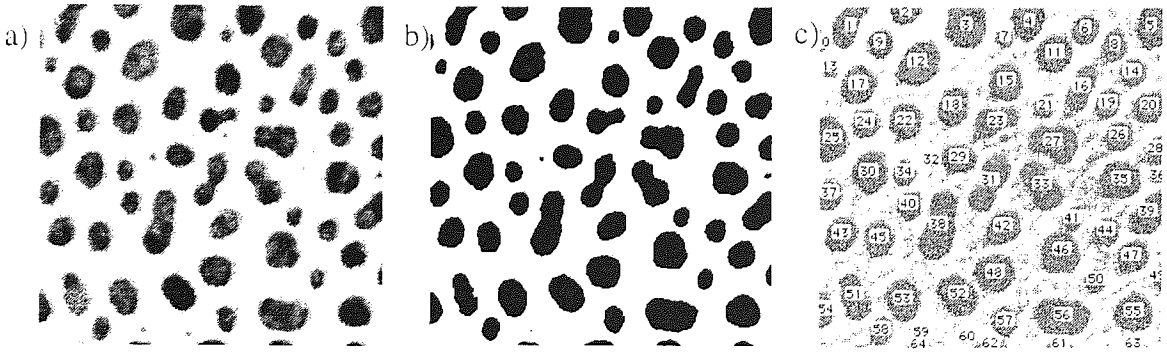

Figure 4.59 a) Original test image, b) converted binary image and c) particle count output

The original image was first made binary to make particle identification easier; the threshold was set by user at this stage, Figure 4.59b). Particle capture preferences, such as those shown in Figure 4.60, were set with result shown in Figure 4.59c).

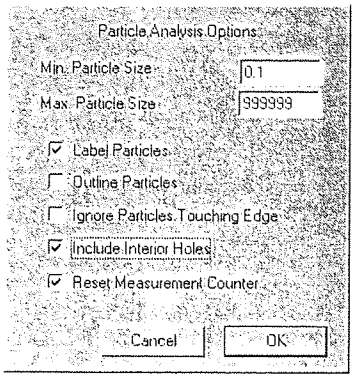

Figure 4.60 Particle analysis settings within Scion Image

All 64 particles were correctly identified. Information was output on particle area for each identified particle. Particle area distribution is shown below for completeness, Figure 4.61.

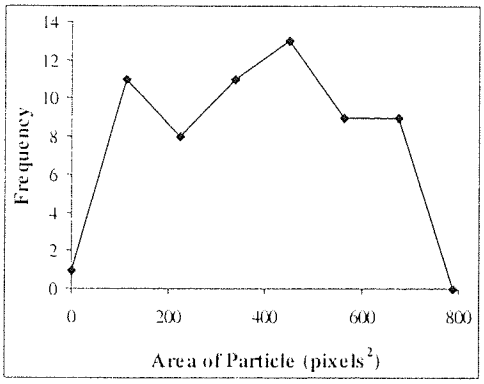

Figure 4.61 Histogram of particle area (unit pixels^2)

Note, for analysis of real images (such as SEM or AFM scans) a set-scale calibration was performed to convert to real units (e.g. μm or nm rather than the default pixel setting). It was also useful to invert the colour scale on real images so that raised features were shown darker than lower areas for ease of identification.

4.3.1.2 Quantifying Debris on Tested Trailing - Leading Edges using Scion Image

Following a 7K cycle CSS test, the leading and trailing edge of a NPAB slider were scanned using AFM, Figure 4.62.

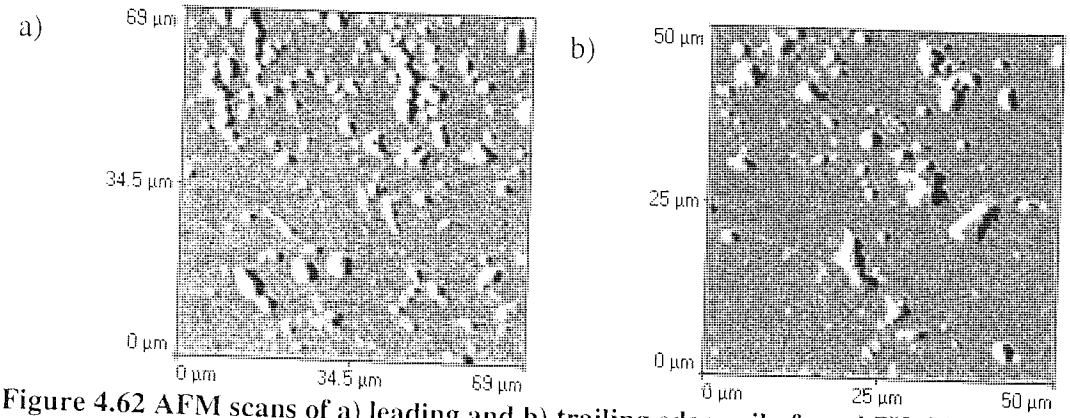

Figure 4.62 AFM scans of a) leading and b) trailing edge rail of used 7K CSS test (Note scan sizes were different)

The leading edge scan was processed first; the scan was converted to grey scale and inverted. A suitable threshold value was then chosen to make the image binary and finally particles were identified. See Figure 4.63a), b) and c) below.

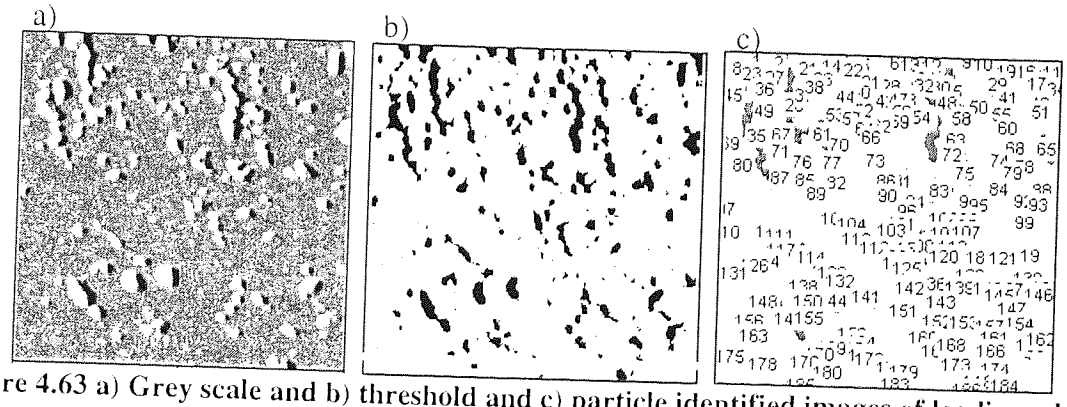

Figure 4.63 a) Grey scale and b) threshold and c) particle identified images of leading edge scan

The above process was repeated for the trailing edge scan, Figure 4.64a), b) and c).

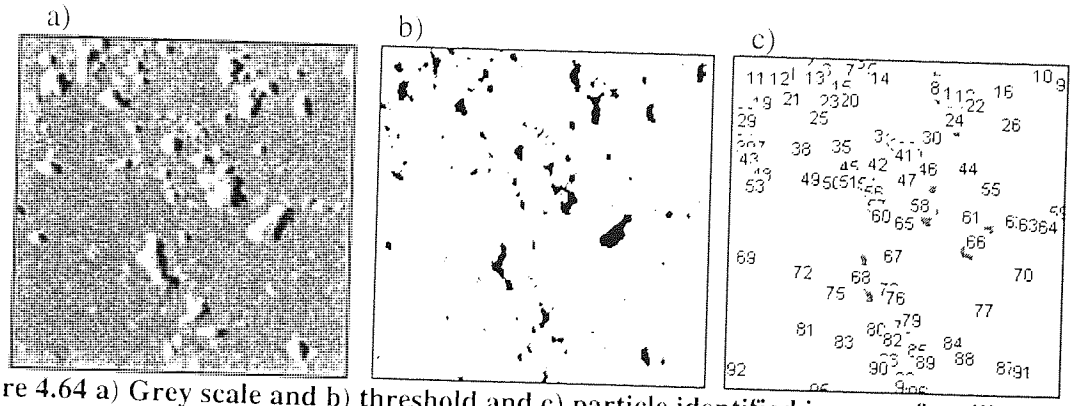

Figure 4.64 a) Grey scale and b) threshold and c) particle identified images of trailing edge scan

The particle analysis routine counted 186 particles on the leading edge slider rail and 96 on the trailing edge. The differences in particle area are illustrated below, Figure 4.65a).

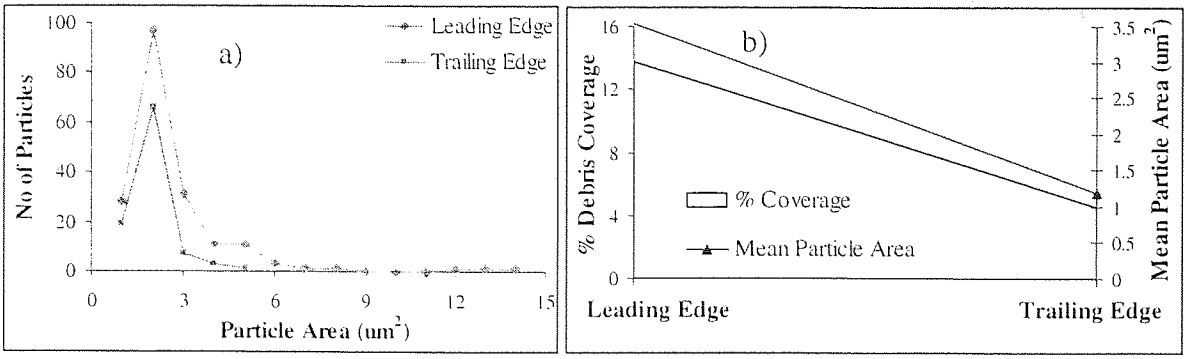

Figure 4.65 a) Particle area distribution b) debris analysis for leading and trailing edges

Notice, as well as the leading edge having the highest number of debris particles per unit area, the largest sized particles were also found in this region. Mean particle area was 3.15μm^2 for leading edge and 1.91μm^2 for trailing edge. The percentage of slider covered by debris was 13.8% and 4.6% respectively, Figure 4.65b).

This result was typical of a slider that had experienced 7K CSS. Results from 5 tests gave that the leading edge could contain 5 times more debris than the trailing edge following testing.

4.3.2 Inner/Outer Rail Comparisons

4.3.2.1 Quantifying Debris on Tested Inner - Outer Rails using Scion Image

It became apparent that the slider outer rail was usually more damaged than the inner, Figure 3.21. Using the above technique, this difference was quantified. Figure 4.66 and Figure 4.67 show processing steps for particle identification at slider inner and outer rails respectively.

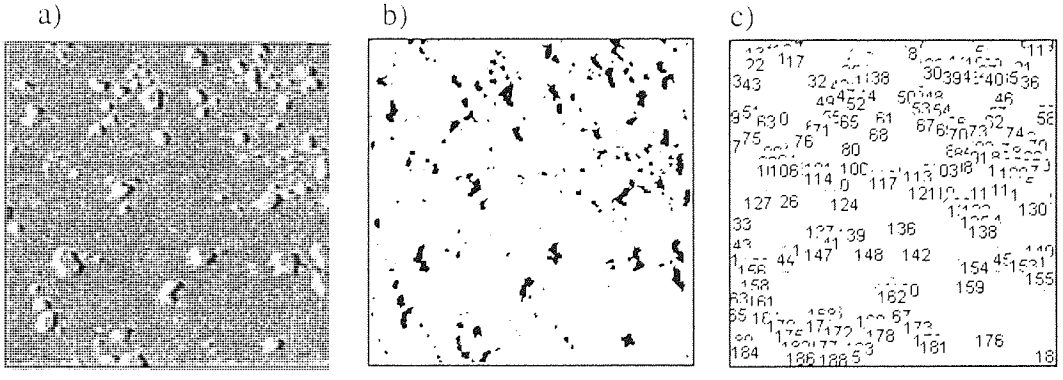

Figure 4.66 Grey scale and b) threshold and c) particle identified images of inner rail

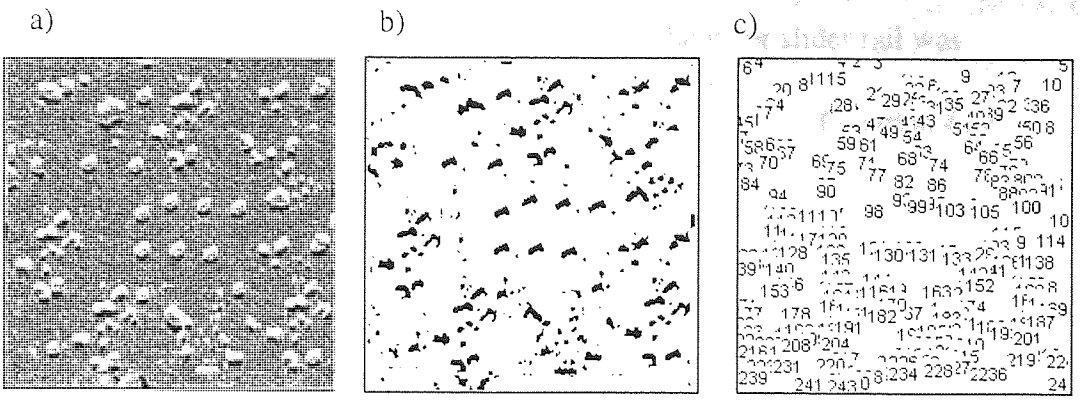

Figure 4.67 Grey scale and b) threshold and c) particle identified images of outer rail

The inner rail scan contained 188 particles and the outer 243. The total amount of debris was larger on the outer rail with coverage 10.1% as opposed to 7.5% on inner rail. Differences in particle area on slider inner - outer rails are illustrated by Figure 4.68 below.

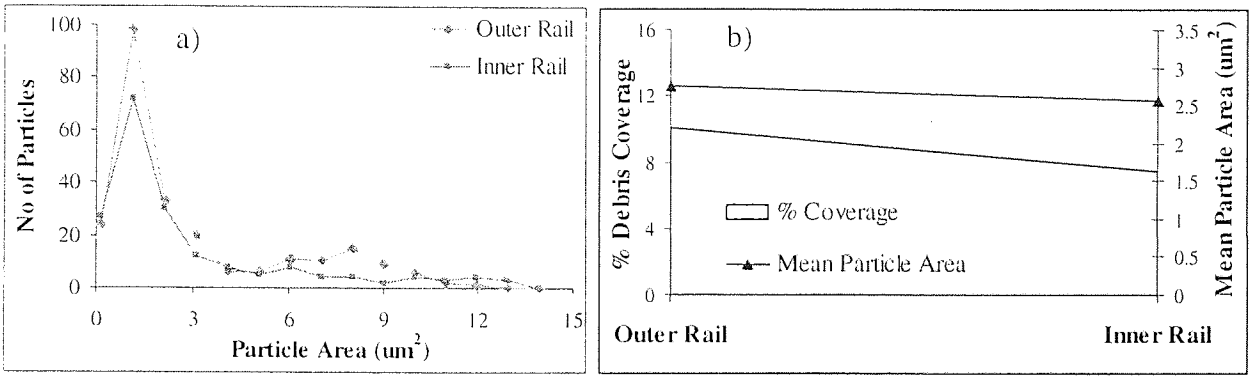

Figure 4.68 a) Particle area distribution and b) debris analysis for slider inner - outer rails

Note, this difference was far less pronounced than the leading - trailing slider difference. The main difference observed here, was in the number of particles counted - since particle size and range was similar, Figure 4.68b). Some explanations for the differences observed are offered below.

4.3.2.2 Sliding Distance Experienced

Since slider rails were a small distance apart (1.21 mm for negative pressure air bearing and 1.22 mm for tri-pad sliders), the inner and outer slider rails travelled different distances during a test. Where the number of CSS cycles in a test was small, perhaps <100, this fact could be neglected. However, since the standard test here consisted of 7K cycles over 18 hours, this was taken into account.

The distance travelled over one complete CSS cycle at the inner slider rail was

$$X_{inner} = V_d T_{dwell} + \frac{2(\alpha V_d T_{up}^2)}{2} \qquad \textbf{Equation 4.29}$$

Thus, the total distance travelled over a complete test consisting of N CSS cycles at this slider rail radius was

$$X_{innerTest} = N(V_{dwell} T_{dwell} + \alpha V_{dwell} T_{ru}^2) \qquad \textbf{Equation 4.30}$$

In order to find the distance travelled at the outer rail, it was necessary to compute the number of disk revolutions undertaken over one complete test.

$$revs = \frac{N(V_{dwell} T_{dwell} + \alpha V_{dwell} T_{ru}^2)}{C_{inner}} \quad \text{where} \quad C_{inner} = 2\pi r_{inner} \qquad \textbf{Equation 4.31}$$

The distance travelled at the radius of the outer slider rail, r_{outer}, was then computed as

$$X_{OuterTest} = C_{outer} revs \quad \text{where } C_{outer} = 2\pi r_{outer} \qquad \textbf{Equation 4.32}$$

For a standard CSS test, distance travelled by the outer and inner slider rails are shown below.

Distance Travelled	Negative Pressure Air Bearing Slider		Tri-pad Slider	
	Outer Rail	Inner Rail	Outer Rail	Inner Rail
Distance over 7K CSS (m)	124527.66	118303.85	124579.10	118303.85
Relative Difference $(\frac{Outer - Inner}{Inner} * 100)$ (%)	5.26%		5.30%	

Table 4.4 Showing distances travelled by outer and inner slider rails over 7K CSS test

Thus, the outer slider rails travelled considerably further (almost 4 miles) than the inner during this test. This could explain the higher amount of debris found on the outer slider rail.

4.3.2.3 Centrifugal Force

In addition, centrifugal force would dictate that flying debris particles moved outwards from the centre of the disk. In normal flying position, this would be towards the outer slider rail.

4.4 Modelling Surfaces and Contacts

Since much of the tribological phenomena observed at the interface were reported to be dependant on surface roughness and contacts between surfaces, it was decided to study these in more detail. Since the contact area was known to be very small AFM was of much use here, a new technique utilising scans of disk and slider for contact area measurement was developed.

The following techniques developed during the project gave realistic estimates for the measurement of these contacts. Techniques were applied to sliders and disks that had been used in both CSS and drag testing.

4.4.1 AFM Scan Exportation Method

As well as providing detailed images, AFM software allowed export of entire scans to file. File entries were numbers representing heights in the case of a topography scan or in the case of a lateral force scan entries were friction forces. The file size was dependent on the original scan resolution. That is, a 400-resolution scan would result in a square matrix of entries with dimension 400 by 400. Scans were analysed numerically using other software applications.

The method followed to export and AFM scan was:

1. Using AFM, obtain high-resolution scan (at least 400) of required surface.
2. Export the scan using *'export'* in file menu in Topometrix analysis package.
3. Alter files slightly in Unix text editor (i.e. remove non-numeric text and blank rows). Then re-save files as tab delimited text format.
4. Import file into other application using e.g. load *'fileneme.txt'* in Matlab or Import Wizard in Excel.

This feature had exciting implications for surface contact studies as well as allowing customised surface analysis to be carried out.

4.4.1.1 Application to Surface Area Characterisation

Surface Area Measurement

Working directly with scan heights still allowed the value of standard surface descriptive parameters to be established. For example, R_{rms} was given by $\sqrt{\sum_i \frac{(h_i - \bar{h})^2}{N}}$ where h_i's are the scan heights and $\bar{h}$ their mean, N is the number of points in the scan, this could be computed by simple code in Matlab.

Having access to scan heights also allowed calculation of some additional values, for example the skewness of the surface. This characterises the departure of a height distribution curve from symmetry. Clearly, Gaussian surfaces have zero skewness.

In addition, kurtosis could be calculated using the raw data, this Kurtosis characterises the relative 'peakedness' or flatness of a distribution compared with the normal distribution.

For surface analysis, the equations used for skewness and kurtosis are shown below

$$Skew = \frac{1}{(R_{rms})^3} \sum_{i=1}^{N} (h_i - \bar{h})^3 \qquad \textbf{Equation 4.33}$$

$$Kurtosis = \frac{1}{(R_{rms})^4} \sum_{i=1}^{N} (h_i - \bar{h})^4 \qquad \textbf{Equation 4.34}$$

These physical significance of these parameters will be examined in Section 4.4.2.3.

Contour Plots

Using the export method described above disk topography scans were loaded into Matlab for analysis. Contour plots, which connect regions of equal height, were used as a tool for visualisation of disk texture. 50μm^2 scans of crosshatched and laser disks are shown in Figure 4.69 a) and b) respectively.

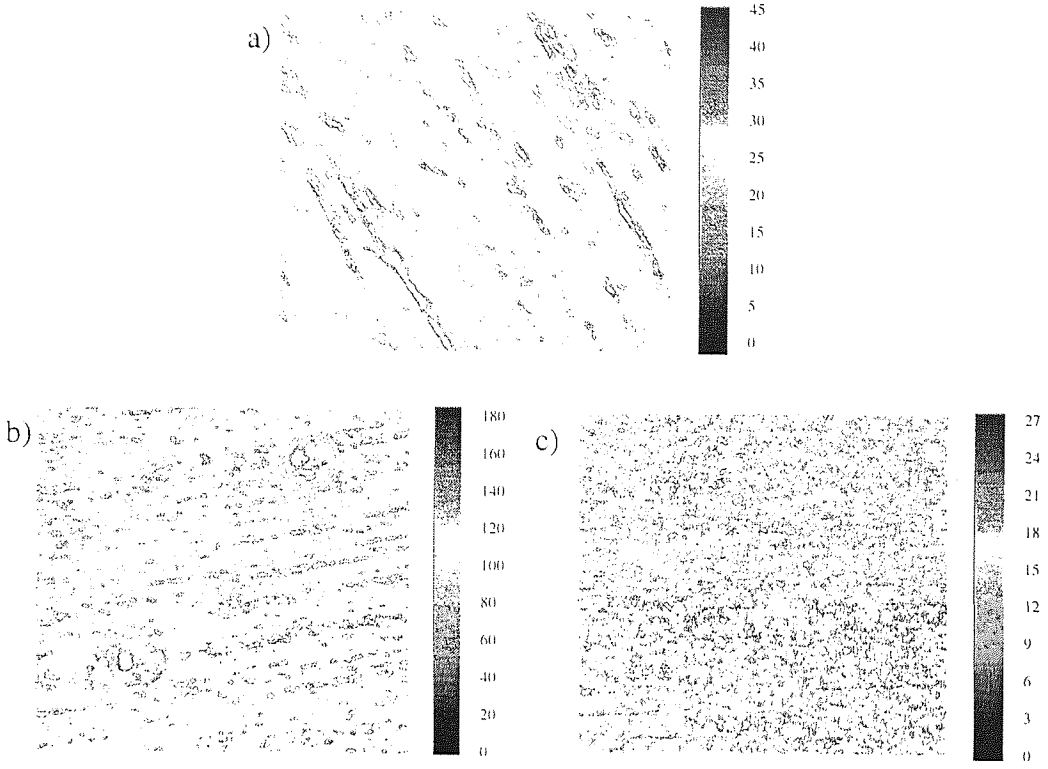

Figure 4.69 Matlab contour plots of a) crosshatched, b) laser disk textured zone and c) laser disk untextured zone

The contour plot picked out laser texture bumps as the highest points on scan Figure 4.69b). Notice the scan heights in untextured area of laser disk, Figure 4.69c), were much lower. This disk type would allow very low flying of slider without giving any surface contact.

Contour plots of slider rail surfaces were also produced; Figure 4.70 shows plots of NPAB and tri-pad rails respectively.

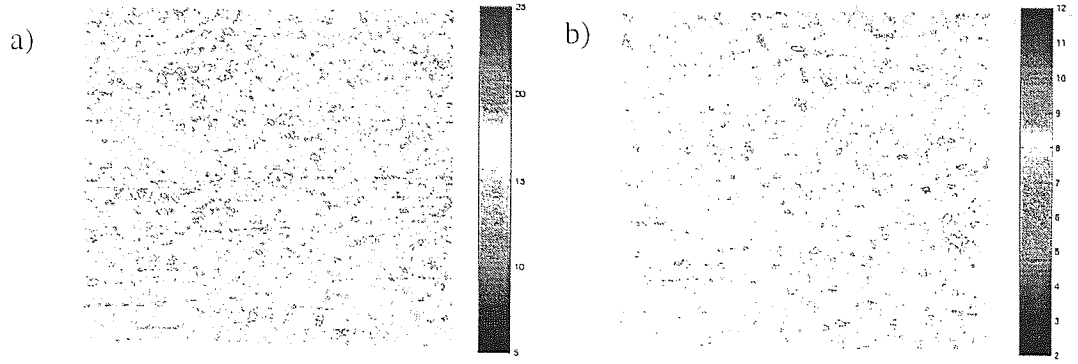

Figure 4.70 Matlab contour plots of a) NPAB rail and b) tri-pad rail

From the heights on the colourbars, clearly slider surfaces were much lower than disk, maximum slider heights were 25 and 12 nm respectively for NPAB and tri-pad, with disk maximum height 45 nm. The heights on the tri-pad rail were commonly half the magnitude of those on the NPAB. However, the NPAB plot contained many more relatively low areas than high, whereas the tri-pad rail had a more peaked surface. In fact, kurtosis was computed as 3.21 nm for NPAB and 4.31 tri-pad respectively, confirming this.

Distribution of Surface Heights

Having access to the actual heights in a scan allowed investigation of surface distribution. For the disk scan, mean height was computed as 25.14 nm and for the NPAB slider scan 9.91 nm. Surface distribution plots are shown in Figure 4.71.

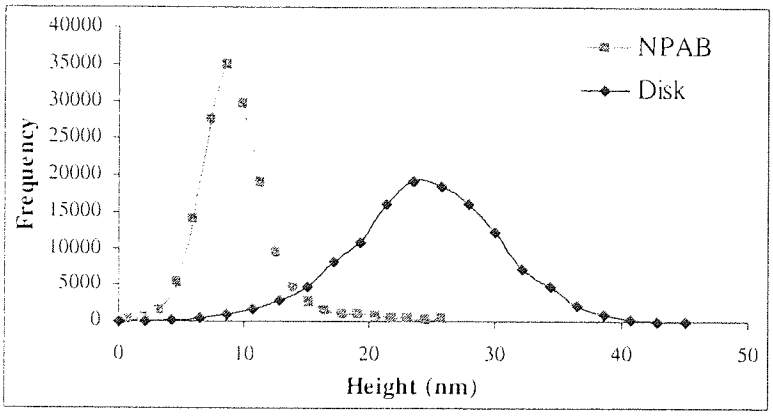

Figure 4.71 Distribution of surface heights for disk and NPAB slider

As expected surfaces had Gaussian distribution, with the disk scan containing the higher range of heights.

Bearing Ratio Curves

A useful tool for visualising how surfaces altered during testing was the bearing ratio curve. This plot showed the percentage of heights in a scan which were above the entire range of heights in the scan. Although, this feature was available in the Topometrix package a separate curve had to be constructed for each surface. By exporting the heights and running some simple Matlab code on the file, curves could be customised and several bearing curves could be shown on the same axis for direct comparison.

Before and after ambient 7K CSS tests with NPAB slider, AFM scans of disk landing zone were taken. These were analysed using the Bearing curve method for successful and failed tests, Figure 4.72a) and b) respectively.

In both cases, the disk surface had changed as a result of testing. For the successful CSS test the majority of the disk surface had gained material (note, % of surface higher for heights < 38 nm). The previously highest points of disk (i.e. those >38 nm) had diminished, indicating some burnishing had occurred. For the crashed test it was found the range of heights in the tested disk surface was almost 10 nm higher than when in its virgin state. This suggested simple damage to the disk surface.

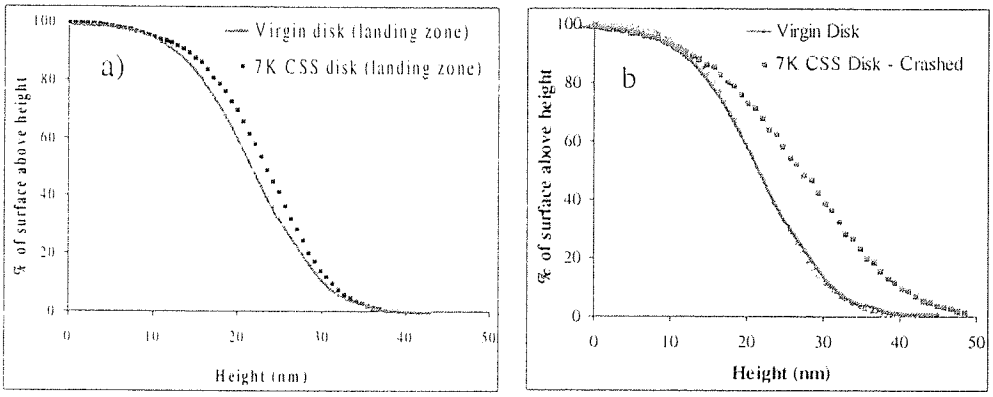

Figure 4.72 Bearing ratio curves for virgin and worn disk area for a) normal 7K CSS and b) crashed 7K CSS test

The debris present in a crashed wear track, transported either from slider or from a neighbouring disk area, Figure 4.72b), also ensured surface heights were higher there.

Similarly, following drag testing the disk also contained a wider range of heights, Figure 4.73. Note scans were taken at disk data zone for this example.

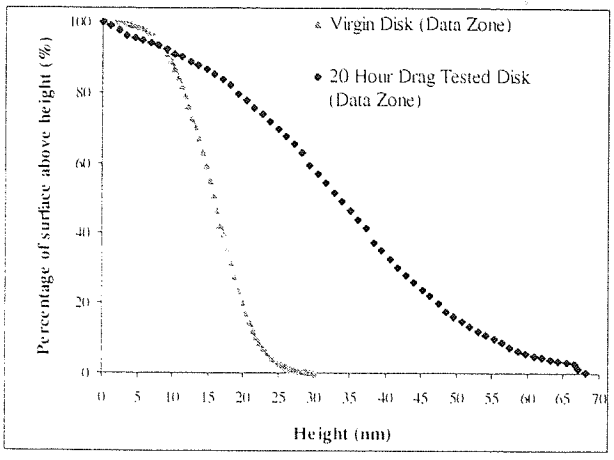

Figure 4.73 Bearing ratio curves for virgin and worn disk area for normal drag test

Conversely, the slider surface lost height during CSS and drag testing, Figure 4.74a) and b) show how the slider's highest asperites were burnished during a 7K CSS test and 20 hour drag test, respectively. Surprisingly the drag test (which was found much more severe) reduced the slider heights by less than the CSS for this example.

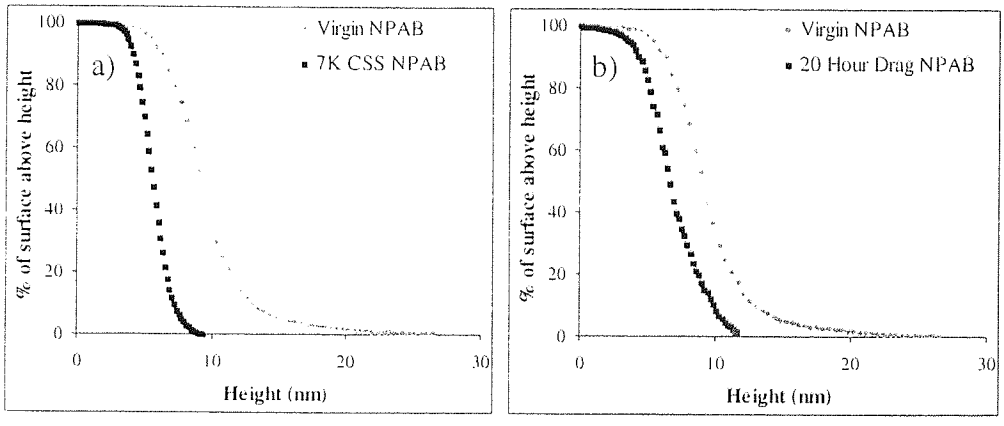

Figure 4.74 Bearing ratio curves for virgin and worn slider trailing edge rail for a) a normal 7K CSS test and b) 20 hour drag test

In Section 4.4.1.6 a new technique will be described whereby bearing curves are used to estimated the amount of contact taking place between slider/disk surfaces.

Fractal Analysis

As an alternative to the Scion Image particle analysis method described in Section 4.3.1.1, the fractal analysis feature in the Topometrix analysis software was adapted to quantify the amount of foreign particles present on AFM scans. Particles were deemed foreign if they exceeded a specified height and/or area. Sunken regions or valleys as well as risen peaks could be identified.

As it stood, the feature gave good visual images of high/low points of various areas on a scan. A logarithmic plot was also output on particle perimeter over area to help categorise the shape of particles.

However, by performing fractal analysis and then an export command as before, the perimeters and areas of individual particles was output to file. This could then be explored to give further information, e.g. the mean debris coverage as before.

An example is shown in Figure 4.75 of the fractal analysis routine finding debris on a 69 μm^2 leading edge tri-pad slider rail scan. This slider had seen 7K of CSS tests in 35°C/65% RH.

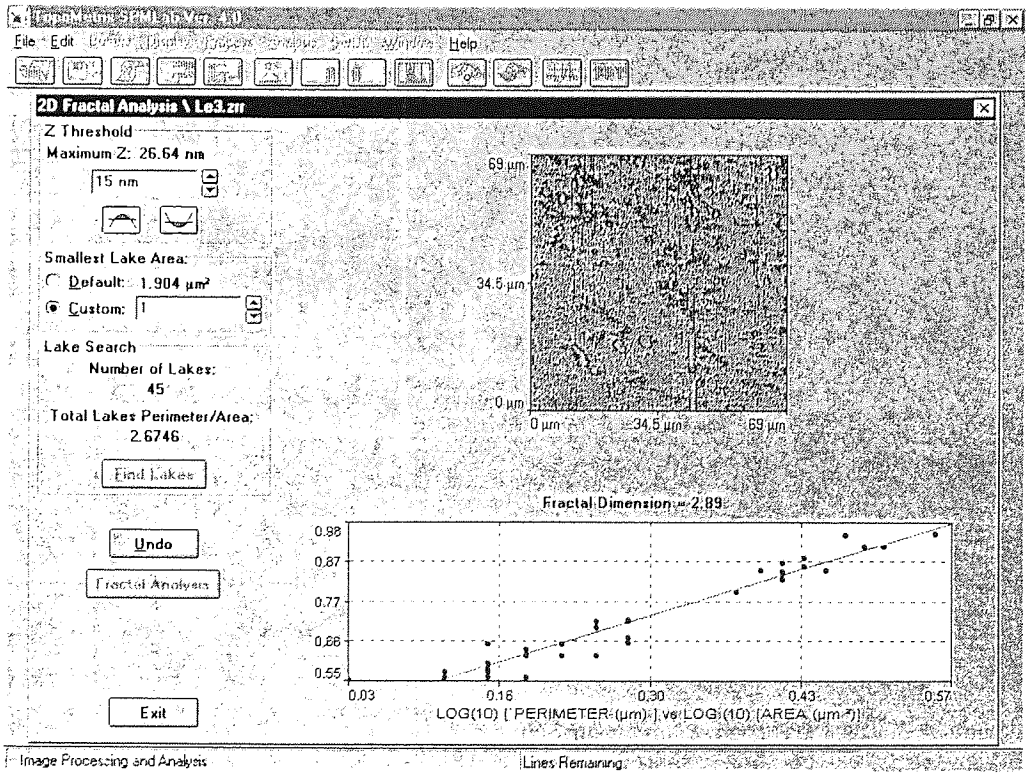

Figure 4.75 Example of Topometrix fractal analysis routine finding debris on a leading edge tri-pad slider rail scan

Here 4.79% of the scan was found to be covered in debris, with total area of coverage at 236.9 μm^2 and mean particle size was 4.26 μm^2. XPS gave debris to be carbon and fluorine transferred from disk overcoat.

The advantage of using this method was that the critical heights above which particles are traced were user defined, this was more scientific than thresholding in Scion Image. However, obviously this method only allowed analysis of AFM scans, whereas Scion image allowed import of any type of image file.

4.4.1.2 Application to Line Analysis

Improved Method of Pole Tip Wear Measurement

As shown in Section 3.2.1.2 standard line analysis proved unreliable when assessing the height of slider read-write elements above the surrounding slider body. By using the matrix of scan heights of slider elements, a new averaging method was proposed which reduced error.

An exported AFM topography scan was loaded into Excel, the row numbers corresponding to the width of pole 2 were found. The area of interest was considered as 73 line scans, Figure 4.76a). These were averaged and a plot drawn, as shown in Figure 4.76b).

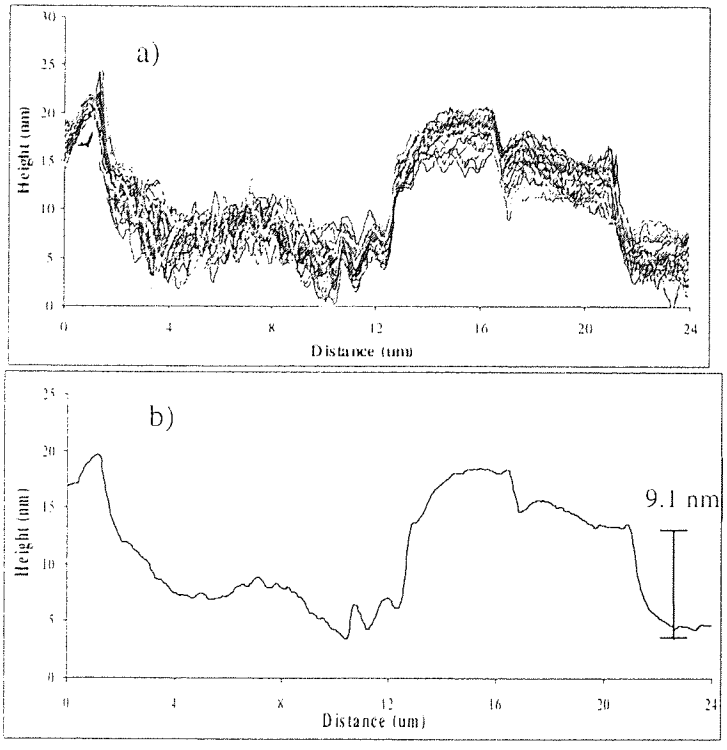

Figure 4.76 a) Multiple line scans and b)average line analysis of used NPAB read-write elements

The average height of pole 2 was then found to be 9.1 nm, this would be a more reliable figure to use in any subsequent models than any single line scan measurement.

Using the above technique, NPAB sliders that had been used in the environmental CSS tests T30H80, T55H10, T60H10, T40H20, T50H50, T40H60 and T70H10 were scanned using AFM. Selected averaged line scans over the elements of the NPAB sliders are shown in Figure 4.77a).

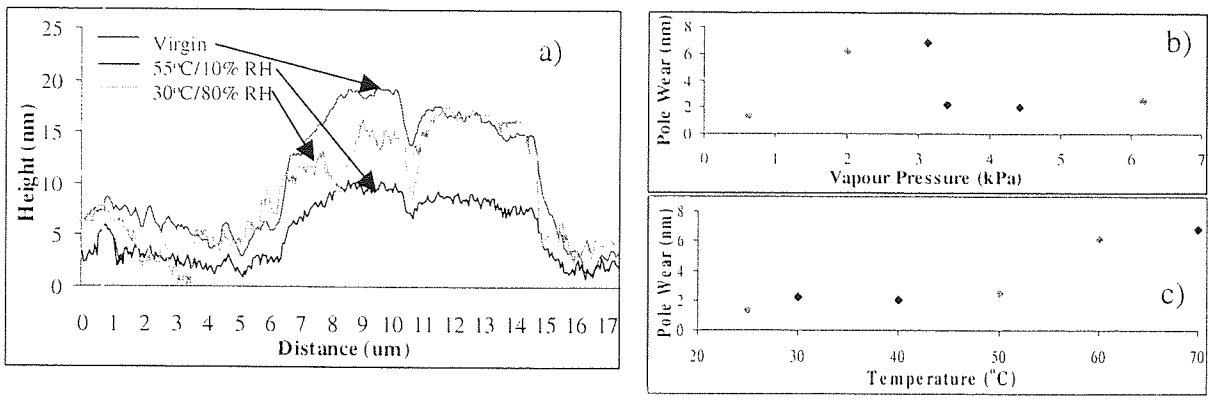

Figure 4.77 a) AFM averaged line scans of NPAB elements and differential heights against b) vapour pressure and c) temperature

Figure 4.77b) and c) show the measurements of pole 2 height above surrounding slider alumina against temperature and humidity respectively. From these graphs, the slider pole material was worn much more in hot/dry environments.

4.4.1.3 Novel Technique for Contact Analysis

Sharma and Talke contact model

Sharma and Talke [58] reported the relationship between real area of contact, A_r and apparent area of contact, A_a as

$$\frac{A_r}{3.2 p_a A_a} \approx \frac{1}{E_c \sqrt{\sigma_p / R_p}} \qquad \textbf{Equation 4.35}$$

where p_a is apparent pressure, R_p is composite radius of asperity peaks, σ_p is standard deviation of peak height distribution and E_c is the composite Young's modulus.

A_r was calculated for our system, using tabulated values of material characteristics and values measured from exported 50 μm^2 AFM scans for topographic parameters.

Standard deviation of asperity heights was deduced by importing AFM scan data into Excel (giving σ =9.99, 2.23 and 2.02, for disk, NPAB and tri-pad respectively).

Radius of asperities was found by locating all peaks which were higher than their immediate neighbours (i.e. points higher that the surrounding 8). The next level of surrounding points were then examined and this was continue until a higher point was found, Figure 4.78 shows a narrow and wide peak observed on disk surface. The mean radius of each peak was recorded. R_p was found to be 0.61, 0.51 and 0.50 μm for virgin disks, NPAB and tri-pad respectively.

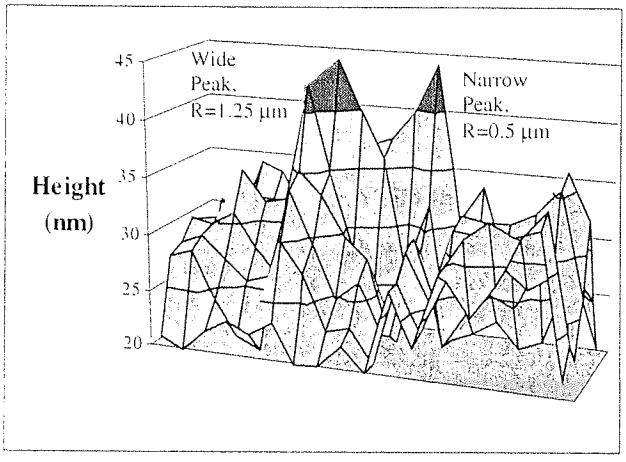

Figure 4.78 Illustrating some disk asperity peaks

Contact Analysis	Using Mean Asperity Radii				Using Max Asperity Radii			
	NPAB		Tri-pad		NPAB		Tri-pad	
	Virgin	Worn	Virgin	Worn	Virgin	Worn	Virgin	Worn
Area total (μm^2)	3.21	6.03	2.89	6.21	7.81	9.72	7.60	10.51
% Surface area	0.13	0.24	0.12	0.25	0.31	0.39	0.30	0.42

Table 4.5 Difference in contact between virgin and worn surfaces

Mean contact areas were smaller than those reported in [58], this was due to detected asperity radii being smaller due to high resolution of AFT. If maximum contact radius was used instead contact values would be more comparable, as shown in end columns of Table 4.5. It was noted that worn surfaces contacted more than virgin surfaces.

Contact Technique Description

By overlaying numerical scan data from slider and disk, information about asperity contacts could be made. Results on the amounts/area of contacting asperities when the slider was parked on disk were given. In addition, flying contacts between slider and disk could be identified. These were then related to measurements of stiction and dynamic friction respectively.

This process is illustrated schematically in Figure 4.79.

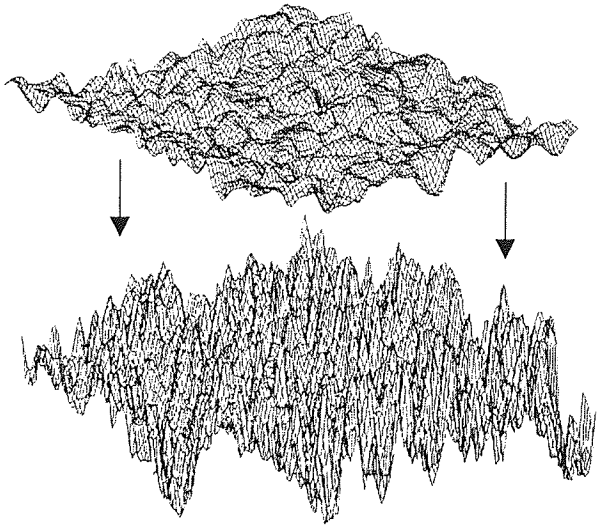

Slider surface scan upturned and lowered on to disk to required separation height.

Figure 4.79 Illustration of upturned slider and disk scan overlay - both 3D images have area 20 um^2 and vertical scales are the same (50nm). Both AFM scans taken perpendicular to direction of slider travel (270°)

Notice the disk surface was much more highly textured than the slider. The method to predict static/dynamic contacts was the same except for the separation distance between scans; this will be explained later.

Guide to Performing Contact Analysis

1. Using AFM, high quality scans (resolution ≥400) of mating surfaces were taken. Care was taken to scan at same size/direction and choose areas that would actually touch in reality. Slider leading edge rail region and disk inner diameter chosen for static contact work, slider trailing edge region and disk outer diameter for flying contact work.

2. Scans were exported and loaded into Matlab, see Section 4.1.10.

3. Scans were 'overlaid' by summing corresponding slider/disk elements in nested loops and checking whether the resulting height was above or below the threshold for contact, which was defined as:

(i) For normal slider parking Poon and Bhushan [134] stated that load, W and real area of contact, A_r, were related to composite surface roughness C_{rms}. A relationship could be formed as

$$\frac{W}{A_r} = 0.3126 C_{rms} \quad \text{with} \quad C_{rms} = \sqrt{D_{rms} + S_{rms}} \qquad \textbf{Equation 4.36}$$

where D_{rms} and S_{rms} were root-mean-square roughness of disk and slider respectively.

Substituting values into this for this system gave an estimate of A_r during normal parking; this was then used to obtain a separation height. The threshold height for contact between mean asperity heights was calculated as 13.24 nm and 12.86 nm for virgin disk contacts with NPAB and tri-pad sliders respectively.

(ii) For flying friction contact threshold between surface mean heights was chosen as slider fly height, see Sections 4.1.5 and 4.1.6.

An output matrix was generated during calculation containing positions/intensity of contacting asperities.

5. Contour plots of output matrices were made, saved and converted to TIFF format using *ImageMajick* image processing program.

6. Resulting files were loaded into Scion Image (see Section 4.1.8.1) and analysis of particles was performed. This picked out and measured all contacts in chosen area range.

7. Finally the results of Step 6 were imported into Excel for analysis/comparison.

Note, if information on the percentage of surfaces in contact only is required, Step 6 above can be omitted and results can be exported direct from Matlab to Excel. If information on the number or area of contacts is required, it was favourable to use Scion Image for analysis.

The method has many advantages, firstly, this gives an actual count of how may asperities are in contact and information on the size area of each of these. In addition, here no assumptions are made of surface height distribution or asperity shape.

Contact analysis for normal parking during drive non-operation

The results of overlaying 50μm^2 virgin and worn (7000 CSS ambient) slider and disk scans are shown in contour plots, Figure 4.80. The same disk scan was used for both slider types. Notice in Figure 4.80 b) and d) contact points were dictated by the disk texture.

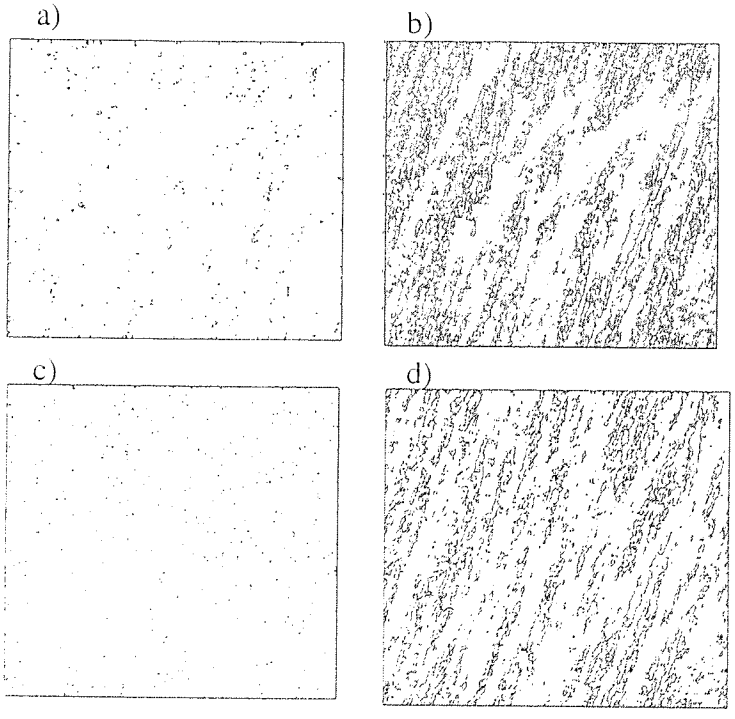

Figure 4.80 Contour plots for NPAB - a) virgin contacts, b) worn contacts and tri-pad, c) virgin contacts and d) worn contacts. Note scan size was 50 μm^2

Although there were actually more points in contact between virgin surfaces, the real area of contact and mean size of asperity contact was smaller for virgin surfaces. Results are shown in graphically in Figure 4.81 and numerically in Table 4.6. Higher contact was experienced between tri-pad slider and disk due to this slider being slightly smoother than NPAB.

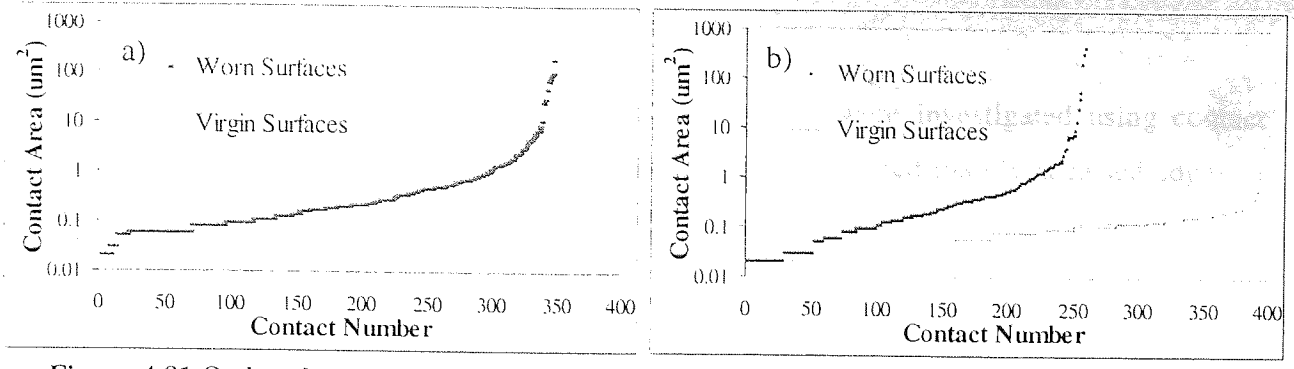

Figure 4.81 Ordered contact area plot for virgin and worn surfaces for a) NPAB and b) tri-pad. Note, logarithmic scale on graphs

Contact Analysis	NPAB		Tri-pad	
	Virgin	Worn	Virgin	Worn
Number of contacts	369	346	378	258
Mean contact area (μm^2)	0.10	2.69	0.08	3.91
Area total (μm^2)	36.68	631.75	34.02	1008.78
% Surface area	1.47	25.27	1.36	40.35

Table 4.6 Difference in contact between virgin and worn surfaces

The growth in contacting asperity area was only partly responsible for the increase in stiction observed during a test. When contact analysis was carried out at various stages of CSS, the increase in mean asperity contact area levelled off after 5000 cycles for NPAB, Figure 4.82. The fact that stiction continued increasing beyond this meant some other factors such as meniscus bond increase and changes in lubricant must have been occurring. For tri-pad the growth in contact area was not smooth with a low area recorded at 5000 cycle, factors such as the slider gaining/depositing debris affected contact area.

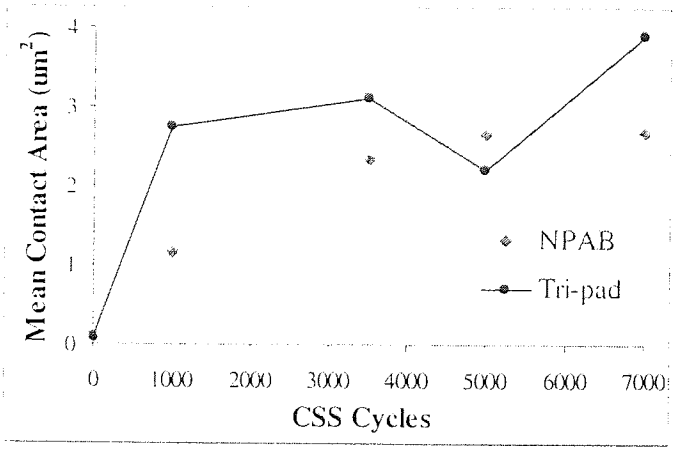

Figure 4.82 Mean contact area against number of CSS cycles.

Laser Textured Disk

The advantages of using laser-textured media on stiction were investigated using contact analysis. As expected, when scans were overlaid contacts occurred mainly at raised edges of laser bumps again confirming disk texture was again responsible for contact, Figure 4.83.

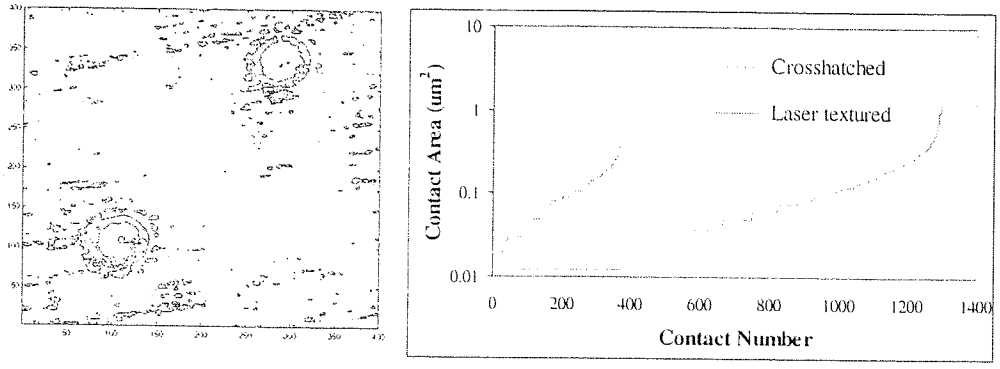

Figure 4.83 Contour plot of virgin contacts for laser textured disk and NPAB slider and b) ordered contact area plot.

Analysis gave that 133.91 μm^2 of surfaces (5.35%) were in contact via 1302 discrete spots. This gave mean contact area of 0.10 μm^2 . Thus, mean contact area was similar to that of a crosshatched texture disk. The fact that the slider rail was mainly supported at raised bumps was thought enough to satisfy low stiction in drives.

4.4.1.5 Using method to identify contacting asperities during drive operation

The read-write elements at trailing edge of a virgin NPAB and tri-pad slider were scanned as was virgin disk outer diameter (the data zone) ensuring correct scan direction and resolution. Scan size chosen was 20 μm^2 .

Scan data files were overlaid as before to determine which points on slider trailing edge contacted disk while flying at 10 nm. Results confirmed that the read/write elements were the highest points on slider trailing edge and would be most likely to contact disk during low flying for both sliders.

Figure 4.84 illustrates the results of overlaying AFM scans, SEM scans shown confirm the shape of read/write elements for each slider type. Note, this would be the level of separation experienced during drag testing.

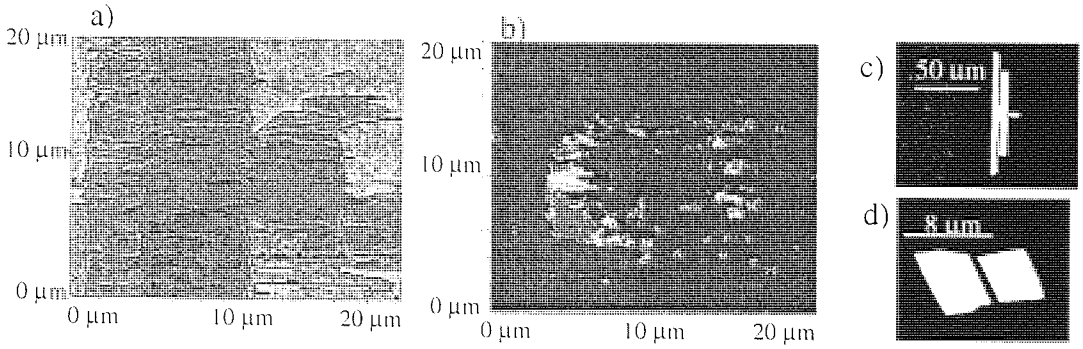

Figure 4.84 a) NPAB overlay, b) Tri-pad overlay, c) SEM of NPAB read/write elements and d) SEM of tri-pad read/write elements

Fly heights values were given by formulae in Section 4.2; these were then used as separation heights between scans to build contact profiles with disk velocity, Figure 4.85a) and b) respectively.

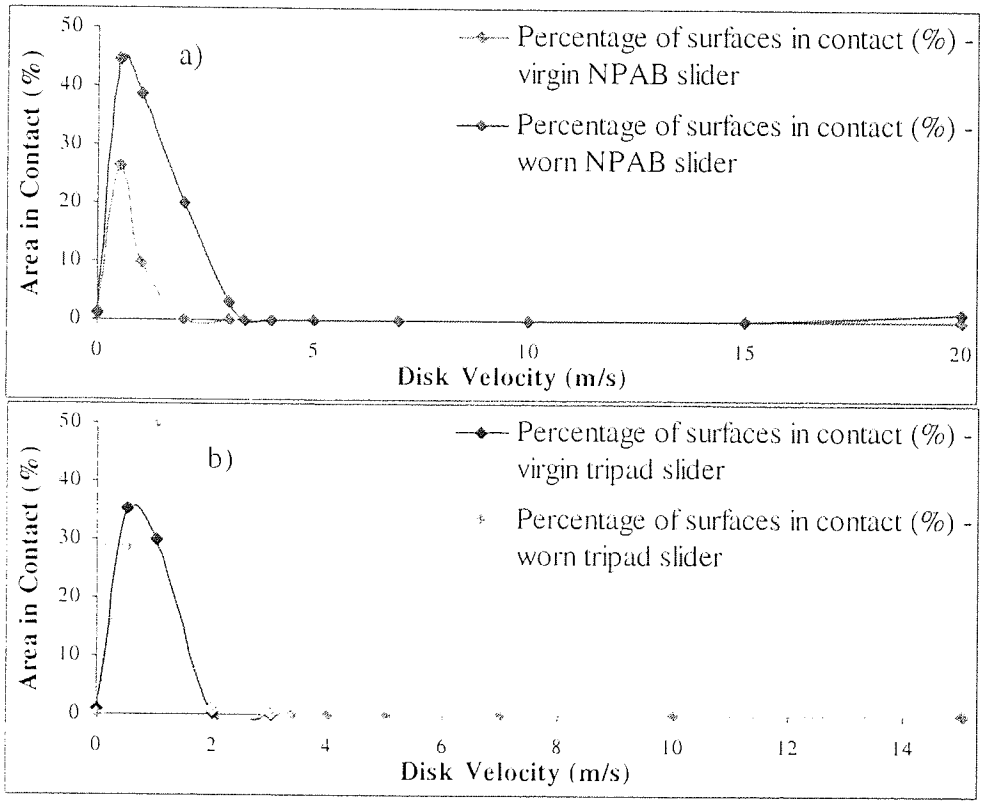

Figure 4.85 Contact area with disk velocity for a) NPAB and b) for tri-pad

Notice that at velocity 0 m/s there was no contact between trailing edge of slider and disk, this is because slider pitch had not increased due to flying so read/write element is far from disk surface.

For both sliders the velocity that gave most contact was around 0.5 m/s, this correlated with experiments performed concluding that highest friction occurred at this velocity, Figure 4.86. Higher contact area was experienced between worn surfaces, this may explain the rise in friction observed from start to end of a CSS test.

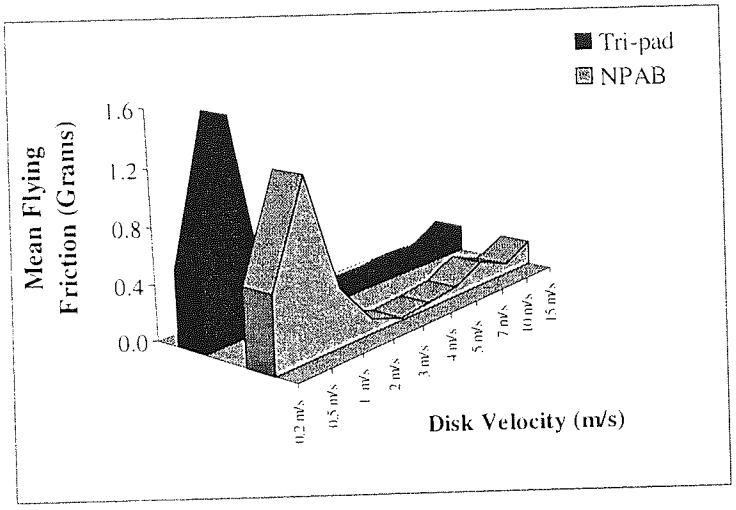

Figure 4.86 Friction readings at various disk velocity

During flying at standard velocity (at 3.37 m/s) flying contacts were minimal (<1% for both sliders). When flying at low fly heights contacts were now dictated by the slider elements rather than disk texture. Figure 4.85 shows that contact mainly fell in pole/shield areas.

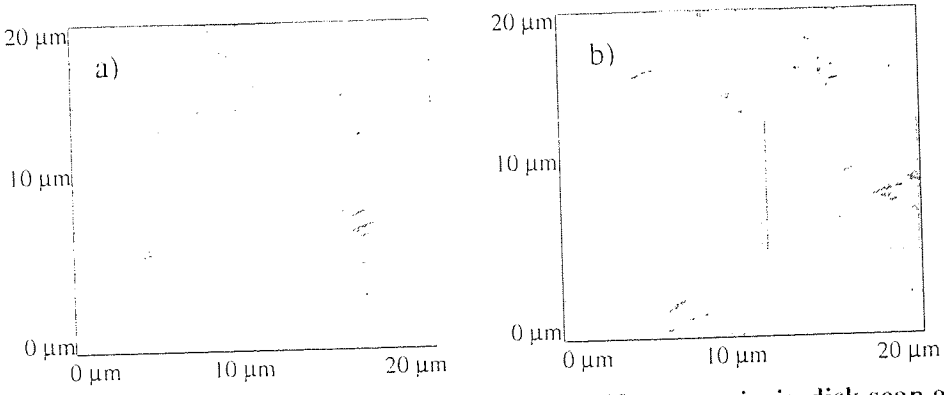

Figure 4.87 Flying contact plots for NPAB flying at a) 20 nm on virgin disk scan and b) 20 nm on worn disk scan

Note when trailing edge scan overlay was performed using the untextured data area of a laser disk contacts were minimal, with flying height of 17 nm required to produce contact.

Effect of Disk Position on Friction/Contact

Overlaying of scans was performed at 4 disk locations to determine if disk circumfrential position affected the amount of contact given. Results on contacts at 5, 10, 20 and 30 nm separations are shown in Figure 4.88 below.

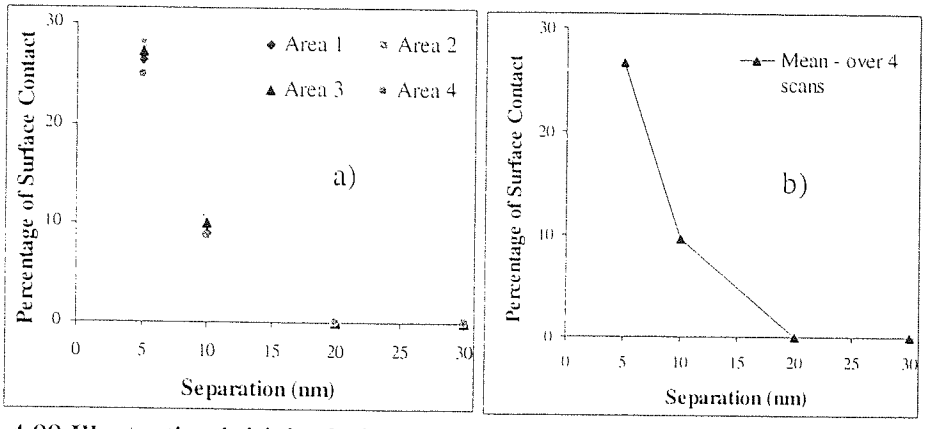

Figure 4.88 Illustrating initial relationships between flying height and contact amount at 4 different disk locations

Disk position did not affect contacts significantly at all fly heights tested. When repeating the experiment for worn surfaces (7K CSS) there was a much higher dependence on location on amount of contact, Figure 4.89. Values were again higher for worn surfaces.

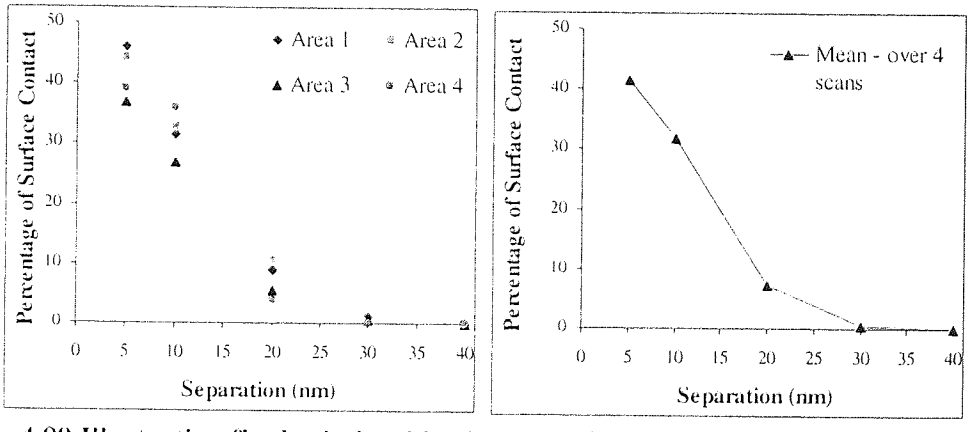

Figure 4.89 Illustrating final relationships between flying height and contact amount at 4 different disk locations

Standard deviation in contact between areas was calculated for virgin and worn surfaces, Figure 4.90 a). These results link with friction results and confirm higher dependence on disk location of contact following testing. Observe the friction plot in Figure 4.90 b), during the flying period of the first cycle in a CSS test very little variation in friction occurs with respect to disk position. Then compare this with a similar friction trace for the final cycle where much more variation occurs.

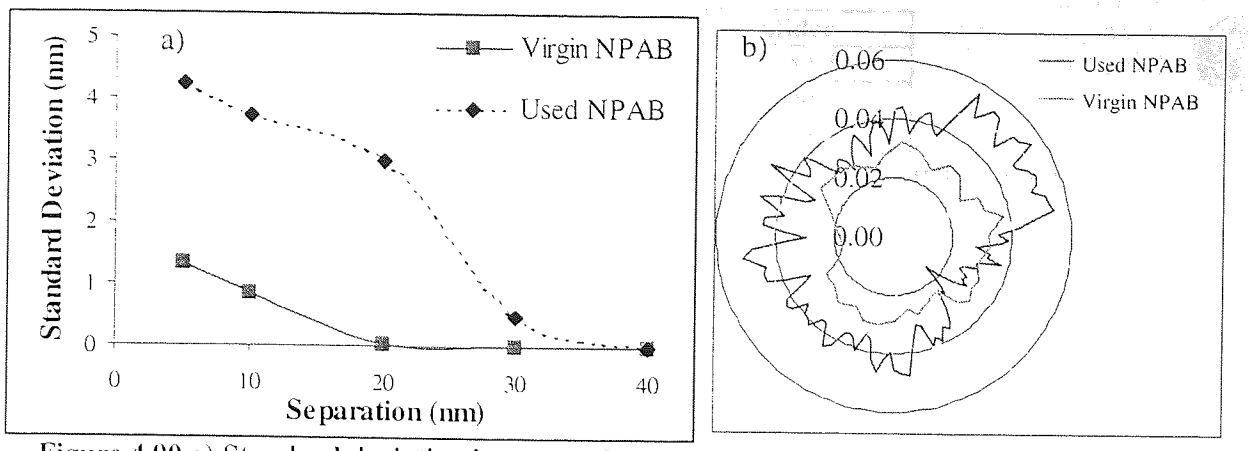

Figure 4.90 a) Standard deviation in contact between areas for virgin and worn surfaces and b) Friction against disk circumfrential position over first and last disk revolutions of a CSS test

Thus, it can be said that disk wear does not occur uniformly and leads to high variation in friction.

4.4.1.6 Bearing Curve Method for Contact Analysis

Since the steps 1-7 in Section 4.4.1.3 were awkward to perform and generally time consuming, a new method was formulated. This method combined modelled bearing curves for slider and disk to get an approximation for how much of those surfaces would be in contact in reality.

Firstly, the bearing curves for virgin slider and disk were modelled as Gaussian curves as shown in Figure 4.91.

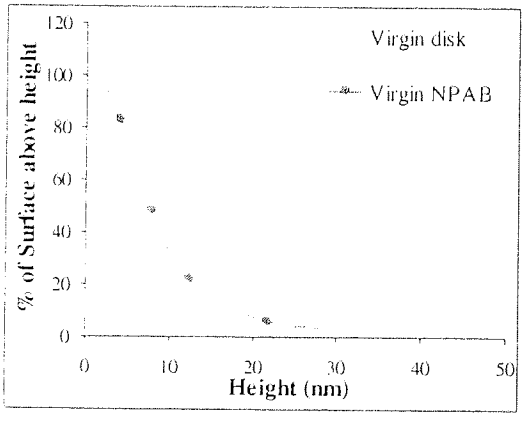

Figure 4.91 Modelled bearing curve for virgin slider and disk

Equations used were of the form $a\exp(-\frac{(h-b)^2}{2c^2})$ with parameters a shown in Table 4.7.

Parameter	Disk	Slider
a	97.37	105.95
b	3.29	2.88
c	15.09	4.96

Table 4.7 Disk and slider parameters used to model bearing curves

By dividing the values provided by these equations by 100, a probability is given of the proportion of a scan being above a certain height. By multiplying these values for disk and slider, probabilities of contact between surfaces were deduced. That is, for any given separation height the probability of finding pairs of asperity which exceeded this could be calculated. The Matlab code used to produce probabilities was

```
for separation=0:100
prob(separation)=0;
 for d=1:50
  for s=1:30
   if (d+s)>separation
      prob(separation)=prob(separation)+dprob(d)*sprob(s);
   end if
  end
 end
end
```

The probabilities were then turned back into percentages as shown in Figure 4.92. Note the procedure was carried out for a set of worn (7K CSS) surfaces also, method confirmed that these surfaces were less likely to contact than virgin. This was due to the removal of highest points from the surfaces.

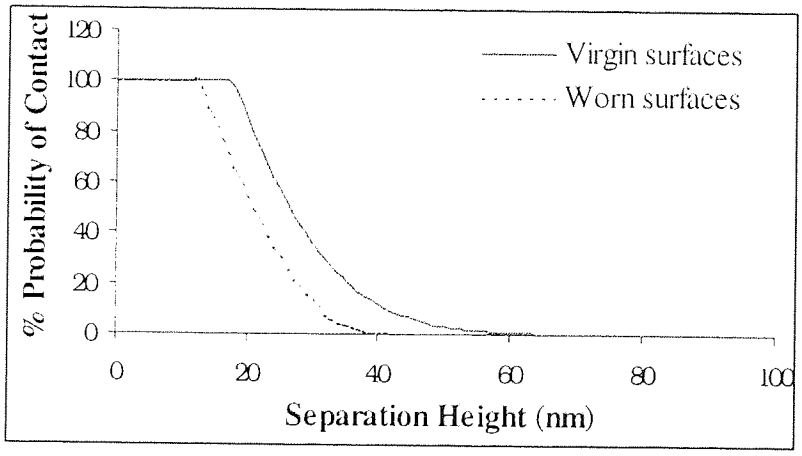

Figure 4.92 Percentage of virgin/worn surfaces in contact as a function of separation height using bearing curve method

4.4.2 Generating Surfaces for Contact Investigation

It was thought interesting to use simulated disk and slider surfaces for contact analysis using the overlay method. This allowed the contacts between surfaces to be emulated using surfaces with customised properties.

4.4.2.1 Generating Surfaces

Method 1 : Equation Based

Several equations were studied to provide accurate estimates for surfaces. One of these was the two dimensional equation

$$h(x,y) = a + b\,x + c\,y + d\,x^2 + e\,y^2 + f\,xy \qquad \textbf{Equation 4.37}$$

Using a customised optimiser program (the Complex method by Box) sets of optimal values were constructed for the unknowns a, b, c, d, e and f. The equation attempted to match a real disk surface with respect to mean height and RMS roughness. To achieve this an objective function was set to monitor the algorithm's performance; this computed the total error between real and modelled surface characteristics at each stage of the iteration.

When running the Box algorithm appeared to successfully reduce the objective function value, Figure 4.93 shows the decreasing objective function values during three attempts at optimising coefficients.

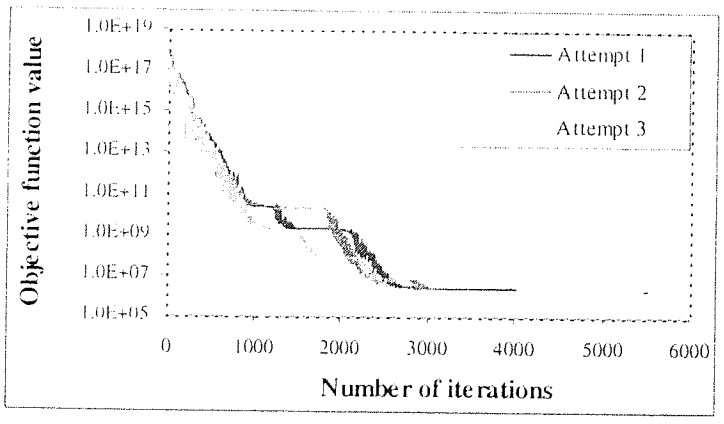

Figure 4.93 Box algorithm optimising coefficients of Equation 4.35

This was incorrect, this model simply estimated the surface by its mean value of 21, Figure 4.94. (Note, the mean value is lower than previously as disk scan is of data zone). This indicated that the wrong equation was being used here.

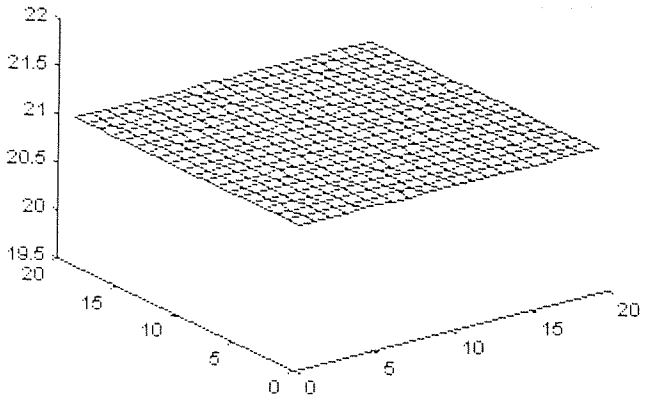

Figure 4.94 Generated surface h(x,y)=21

An isotropic equation was next used to model the disk surface, the chosen equation was

$$h(x,y) = a + b\sin(cx) + d\cos(ey) + f\cos(gxy) \quad \textbf{Equation 4.38}$$

This time an extra component was added to the objective function, this monitored the range of heights in the generated surface and matched it to those found in the real surface. Thus, a coefficient set was penalised if it provided an unrealistic height range; this prevented a completely flat surface being generated as before. The Box algorithm quickly minimised the objective function, Figure 4.95 and provided a set of non-zero values for coefficients as shown in Table 4.8.

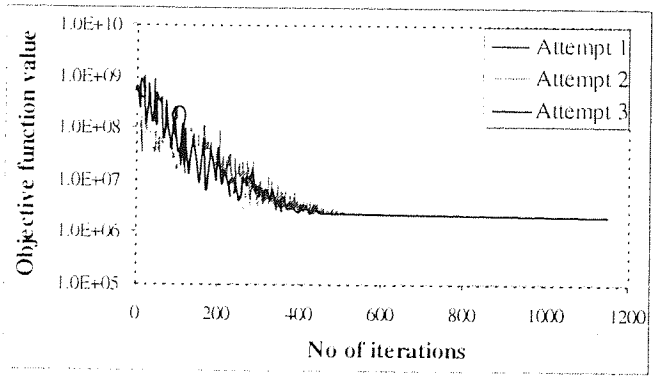

Figure 4.95 Box algorithm optimising coefficients of Equation 4.36

Coefficient	Optimal Value
a	21.565
b	2.984
c	3.329
d	2.528
e	3.859
f	3.539
g	3.606

Table 4.8 Optimal values for coefficients of Equation 4.38

In fact, during 100 runs of the Box algorithm almost the same optimal solution was arrived at each time. It was common to perform multiple runs of any optimiser to ensure that global not local solutions were being arrived at.

The result of graphing Equation 4.36 with optimal coefficients is shown in Figure 4.96. Characterisation parameters for this surface and the one it emulated are shown in Table 4.9.

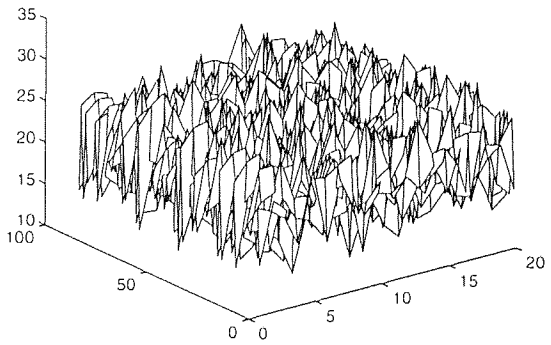

Figure 4.96 Generated surface
h(x,y)= 21.565+2.984sin(3.329x)+2.528cos(3.859y)+3.539cos(3.606xy)

Disk Region	R_a (nm)	R_{rms} (nm)	Height (nm)	Maximum P-V (nm)
Generated	0.67	1.74	21.43	17.96
Real	3.62	4.48	21.41	32.52

Table 4.9 Comparing real and generated disk surfaces

Although the equation provided accurate mean height estimate, all the other parameters were underestimated implying a surface that was too flat had again been generated. In fact, on exploring several other equations it was often found difficult to replicate required texture using this method.

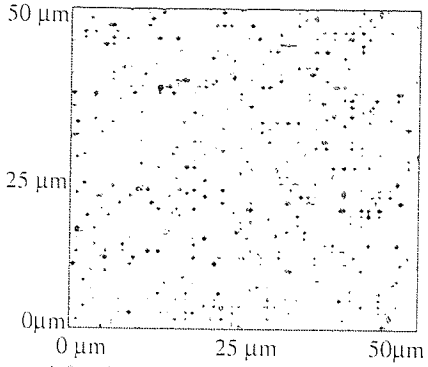

Figure 4.97 Results of generated surface overlay

Method 2 : Random Number Based

To introduce the randomness that was present in real surfaces, surfaces were simulated from Gaussian distributed random numbers (UCLA statistics generator code). Disk surface was chosen to give mean height 25 nm, standard deviation 7 nm, slider surface was chosen to give mean height 10 nm and standard deviation 3 nm to match real surfaces.

Surface distribution matched that expected as shown. Solid lines on graphs represented Gaussian models that gave best fit, Figure 4.98.

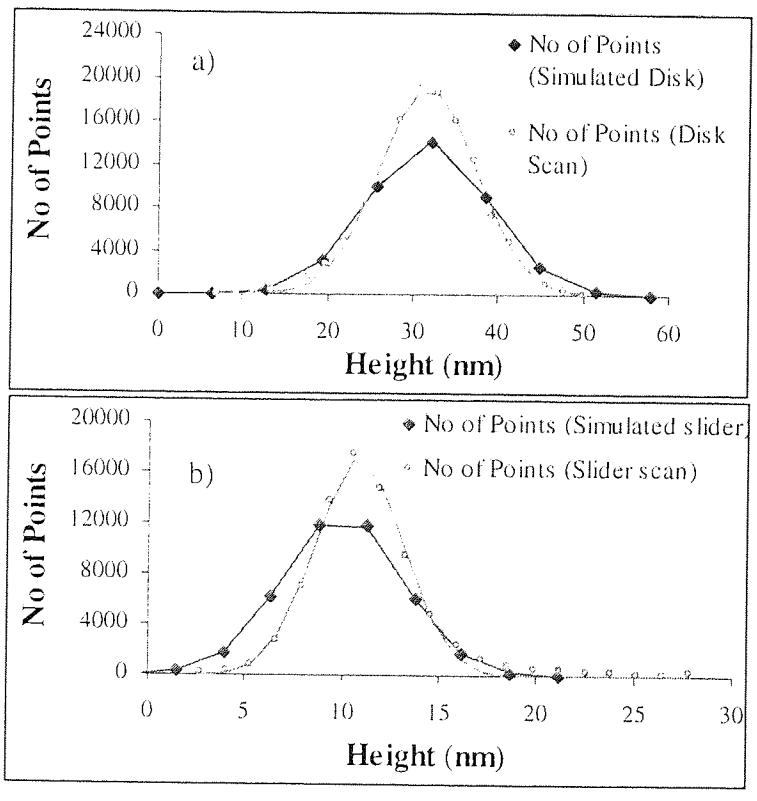

Figure 4.98 Surface distribution for real/simulated surfaces a) disk and b) slider scan

Equation 4.39 gives model used and Table 4.10 shows the Gaussian parameter for each data set.

$$G(h) = ae^{\frac{-(h-b)^2}{2c^2}}$$ **Equation 4.39**

Where h represents height in nm.

Gaussian Parameter	Disk		Slider	
	Actual Scan	Simulated	Actual Scan	Simulated
a	18867.29	14273.70	17058.50	12750.53
b	31.66	31.79	10.87	10.01
c	5.72	7.18	2.27	3.07

Table 4.10 Gaussian parameters for models

This method gave surfaces that were more realistic; it was also possible to further customise these 'random' surfaces to give required characteristics by using Box optimisation software as before.

Contact Investigation

Generated values were read into two-dimensional matrices for plotting purposes, overlay is shown below in Figure 4.99.

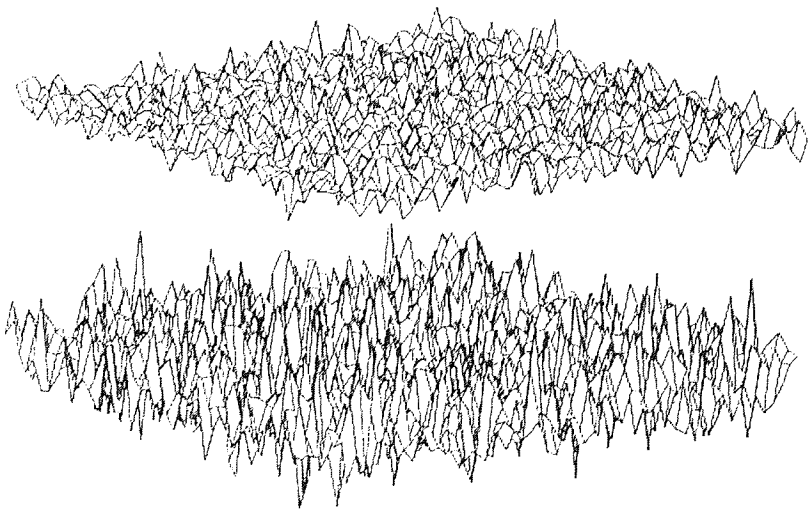

Figure 4.99 Generated surface overlay

Intersection points over 10 nm (intersection above mean 25+10 >10; i.e. total height > 45 nm) between parked simulated and simulated disk were studied. Contacting points were evenly distributed about surface and analysis gave that 1.75% of surfaces were in contact. Obviously, the simulation did not give the dependence on disk texture of contact points as seen in real surfaces.

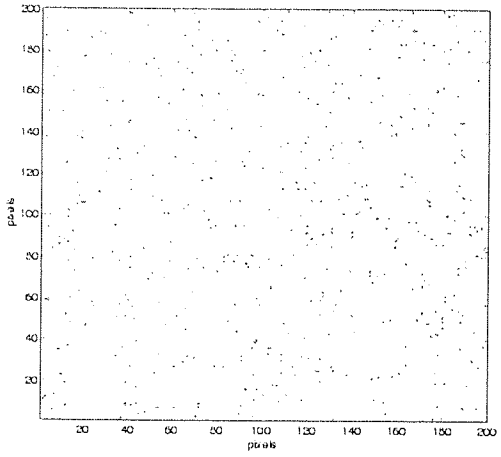

Figure 4.100 Results of generated surface overlay

Also, areas of contacting asperities was studied for each contact height, results were smaller than in reality, Figure 4.101.

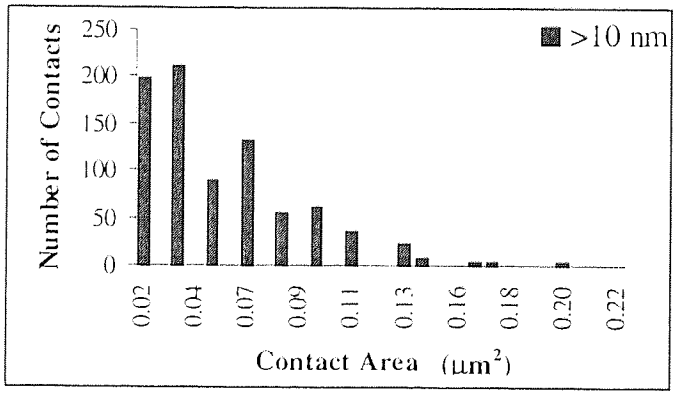

Figure 4.101 Contact area analysis for generated surface overlay

Method 3 : Altering Real Surfaces

For surface simulation it was decided to use real, exported AFM data and alter it using the Box optimiser to give required characteristics. This was achieved by creating an objective function which computed the error between the randomly altered surface characteristic and that desired at each iteration. The algorithm halted when this error fell below a predefined tolerance.

Surface alteration was accomplished by applying functions to each value of the real surface, the nature of the functions changed depending on the required characteristics. For example, to increase surface roughness whilst maintaining the peak to valley height, each value could be altered by adding/subtracting a random height (range to be chosen by the optimiser) with the objective function checking peak to valley height at each iteration and penalising the function if it strayed from the desired value.

Thus, the aim would be to minimise the value of

$$\text{Objective Function} = \frac{\left| \text{True } R_{rms} - \text{Desired } R_{rms} \right|}{w_1} + \frac{P\left| \text{True P - V - Desired P - V} \right|}{w_2}$$

Equation 4.40

where w_1, w_2 are weighting functions which need to be found experimentally and P is the penalty function.

Creating surfaces in this manner meant that the cross-hatched texture of disks usually remained adding to the reality of the surfaces.

4.4.2.2 Determining which Surface Parameters affected Flying Contact

It was of interest to find out which surface parameters influenced contact when surfaces were mated. Using Method 3 for surface generation, 150 surfaces having a wide range of characteristics were produced. These then had real slider scans, both NPAB and tri-pad, overlaid on them (using method described in Section 4.4.1.5 with separation height 20 nm). The percentage of surfaces in contact was computed.

Disk were generated to give rougher/smoother surfaces, to have distributions with differing amounts of skew. In addition, high peaks were added to some surfaces in random positions. An example is shown in Figure 4.102. The density, height and width of peaks was also investigated.

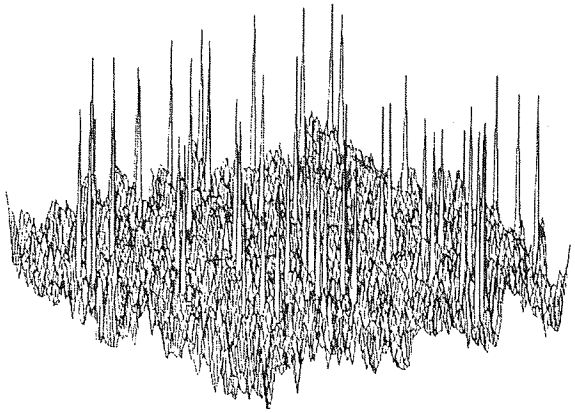

Figure 4.102 Example of generated peaked disk surface, 50 thin peaks added of height 70-80nm

Samples of disk surfaces generated are shown in Table 4.11 together with overlay contact results with real NPAB and tri-pad slider surfaces.

Surfaces Generated and Resulting Contact							% Contact NPAB	% Contact Tri-pad
Surface Description	**H**	**P-V**	**R_a**	**R_{rms}**	**Skew**	**Kurt**		
Real disk surface (unaltered)	19.14	38.35	3.89	4.98	-0.0096	2.365	4.85	3.24
Rough disk - similar P-V	19.64	41.34	8.15	9.95	-0.008	2.366	5.82	5.22
Rough disk - high P-V	19.15	60.18	9.35	11.55	0.0226	2.591	7.67	8.01
Very rough disk - very high P-V	44.08	90.13	14.55	17.57	0.006	2.355	13.49	18.80
Smooth disk - low P-V	19.99	10.35	2.56	2.95	0.014	1.804	0.05	0.01
Smooth disk - low P-V, positively skewed distribution	24.12	9.00	2.19	2.56	0.211	1.895	0.01	0.00
500 narrow peaks (0.2 µm/40-60 nm) randomly inserted on to disk surface	19.28	49.87	8.25	10.12	0.048	2.458	5.97	5.68
50 high wide peaks (60 nm high/1µm diameter) randomly inserted on to disk surface	19.40	69.78	8.36	10.50	0.393	3.939	6.28	5.72

Table 4.11 Generated disk surfaces and resulting contacts with real slider rail scan, where H is mean surface height

From the table it appears that rougher disks with higher P-V gave more contact with slider. Also, the NPAB appears to contact the disk more than the tri-pad. It was found that when adding high asperities to the surface the height of these was not significant, although the quantity and width of these peaks did affect contact.

Neural network modelling of all 150 surfaces will be carried out in Section 4.5.4, this will allow more detailed conclusions to be drawn.

4.5 Neural Network Tools for Prediction, Classification and Sensitivity Analysis

Neural Network Tools's (NNT's) are highly interconnected, computational structures used for relating multiple input data to one or many outputs. Classification and prediction are two of the most popular uses of NNT's.

4.5.1 Using NNT Tools on 1 rpm CSS Test Data

It was decided to investigate trends in the 1rpm CSS data using a NNT. Since all tests were performed under identical set-up with respect to disk velocity, track radius, fly height and duration, environmental parameters only were used as input parameters. To investigate which humidity measurement was most relevant; several different measures were input to the NNT.

4.5.1.1 Data Correlation

Before using NNT, calculation of the correlation coefficient, R^2, between each input parameter and stiction was calculated. Water vapour pressure had closest relationship to stiction, this was followed closely by dew point temperature, Figure 4.103.

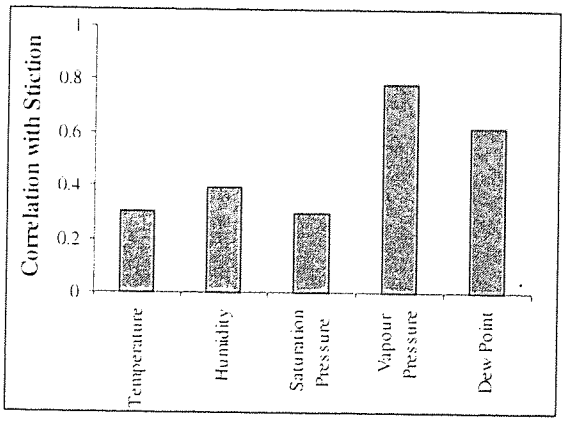

Figure 4.103 Correlation between stiction and each input parameter

4.5.1.2 Training the NNT

Data columns were tagged as input and the desired rows as training, a NNT was then created and trained. Training results are shown in Figure 4.104 below, mean square error did decrease monotonically but refused to fall below 0.01 even after 1000 iterations.

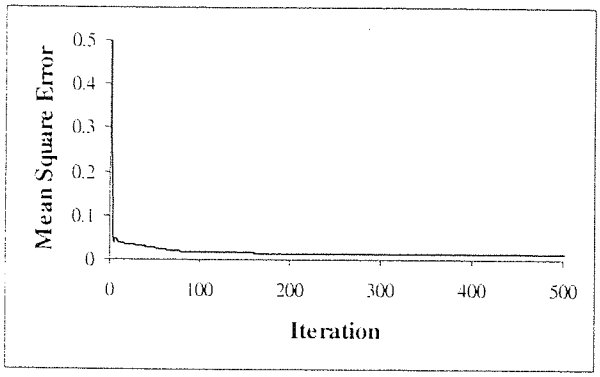

Figure 4.104 Training results

4.5.1.3 Testing the NNT

After training NNT once, testing gave the results shown in Figure 4.105. R^2 between actual and NNT output was 0.885.

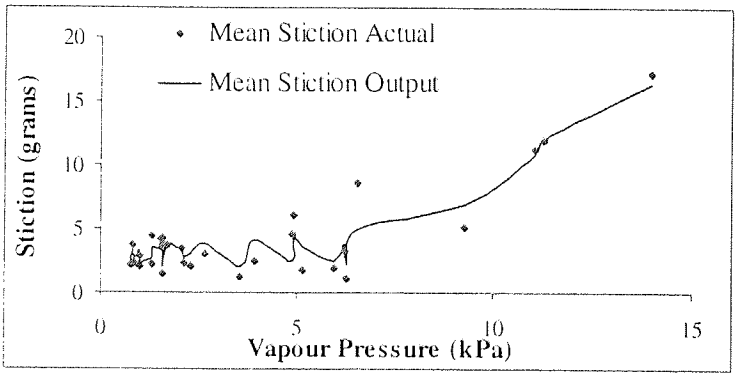

Figure 4.105 NNT output on mean stiction

It was decided to investigate whether further training of the NNT would improve its performance. The NNT was re-trained 5 times and re-tested, Figure 4.107.

The NNT gave very similar values to previously, increasing R^2 only slightly to 0.891. Thus, extra training time was not considered beneficial in this instance.

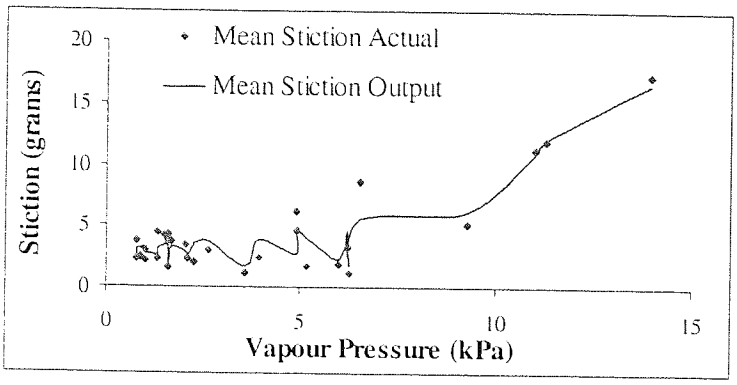

Figure 4.107 NNT performance after batch training (5 times)

4.5.1.4 Parameter Sensitivity Analysis

The NNT was next used to determine which environmental parameters were most important with respect to stiction, Figure 4.108.

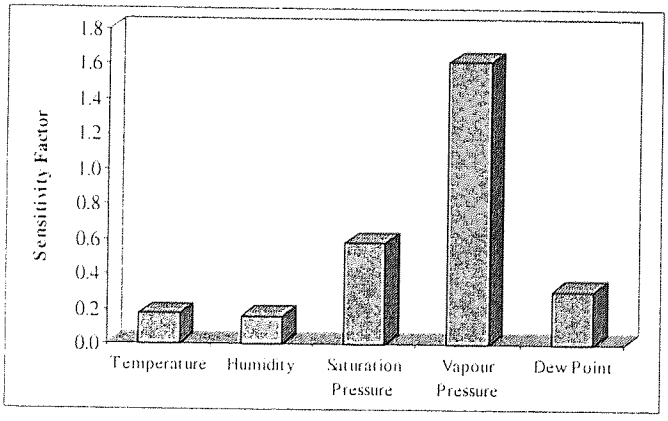

Figure 4.108 Sensitivity of stiction to environmental parameters

It was obvious that changes in vapour pressure had the most impact on stiction, this parameter had previously been identified as the most important on friction/stiction at the interface from manual observation of data, Section 4.1.4.2.

Figure 4.109 illustrates the changes in stiction as each parameter was varied $\pm 3\sigma$ about it's mean.

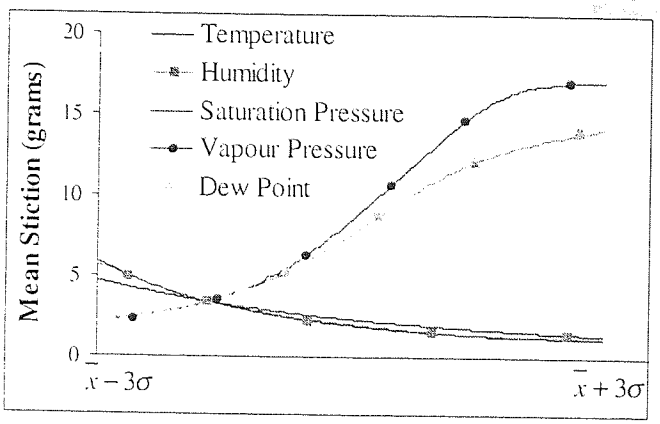

Figure 4.109 Stiction variation with changes in each parameter

4.5.1.5 New NNT with Only Vapour Pressure as Input

A new NNT was created having only one input, water vapour pressure. Training and testing results are shown below in Figure 4.110a) and b) respectively.

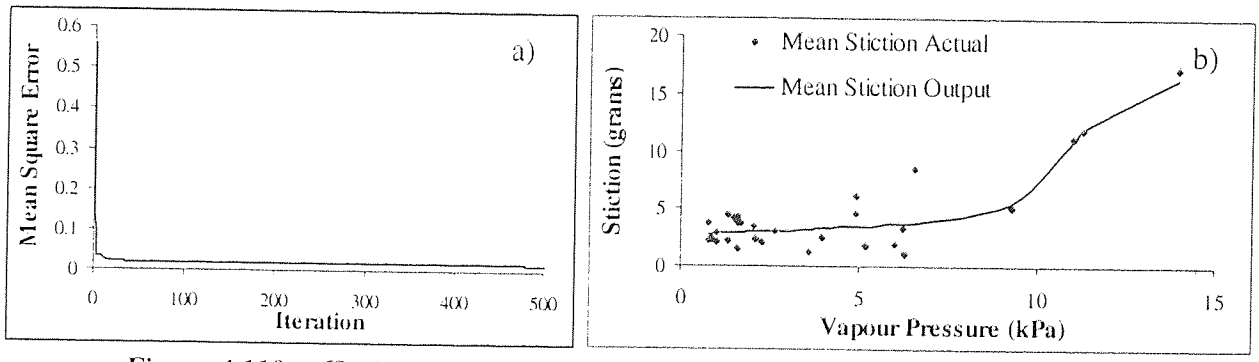

Figure 4.110 a) Training profile for new NNT and b) results on testing NNT

Mean square error was slightly higher than previously, now refusing to fall below 0.016 during training. Resulting NNT output gave slightly decreased correlation with actual values at R^2=0.829, but NNT still provided an adequate fit of stiction values.

4.5.2 Using NNT to Model Dynamic Friction Trace over 1 CSS at 1400 rpm with NPAB

It was decided to use a NNT to model the friction trace over a standard CSS cycle. Since the trace was shown to be almost symmetrical the take off and dwell phase data only was used. Slider type chosen was NPAB.

For friction analysis, slider fly height, disk velocity, disk circumfrential position cumulative distance travelled and time were tagged as NNT inputs and friction as NNT output. The NNT was trained on existing data from an early cycle and then tested on data it had not seen before (a later cycle in the same test).

Again before using the NNT, cross correlation of data was performed with friction for each input, results are shown in Figure 4.111.

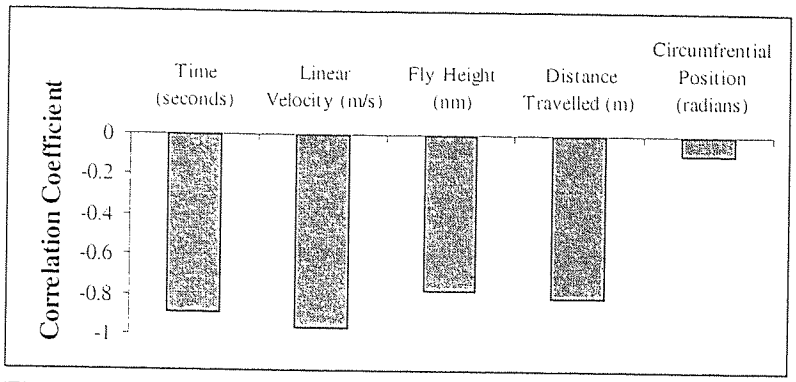

Figure 4.111 Showing negative correlation of variables with output

From the correlation values it seems all parameters were inversely related to friction, this was as expected. The parameter that appeared least likely to affect friction was disk circumfrential position, further investigation will confirm whether or not this parameter could be made redundant in the model.

4.5.2.1 Training the NNT

As files for this experiment were large (around 1000 elements) it was necessary to sample the data. Each eighth value was chosen to give a data set of size around 125.

Since, this was still quite large care was taken not to over-train the NNT by randomising the data and then tagging only the first 100 rows as training. The remaining rows were used as cross-validation which confirmed the model on existing data as it is built. Figure 4.112 shows training and testing results.

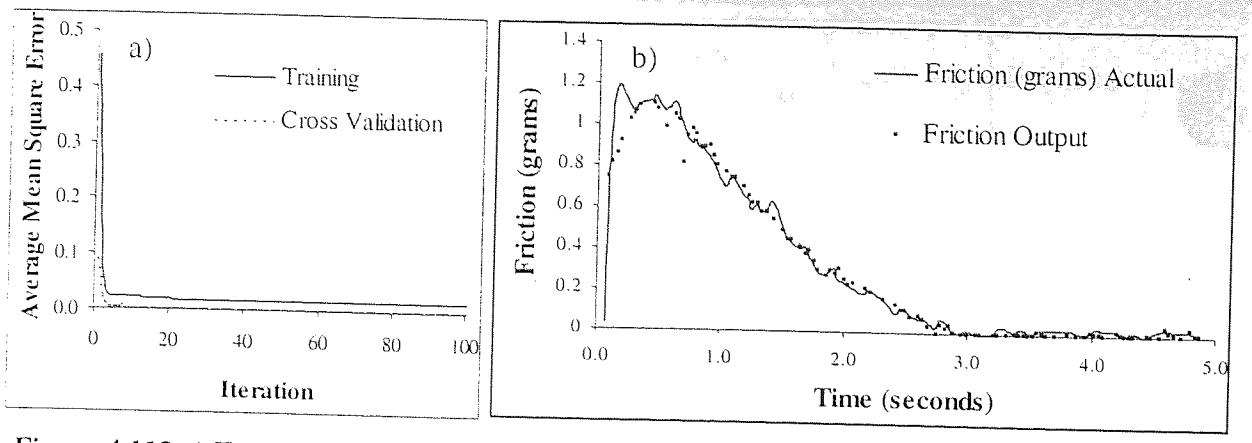

Figure 4.112 a) Training and cross-validation progress for NNT and b) testing results and actual data

The NNT learned quickly and was yielding errors <0.001 after only 100 iterations. Figure 4.112b) shows that NNT results matched the experimental data well, giving R^2 of 0.95. The only downfall was the lack of predictions for the very early readings (below 0.1 seconds); this could be due to the sampling process choosing only 2 values in this period and rendering the period under-represented. However, a separated network was built and trained for this period, testing results are shown in Figure 4.113.

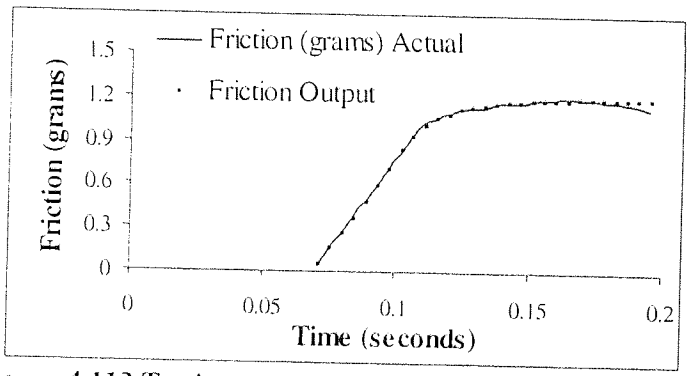

Figure 4.113 Testing results on initial time period NNT

4.5.2.2 Sensitivity Analysis using NNT

The NNT could also help eliminate irrelevant inputs into the model yielding simplicity and cutting computational expense. Sensitivity analysis was performed to see how each parameter affected friction when varied $\pm 3\sigma$ about it's mean. Figure 4.114 showed friction was inversely related to time, linear velocity and fly height, these parameters were also the most significant.

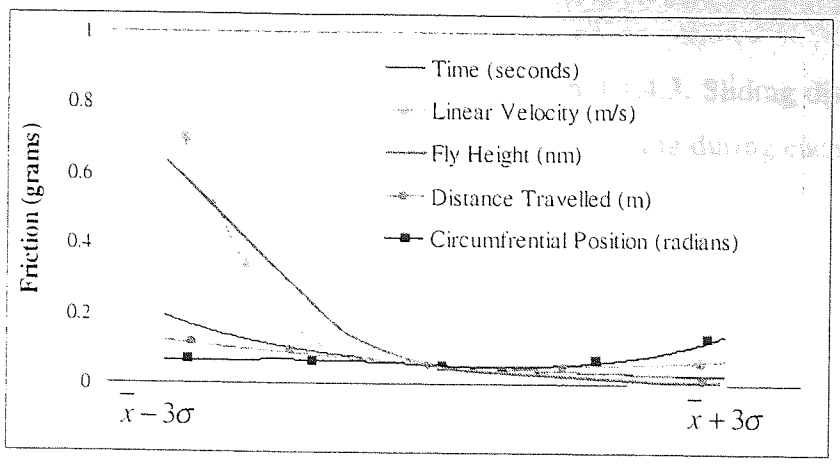

Figure 4.114 Friction variation with changes in each parameter

It was decided to disregard the parameters distance travelled and circumfrential position and re-train the NNT using only the three remaining inputs.

This did not mean these parameters would be redundant in all models. For instance, distance travelled was important when modelling friction over a long run (20 hours or more) and disk position was critical if the disk is damaged at a specific location giving high friction. Figure 4.115 shows the testing results of the reduced NNT. The fit was not as good as previously, with R^2=0.92, but the NNT trace predicted the slope of decrease in friction on take-off well.

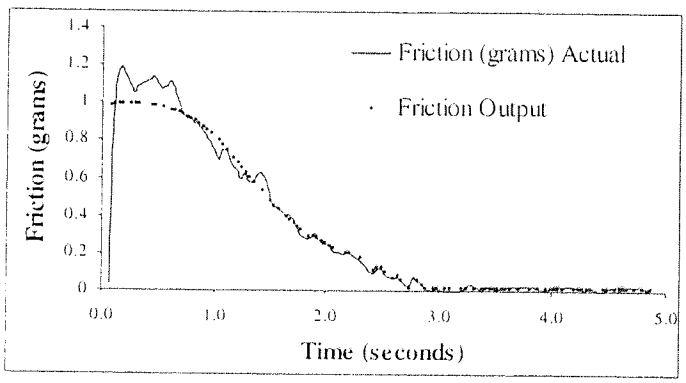

Figure 4.115 Reduced NNT output

4.5.3 Using NNT to Model Changes in Dynamic Friction with Cycle Number for Tri-pad

It was decided to study how the NNT coped with the changes in friction over a 7000 CSS test. Experiments have shown that using the tri-pad type slider, flying friction increases with time during a test, Figure 4.116. This was explained by smoothing of disk/slider surfaces allowing high real area of contact to occur when the slider is flying in close proximity to the disk. The test chosen was 7000 CSS performed in 55°C /10% RH, hot/dry conditions were chosen since

these gave most noticeable increase in friction, Section 4.1.4.3. Sliding distance was thought relevant again, since the slider experienced over 12m of sliding during each cycle, so this was again included as an input parameter to the NNT.

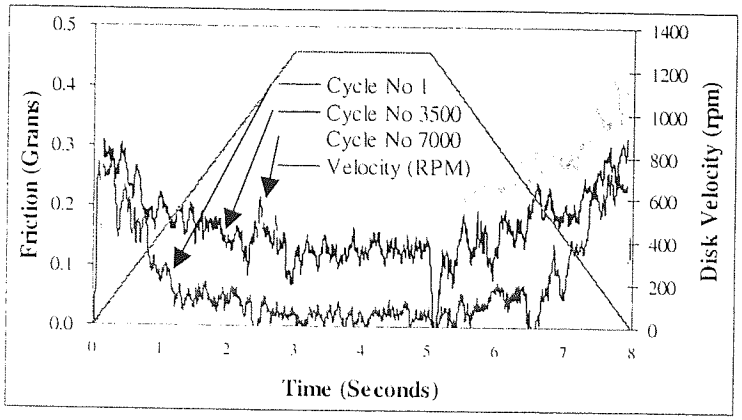

Figure 4.116 Increasing friction with cycle number using tri-pad slider

Another interesting parameter here was fly height. Using the model formulated in Section 4.1.6, it was observed that slider fly height was related to disk roughness. Thus, as the smoothing process takes place changes will occur in slider fly height, Figure 4.117. Values were predicted using measured disk R_a roughness values, 4.33, 3.43 and 3.12 nm for virgin, part-used and used disks respectively.

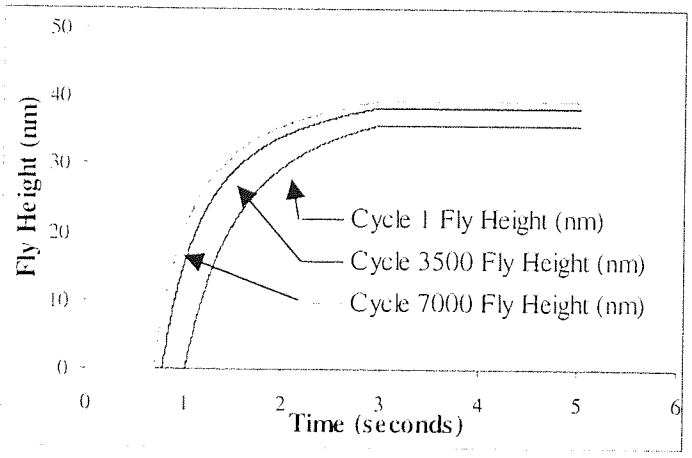

Figure 4.117 Estimated fly height for initial, mid and final cycle

Notice the slider flew marginally higher over the worn disk than virgin (by around 4 nm), which implied that friction should be lower near the end of a test and not higher. Thus, source of increase in friction could be related to debris accumulation on slider giving more contact.

A NNT was developed using the three strong parameters - time, linear velocity and fly height plus sliding distance as inputs. The NNT was successfully trained on friction data, Figure 4.118; testing results are shown in Figure 4.119.

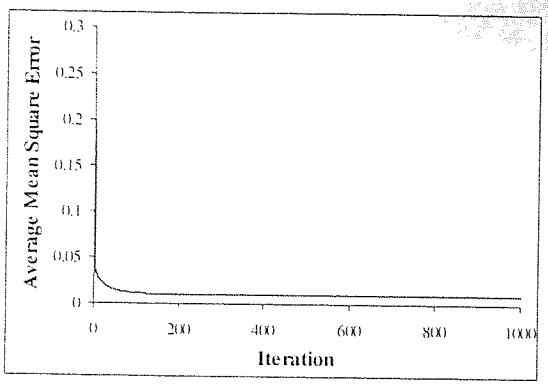

Figure 4.118 Training results for new NNT

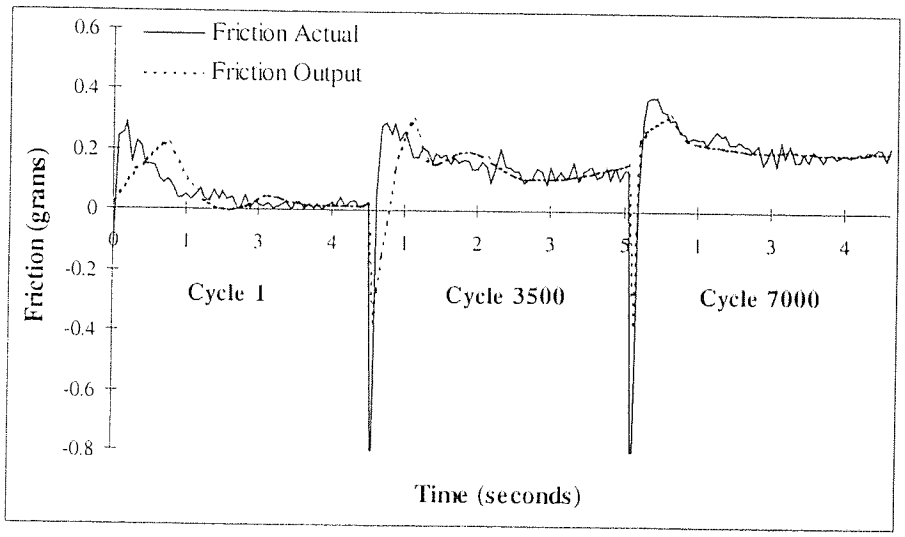

Figure 4.119 Testing results for new NNT

4.5.3.1 Classification of CSS Cycle from Friction Trace

It was decided to test how readily the NNT could distinguish between CSS cycles at different stages of a test. A new NNT was created with three output columns tagged as test number classifiers - cycle 1, cycle 3500 and cycle 7000. That is, these columns contained '1' if friction belonged to that cycle and '0' if not. Friction was now used as the only NNT input.

Using data from the above test the NNT was trained and then tested, Figure 4.120. Notice the network did not train well, having error 0.3 even after 1000 iterations.

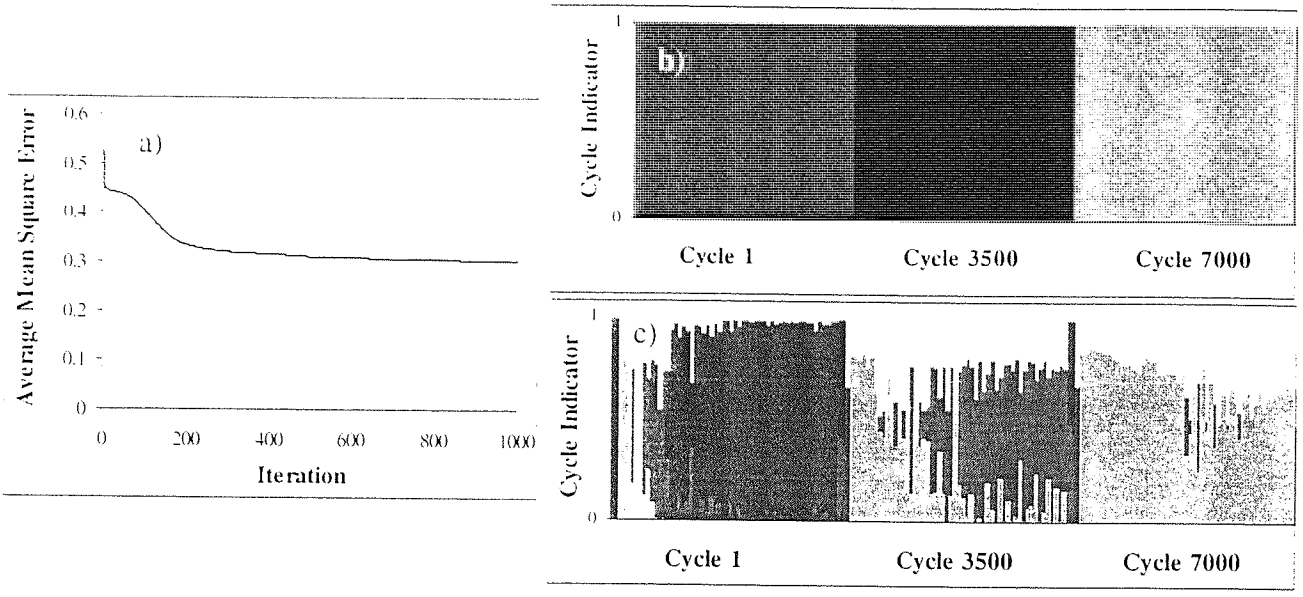

Figure 4.120 a) Training, b) classification actual data and c) testing results for NNT

Despite the persistent training error the NNT managed to correctly classify the majority of friction values to the cycle they belonged to, Table 4.12 illustrates the truth table showing the percentage of values correctly classified.

Output Desired	Cycle 1	Cycle 3500	Cycle 7000
Cycle 1	78.95	3.51	3.51
Cycle 3500	12.28	73.68	14.04
Cycle 7000	8.77	22.81	82.46

Table 4.12 Truth-table showing how friction values were classified (training data)

The NNT was then tested on new data, this was from a CSS test conducted in 45°C/10% RH. Figure 4.121 shows the actual friction traces from this test. NNT testing results are shown in Figure 4.122 with truth table shown in Table 4.13. It seemed the NNT could identify from which cycle the majority of friction values hailed.

The main confusion in results seemed to be between cycle 3500 and 7000; this was most likely due to the numerical similarity of friction traces from these cycles.

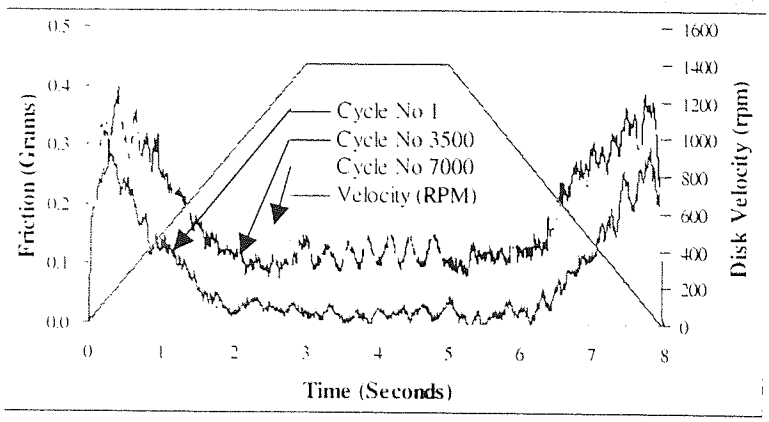

Figure 4.121Friction traces from 45°C/10% RH CSS test

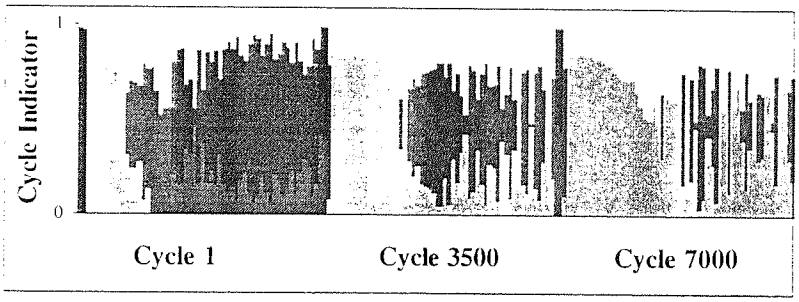

Figure 4.122 Classification test results

Output Desired	Cycle 1	Cycle 3500	Cycle 7000
Cycle 1	64.91	3.51	3.51
Cycle 3500	19.30	63.16	36.84
Cycle 7000	15.79	33.33	59.65

Table 4.13 Truth-table showing how friction values were classified (new data)

4.5.4 Optimal Disk Surface for Least Flying Contact

Using the 150 generated disk parameters and slider overlay figures from Section 4.4.2.1 a new NNT was built. This time inputs to the network were disk height, P-V, R_a, R_{rms}, skew and kurtosis. Network outpouts were the percentage contacts occuring followomg overlay with NPAB and tri-pad sliders.

Care was again taken not to over-train the NNT by randomising the data and then tagging only the first 100 rows as training. The remaining 50 rows were used as cross-validation to confirm the model. Training and testing results are shown in Figure 4.123.

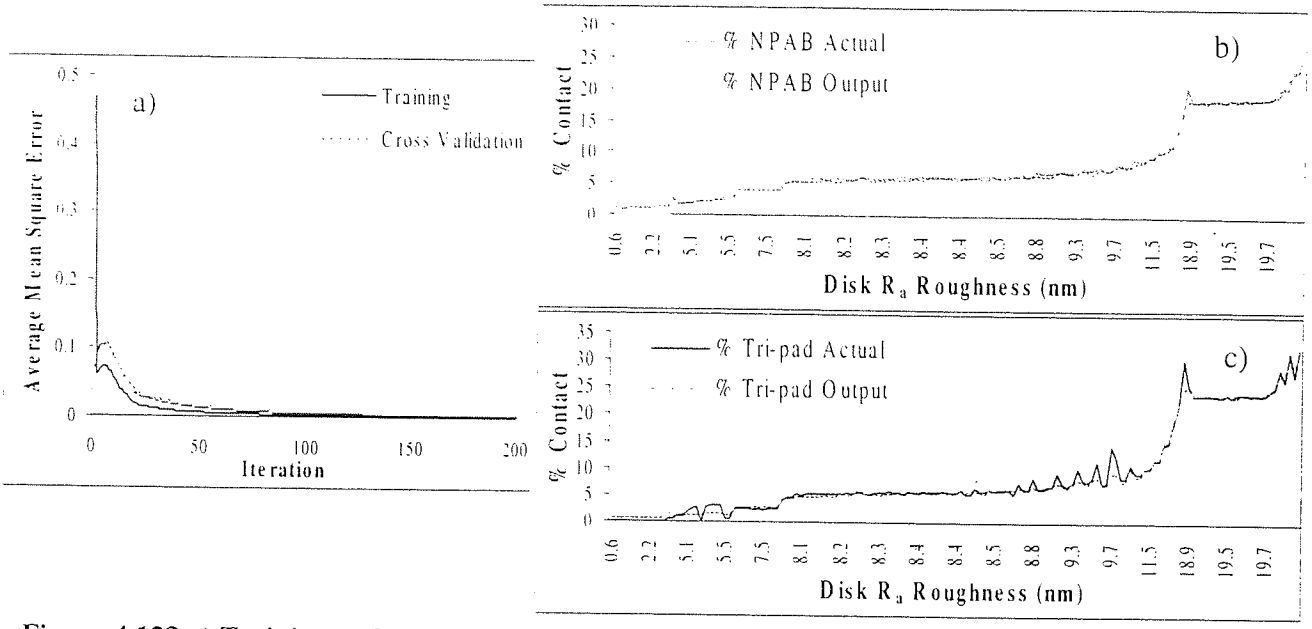

Figure 4.123 a) Training and cross-validation progress for NNT and b) testing results and actual data

Thus, the NNT could easily predict percentage of surface contact given the inputs height, P-V, R_a, R_{rms}, skew and kurtosis. R^2 between actual and output results were >0.98 for both sliders. It was decided to use sensitivity analysis to determine which of these most affected contact, results are shown in Figure 4.124.

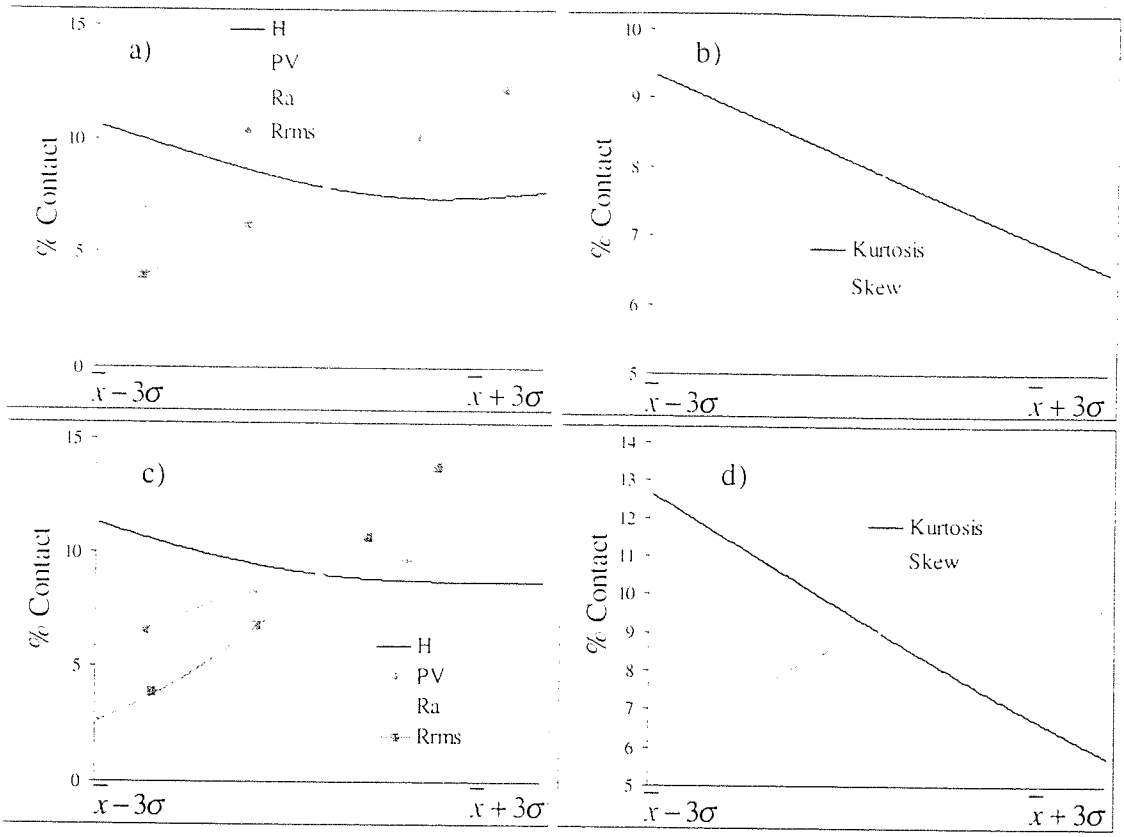

Figure 4.124 Effect of a) surface roughness and b) surface distribution parameters on % contact with NPAB and c) surface roughness and d) surface distribution parameters on % contact with tri-pad

Clearly, disk roughness was strongly related to contact especially for the tri-pad, with rough disks yielding highest values. Surface height and P-V did not affect contact greatly. Disk height distribution was found to be important, with negative skewness and high kurtosis necessary for low contact.

To confirm this 2 disk surfaces were generated - one having negative skewness and high kurtosis (-0.004 and 4.10 respectively) and the other having positive skewness and low kurtosis (0.21 and 2.30 respectively). It was attempted to keep all other surface parameters constant. Overlays were performed for a tri-pad slider with resulting contact areas of 3.23% and 5.15% given.

5 Discussion

5.1 CSS Testing

5.1.1 Friction

5.1.1.1 Dynamic Friction Trace over CSS Cycles

For both sliders the friction trace over each CSS cycle followed the Stribeck curve from high initial values and decreased as disk velocity increased, Figure 3.2. The lubrication regime changed from boundary to hydrodynamic as the head started to fly. Friction then became near zero as the head, now supported by the air bearing which formed at high velocity, flew with little contact to the disk and increased again as the disk came to rest.

A 6th order polynomial, in terms of disk velocity, was originally used to describe friction over each CSS cycle, Section 4.1.1. However when looking for a general form of model the 7 polynomial coefficients proved problematic. It was decided instead to use the near symmetrical property of the friction trace to produce a 3rd order or Cubic model for friction with respect to disk velocity, thus reducing the number of model coefficients to 4, Figure 4.3. Cubic models were fitted to friction traces at a range of velocities. Coefficients were used to form a matrix, which when multiplied by a second matrix containing the appropriate disk velocity figures reproduced the trace 'bathtub' shape. By interpolation between coefficient matrix columns estimates of the friction trace shape could be produced for any disk velocity in the range [2-15] m/s by using the relationship

$$\underline{f}_i(t) = \sum_{k=3}^{0} \sum_{j=1}^{4} \sum_{i=0}^{6} \left[(D^T)_{j,(i+1)} (V_d)_{(i+1),j}{}^{(6-i)} \right]^T v_i(t)^k$$

where D is the coefficient matrix, V_d the dwell velocity matrix and v_i the vector containing the appropriate velocity value at time t. To attain the vector v_i integration of the known motor acceleration value was used. Section 4.1.1.1

The modelled traces were found to match the take-off/landing slope values of real friction curves well, Figure 4.9.

It was common for sliders not to fly correctly on their first CSS cycle (see Figure 3.3a) and Figure 3.4), this was also observed by Gui and Marchon [100]. This was due to the long parking time before test while pre-test checks were being made (up to 30 minutes) allowing adhesion of slider to disk.

For both sliders, take-off friction slopes grew steeper as CSS testing progressed. This implied a more rapid advancement to the slider flying free of disk with increasing cycle number. The steepness of landing slopes was also found to increase. The suggested mechanism was burnishing of disk and slider highest asperities with test progression. This meant that surfaces generally would be smoother and would thus experience 'complete' separation more suddenly. This was confirmed by bearing curve analysis of corresponding AFM scans in Section 4.4.1.1, which confirmed the loss of the highest slider/disk asperities following testing. Figure 4.72a) shows bearing curves for a virgin disk and that used in a standard 7K CSS test, for the used disk surface heights were around 5 nm lower than virgin. Note although the AFM Topometrix analysis package facilitated bearing curve analysis, in order to examine multiple bearing curves on the same graph scan files were exported numerically and the curves were then manufactured and graphed in *Microsoft Excel*.

Friction also decreased more rapidly during take-off for the NPAB than the tri-pad slider. This was illustrated for CSS testing at dwell velocities in the range [1-15] m/s, see Table 3.1. Differences in slider geometry could explain this behaviour. For the NPAB slider once sufficient pressure had built up in the cavity, pitch alteration to slider flying position would be rapid, due to this slider having shorter rail length [122].

Additionally, the NPAB slider flew with lower friction than the tri-pad during standard velocity tests, this was due to the more advanced flying characteristics of this slider type [55,122]. The absence of a contact pad on the NPAB's trailing edge also meant there would be less contact with disk once the slider pitch was orientated for normal flying,

Increases in dynamic friction with cycle number observed in this work were similar to those reported elsewhere [40,106]. Worn regions of disk were found to be smoother than virgin regions by AFM, Table 3.9, and theoretically had higher real area of contact associated with them.

The significance of surface smoothness was additionally highlighted in Section 3.1.5.2 by experiments on graded texture disks, where higher friction was experienced over smoother disk landing regions using identical test set-up. The friction performance of this disk type in ambient was better than that of crosshatched disks. This could be attributed to the presence of nitrogen in the disk overcoat (as detected by XPS) resulting in an overcoat to which lubricant bonded favourably for friction and wear performance [47]. However, this overcoat type was reported to be susceptible to voids by Fung et al [67] and Cutiongco et al [32]. This would mean that high humidity testing could possibly lead to corrosion of magnetic and substrate layers.

The extent to which surface smoothing was responsible for dynamic friction increases could be measured by performing contact analysis of AFM disk and slider scans. Section 4.4.1.5 described a technique in which AFM disk and slider scans were exported numerically and 'overlaid' to establish how much of the surfaces were actually touching. Corresponding 20 μm scans of slider trailing edge and disk data zone were overlaid, scans were taken perpendicular to the length of read-write shields and parallel to disk tracks to ensure mating of scans would simulate real contact. It was found that contact area for worn surfaces was much higher than that expected for virgin, Figure 4.85a) and b). As expected the difference in contact area for virgin/worn contacts decreased at higher testing velocity whereby surfaces were thought to be separated by a hydrodynamic air bearing.

5.1.1.2 Mean Flying Friction over CSS Tests

Mean flying friction was a function of cycle number for both slider types. A linear model was used to describe the increase for NPAB sliders. For the tri-pad slider the Gompertz model was employed to describe the initial increase and subsequent levelling off of friction, the model is given as

$$f(t) = f(0)e^{\frac{r}{l}(1-e^{-lt})} \qquad \textbf{Equation 5.1}$$

where parameter r gave the rate of increase in mean friction, with highest values yielding the highest slope. In addition to slider geometry, this observed mean friction difference was possibly due to the NPAB's ability to constantly readjust it's fly height in response to disk texture. This would mean some slider/disk contact would occur even after the initial burnishing phase had expired giving continually increasing friction. Conversely for the tri-

pad, burnishing of the virgin disk/slider highest asperities occurred during the first 2-4 hours of a test only.

The tri-pad exhibited higher final flying friction than the NPAB, with values reaching around 0.1 grams as opposed to 0.05 grams for the NPAB, see Figure 3.8 and Figure 3.10 respectively. This could be explained by differences in slider material since the absence of slider overcoat on the tri-pad meant direct contact between Al_2O_3-TiC and disk which was reported by Pan and Novotny [59] to lead to escalated lubricant degradation and depletion. In the study Al_2O_3-TiC was found to cause breakdown of PFPE lubricant to form fluorides, this was especially notable at elevated temperature/humidity.

Additionally, NPAB slider gave the lowest variation in mean friction during flying, Figure 3.12. This was as expected since this slider was designed to fly with a more level profile and would therefore contact the disk less erratically than the tri-pad. Peng and Hardie [55] also reported that the NPAB sliders exhibited more stable flying characteristics than tri-pads.

For both sliders, the observed increase in friction variation with cycle number was attributed to uneven wear of the disk around it's circumference. Contact analysis of corresponding slider trailing edge and disk testing radius confirmed this. Sets of 4 AFM scans were taken at 90° around the circumference of virgin and tested disks and contact analysis performed. Results in Figure 4.90 show that standard deviation in % real area of contact between regions was significantly less for virgin scans than worn.

5.1.1.3 Environmental Effect on CSS Tests Friction

With regards to humidity the apparatus had to be heated thoroughly before introducing moisture to prevent condensation occurring. Controlling humidity was problematic due to the on/off switching of the water heating thermostat, unavoidable oscillations in humidity were recorded Figure 2.17b). In all modelling work mean humidity values were used.

The effects of environment on mean flying friction were difficult to detect, this was as expected since the slider was largely supported by the air bearing, whilst the mean friction calculation was made. Consequently, plotting mean friction directly against environmental parameters revealed no trends. By applying the Gompertz model to environmental mean

friction results some general relationships could be developed. The Gompertz parameter 'r' (representing rate of initial friction increase) was studied as a function of temperature and humidity in Figure 4.20.

High temperature was shown to be associated with slightly higher 'r' values, this was due to decreased load capacity of the slider resulting in lower fly height. This would increase the burnishing rate at the start of a test. Additionally, high temperatures would render the lubricant less viscous and thus less able to provide adequate interface protection [111].

Conversely, high humidity was associated with lower 'r' values. Increased humidity acted as an extra lubricant between disk and slider in the event of contacts. Thus, the rate of increase in mean friction was observed to be slightly lower under humid conditions. This result was supported by Cha et al [111] who reported that some additional water at the interface meant the shear strength of asperity junctions decreased aiding friction on disk lubricated with long chain PFPE's. However, at very high humidity the adsorbed water layer could be of comparable thickness to lubricant layer, this meant the surface tension of adsorbed layers would increase and again raise friction.

Yang et al [86] reported rapid increases in friction in humid environments, in the study humidity was quoted as 53% RH, but since temperature was not given it was difficult to ascertain exactly how wet the air was. For instance, air at 40°C would be around 3 times more humid than air at 20°C with respect to water content whilst both sharing the relative humidity value 53% RH. It was also recognised in this work that extremely wet environments could give increased and erratic friction. When air became at or near saturation values, water molecules could displace lubricant and render the interface unprotected giving high friction [41]. It was found that the tri-pad slider performed worst in humid environments, this was as expected since Al_2O_3-TiC was reported to attain highest water layer thickness due to the Al_2O_3 phase being a good absorber of water [117].

5.1.2 Fly Height over CSS Tests

Friction was found to decrease rapidly above a velocity of around 1 m/s - this was thought to be the critical velocity for flying for both slider types under this test set-up, Figure 3.21. For the tri-pad slider friction continued to decrease as velocity was further increased to 7 m/s. For

the NPAB an additional critical velocity of 5 m/s was established above which friction again began to increase. It was noted that CSS testing above 10 m/s introduced instability into AFT results, thus it was decided this was the limiting velocity of this particular testing apparatus, Figure 4.58.

Based on the relationship $V_{rms} \propto \frac{V}{FH}$ as given by Khurdoshov and Talke [110], where V_{rms} is the root-mean square of AE signal, V is velocity and FH is fly height, a velocity based model was developed for fly height in terms of velocity and friction for each slider type (Section 4.2.1). The NPAB model showed a decrease in fly height at 5 m/s which was thought to be due to the negative pressure affect of the slider initiating around this velocity, see Figure 4.35.

Donovan and Bogy [68] accurately measured the fly heights of a tri-pad slider over 4 disks with varying roughness, for each disk R_a, R_{rms} and R_p were quoted. The figures given were used here to develop a disk roughness based fly height model (Section 4.2.2). Firstly a neural network was built to model the data and determine via sensitivity analysis which of the given roughness parameters most affected slider fly height. It was established the disk average roughness, R_a, was most important and this was used as the basis for the model as follows

$$FH = 38.02 + 2.97\left(\frac{V}{R_a}\right) - \frac{2.74}{\left(V/R_a\right)^2} \qquad \textbf{Equation 4.28}$$

where V was again disk velocity. This model predicted dwell time fly height over a virgin crosshatched disk which was 8.32% lower than that given by the velocity based model during a standard CSS test. The model gave that fly height increase occurred over smooth surfaces, but it should be noted that the amount of smoothing taking place during a CSS would result only a negligible effect on fly height in the order of 2 nm for a standard test.

The model supported the notion that the time at which friction suddenly decreased (i.e. the time when the slider is completely flying) will be earlier for smooth disks than rough. Obviously, this is due to smooth disks containing lower asperities than rough, meaning the slider flew clear of the disk sooner. This phenomena was observed with work at the rough inner and smooth outer diameters of graded texture disks, Figure 3.35.

It was impossible to locate manufacturers dynamic fly height data for the sliders used, but predicted fly heights for the same slider types were in the ranges stated by Talke et al in [155].

5.1.3 Stiction

5.1.3.1 Stiction over CSS Tests

Smoothing of surfaces similarly led to higher stiction, with an increase observed with CSS cycle number for both slider types. Smoothing was again confirmed by AFM scanning of surfaces.

It was found that the maximum AFM scan size possible should be used to minimise error and variation in roughness calculations. Figure 3.65. For disks, this was usually dictated by the maximum instrument size of 100 μm^2 and for sliders by rail width and curvature, which usually resulted in scans of 50 μm^2. Scan direction was also critical when imaging surfaces, it was found that running the AFM scanning tip at 270° , i.e. perpendicular to disk track direction gave sharpest images. Figure 3.63a) and b) compares disk scans taken at 0° and 270°. For sliders scanning across the length of rails gave improved images. Scan directions used for disks and sliders are illustrated schematically in Figure 2.23a) and b) respectively.

Contact analysis of AFM disk inner diameter and slider leading edge scans gave that the mean area of contact spots had a more significant affect on recorded stiction than the actual number of asperities in contact, with largest area contacts leading to highest stiction as seen in Figure 4.81.

Analysis also confirmed that once the highest asperities had been worn from the disk, contact area shape was dictated by disk topography and could be clearly seen to follow crosshatched texture shape. Note, the similarity of disk contour plot in Figure 4.69a) and worn contact area plots for NPAB and tri-pad in Figure 4.80b) and d) respectively.

A track change experiment revealed that stiction once again decreased to initial values on moving the slider to a different disk region following 7000 CSS cycles. This again suggested that disk smoothing, rather than slider, was most heavily responsible for the observed stiction rise. Since virgin disks contained a much wider range of heights than slider surfaces, it agreed with intuition that the smoothing of these would have relatively more impact. Gaussian height

distributions for disks and sliders area shown in Figure 4.71. The distributions were obtained by numerically exporting AFM scans to file and then performing histogram analysis.

No explainable relationship between stiction and disk pull off velocity could be found, see velocity work in Section 3.1.2.3. The lack of an obvious relationship of stiction with velocity was common using crosshatched disks and was also reported by Sullivan and Chao [81]. However, it has been shown in other literature that using laser textured disks linearity between stiction and velocity was presented.

5.1.3.2 Environmental Effect on CSS Stiction

Environment was an incredibly important parameter at the interface where stiction was concerned, with high temperature and/or humidity both resulting in high stiction. Moisture at the interface increased the adhesive force of stiction; this was widely recognised. However, in this work relative humidity was found to be a inadequate measure of moisture content of air since it has strong temperature dependence. Figure 4.18b). Water vapour pressure or dew point temperature were instead used for modelling purposes, Figure 4.18a). Modelling stiction as a function of several measures of humidity using a Neural Network and performing sensitivity analysis confirmed the high parameter weighting of the water vapour pressure in particular, Figure 4.108. In fact, mean stiction over a CSS test was found to be an exponential function of water vapour pressure, Figure 4.19.

It has been reported by Bhushan and Zhao [117] that at humidity in excess of 50% RH water can displace the disk lubricant due to its high surface tension. This means that slider/disk contact can be either unlubricated or overlubricated due to lubricant migration. Both of these effects can lead to high stiction.

CSS stiction inversely followed sudden increases/decreases in humidity almost immediately, Figure 3.28. Often where rogue friction/stiction results were observed, investigating the environment could offer an explanation. Short periods of severe environmental conditions were often tolerable by the interface. However, where changes lasted longer than around 2 minutes usually caused complete and irreversible interface failure.

High temperatures also had high stiction associated with them, this again could be due to the ability of air to hold more moisture when warm and increase stiction via adhesive forces. Additionally, decreases in lubricant viscosity with increasing temperature could additionally be responsible as reported by Cha et al [111], since this would give the same affect as increasing the mobile or unbonded fraction of disk lubricant.

Stiction distribution shape enabled tests to be classified as successes or failures. A normal test was usually represented by a positively skewed uni-modal distribution, as shown in Figure 3.15. Pearson's coefficient of skew could be used to simply quantify the distribution shape, Equation 3.2, with expected values being in the range [0.85-0.9]. Where more than one peak was observed this indicated that a problem had occurred, an example shown in Figure 3.49b). Multi-modal behaviour arose due to slider rails not becoming unstable simultaneously. Thus, for a failed tri-pad slider a tri-modal distribution was found as expected, Figure 3.50b).

Producing a map of stiction against slider parking position on disk was also a useful technique in failure analysis. Slider parking position was deduced by integration of the CSS velocity curve and then translation to give disk polar position. High values recorded at one particular disk site could suggest some localised damage of disk, which would then merit further investigation by surface analysis techniques. For example in Figure 4.15 the shaded area of disk appeared to contain highest values, it was concluded that localised disk damage had occurred there although little evidence could be supplied by surface analysis techniques in this instance. The stiction map shown in Figure 3.49c) shows two distinct levels of stiction at all disk positions which inferred that slider rather than disk had become damaged during testing. From the time series stiction plot it could be estimated that this damage occurred around 3 hours into the test. Investigation by SEM confirmed this, with an abundance of debris/damage observed on slider leading edge, Figure 3.106.

Increase to some stiction maximum with slider parking or dwell time was observed in the pause work in Section 3.1.4,. It could definitely be said that following a long pause the slider had great difficulty pulling-off from disk, Figure 3.33 illustrates. When a body comes to rest upon another, the liquid film interface is not in equilibrium; liquid will redistribute itself to form menisci around contacting points increasing stiction. The equilibrium times presented in [40] were longer than observed in this work, with saturation times of 1-4 days quoted under

ambient conditions. However, Bhushan et al [91] gave equilibrium time as around 1000 s, which was consistent with the 20 minutes observed in this work.

A relationship between equilibrium time and disk roughness was with rougher disks having shorter equilibrium times. This could explain the differences between this work and others noted above. Bhushan and Zhao [117] concluded that equilibrium time is also dependent on chemical structure, viscosity and bonding of the lubricant, and environmental conditions.

It was found that high humidity in particular, when coupled with long dwell time, increased stiction dramatically. The force was such that sliders were actually removed from their suspension mechanisms when the interface was manually separated. This also resulted in disks being badly marked with slider footprints, an SEM image of this is shown in Figure 3.96. Wang [36] reported that some pause between cycles could be beneficial to the interface since it allowed migration of lubricant back to test track, however this certainly would not be the case under conditions of elevated humidity.

5.1.4 Material Transfer during CSS Tests

Contact analysis also suggested that smoothing was not solely responsible for increasing stiction, with stiction continuing to increase after mean contact area had reached equilibrium, Figure 4.82. Xu and Bhushan [53] reported that transfer of disk materials, such as lubricant, to slider during testing would additionally increase stiction by enhancing the meniscus effect at the interface. XPS results confirmed that material transfer was definitely occurring in this work with disk lubricant material and carbon overcoat detected on sliders (Section 3.2.2.2).

The leading edge of NPAB slider rails collected most disk lubricant, this may have occurred during slider inter-cycle parking time on disk. Conversely for the tri-pad, most transferred disk lubricant was detected on the slider contact pad at the trailing edge. This transfer could have occurred during slider flying phase. Results were confirmed by XPS, Table 3.12.

The leading edge of NPAB slider rails also collected most debris, this was confirmed by customised analysis of AFM scans. Scans were imported in *Scion Image* and altered to become grayscale binary images, as described in Section 4.3.1.2, allowing foreign particle quantification to be conducted. Again, the transfer may have occurred during slider parking

time on disk between CSS cycles. Disk lubricant was thought to be a possible mechanism for debris transferral.

By considering the types of flying contacts that could occur when a slider impacts a disk asperity some alternative explanations for debris location are implied. Uy [63] classified contacts as Types 1 or 2 depending the height of the asperity. If it was less than slider fly height the slider leading edge was said to contact it as shown in Figure 1.26, if it was greater than slider fly height the trailing edge contacted as shown in Figure 1.27. By bearing curve analysis of disk, Figure 4.72a), it could be said that highest disk asperities lay in the range 30-40 nm. This would be below the predicted fly height for a NPAB during a standard CSS test, Figure 4.30, but above the prediction for a tri-pad slider, Figure 4.31. This would imply that for the former slider type contacts would be of Type 1, i.e. the leading edge would be most susceptible to debris collection. For the tri-pad slider contacts would be of Type 2 and the trailing edge would be most receptive, thus justifying the surface analysis results observed.

It was also found that the outer slider rail collected slightly more debris than the inner, this was probably due to the longer sliding/flying distance experienced by this rail. Since integration of disk velocity gave that it travelled almost 4 miles further, Table 4.4. Also, centrifugal force would dictate the final position of any smaller flying particles was towards the outer rail.

Increases in initial slider-disk surface separation peak times with CSS cycle number were observed for both slider types, Figure 3.7. In addition to surface smoothing, the suggested mechanism responsible was lubricant transfer to slider from disk. As mentioned above, this was proven by XPS analysis which confirmed that following normal CSS testing disk lubricant originated fluorine was found on slider surfaces. Notice, the most significant increase was found to be between 1st and 3500th cycles - indicating that most smoothing and transfer took place during the first half of the test.

It was also observed that separation peak times were marginally longer for the NPAB slider than tri-pad, Figure 4.12. Differing slider mass/geometry could have been responsible for this. Additionally, the NPAB had a DLC overcoat which was known to have relatively high sp_2 bond content, this meant that lubricant bonded well to the surface and would increase

adhesive force of stiction. Note for both sliders an inverse relationship of peak time with disk acceleration was present as expected.

5.1.5 Wear during CSS Tests

Pugh [104] states that wear should be minimal under steady operating conditions, however where start/stopping takes place much wear will occur. This was a major factor in choosing to perform CSS tests.

Distance boundaries for wear progression as given in [21] were projected onto CSS results. It was established that during the initial stages of CSS testing the sliding distance experienced could be split up into stages as shown below.

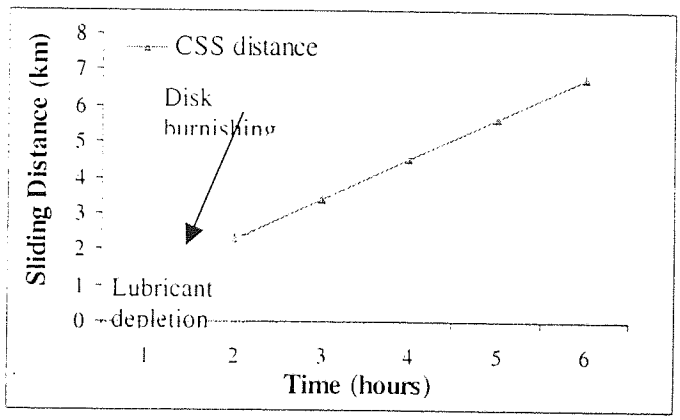

Figure 5.1 Wear progression during CSS testing

Applying the reported boundaries to the CSS sliding distances gave that lubricant depletion and disk burnishing occurred for the initial 2 hours of a test. Chun et al [106] stated that sliding contact was the active element in lubricant depletion.

The effect of disk lubricant depletion was studied in Section 3.1.6.1. Friction was much higher for the disk without lubricant, especially in early cycles of the test. Take-off and landing seemed erratic and very sudden events. Flying friction in early cycles was also higher for the unlubricated disk, Figure 3.39. After around 4 hours however, flying friction was similar to that of a lubricated disk. This implied that some protective layers might have been formed at the interface. Or perhaps that some lubricant held in disk porosity had migrated back to the surface.

The slight scoring observed on disks following CSS testing by AFM suggested that alumina particles may have been responsible, since the wear scans observed were similar to those presented by Altshuler [143]. This could be validated by the loss of material from slider trailing edge observed and measured by SEM and AFM respectively. Scoring in general was commonly thought to be an indication that abrasive wear had occurred [105]. Scores on slider trailing rather than leading edge were more probable due to slider flying pitch.

The CSS testing track was found to be worn unevenly around the disk circumference, this led to different areas of contact at different disk locations. This accounted for the larger variation in friction readings with disk position observed with worn disks.

Disk wear tracks proved problematic during surface analysis, Talysurf profiling across the wear track was attempted but the technique was found to be insensitive to the shallow depth of tracks. Neither was AFM ideal, since the disk area was relatively large and locating the tracks exactly with the small scanning tip was difficult. SEM proved fairly useful in examining tracks, but unfortunately this technique only allowed imaging and no quantification of wear depth.

In the event of abrasive wear occurring, usually presented as light scores on disk, lateral force mode AFM proved useful for identification. Figure 3.76 and Figure 3.83 show examples of disk scoring which was either not visible or only barely visible by topographic mode AFM imaging. The corresponding lateral force scans can be seen to highlight the scores fairly clearly. In general, this mode of AFM was useful in identifying features of very small scale height/depth or where height was equal but material properties changed. It was reported that exact correlation between topographic and lateral force scans was rarely given with some shift or misalignment common [40]. This was due to an atomic scale stick-slip processes between scanning tip and sample.

Contact analysis techniques revealed that contacts were limited to the pole/shield regions of slider trailing edge during flying. This could account for pole tip recession (PTR) of these regions observed by AFM line analysis, Figure 3.72. Wear of tri-pad inductive elements was by far the most severe, in fact great difficulty was experienced in trying to locate and AFM scan elements following 7K CSS. XPS detected aluminium on a crosshatched disk CSS tested with a tri-pad slider, since no disk magnetic materials were found (hence carbon

overcoat was assumed to be intact) it was deduced that the source of this was slider pole material rather than disk substrate. Patton and Bhushan [79] also describe the preferential wear of the softer Ni-Fe poles over the surrounding alumina of an inductive head.

Where PTR had occurred, AFM file export allowed more reliable measurement of true wear depth than individual line scanning. Section 4.4.1.2 illustrates a technique that averaged material loss over the entire pole/shield region of interest. Environment influenced the amount of wear occurring, with hot/dry environments proving most severe recession at around 6-8 nm and humid environments resulting in negligible PTR in NPAB sliders. Since in this AFT apparatus read-write operation of heads was disabled it was unknown to what extent signal performance would be affected by the observed PTR. However, using the Wallace relationship , Equation 1.23, and assuming constant signal wavelength this would translate to a 5% increase in signal loss per 1 nm of PTR.

Particle transfer to slider indicated that adhesive wear had occurred, with the leading edge being the most likely site for deposition. It was shown by XPS that particles were composed of disk material, lubricant and/or carbon overcoat during a normal test. If the test had failed, disk magnetic layer materials could also be detected. The amount of material transferred was dependent on parking time length and humidity, with long duration parking in high humidity being responsible for transferring most material. Customised AFM scan processing again allowed accurate quantification of debris on surfaces.

Flying particles were also found on disk by AFM following testing, Figure 3.75b), usually spherical and sub-micron in area these particles were again more abundant to the outside diameter side of disk testing track. This would again suggest that centrifugal force dictated the landing positions of these particles.

Particle removal would occur as a result of fatigue wear, continuous stressing at the interface initiates the formation of cracks which can lead to delamination at the surface. The reported fatigue wear of a recording head by Xu and Bhushan [53] was illustrated in Figure 1.24. The SEM image shown of cracked poles of an Al_2O_3-TiC slider - indicating fatigue wear had occurred - was similar to the AFM scan of slider poles following a CSS test in this work, Figure 3.98a).

5.2 Drag Testing

5.2.1 Friction during Drag Tests

The low velocity nature of drag tests meant that air bearing force was below that required for normal slider flying (i.e. 0.5 m/s < critical velocity for flying established to be around 1 m/s). Thus, the slider was actually dragging on the disk surface which meant the test was very aggressive to the interface. Additionally, 0.5 m/s was high enough to allow tribochemical reactions to occur. Yang et al [86] stated these occurs above 0.4 m/s due to temperature increases at the interface. The critical speed of 0.5 m/s also gave maximum slider-disk contact in the fly height-contact analysis shown in Figure 4.85 a) and b).

5.2.1.1 Environmental Effect on Drag Test Friction

High humidity decreased friction during drag testing, since increased humidity decreased the amount of solid-solid contact at asperity junctions - this in turn decreased friction. In addition, water molecules filled the gaps between long chain lubricant molecules for better surface coverage.

However, where humidity became very high friction was observed to increase, this could be due to surface tension of the water/lubricant which may increase and thus increase friction. Additionally, when air temperature suddenly dropped below dew point temperature and formation of condensation occurred friction was observed to rise and generally behave erratically, Figure 4.25 and Figure 4.26 illustrate this.

As for CSS testing relative humidity was shown to be an inadequate measurement for modelling drag test friction. When measuring in-situ changes in humidity against water vapour pressure, VP, an inverse relationship could be formed with drag test friction, Figure 4.22 and Figure 4.23 show examples. Friction during drag tests was clearly related to $\varsigma/_{VP}$, where ς is a scaling factor, Figure 4.24. Drag tests conducted in low vapour pressure always showed highest friction. A critical value of VP=2 was established below which friction grew dramatically with time, Figure 4.21.

Drag test failure was inevitable under hot/dry conditions, it appeared that high temperature rendered lubricant unable to protect the disk. Figure 4.21 shows that tests performed above

70°C quickly exhibited high friction. Lubricant was observed by AFM to have reformed into discrete spherical shapes on disk/slider surface following high temperature drag tests and thus disk lubricant coverage became discontinuous. Temperature rise was also reported by Sharma et al [112] to cause a reformation of lubricant molecules, with 60°C quoted as being sufficient, thus AFM images of disks with reformed lubricant at 70°C and 77°C were as expected, Figure 3.115 and Figure 3.116. Chao and Russak [52] also found hot dry conditions to be very aggressive to the interface during close proximity sliding.

5.2.2 Wear during Drag Tests

Using bearing curve analysis on drag test disk slider AFM scans, it was found that once more the slider had been burnished during operation with lower heights present in the scan. Analysis of the disk scan however showed a higher range of heights were present, this was probably not entirely due to debris deposition, but more likely due to the irregular depths of the wear track that had been produced by harsh continuous sliding.

Wear tracks observed following drag testing were likely to be more severe than those observed in a real drive. Since, in this work testing radius was held constant, the slider was wearing the same track repeatedly. Coupled with low sliding velocity, it was not surprising that so many of these tests were deemed failures.

Using the distance boundaries for wear progression given by Bhushan and Forehand [21], it was established that during drag testing wear could progress to it's most severe form - total overcoat penetration - in under 3 hours. Figure 5.2 shows the wear boundaries mapped to drag test sliding distance using AFT apparatus at 0.5 m/s.

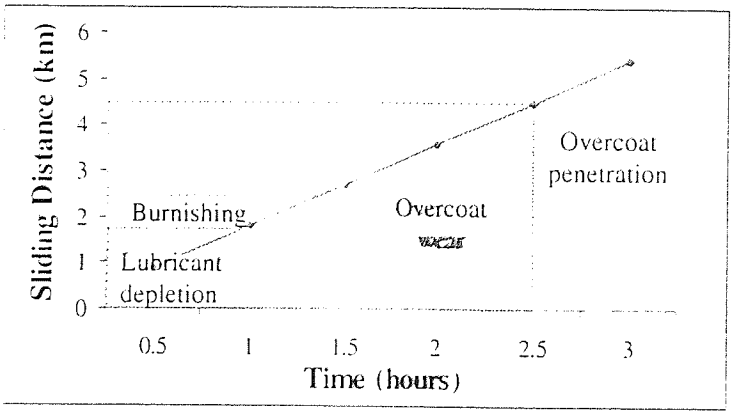

Figure 5.2 Wear progression during drag testing

This explained the frequent failure observed during drag testing. Severe abrasive and erosive wear was frequently evident following drag testing, with hard particles of alumina chipped from slider thought to be responsible. Note, in drag tests lubricant would be degraded via shear thinning rather than thermal, due to the low velocity nature of tests [107].

Where slider pole/shield cracking had occurred, it could be said that extreme temperature rise due to slider-disk contacts were responsible. Unlike the work by Chung et al [105] large thermal expansion of thin film coils due to read-write process would not occur, since the sliders used in this work were not signal enabled, thus this would not be the responsible mechanism. The associated disk SEM scan, Figure 3.114a), would indicate that fatigue wear had occurred. Thin flakes or laminae of carbon overcoat or magnetic layer were removed from the disk surface leading to erratic friction behaviour and sudden failure, this was also observed in work by Kaneko and Koshimoto [41].

5.3 Applications of NNT's in Slider-Disk Tribology

Neural network tools (NNT's) proved useful in this work since large volumes of data were under study and values did contain some spread.

5.3.1 NNT Modelling of a CSS Friction Trace

In Section 4.5.2 the friction trace over a standard CSS cycle was used as the desired output to a NNT with slider fly height, disk velocity, disk circumfrential position cumulative distance travelled and time tagged as NNT inputs. The NNT trained quickly and could easy replicate the original friction trace from the given inputs. Sensitivity analysis clearly identified slider fly height and disk velocity as the most important parameters on recorded friction, Figure 4.114.

5.3.2 Classification of CSS Friction Traces

Since of the most common uses of NNT's is classification, it was decided to train a network using friction traces from the start, middle and end of a 7K CSS test as inputs. The desired

output was '1', '2' or '3' depending on from which cycle the trace came. When the trained network was fed with friction values from different CSS tests it was able to classify to which cycle the majority of values came. Table 4.12 shows the truth table for these testing results, note >59 % of traces were correctly classified. The main confusion in results seemed to be between cycle 3500 and 7000: this was most likely due to the fact that most surface changes occurred during the early stages of the test.

The result meant that even between tests with different disk and slider, consistent changes in friction trace shape were taking place as CSS cycles progressed. These changes could be learnt numerically by the network. It is proposed that by training the network on a larger number of tests, even higher accuracy could be gained. One application of this feature would be the ability to feed the network with a friction trace from a drive of unknown age and judge how many cycles the interface had seen.

5.3.3 NNT Modelling of Contact Analysis Data

In order to decide what type of surfaces would display the least contact, and hence friction, stiction and wear, it was beneficial to study various designs and work out which topographical features were most significant. In Section 4.4.2.1 surfaces were generated using 3 methods.

Firstly, an equation based method was used, whereby a homogenous equation was formed using the Box optimisation technique to choose coefficients. The optimiser attempted to match surface roughness parameters of the simulated surface to that of a real surface by altering coefficients during each iteration. However, the process was expensive in terms of computer time and Box failed by choosing all but one coefficient value of 0, this resulted in a perfectly flat surface being generated, Figure 4.94.

Next it was attempted to match the known distribution of real surfaces by using a random number generator. Although the generated and real surfaces had very similar Gaussian shapes, Figure 4.98, the asperities on the simulated surface were too regular and this was reflected in the contact analysis results.

Finally, it was decided to manipulate real AFM scans to generate the required topographical characteristics. Real AFM scans were exported numerically to large matrices and then the Box optimiser was again used to alter matrix entries in order to match requirements. Various surfaces were simulated as described in Table 4.11. The advantages of this method was that surfaces were more akin to that of real disks and sliders.

Using the latter method, disk surfaces were generated having a wide range of characteristics, contact analysis was performed with each using real AFM slider scans. A neural network was built and trained using disk surface parameters as inputs and contact area as desired output Sensitivity analysis confirmed that disk height distribution was important, with negative skewness and high kurtosis necessary for low contact.

Poon and Bhushan [134] also reported that surfaces with less skewness will have less meniscus effect and therefore lower friction/stiction. However the results contradict work by Tian and Chao [22] who found that near symmetric asperity distribution (i.e. skew=0) gave best performance. It should be noted that in both mentioned work surfaces used were purely theoretical.

Although useful exporting AFM scans was computationally expensive, since each simulated surface consisted of a 400x400 matrix of values due to the high resolution of scans. Ironically, storage and processing of these files became costly in terms of hard drive memory.

6 Conclusions and Further Work

In this project modelling hard drive interface behaviour was attempted. Many possible parameters were investigated with respect to their tribological impact on the interface. The significance of parameters was highlighted both by in-situ friction and stiction results and post test surface analysis. The interaction of many parameters did lead to spread in results, however certain trends were repeatedly observed which can be used to explain drive behaviour.

6.1 Conclusions

Environmental conditions were the most significant factor on friction, stiction and wear. The effects of temperature and humidity were not independent. Relative humidity was shown to be an inadequate measure of air moisture content and should only be used when temperatures are around ambient or are constant over the set of tests being compared. For the purposes of modelling or calibration water vapour pressure or dew point temperature were found to give better correlation with experimental results.

With respect to stiction, high humidity was particularly detrimental if a long dwell or rest time was present before drive start up. Regarding friction and wear, combined hot and dry conditions were intolerable in both CSS and drag tests. In general, extreme environments should be avoided to prevent drive failure.

Generally, it was found that drive vapour pressure should be maintained in the range >2 KPa and <4 KPa to avoid excessive friction/wear and high stiction respectively. Additionally, drive temperature should be preserved below 35°C.

Surface topography and texture also affected friction, stiction and wear. Contact analysis of AFM scans gave insight into the nature of slider–disk interactions, both during flying and parking phases. Information on the number, size and shape of contacts was given along with the expected location of these. Simulation techniques coupled with contact analysis gave information on the optimum topography of surfaces for minimum contact. This theoretical

approach enabled many different textural designs to be investigated cheaply and relatively quickly. It was found that rather than generating surfaces completely from formulae, real AFM scan data could be manipulated to simulate surfaces with required characteristics but which kept some true properties, such as anisotropy, waviness.

Disk texture was found to be more critical than slider texture on the contacts occurring at the interface and hence friction/stiction. This was as expected since the scale of disk texture was larger for samples studied. For very modern, ultra-smooth disks it is expected that the ratio of responsibility of disk/slider topography on contacts would be more even.

During slider flying, contact analysis pin-pointed the raised poles/shields as the locations where collisions would occur. PTR of these regions, measured by AFM, was therefore not surprising since high speed contacts would readily wear these Ni-Fe relative to the harder surrounding material (alumina). An improved measurement technique for slider PTR was found.

During CSS and drag testing, material transfer between disk and slider was proven to be unavoidable. However, as long as this was limited to disk lubricant and some overcoat little loss of performance was noted. But in the case of disk magnetic materials being detected on slider, this would most likely lead to recorded signal dropouts.

Modern optimisation techniques such as Neural Network Tools allow investigation into non-linear systems with large number of parameters. As well as being used to model the AFT system, these techniques can be used to predict and classify behaviour with very little training. The network also allowed parameter weightings to be deduced, this would save investigating parameters that had little or no impact on behaviour. Unfortunately, the use of such techniques was only investigated in the latter stages of the project, meaning their full potential could not be explored due to time limitation.

Overall, the models developed during the project go some way towards predicting drive behaviour. However parameter interaction for example that observed humidity and inter cycle pause length, did cause divergence from expected behaviour.

6.2 Further Work

Experiments using current AFT apparatus were limited due to velocity induced vibration. Improved damping of the system would allow experiments to be conducted at velocities which match current drive specifications.

AFT apparatus could be further improved by the addition of an AE sensor to the cantilever arm, this would provide additional information on slider-disk contact. The AE signal measurements could then be incorporated into the Neural Network model to deduce whether this technique is more significant than friction reading to the interface. If so, completely new models could be built using AE values instead of friction. If not, it may be established that adding AE as an additional parameter to existing models would have some benefit.

Understanding of slider-disk contact is of vital importance if further improvements in areal density are to be made. New types of disk and slider textures could be investigated to determine their effect on friction, stiction and wear. Computer simulation and contact analysis makes this task less costly and would allow unsuitable designs to be ruled out prior to their fabrication. More efficient techniques of contact analysis could be investigated with respect to computation time, since this could be lengthy due to the high resolution nature of AFM scans resulting in large file sizes.

Neural Network Tools are ideal for modelling large non-linear systems such as head disk contact problems. The classification operation in particular is extremely useful, it is thought that a network could be trained on successful CSS friction results and also the friction traces leading up to and including drive failure. Thus, subtle changes in behaviour could be learnt by the network. By then feeding sampled traces to the network, whilst simultaneously running a CSS or drag test, a flag or warning of drive failure could be raised preceding the actual event. This would allow investigation into the fault via surface analysis, before slider and disk became too severely damaged to evaluate the cause.

CSS and drag testing of a wider range of disks and sliders, including more modern designs would prove useful. Differences in their friction, stiction and wear behaviour could be

highlighted by comparison to the established database of results. This would probably require further project sponsorship by a commercial drive company for supply of materials.

Improved surface topographical analysis could be performed using a more advanced AFM instrument, such as the *Thermomicroscopes model M5*. This would have particular benefits when analysing disks, since the large sample stage would allow an entire disk to be mounted. This would save cutting disks up for analysis and would mean the same disk could be scanned at various times during a CSS/drag test. The precise tip positioning feature of this instrument would also allow better scan positioning, in fact the track of interest could be followed accurately around the complete circumference of the disk if required.

The use of an off-the-shelf environmental generator would allow for better control over conditions. Additionally, the fitting of a refrigeration device would allow below ambient temperature studies to be performed. Ideally, the entire AFT apparatus could be placed in an environmental chamber - such as those made by Votsch - for best control in reaching and maintaining required conditions. However, this would entail separation of the AFT apparatus from the large granite block required for vibration reduction. Once in place, the improved AFT/environmental generator system could be used to perform a new set of results under a wider variety of conditions. Improvement in humidity stability alone should definitely improve the models.

It was also thought that fitting electronics to the apparatus - which would actually allow signals to be written to the disk by the heads - would supplement results. This would provide an additional measure of failure/success of tests by means of signal dropout calculation. For example, correlation of dropouts to slider PTR would indicate at which point wear becomes an issue. Again an more advanced AFM instrument would prove useful here by allowing Magnetic Force Microscopy images of surfaces to be taken.

Bibliography

[1] Grochowski, E., "The era of magnetoresistive heads.", Conference Proceedings, 1995, All.

[2] Grochowski, E. and Thompson, D.A., "Areal density growth in magnetic recording.", Access (IBM San Jose), Volume IX, Number 3, Third Quarter, 1995, pp 1-3.

[3] Menon, A.K. "Critical requirements for 100 Gb/in2 head/media interface.", Read-Rite Internal Document, 1999, pp 1-9.

[4] Grundy, P.J. , "Thin film magnetic recording media", Journal of Applied Physics (D), Volume 31, 1998, pp 2975–2990.

[5] White, R.L. , " The physical boundaries to high-density magnetic recording.", Journal of Magnetism and Magnetic Materials, Volume 209, 2000, pp 1-5.

[6] Bertram, H.N., "Fundamentals of the magnetic recording process.", Proceedings of the IEEE, Volume 74, Number 11, November, 1986, pp 1494-1512.

[7] Begun, J., "Magnetic recording.", Murray Hill Books Inc. (England), 1949, pp 226-232.

[8] Mee, C.D. and Daniel, E.D., "Magnetic recording handbook, technology and applications.", McGraw-Hill Publishing Company, 1989, pp 24-38.

[9] Mallinson, J.C., "The foundations of magnetic recording.", Academic Press, Inc. (London), 1987, pp 1-30.

[10] Hoagland, A.S., "Digital magnetic recording.", John Wiley & Sons, Inc.(New York), 1963.

[11] Cox, Gary W., "All about hard drives.", Internet Report, 1996, All.

[12] Jiang, L. and Miles, R.N., "A passive damper for the vibration modes of the head actuator in hard disk drives", Journal of Sound and Vibration, Volume 220, Number 4, 1999, pp 683-694.

[13] Elford, C.L. and Reed, D.A., "Technology Trends and Disk Array Performance", Journal of Parallel and Distributed Computing , Volume 46, 1997, pp 136–147.

[14] Jorgensen, Finn, "The complete handbook of magnetic recording.", Tab Books Inc., 1980.

[15] Anon, "The Gensys guide to networks and storage.", Internet Report (GenSys Web site), 1996, All.

[16] Tian, H. and Lee, J.J.K., "Effect of disk surface contours on head flyability.", Journal of Magnetism and Magnetic Materials, Volume 155, 1996, pp 329-331.

[17] Tan B. et al, "A new servo method using servo layer and transverse MR head for submicron track servo on hard computer disks.", Journal of Magnetism and Magnetic Materials, Volume 155, 1996, pp 345-347.

[18] Komvopoulos, K., "Head-disk interface contact mechanics for ultrahigh density magnetic recording.", Wear, Volume 238, 2000, pp 1-11.

[19] Renshaw, A.A., "Increasing the maximum stable rotation speed of a circular disk using speed dependent clamping.", Journal of Sound and Vibration. Volume 210, Number 4, 1988, pp 431-439.

[20] Ishimaru, N., "Experimental studies of a head/disk interface subjected to impulsive excitation during nonoperation.", Journal of Tribology, October , Volume 118, 1996, pp 807-812.

[21] Bhushan, B. and Forehand, S.M., "In situ instrumentation for localized wear studies of magnetic thin-film disks.", Proceedings of Institute of Mechanical Engineers, Volume 211, Part J, 1997, pp 249-262.

[22] Tian, H and Chao, A.M., "Optimisation of disk surface texturing and lubrication on CSS performance.", IEEE Transactions on Magnetics, Volume 32, Number 5, September, 1996, pp 3666-3668.

[23] Mirzamaani, M. and Doerner, M.F., "Magnetic performance and tribology of sputter-textured thin film disks (Invited).", IEEE Transactions on Magnetics, Volume 32, Number 5, September, 1996, pp 3638-3641.

[24] Hu, Y. and Bogy, D.B., "Effects of laser textured disk surfaces on a slider's flying characteristics.", Transactions of the ASME, Volume 120, April, 1998, pp 266-271.

[25] Yao, W.H., et al., "Head-disk dynamics of low resonance laser textures - A spectrogram analysis .", Transactions of Magnetics, Volume 34, Number 4, July, 1998, pp 1699-1701.

[26] Ranjan, R., Lambeth, D.N., Tromel, M., Goglia, P. and Li, Y., "Laser texturing for low-flying-height media.", Journal of Applied Physics, Volume 69 Number 8, 15 April, 1991, pp 5745-5747.

[27] Zhao, Q. and Talke, F.E., "Effect of environmental conditions on the stiction behaviour of laser textured hard disk media.", Tribology International, Volume 33, 2000, pp 281-287.

[28] Kitamoto, Y., Abe, M., and Naoe, M., "Deposition of Co-Cr films with excellent c-axis orientation and uniform thickness for rigid disks using compact sputtering apparatus.", IEEE Transactions on Magnetics, Volume 32, Number 5, September, 1996, pp 4547-4549.

[29] Sui,X and Scherge, M and Kryder, M.H. and Snyder, J.E. and Harris, V.G. and Koon, N.C., "Barium ferrite thin-film recording media.", Journal of Magnetism and Magnetic Materials, V155, 1996, pp 132-139.

[30] Anoikin, E.V. et al, "Ultrathin protective overcoats on magnetic hard disks.", IEEE Transactions on Magnetics, Volume 34, Number 4, July, 1998, pp 1717-1719.

[31] Huu, T.L., Zaidi, D. and Paulmier, D., "Friction and wear properties of hard carbon coatings at high sliding speed.", Wear 203-204, 1997, pp 442-446.

[32] Cutiongco, E.C., Li, D., Chung Y. W. and Bhatia, C.S., "Tribological behavior of amorphous carbon nitride overcoats for magnetic thin-film rigid disks.", Journal of Tribology, Volume 118 July, 1996, pp 543-548.

[33] Koinkar, V.N. and Bhushan, B., "Microtribological properties of hard amorphous carbon protective coatings for thin-film magnetic disks and heads.", Proceedings of Institution of Mechanical Engineers, Volume 211, Part J, 1997, pp 365-372.

[34] Suganuma, Y., Tanaka, H., Yanagisawa, M., Goto, F. and Hatano S., "Production process and high density recording characteristics of plated disks (Invited).", IEEE Transactions on Magnetics, Volume Mag-18, No 6, November, 1982, pp 1215-1220.

[35] Gao, C. et al, "Tribological implications of solvents in dip-coating lubrication of thin film magnetic disks.", IEEE Transactions of Magnetics, Volume 32, Number 5, September 1996, pp 3699-3701.

[36] Wang, S. and Komvopoulos, K., "Static friction and initiation of slid at magnetic head-disk interfaces.", Transactions of the ASME, Volume 122, January 2000, pp 246-256.

[37] Gao, C. et al, "Dip-coating of ultra-thin liquid lubricant and its control for thin-film magnetic hard disks.", IEEE Transactions of Magnetics, Volume 31, Number 6, November 1995, pp 2982-2984.

[38] Zhao, Z. and Bhushan B., "Effect of environmental humidity on the friction/stiction and durability of lubricated magnetic thin-film disk.", Proceedings of Institution of Mechanical Engineers, Volume 211, Part J, 1997, pp 295-301.

[39] Zhao, Z. and Bhushan B., "Effect of bonded lubricant films on the tribological performance of magnetic thin-film rigid disks.", Wear Volume 202 , March, 1996, pp 50-59.

[40] Bhushan, B., "Macro and microtribology of magnetic rigid-disk storage devices.", Journal of Magnetism and Magnetic Materials, V155, 1996, pp 318-322.

[41] Kaneko, R. and Koshimoto, Y., "Technology in compact and high recording density disk storage.", IEEE Transactions on Magnetics, Volume Mag-18, Number 6, November, 1982, pp 1221-1226.

[42] Bhushan, B., "Tribology and mechanics of magnetic storage devices.", Springer-Verlag, 1990.

[43] Mate, C.M., Lorenz, M. R., and Novotny, V.J., "Determination of lubricant film thickness on a particulate disk surface by atomic force microscopy.", IEEE Transactions on Magnetics, Volume 26, Number 3, May, 1990, pp 1225-1228.

[44] Jakusch, H and Veitch, R. J., "Particles for magnetic recording.", Journal of Information Recording Materials, Volume 20, 1993, pp 325-344.

[45] Sato, H. et al, "Effects of grain size and intergranular coupling on recording characteristics in CoCrTa media.", IEEE Transactions on Magnetics, Volume 32, No 5. September, 1996, pp 3596-3598.

[46] Wu, T.H. et al., " Pinning magnetic domain via patterning artificial lattice under amorphous magnetic layer.", Journal of Magnetism and Magnetic Materials, Volume 193, 1999, pp 155-158.

[47] Talke, Prof. F., "A review of 'contact recording' technologies.", Wear, Volume 207, 1997, pp 118-121.

[48] Agarwal, S. et al, "Media requirements for proximity recording.", IEEE Transactions on Magnetics, Volume 33, Number 1, January , 1997, pp 908-913.

[49] Doan, T.Q., "Proximity recording design considerations.", IEEE Transactions on Magnetics, Volume 33, Number 1, January, 1997, pp 903-907.

[50] Meyer, D., Boutaghou, Z.E. and Wei, B., "Proximity recording - the concept of self-adjusting fly heights.", IEEE Transactions on Magnetics, Volume 33, Number 1, January , 1997, pp 912-919.

[51] Hsiao H.S., Bhushan, B. and Hamrock, B.J., "Ultrathin liquid lubrication of magnetic head-rigid disk interface for near-contact recording : Part I - A closed form solution to the Reynolds equation.", Transactions of the ASME, Volume 118, April, 1996, pp 388-395.

[52] Chao, J.L. and Russak, M.A., "Media tribology optimization for proximity recording.", IEEE Transactions on Magnetics, Volume 33, Number 1, January, 1997, pp 897-901.

[53] Xu, J. and Bhushan, B., "Friction and durability of ceramic slider materials in contact with lubricated thin-film rigid disks.", Proceedings of Institution of Mechanical Engineers, Volume 211, Part J, 1997, pp 303-316.

[54] Gatzen, H.H., "Observations regarding the tribological properties of SiC and Al-TiC sliders.", IEEE Transactions on Magnetics, Volume 32, No 5, September 1996, pp3783-3785.

[55] Peng, Jih-Ping and Hardie, C.E., "Characteristics of air bearing suction force in magnetic recording disks.", Journal of Tribology Volume 118 July, 1996, pp 549-554.

[56] O'Hara, M. and Bogy, D.B., "Robust design optimization techniques for ultra-low flying sliders .", IEEE Transactions on Magnetics, Volume 31, No 6, November, 1995, pp 2955-2957.

[57] Kaneko, R. et al, "Recent progress in microtribology.", Wear, Volume 200, 1996, pp 296-304.

[58] Sharma, V. and Talke, F.E., "Silicon carbide - a potential material for magnetic recording sliders.", Proceedings of Institution of Mechanical Engineers, Volume 211, Part J, 1997, pp 317-326.

[59] Pan, X. and Novotny, V.J., "Head material effects on interface tribochemistry.", IBM internal report (San Hose, California).

[60] Bhushan, Bharat, "Tribology and Mechanics of Magnetic Storage Devices.", Springer - Verlag, 1990.

[61] Li, Y., Menon, A. and Goglia, P., "Evaluations of diamond-like-carbon film optical constants and their effects on flying height determination.", Journal of Tribology, Volume 118, October, 1996, pp 767-773.

[62] Zhou, L. et al, " Friction and wear properties of hard coating materials on textured hard disk sliders", Wear, Volume 243, 2000, pp 133–139.

[63] Uy, James C., "Head/disk interface failure mechanism.", IEEE Transactions on Magnetics, Volume 26, Number 5, September, 1990, pp 2697-2699.

[64] Li, Y. and Bhushan, B., "Wear and friction studies of contact recording interface with microfabricated heads.", Wear Volume 202, 1996, pp 60-67.

[65] Suk, M., "The effect of disk roughness on the wear of contact recording heads.", Transactions of the ASME, Volume 118, October, 1996, pp 794-799.

[66] Cha, E. and Bogy, D.B., "Numerical simulation and animation of head-disk assembly dynamics.", IEEE Transactions on Magnetics, Volume 27, Number 6, November, 1991, pp 5136-5138.

[67] Fung, M. K. et al, " Mechanical properties and corrosion studies of amorphous carbon on magnetic disks prepared by ECR plasma technique", Thin Solid Films, Volume 368, 2000, pp 198-202.

[68] Donovan, M.J. and Bogy, D.B., "Experimentally observed roughness effects on the air bearing in the pseudo-contact spacing regime.", IEEE Transactions on Magnetics, Volume 31, Number 6, November, 1995, pp 2994-2996.

[69] Schardt, B.C. et al., "Flying height measurement while seeking in hard disk drives.", IEEE Transactions on Magnetics, Volume 34, No 4, July, 1998, pp 1765-1767.

[70] Bailey, D.A., "Limits of the Reynolds equation for negative pressure sliders.", IEEE Transactions on Magnetics, Volume 31, Number 6, November, 1995, pp 2979-2981.

[71] Han, S.H., Han, S.M., Kim, H.J. and Kang, I.K., "Soft magnetic properties of Fe-(Si3N4, Al2O3) thin films.", IEEE Transactions on Magnetics, Volume 32, Number 5, September, 1996, pp 4499-4501.

[72] Yuan, Z. and Liu, B., " Anti-thermal asperity head: design and performance analysis.", Journal of Magnetism and Magnetic Materials, Volume 209, 2000, pp 166-168.

[73] Tian, H. and Lee, J.J.K., "Electrostatic discharge damage of MR heads.", IEEE Transactions on Magnetics, Volume 31, Number 6, November, 1995, pp 2624-2626.

[74] Lambeth, D.N., "Hard disk media: future problems and possible solutions.", Vacuum Volume 59, 2000, pp 522-530.

[75] Ishiwata, N., Ishi, T., Matsutera, H. and Yamada, K. "Narrow track MR head technology.", IEEE Transactions on Magnetics, Volume 32, Number 1, January, 1996, pp 38-42.

[76] Suzuki, T., Motomura, Y. and Tagami, K., "Offtrack characteristics of shielded magnetoresistive head.", IEEE Transactions on Magnetics, Volume 27, Number 6, November, 1991, pp 4690-4692.

[77] Obernosterer, F. and Oehme, W.F., "Pulse noise in thin film disk recording systems.", Journal of Magnetism and Magnetic Materials, Volume 155, 1996, pp 338-340.

[78] Sullivan, John L., "The tribology of flexible magnetic recording media.", Journal of Magnetism and Magnetic Materials, V155, 1996, pp 312-317.

[79] Patton, S.T and Bhushan, B., "Micromechanical and tribological characterization of alternate pole tip materials for magnetic recording heads.", Wear, Volume 202, 1996, pp 99-109.

[80] Yang, M. M. et al. "Improved recording performance and optimized durability of thin film disks with zone carbon overcoats.", IEEE Transactions on Magnetics, Volume 32, Number 5, September, 1996, pp 3672-3674.

[81] Sullivan, M. and Chao, J., "Inertia effects on static friction measurements of laser textured media.", IEEE Transactions on Magnetics, Volume 34, No 4, July, 1998, pp 1801-1803.

[82] Roizard, X. et al., "Influence of sliding direction and sliding speed on the micro-hydrodynamic lubrication component of aluminium mill-finish sheets.", Tribology International, Volume 32, 1999, pp739-747.

[83] Linda Reeves, "Floppy Disk Thesis, Stribeck Curve.", Aston University PhD Thesis, pp 60-130.

[84] Jiang, Z., Lu, C.J., Bogy, D.B., Bhatia, C.S. and Miyamoto, T., "Nanotribological evaluations of hydrogenated carbon films as thin as 5 nm on magnetic rigid disks.", IEEE Transactions on Magnetics, Volume 31, Number 5, November, 1995, pp 3015-3017.

[85] Yoon, E.S., Kong, H., Kwon, O.K. and Oh, J. E., "Evaluation of frictional characteristics for a pin-on-disk apparatus with different dynamic parameters.", Wear Volume 203, 1997, pp 341-349.

[86] Yang, M. et al, "The frictional behavior of thin film magnetic disks.", IEEE Transactions on Magnetics, Volume 27, Number 6, November, 1991, pp 5157-5159.

[87] Mate, C.M. and Homola, "Tribology of disk drives", Proceedings of NATO., June 1996, pp 647-710.

[88] Li, Y. and Menon, A.K., "A theoretical analysis of breakaway friction measurement.", Transactions of the ASME, Volume 116, April, 1994, pp 280-286.

[89] Wang, R.H et al, "The effect of hydrogen in carbon overcoats on the tribology of the head-disk interface.", IEEE Transactions on Magnetics, Volume 31, No 6, November, 1995, pp 2919-2921.

[90] Milby, R., Schreck, E. and Sonnenfeld, R., "Measurement of the head-to-disk stiction force in an unmodified hard drive using external Hall sensors.", IEEE Transactions on Magnetics, Volume 34, No 4, July, 1998, pp 1780-1782.

[91] Bhushan, B.,Kotwal, C.A. and Chilamakuri, S.K., "Kinetic meniscus model for prediction of rest stiction.", Transactions of the ASME, Volume 120, January, 1998, pp 42-53.

[92] Koka, R., "Studies of effects of some organics on head/disk tribology.", IBM Confidential Report, Materials and Process Engineering, ADSTAR, 1994, pp 39-41.

[93] Morehouse, Dr. James, "Dynamic head loading.", Internet Report (Integral Peripherals Incorporated.), 1994, pp All.

[94] Fu, T.C. and Bogy, D.B., "Analysis of stresses induced by dynamic load head-disk contacts", Journal of Tribology, Volume 122, January 2000, pp 233-236.

[95] Suk, M. and Jen, D., "Potential data loss due to head/disk contacts during dynamic load/unload.", IEEE Transactions on Magnetics, Volume 34, Number 4, July 1998, pp 1711-1713.

[96] Peng, J.P., "Theoretical prediction of ramp loading/unloading process in hard disk drives.", Transactions of the ASME, Volume 121, July 1999, pp 568-574.

[97] Best, G.L., "Precise stiction mapping.", IEEE Transactions on Magnetics, Volume 27, Number 6, November, 1991, pp 5169-5171.

[98] Kasamatsu, Y., Yamamoto, T., Yokohata, S. and Mizoshita, Y., "Stiction free slider for smooth surface disk.", IEEE Transactions on Magnetics, Volume 31, Number 6, November, 1995, pp 2961-2963.

[99] Harris, D., Venkatesan, S. and O'Brien, K., "Take-off measurement of Pico sliders on laser zone textured media.", IEEE Transactions on Magnetics, Volume 34, Number 4, July, 1998, pp 1693-1695.

[100] Gui, J. and Marchon, B., "Fly/Stiction : Mechanical instability of a head-disc interface.", IEEE Transactions on Magnetics, Volume 34, Number 4, July, 1998, pp 1804-1806.

[101] Knigge, B., Zhao, Q. and Talke, F.E., "Tribological properties and environmental effects of nano and Pico sliders on laser textured media.", IEEE Transactions on Magnetics, Volume 34, Number 4, July, 1998, pp 1732-1734.

[102] Meyer, D., Goglia, P., Menon, A.K. and Li, Y., "A statistical model for interpreting hard disk drive stiction measurements.", Journal of Tribology, 1997, pp 43-48.

[103] Marchon, B., Heiman, N. and Khan, M.R., "Evidence for tribochemical wear on amorphous carbon thin films.", IEEE Transactions on Magnetics, Volume 26, Number 1, January, 1990, pp 168-170.

[104] Pugh, B., "Friction and wear - A tribology text for students.", Newnes-Butterworth, London, 1973, pp All.

[105] Chung, K.H., Lee, S.C. and Kim, D.E., "Assessment of surface damage mechanisms of head/disk interface using CSS and drag tests.", IEEE Transactions on Magnetics, Volume 34, Number 4, July, 1998, pp 1714-1716.

[106] Chun,K., Gudeman, C.S., Schouterden, K. and Lairson, B.M., "Friction and head and disk interface durability in contact recording.", Wear, Volume 216 , 1998, pp 70-76.

[107] Hsiao H.S., Bhushan, B. and Hamrock, B.J., "Ultrathin liquid lubrication of magnetic head-rigid disk interface for near-contact recording : Part II - Shear thinning and thermal thinning.", Transactions of the ASME, Volume 118, April, 1996, pp 396-401.

[108] Halling, J., "Principles of tribology.", McMillan Press Ltd, 1983, pp 22-35.

[109] O'Brien, K. and Harris, D., "Head/disk interface contact detection using a refined Acoustic Emission technique.", Journal of Tribology, Volume 118, July 1996, pp 539-542.

[110] Khurshudov, A.G. and Talke, F.E., "A study of subambient pressure tri-pad sliders using acoustic emission.", Transactions of the ASME, Volume 120, January 1998, pp 54-59.

[111] Cha, K.H. et al, " Experimental investigation of AE and friction signals related to the durability of head/disk interface." Tribology International, Volume 32, 1999, pp 399–405.

[112] Sharma, V., Yang, M. and Talke, F.E., "Environmental effects on the tribology of the head/disk interface.", SPIE, Volume 2604, 1998, pp 228-235.

[113] Jiang, J., Stott, F.H. and Stack, M.M., "A mathematical model for sliding wear of metals at elevated temperatures.", Wear 181-183, 1995, pp 20-31.

[114] Xie, Y. and Bhushan, B., "Effects of particle size, polishing pad and contact pressure in free abrasive polishing.", Wear, Volume 200, 1996, pp 281-295.

[115] Sullivan, J.L., "Boundary lubrication and oxidational wear.", Journal of Applied Physics D, Volume 19, 1986, pp 1999-2011.

[116] Karis, T.E., Tyndall, G.W. and Crowder, M.S., "Tribology of a solid fluorocarbon film on magnetic recording media.", IEEE Transactions on Magnetics, Volume 34, Number 4, July, 1998, pp 1747-1749.

[117] Bhushan, B. and Zhao, Z., "Friction/stiction and wear studies of magnetic thin-film disk with two polar perfluropolyether lubricants.", IEEE Transactions on Magnetics, Volume 33, No1, January, 1997, pp 918-925.

[118] Moulder, J.F., Hammond, J.S. and Smith, K.L., "Using angle resolved ESCA to characterize Winchester disks.", Applied Surface Science, Volume 25, 1986, pp 446-454.

[119] Linder, R.E. and Mee, P.B., "ESCA determination of fluorocarbon lubricant film thickness on magnetic disk media.", IEEE Transactions on Magnetics, Volume Mag-18, Number 6, November, 1982, pp 1073-1076.

[120] Yokozawa, H., Nanba, M. and Tagami, M., "Analysis of Perfluoropolyether lubricant using static - SIMS.", Second Ion Mass Spectrometry, Proceedings International Conference, 9th (Published)., 1994, pp 804-807.

[121] Li, Y. and Menon, A., "A model of slider/disk interface wear for proximity recording.", Journal of Tribology, Volume 118, October, 1996, pp 813-818.

[122][122] Hu, Y., Jones, P.M., Chang, P.T. and Bogy, D.B., "Partial contact air bearing characteristics for tripad sliders for proximity recording.", Transactions of the ASME, Volume 120, April, 1998, pp 272-279.

[123] McMillan, T.C., Talke, F.E. and Harrison, J.C., "Identification of slider/disk contacts using the energy of the acoustic emission signal.", IEEE Transactions on Magnetics, Volume 34, No 4, July, 1998, pp 1819-1821.

[124] Suzuki, S. and Nishihira, H., "Study of slider dynamics over very smooth magnetic disks.", Transactions of the ASME, Volume 118, April 1996, pp 382-387.

[125] Bhushan, B. and Blackman, G.S., "Atomic force microscopy of magnetic rigid disks and sliders and it's applications to tribology.", Transactions of the ASME, Volume 113, July, 1991, pp 452-457.

[126] Archard, J.F., ".", Proceedings of the Royal Society, Part A, Volume 243, 1957, pp190

[127] Greenwood, J.A. and Williamson, J.B.P., "Contact of nominally flat surfaces.", Burndy Corporation Research Division, Volume 295 A. April, 1966, pp 300-319.

[128] Onions, R.A. and Archard, J.F., "The contact of surfaces having a random structure.", Journal of Physics D., Volume 6, 1973, pp 289-304.

[129] Polycarpou, A.A. and Etsion, I, "Analytical approximations in modelling rough surfaces.", Transactions of the ASME, Volume 121, April, 1999, pp 234-239.

[130] Poon, C.Y. and Bhushan, B., "Nano-asperity contact analysis and surface optimization for magnetic head slider/disk contact.", Wear Volume 202 , 1996, pp 83-98.

[131] Majumdar, A. and Bhushan, B., "Role of fractal Geometry in roughness characterization and contact mechanics of surfaces", Journal of Tribology, Volume 112, April 1990, pp 205-216.

[132] Chilamakuri, S.K. and Bhushan, B., "Contact analysis of non-Gaussian random surfaces", Proceedings of Industrial Mechanical Engineers, Volume 212 Part J, 1988, pp 19-32.

[133] Chilamakuri, S.K. and Bhushan, B., "Effect of peak radius on design of W-type donut shaped laser textured surfaces.", Wear, Volume 230, 1999, pp 118–123.

[134] Poon, C.Y. and Bhushan, B., "Numerical contact and stiction analyses of Gaussian isotropic surfaces for magnetic head slider/disk contact.", Wear Volume 202 , March, 1996, pp 68-82.

[135] Bhusan, B., "Micro/nanotribology using atomic force microscopy/friction force microscopy: state of the art.", Proceedings of Institution of Mechanical Engineers, Volume 212, Part J, 1998, pp 1-18.

[136] Menon, A.K., Internal Read-rite Report, 1998.

[146] Liu, B. et al. "Particle build-up on flying sliders and mechanism study of disk wear and head-disk interface failure in magnetic disk drives.", IEEE Transactions on Magnetics, Volume 32, Number 5 , September, 1996, pp 3687-3689.

[147] Goodwin, Mark D and Dennis Mark, "Power of Qbasic.", New York, MIS Press, 1991, pp All.

[148] Kennedy, J. B. and Neveille, A. M., "Basic statistical methods for engineers and scientists.", Harper & Row, Publishers, 2nd edition, 1976, pp 255-270.

[149] Murdoch, J. and Barnes, J.A., "Statistical tables for science, engineering, management and business studies.", MacMillan Education Limited, 1986, pp 17.

[150] Chirlian, Paul M., "Programming in C++.", MacMillan Publishing Company, 1991, pp All.

[151] Anon, "Standard recommended practice for maintaining constant relative humidity by means of aqueous solutions.", American Society for Testing and Materials, E104-51 (Reapproved 1971), 1971, pp 572-575.

[152] Watts, John F., "An introduction to surface analysis by electron spectroscopy.", Oxford University Press, Royal Microscopical Society, 1990, pp All.

[153] Smith, G.C., "Quantitative surface analysis for materials science.", The Institute of Metals, 1991, pp All.

[154] Li, Y. and Wang, G., "In-situ alumina recession and protrusion measurement on a magnetic head.", IEEE Transactions on Magnetics, Volume 34, No 4, July 1998, pp 1771-1773.

[155] Talke, F., et al., Talke Laboratory Head/Disk Interface Research Web Site, 2000.

FRICTION, STICTION AND WEAR IN RIGID DISK DRIVES

J.Collins (*) and J.L. Sullivan, Aston University, Birmingham, B4 7ET, UK

The effect of AFT testing on slider debris was studied with explanation offered for debris location.

Accelerated Friction Test (AFT) apparatus was used to perform Contact Start Stop (CSS) tests using standard rigid disks and two different air bearing slider types. Dynamic and static friction (stiction) were measured during cycling.

Dynamic friction over the CSS cycles was modelled using a set of matrix equations to describe the friction trace at particular instances during the tests. A logistic model was used to describe mean friction over the flying period of each cycle in the test, with parameters representing the initial rate of surface smoothing and eventual wear level. Increase in friction variation with time was also examined. Stiction values were modelled as highly positively skewed and increased during the tests due to surface wear.

Atomic Force Microscopy (AFM) and Scanning Electron Microscopy (SEM) were used to study head and disk topography at various test stages and to provide physical parameters to verify the models. X-ray Photoelectron Spectroscopy (XPS) was employed to identify surface composition and determine if any chemical changes had occurred as a result of CSS testing.

Test results where interface failure had occurred conflicted with those predicted by the mathematical models. Surface analysis of crashed surfaces revealed severe, irreversible wear damage that could not be attributed to one, but many interacting modes of wear.

Keywords: - Modelling, debris location, surface analysis, failure.

FRICTION, STICTION AND WEAR IN RIGID DISK DRIVES

J.Collins (*) and J.L. Sullivan, Aston University, Birmingham, B4 7ET, UK

The effect of AFT testing on slider debris was studied with explanation offered for debris location.

ENVIRONMENTAL EFFECT IN RIGID DISK DRIVES

J.Collins (*) and J.L. Sullivan, Aston University, Birmingham, B4 7ET, UK

Modelling environmental effect on stiction and wear was best achieved using water vapour pressure, not relative humidity, to quantify the moisture content of air.